Augmented Reality and Numerical Simulations for Hepatic Tumors Resection

Rosalie Plantefève

Université de Lille 1 SCIENCES ET TECHNOLOGIES

Document soumis pour obtenir
le titre de Docteur de l'Université
des Sciences et Technologies de Lille

EDSPI: Section Informatique

Augmented Reality and Numerical Simulations for Hepatic Tumors Resection

Rosalie Plantefève
INRIA MIMESIS
ALTRAN

Defended on the 8^{th} of June 2016

Jury:

Advisor:	Stéphane Cotin	-	MIMESIS Team, Inria
Industrial advisor:	Jean-Pierre Radoux	-	ALTRAN
Reviewers:	Thomas Langø	-	Department of Medical Technology, SINTEF
	Yohan Payan	-	TIMC-IMAG, Université Grenoble I
Examiners:	Stefanie Speidel	-	Medizintechnik, KIT
	Patrick Pessaux	-	Université de Strasbourg

Acknowledgements

Firstly, I would like to thank my thesis director, Stephane Cotin, for his help, his patience, his kindness, and the confidence that he has placed in me during these three years. Thank you for the time you spend to explain to me some concepts, to discuss ideas, and to give me hints and directions (and also to bring very often candies in my office and to put some 's' where they were missing ^^). I greatly appreciate that you always tried to widen my research topic, even if I did not explore all the ways you opened for me. I really enjoyed being a member of your team!

J'aimerais également remercier mon responsable industriel, Jean Pierre Radoux. Même si je n'ai pas passé beaucoup de temps à ALTRAN durant ma thèse, j'ai apprécié ta sincérité et ton écoute attentive à la fois sur des sujets scientifiques et plus personnels.

Beside my two supervisors, I would like to express my gratitude to the rest of my thesis committee: Dr. Thomas Lango, Dr. Yohan Payan, Dr. Stefanie Speidel, Prof. Patrick Pessaux and Dr. Igor Peterlik. I want to address a special thanks to my two reviewers Dr. Thomas Lango, and Dr. Yohan Payan, who have, despite their busy schedule, taken the time to perform this review.

Ma thèse n'aurait pas été aussi intéressante sans l'aide précieuse du professeur Patrick Pessaux qui m'a permis de venir assister à de nombreuses opérations chirurgicales et qui a toujours répondu présent lorsque j'avais besoin d'obtenir des images médicales. Merci d'avoir pris le temps d'essayer les différents protocoles d'acquisitions que nous voulions tester et d'avoir été patient lorsque les résultats tardaient à arriver. Merci également aux autres chirurgiens impliqués dans le projet, Riccardo Memeo et Vito De Blasi.

Je souhaite également remercier tout particulièrement Igor Peterlik pour son aide précieuse durant ces trois ans. Merci d'avoir veillé tard avec moi les soirs de deadline, et d'avoir toujours attentivement relu tous mes papiers, même ceux dont tu n'étais pas co-auteur. Merci d'avoir toujours pris le temps de répondre à mes questions et de les avoir prises avec sérieux même lorsque que je les pensais un peu idiotes ^^ . Merci aussi pour les déjeuners sushi !

Merci à Hadrien Courtecuisse pour ses conseils avisés. J'ai été contente de pouvoir partager ton bureau pendant quelques mois et de suivre ta préparation au concours de chargé de recherche du CNRS. Merci d'avoir

pris le temps de discuter avec moi des directions à prendre dans ma thèse. Merci pour tes encouragements et ton intérêt pour mon travail !

Christoph, merci pour ton écoute, tes conseils et ton aide qui ont vraiment compté pour moi, surtout durant ces derniers mois. Merci pour les entraînements d'aviron, pour les balades en canoë, pour tes 'linzertorte', et pour tes barres de céréales ^^. Merci pour les soirées passées à travailler (ou pas) en ta compagnie. Merci pour ta bonne humeur et ta gentillesse. Je suis très heureuse de t'avoir rencontré et je te souhaite le meilleur pour ta fin de thèse. J'espère que tu n'hésiteras pas à me demander de l'aide si tu en as besoin !

Merci à Bruno et Marc, mes ingénieurs préférés, pour m'avoir si souvent aidé lorsque mon ordinateur ne me comprenait pas, ou lorsque je ne comprenais pas mon ordinateur.

Bruno, merci d'être si souvent resté tard et arrivé tôt pour pouvoir terminer à temps la préparation des données pour les tests en salle d'opération. Je m'excuse auprès d'Aidee pour toutes ces heures supplémentaires. Merci pour ton aide en général et plus spécifiquement sur des questions d'informatique ou d'anglais. Merci pour les soirées barbecue, et la tradition des sushis après les tests en salle d'opération.

Marc, merci de m'avoir patiemment expliqué l'intérêt de git et d'avoir toujours détaillé ta démarche pour solutionner mes problèmes. Merci d'avoir corrigé tant de bugs dans SOFA ^^. Merci de m'avoir supporté lorsque je t'envoyais des grenouilles ou que je cachais ton dessert et de m'avoir écouté lorsque j'avais besoin de parler.

Jaime, merci d'avoir été un co-bureau si sympathique et de m'avoir initié aux techniques de calibrations et à Mevislab. Merci également pour la relecture d'un des chapitres de cette thèse. Bonne chance pour la fin de ta thèse !

Raffaella, merci pour ton travail sur l'atlas lors de ton stage, pour toutes les tâches d'organisation que tu as remplies dans l'équipe, et pour les papotages de bureau. Bon courage pour la fin de ta thèse et pour ta futur maternité, je suis sûre que tu vas très bien réussir les deux !

Myriam, j'ai beaucoup aimé partager ton bureau. Ton calme et ta concentration sont vraiment remarquable ! J'espère que tout continue à bien se passer pour toi !

Santiago, thank you for your work on the visualization part of this work. I will be very happy to work again with you for your diploma thesis.

Valentin, merci pour les heures passées à lancer des tests de simulation et à réaliser des graphiques, parfois jusqu'à très tard le soir. J'ai hâte d'avoir plus de temps pour m'impliquer davantage dans l'encadrement de ton stage.

Merci aussi aux autres membres de l'équipe : Emmanuel pour tes conseils lorsque je stressais pour la fin de ma thèse, et pour ta patience sur le projet SofaOR, Étienne pour ton patriotisme alsacien (et désolée d'avoir si souvent détartré la bouilloire avec du vinaigre), Fred pour avoir si souvent aidé Santiago avec les shaders, Guillaume pour t'occuper si bien du développement de SOFA, Hugo pour ton esprit d'équipe et ton implication dans les tâches plus "administratives", Lionel pour tes conseils toujours judicieux et pour avoir relu attentivement un chapitre de ma thèse, Nazim pour l'ambiance que tu mets en salle de pause, Phuoc pour ta gentillesse, et Rémi pour l'aide que tu apportes si facilement aux autres.

Merci aux membres d'Insimo qui ont partagés leur bureaux avec moi au tout début de ma thèse !

Merci Abdelkrim pour tes questions tout au long de ma thèse qui m'ont permis de remettre en causes certaines choses et pour tes remarques et conseils.

Merci à nos assistantes d'équipes, Anne, puis Isabelle, qui ont toujours réussi à trouver des solutions même lorsque je leur soumettais des demandes de dernière minute.

Merci aux stagiaires de l'équipe : Alex, Andréa, Mohamed, Nicolas et Thomas sans lesquels l'ambiance ne serait pas la même.

Thanks to the IRCAD fellows and in particular to Ben and Albert for their proofreading of some parts of my thesis and some other documents.

Thanks to Pietro for his smile and his help in the "ink-spray" project.

Merci également à tous les gens de l'IHU que je croise tous les matins, et en particulier à Clélia pour avoir toujours réussi à répondre à mes demandes malgré son importante charge de travail.

Un très grand merci à ma famille pour m'avoir toujours témoigné sa confiance et soutenu dans mes choix lors de mes années d'études.

Merci à Bernard et Béatrice de m'avoir accueilli si naturellement dans votre famille, et de m'avoir rendu tant de services.

Merci enfin à Jonathan à qui je n'ai pas vraiment rendu la vie facile ces derniers mois. Merci d'avoir pris en charge les courses, la cuisine et le ménage pendant que je passais des heures devant mon écran d'ordinateur. Merci d'avoir accepté que je ne puisse pas vraiment sortir, ni regarder de films, ni passer du temps à discuter avec toi pendant ma période de rédaction. Et merci de m'avoir toujours rassurée lorsque je stressais.

Abstract

Liver cancer is the 2nd most common cause of cancer death worldwide, with more than 745,000 deaths from liver cancer in 2012. When including deaths from liver cirrhosis, the toll reaches nearly 2 million people worldwide. Today, surgical tumors ablation remains the best treatment for liver cancer. To localize the hepatic tumors and to define the resection planes, clinicians rely on pre-operative medical images (obtained with computed tomography scanner or magnetic resonance imaging). However, the liver lesions and vascular system are difficult to localize during surgery. This may lead to incomplete tumor resection or haemorrhage. The purpose of this thesis work is to provide surgeons with an augmented view of the liver and its internal structures during surgery to help them to optimally resect the tumors while limiting the risk of vascular lesion. Therefore, an elastic registration method to align the pre-operative and intra-operative data has been developed. This method, which uses a biomechanical model and anatomical landmarks, was designed to limit its impact on the clinical workflow and reaches a registration accuracy below the resection margin even when the liver is strongly deformed between its pre-operative and intra-operative state. This registration algorithm has been integrated into a software, sofaOR, to conduct the first clinical tests.

Keywords: Registration, Hepatic surgery, Laparoscopic surgery, Intra-operative guidance, Biomechanical model, Atlas, Boundary conditions, Augmented reality.

Résumé

Les cancers du foie sont la seconde cause de mort par cancer avec plus de 745,000 morts en 2012. Si l'on inclu les cas de cirrhose du foie, le nombre total de morts par an dans le monde atteint presque 2 million. Le meilleur traitement actuel pour ces patients est l'ablation chirurgicale de ces tumeurs. Pour les localiser et planifier l'opération, les chirurgiens se basent sur des images médicales pré-opératoire (obtenues par tomodensitométrie ou imagerie à résonance magnétique). Cependant, durant l'intervention, ces tumeurs, ainsi que le réseau vasculaire du foie, sont difficiles à localiser pour le chirurgien. Cela peut conduire à une résection incomplète des tumeurs où à la lesion accidentelle de vaisseaux sanguins. Le but de ce travail de thèse est de proposer aux chirurgiens une vue du foie et de ses structures interne en réalité augmentée durant l'opération pour les aider à réséquer les tumeurs de manière optimale en limitant les risques pour le patient. Pour cela, une méthode de recalage élastique des données pré-opératoires sur la vue intra-opératoire a été développée. Cette méthode, qui utilise un modèle biomécanique et certains repères anatomiques présents sur le foie, a été conçue pour limiter son impact sur la routine clinique et permet d'atteindre une erreur de recalage inférieure aux marges chirurgicales même en cas de déformation importante du foie entre son état pré-opératoire et intra-opératoire. Cet algorithme de recalage a été intégré à un logiciel, sofaOR, pour permettre les premiers essais cliniques.

Mots clés : Recalage, Chirurgie hépatique, Chirurgie laparoscopique, Guidage intra-opératoire, Modèle biomécanique, Atlas, Conditions limites, Réalité augmentée

Contents

Abbreviations

Acronym	Description
AM	Anterior margin
AR	Augmented reality
CT	Computed tomography
DRR	Digitally reconstructed radiographs
FEM	Finite element method
FRE	Feature registration error element method
GPA	Generalized Procrustes analysis
ICP	Iterative closest point
IGS	Image guided surgery
MIS	Minimally invasive surgery
MST	Minimum spanning tree
MR	Magnetic resonance
MRI	Magnetic resonance imaging
ODT	Optimal Delaunay triangulation
OR	Operating room
PCA	Principal component analysis
RPM	Robust point matching
SFM	Structure from motion
TRE	Target registration error
TRUS	Transrectal Ultrasound
UN	Umbilical Notch

Notations

Chapter 1

α	Facet angle: minimum admissible angle of a surface triangle. Parameter of the CGAL mesh generation algorithm.
s	Facet size: maximal size of a surface triangle. Parameter of the CGAL mesh generation algorithm.
d	Facet distance: maximal distance between a face and the domain boundary. Parameter of the CGAL mesh generation algorithm.
γ	Cell radius edge ratio: maximal value of the ratio of a tetrahedra circumsphere radius on the smallest edge of the tetrahedra. Parameter of the CGAL mesh generation algorithm.
ζ	Cell size: maximal size of a tetrahedra. Parameter of the CGAL mesh generation algorithm.
ξ	Face topology. Parameter of the CGAL mesh generation algorithm.
σ_0	Minimum dihedral angle.
v_i	i^{th} mesh vertex.
Ω_i	Star of vertex i.
V_i	Voronoi cell of vertex i.
$\rho(x)$	Density function.
S	Centerline source node. Distance from segmented map boundary.
E	Pathlink end point.
C	Centerline point.
$B(u, v)$	Branch starting at point u and ending at point v corresponding to a vessel centerline.
$\mathbf{c}$	Camera coordinate system.
$\mathbf{o}$	Optical center of the camera.
$\mathbf{x}$	Point of the three dimensional world.
$\mathbf{x}_{proj}$	Projection of $\mathbf{x}$ in the image plane expressed in the world coordinate system.
$\mathbf{p}$	Vector joining $\mathbf{o}$ and $\mathbf{x}_{proj}$.
$\mathbf{P}$	Projection matrix.
σ	Scale factor.
$\widetilde{\mathrm{p}}$	Augmented image coordinate of $\mathbf{x}_{proj}$.
$\mathbf{A}$	Matrix of intrinsic parameters.
k_u	Ratio between the unit of the first ideal image axis and the first pixel image axis.
k_v	Ratio between the unit of the second ideal image axis and the second pixel image axis.

θ	angle between the two pixel image axis.
u_0	First coordinate of the real image center in the ideal image reference frame.
v_0	Second coordinate of the real image center in the ideal image reference frame.
$\widetilde{\mathrm{p}}_{pixel}$	Augmented image coordinate of $\mathbf{x}_{proj}$ in pixels.
p	Pixel image coordinate of $\mathbf{x}_{proj}$.
$\mathbf{R}$	Rotation between the two camera coordinate system.
$\mathbf{t}$	Translation between the two camera coordinate system.
$\mathbf{H}$	Hessian matrix.
$D_{ij_\sigma}(\mathrm{p})$	Approximation of the Gaussian second order derivative $\frac{\partial}{\partial ij}g(\sigma)$ convolved with the image intensities around point p.
$\mathcal{D}(\mathrm{p})$	descriptor of p.
τ_d	Threshold for the detection of feature points.
$\mathcal{M}(\mathrm{p}_1)$	Matching point of p_1 in the image 2.
d_{12}	Distance between the descriptors of points p_1 and p_2.
$\mathcal{S}$	Similarity measure between descriptors.
τ_m	Threshold for the matching of points.
$\mathbf{F}$	Fundamental matrix.
$\mathbf{E}$	Essential matrix.
Δ_{12}	Reprojection error.

Chapter 3

$\mathbf{f}_{ext}$	External forces.
$\mathbf{f}_{int}$	Internal forces.
$\mathbf{n}$	Normal vector.
$\mathbf{t_n}$	Stress vector in the direction $\mathbf{n}$.
ρ	Mass density.
$\mathbf{v}$	Velocity.
$\mathbf{T}$	Cauchy stress tensor.
T_{ij}	Element (i, j) of the Cauchy stress tensor.
$\mathbf{u}$	Displacement vector between the non-deformed and the deformed configuration.
$\mathbf{p}$	Point of a physical object in the rest (or non-deformed) configuration.
$\widetilde{\mathbf{p}}$	Point of a physical object in the deformed configuration.
Φ	Physical transformation.
$\mathbb{F}$	Gradient of the physical transformation.
ϵ_c	Right Cauchy-Green strain tensor.
ϵ_g	Green-Lagrange strain tensor.
$\boldsymbol{\epsilon}$	Infinitesimal strain tensor.
Ξ	Constitutive law of the material.

c_{ijkl}	Four order tensor of a linear constitutive law.
$\mathbf{C}$	Matrix form of c_{ijkl} (obtained using the Voigt notation), also called stress-strain matrix.
$W(\boldsymbol{\epsilon})$	Strain energy.
λ	First Lamé's Coefficient.
μ	Second Lamé's Coefficient.
E	Young's modulus.
ν	Poisson's coefficient.
$d\Omega$	Domain boundary.
Γ_D	Sub-part of $d\Omega$ where Dirichelet boundary condition are applied.
Γ_N	Sub-part of $d\Omega$ where Neumann boundary condition are applied.
N	Shape function.
$\mathbf{K}$	Stiffness matrix.
$\mathbf{M}$	Mass matrix.
$\mathbf{D}$	Damping matrix.
$\mathbf{B}$	Strain-displacement matrix.
$\mathbf{R}$	Rotation matrix.
$\mathfrak{u}$	vector of nodal displacement.
N_{tot}	Number of note in the finite element mesh.
Δ_t	Time step for temporal integration.
$\mathbf{J}$	Jacobian matrix.

Chapter 4

$\mathbb{S}$	Source data (which is to register).
$\mathbb{T}$	Target of the registration.
$\mathcal{E}$	Distance measure between the source and target data.
$\mathcal{S}$	Similarity measure between the source and target data.
$\mathcal{T}$	Transformation between the source and target data.
$\mathcal{R}$	Regularization term.
$\mathbf{f}_{ext}$	Penalty forces.
p_s	Point of the source model.
p_t	Point of the target model.
$\mathbf{p}_{ts}$	Vector which goes from p_t to p_s.
E	Young's modulus.
ν	Poisson's coefficient.
k	Stiffness coefficient.
d_{90}	Distance at wich te force intensity is equal to 90% of its maximal value.
$\mathbf{K}$	Stiffness matrix.
$\mathbf{M}$	Mass matrix.
$\mathbf{D}$	Damping matrix.

$\mathfrak{u}$ vector of nodal displacement.

Chapter 5

$SIM(.)$ Similarity transformation of the GPA.
$\{e\}$ Set of all mesh edges.
E_{seeds} Set of all seed edges.
$\mathbf{n}$ Normal vector.
τ_1 "Sharpness" threshold for seed edges selection.
τ_2 Direction threshold for extension of the anterior margin from the seed edges.
τ_3 "Sharpness" threshold for extension of the anterior margin from the seed edges.
G Gravity center of a mesh.
V Mesh volume.
$\mathcal{S}_i$ Space of the i-th segmented model.
$\mathcal{C}$ Space of the aligned models.
$\mathbf{P}_i$ Initial point cloud corresponding to the mesh of the i-th segmented model.
$\mathbf{P}'_i$ Aligned point cloud corresponding to the mesh of the i-th segmented model.
$\mathbf{T}$ Translation matrix.
$\mathbf{R}$ Rotation matrix.
s Scale factor.
$\bar{\mathbf{P}}$ Mean shape.
SVD(.) Singular value decomposition.
tr(.) Trace of a matrix.
$\|.\|_F$ Frobenius norm.
$\mathbf{P}$ Matrix gathering the data about all the liver shape after the GPA.
$\mathbf{C}$ Covariance matrix.
$\mathbf{U}$ Matrix of eigenvectors.
$\mathbf{D}$ Diagonal matrix of eigenvalues.
σ_{UN} Standard deviation associated to the umbilical notch position.
σ_{VC} Standard deviation associated to the *vena cava* position.

Chapter 6

v_i i-th vertex of the mesh.
α_{surf_i} Alpha value (transparency) of v_i of the surface mesh.
$\mathbf{n}$ Normal vector.
$\mathbf{d}_c$ Camera direction.
α_{int_i} Alpha value (transparency) of v_i of the internal structure meshes.
$d_{\max}$ Depth at which the internal structures are completely transparent.

General Introduction

The liver is a vital organ particularly exposed to diseases because of its role in organism detoxification. One of the most lethal liver pathologies is the primary liver cancer with 47,000 deaths in Europe and 745,000 deaths worldwide per year according to the world health organization (WHO). Besides, these statistics do not take into account liver metastasis originating from other cancerous organs, in particular colorectal liver metastasis (incidence ~15% according to Landreau *et al.* (2015)).

Figure 0.1: A laparoscopic surgery

Without treatment, the 5-year survival rate of liver cancer is only 5% (EASL), but with surgical treatment it increases to 38-61% (Torzilli *et al.*, 2013). Each patient with suspected liver cancer is first directed to a medical imaging center where images of its anatomy are acquired thought Magnetic Resonance Imaging (MRI) or Computer Tomography (CT). These acquisitions are lengthy and require the use of contrast agent to visualize properly the different organs and their internal structures. Then, the resulting volume images are analyzed by the clinicians to confirm the diagnosis and to locate the tumor(s). If surgery is selected as the best treatment for the patient, the surgeons decide between classical open procedure or minimally invasive surgery (MIS). This relatively new technique, first introduced in 1987 by Mouret for a cholecystectomy, has developed significantly in last fifteen years thanks to the improvement of surgical tools and procedures. MIS is now performed in various surgical specialties, ranging from orthopedics to gynecology.

In MIS — called laparoscopy in digestive and pelvic surgery — only a

few numbers of small incisions are required to access the wounded area. Thus, the damage to healthy tissue is reduced compared to open surgery. Therefore, MIS procedures provide important benefits for the patients: reduced post-operative morbidity, reduced pain, shorter recovery time and smaller scars (Vigano *et al.*, 2009).

During a typical laparoscopy, carbon dioxide is first insufflated in the patient's abdominal cavity to create a sufficient working space around the organs (pneumoperitoneum). Then, a camera (the laparoscope or the endoscope) and long surgical instruments enter through trocars placed in the small apertures made in the abdominal wall (see Fig. 0.1). From that moment, the clinicians follow the movements of the instruments on a monitor which displays the images captured by the laparoscope. They usually rely on pre-operative images to precisely localize the wounded areas. Additionally, a two dimensional laparoscopic ultrasound probe may be used to image the liver internal structures during the intervention. In spite of its advantages and high sensitivity for tumor detection, laparoscopic ultrasound is not widespread, mainly because of its complex manipulation (Rethy *et al.*, 2013). Additionally, due to the small imaging range of this kind of probe, large organ cannot be entirely captured and an important amount of time is required to obtain relevant information.

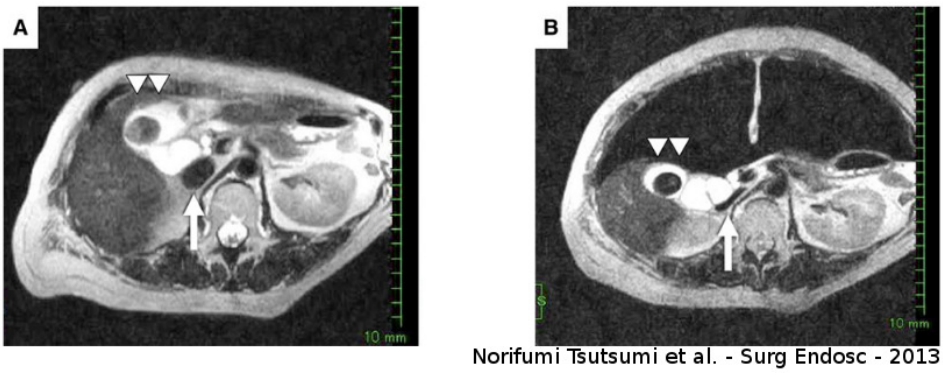

Figure 0.2: Important deformation of the liver induced by the pneumoperitoneum (MRI images from Tsutsumi *et al.* (2013))

Despite its advantages, MIS suffers from important drawbacks. Firstly, organ manipulation is more challenging in MIS than in open surgery. Indeed, while in open surgery the clinicians have a wide access to the operating field, in MIS they can only access the organs through the laparoscopic instruments. The loss of direct manipulation and the fulcrum effect make the surgical gestures more complex to perform. Secondly, the operating field is only seen through a camera, generally held by an assistant, making the eye hand coordination challenging. Thirdly, the navigation inside the patient's

body is demanding due to the reduced field of view of the laparoscope and to the loss of the depth information. Lastly, as the clinicians employ undeformed pre-operative images to locate lesions, the strong deformation of the abdominal organs caused by the pneumoperitoneum amplifies the difficulty.

The consequences of these limitations are an increased risk of tissue damage due to manipulation errors, difficulties to locate tumors and to define resection margins and an increased operating time (Vigano *et al.*, 2009). Therefore, the patient safety can be threatened. Today, one of the major risks related to the laparoscopic liver resection is haemorrhage which leads to 80% of conversion to an open surgery (Gagner *et al.*, 2004). For this reason, some patients whose tumors are close to blood vessels undergo the open surgery (Vigano *et al.*, 2009).

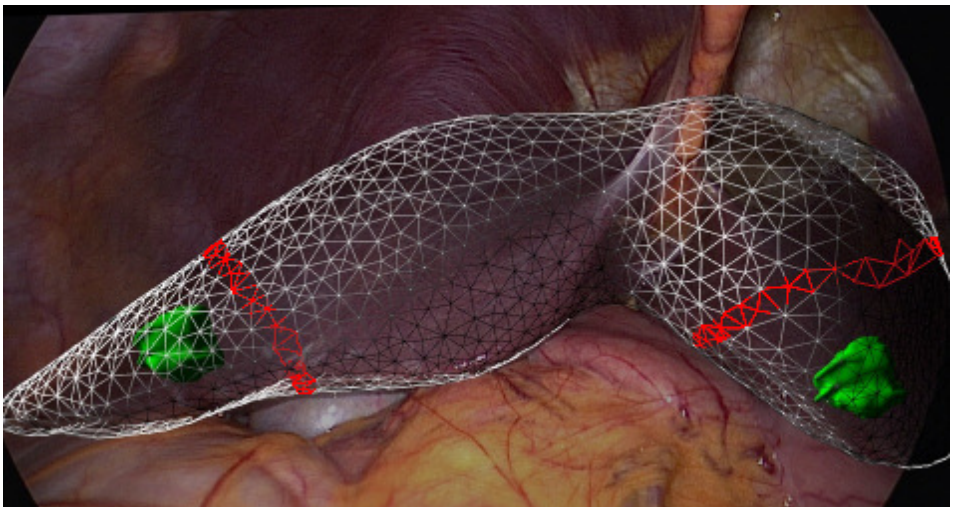

Figure 0.3: Augmented reality view of the liver

Guidance systems for MIS have been developed in the last decade to improve patient safety, to help surgeons better target the wounded area and to reduce the operating time. Let us note that this is an important economic issue for hospitals. These guidance systems provide relevant information to the surgeon that are related to the patient anatomy, not visible through the laparoscope and that help them taking informed decisions during the intervention. Guidance system requires the intra-operative fusion of data from different sources (laparoscope, ultrasound probes, pre- or intra-operative radiography, CT or MRI, electromagnetic devices ...). For standard laparoscopy, only laparoscopic images, pre-operative images and eventually ultrasound images are available. The result of this fusion can then be used in different ways, but the most common solution is to display the result as

images. In this case, the guidance system is referred to as an Image Guided Surgery (IGS) system. IGS systems may show the fused information on a separate display or integrate it directly in the laparoscopic view. This second option has the important advantage of reducing the number of information sources that the surgeon follows. In addition, an integrated view can be updated in real-time to match the intra-operative laparoscopic view. This approach, known as Augmented Reality (AR), is an appealing solution which intuitively concentrates all the relevant information in a unique view. This allows the surgeon to focus only on the operating field.

However, the intra-operative fusion of the different data sources is a challenging issue. The various devices that are used to acquire the data do not share a common reference frame. Moreover, if pre-operative images are employed, the actual shape of the abdominal organs does not correspond to the intra-operative shape because of the deformations induced by the pneumoperitoneum. Thus, the data fusion implies the resolution of a non-rigid registration problem. This problem is usually described as a constrained minimization problem and seeks a transformation which optimally aligns the data. To solve this problem, a similarity measure is first defined between the different data. This distance represents the error in the data alignment. Then, a prior knowledge is introduced into the problem as a constraint imposed on the possible set of solutions. Finally, a minimization algorithm is employed to find the optimal transformation. A wide number of registration methods exists, generally developed for a particular application case.For a comprehensive survey on medical image registrations, the reader is referred to Sotiras *et al.* (2013).

The main challenge of registration algorithms is to avoid the pitfall of local minima. When one of these minima is clearly a global minimum, the algorithm usually converge to the solution upon a good initial alignment of the input data. However, the absence of a well defined global minimum indicates that the registration problem is ill-posed. In this case, several solutions are acceptable according to the similarity measure, which is an issue because the registration problem should have a unique solution. In other words, many of the acceptable solutions are actually wrong. To alleviate this problem, additional prior knowledge is required.

In the case of AR surgical guidance system, two registration phases are usually distinguished: the initial registration which occurs when the surgeon decides to start the guidance system, and the temporal registration which begins after the initialization phase is completed. These two phases raise different difficulties. During the first phase, the registration has no strict time constraint but no assumption can be made regarding the initial configuration of the pre-operative data relatively to the intra-operative data.

Moreover, the deformation between the data may be important. Conversely, as the initial configuration of the data at one time frame of the temporal registration is provided by the registration result of the last time frame, the initialization of the temporal registration problem is fair. The difficulty comes from the fact that the registration should be performed in real-time. To solve the this, efficient methods based on a mechanical formulation and optical tracking have been proposed (Haouchine *et al.*, 2013). However these methods require a good initial alignment and an accurate definition of boundary conditions, which determine the relation of the studied object with its environment. Concerning the liver, the boundary conditions reflect the fact that the liver is attached to and in contact with other structures in the abdominal cavity.

The work presented in this thesis focuses on the elaboration of a system for laparoscopic liver surgery guidance that provides an intuitive AR view of hepatic internal structures (tumors and vascular tree). As a strong constraint, we require that the desired solution preserves the clinical workflow. First, many hospitals cannot afford intra-operative CT or MRI or limit their use to the sole interventional radiologists. On the other hand, laparoscopic surgeons, and more generally the hospital staff, are familiar with the standard procedure and may be reluctant to change their habits. In other words, changing the clinical workflow may hinder the adoption of a new system. As a consequence, our solution prohbit the use of intra-operative imaging devices, apart from the laparoscope and an ultrasound probe. Since the ultrasound probe is not routinely used, the solution developed in this thesis supposes that the only available data are the undeformed pre-operative images and the laparoscopic view and leaves the integration of ultrasound data as future works.

The core of the surgical guidance system we propose, is an automatic, accurate and robust non-rigid registration method which aligns the internal structures onto the intra-operative laparoscopic view. This thesis deals with the development of an initial registration method that may be combined with temporal registration, possibly based on optical tracking. However, due to the sparse intra-operative data, the initial registration problem is actually ill-posed.

Actually, the only available intra-operative information is the partial surface lying on the field of view, while the registration has to be performed for the whole liver. For this purpose, additional knowledge is required. The nature of the prior knowledge we want to use in this work is threefold. First, anatomical knowledge is used to facilitate the matching between the partial intra-operative view of the liver surface and the pre-operative images. Second, the knowledge of the liver mechanical behavior helps to find

the deformations that this organ undergoes due to the pneumoperitoneum. This behavior is generally patient-specific and should be determined either from literature data (for instance according to the fibrosis of cirrhosis degree) or from a direct measurement. However, in the employed method we will see that the parameter relative values, rather than absolute value, influence the registration result. Finally, the knowledge of both physical and anatomical properties in an atlas permits the definition of the organ boundary conditions. This information can be advantageously exploited in the temporal registration algorithm. Fig 0.4 summarizes the pipeline.

The main contributions of this thesis can be summarized as follows:

- A non-rigid initial registration method which relies solely on routinely available data and uses both anatomical and physical prior knowledge to align the pre- and intra-operative images.
- The construction of a statistical atlas which contains information about the boundary conditions of the liver to facilitate the temporal registration.

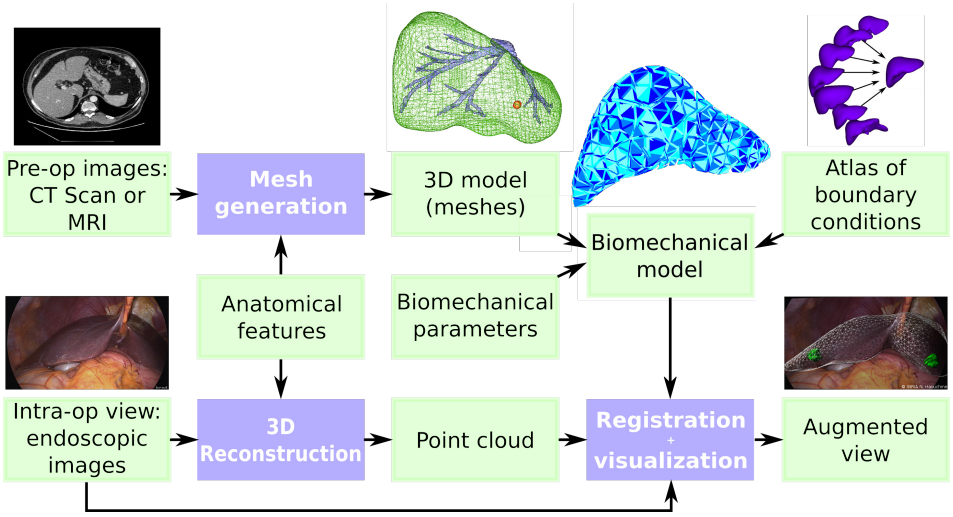

Figure 0.4: General scheme of the method developed in this thesis.

Structure of the manuscript

This manuscript is divided into three parts. The first part deals with the pre- and intra-operative data processing. The aim is to extract as much *a priori* information as possible to facilitate the registration process.

Chapter 1 describes how to convert the iconic pre- and intra-operative data into geometric objects to formalize the registration problem. The

pre-operative volume images are converted into meshes to be used within a physical framework, while the intra-operative laparoscopic images are converted into three dimensional point clouds.

Chapter 2 introduces the background on the liver anatomy and one of the main pathologies of this organ: the liver cancer. It also presents the possible treatments of this disease with a focus on the laparoscopic surgical treatment. This information allows us to select relevant anatomical features to facilitate the registration task.

Chapter 3 gives an introduction to continuum mechanics and the finite element method and presents the biomechanical models employed in this thesis.

The second part contains two main contributions: an efficient registration method for laparoscopic liver surgery and the construction of a statistical atlas of the liver boundary conditions.

Chapter 4 begins with a state of the arts of registration methods with a focus on registration between point clouds and meshes, physically based regitration, and intra-operative registration methods. Then, based on Plantefève *et al.* (2014a) and Plantefève *et al.* (2016), the registration method employed in this work is described and evaluated.

Chapter 5, based on Plantefève *et al.* (2014b), introduces the importance of boundary conditions for mechanical simulations and the difficulties associated to their determination for abdominal organs. Then, a method for the identification of boundary condition based on a statistical atlas is depicted and its accuracy is assessed.

The third part of this manuscript describes the deployment of the proposed method in the operating room and present the third contribution of this thesis, the development of a new visualization method for laparoscopic AR surgical guidance system.

Chapter 6 describes the operating room (OR) as well as the test protocol and the hardware and software setup to acquire and process the intra-operative data. The results obtained on real patient data are then detailed and analyzed and several visualization thechniques are proposed to display the results to the surgeons.

Finally, the perspectives as well as some directions for future work are discussed in a general conclusion.

Part I

Enrich the Pre- and Intra-Operative Data

Introduction

To construct an augmented view of the liver lesions and vascular structures during laparoscopy the shape and location of these anatomical structures is needed. Clinically, before each liver tumor resection the surgeon ask for pre-operative images of the patient's abdomen. These images are used by clinicians to locate the tumors and their irrigating vessels, which have to be resected. This pre-operative information can be used to find the intra-operative shape of the organ internal structure.

However, the nature of the pre- and intra-operative data is very different. While the pre-operative data are three dimensional images of the organ volume, intra-operative data are two dimensional images of the organ surface. Thus, these data should be processed to share a common representation. In addition pre-operative data should be registered, that is aligned, with the intra-operative data. Indeed, the position and shape of the liver in the pre-operative images and in the laparoscopic view are different. This is due to the fact that the reference frame of the pre-operative imaging device and the one of the camera are not the same. Thus, a mean to compute the transformation between the two reference frames should be found. Moreover, as in laparoscopic interventions gas is inflated in the abdominal cavity to provide surgeons with a sufficient working space, abdominal organs are deformed. Due to this deformation, the pre-operative shape of the organs and their internal structure cannot be used during the intervention. The pre-operative data should therefore be deformed in order to match their intra-operative shape, thus making the registration problem is ill posed.

In this part, we will see how to process the pre- and intra-operative data to obtain additional information to better formulate the registration problem. We will first adopt a scientific point of view and analyze the pre- and intra-operative to find a common representation for both. Then, we will switch to a medical point of view and study the particularities of the liver and the specificity of laparoscopic interventions that may be useful to enrich the pre- and intra-operative data. Finally, we will see how to model the biomechanical behavior of the organ to better estimate the deformation that occur between the acquisition of pre-operative images and the operation.

CHAPTER 1

From an Iconic to a Geometric Problem

Contents

To obtain an augmented view of the liver internal structures, the pre-operative data have to be registered into the intra-operative data. Two main types of input can be distinguished for registration algorithms: iconic and geometric inputs. The first type cast the registration problem as an intensity-based registration problem, while the second implies the use of feature-based registration methods. Hybrid methods which combine geometric and iconic inputs have also been proposed (see for instance Lange *et al.* (2009) 1.1(a)).

As we want to keep the clinical workflow unchanged, we have to use standard available clinical data. The pre-operative data — usually generated using Magnetic Resonance Imaging (MRI) devices or Computed Tomography (CT) scanners — are three dimensional (3D) grey level images representing the internal structures of the human body (Fig. 1.1(a)).

On the other hand, the standard intra-operative data are laparoscopic color images of the patient's abdomen, where only the surface of the organs is visible (Fig. 1.1(b)). The intensities of both types of images are unrelated (Fig. 1.1), making intensity-based registration approaches pointless. Therefore, geometric representations of these data have to be used to solve the registration problem.

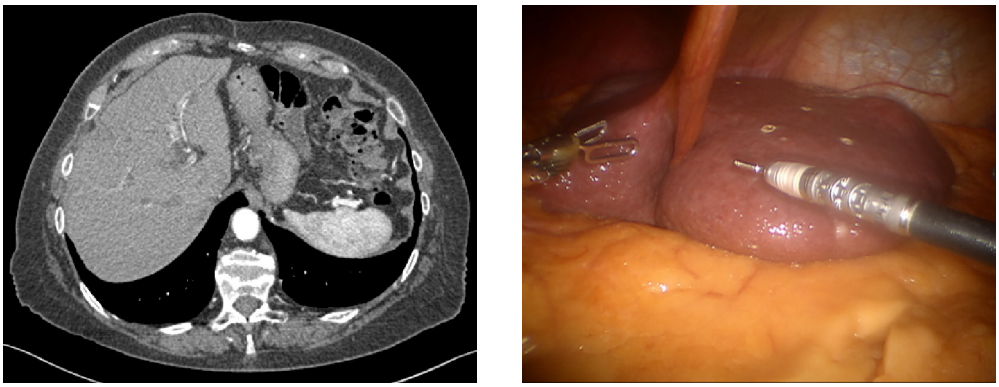

(a) A pre-operative CT image (b) An intra-operative laparoscopic image

Figure 1.1: The pre- and intra-operative images cannot be used directly to formulate the registration problem.

Several types of geometric representation can be adopted, the simplest one being a point cloud. This representation of objects do not provide any connectivity information, the points are independent of each other. For the intra-operative data, as we are only interested by the position of the liver surface, a point cloud representation is sufficient. However, due to the important deformation of the organs between the pre- and intra-operative data acquisition, the pre-operative data should be deformed to match the intra-operative configuration of the organs. This deformation is the result of physical forces exerted on the organ, and therefore the organ physical behavior should be taken into account. Thus, we employ a biomechanical model and the finite element method (FEM) to restrain the set of possible deformations (see chapter 3). This biomechanical formulation require the use of an advanced geometric representation which contains connectivity knowledge: a volume mesh.

To obtain these two geometric representations of the liver, it is necessary to process the pre- and intra-operative images. This chapter first describes the different steps which transform the volume images into a volume mesh. Then, the procedure to obtain a point cloud from the laparoscopic images is detailed.

1.1 From pre-operative images to meshes

In this section, we describe how to transform a pre-operative image of the liver, acquired with a Magnetic Resonance Imaging (MRI) device or a Computer Tomography (CT) scanner, to a geometric representation of this organ. As the standard imaging modality for liver diagnostic is CT, we detail the procedure only for CT images. However, the method presented here can be applied onto MRI or CT images indistinctively. Firstly, we outline some important characteristics about CT images for the construction of a complete 3D model of the liver, including vascular structures and tumors. For more details about the principles of CT imaging the interested reader is referred to the review Kalender (2006) and to the book Hsieh (2009). Secondly, the segmentation process, which selects the organs and structures of interest in the pre-operative images, is detailed. Thirdly, the conversion from the segmentation result into a geometric model, namely a mesh, is described.

1.1.1 Typical pre-operatives images

Pre-operative images are useful for clinicians, who routinely analyze them, but their characteristics make their transformation into a geometric object not straightforward.

CT images are slightly distorted 3D grey level images whose voxel intensities depend on the tissues absorption coefficient of X-rays. The images used in this thesis are provided by the *Nouvel Hopital Civil* of Strasbourg (NHC) and their typical resolution is $0.7 \times 0.7 \times 0.7\,\text{mm}$.

One of the main problem with the generation of a good quality CT image is motion artifacts. Indeed, the CT scanner acquires one image slice at a time, thus if the organs move during the acquisition — for instance because of the respiration — motion artifact may appear. Algorithms for respiratory motion compensation exist, but with fast modern multi-detector CT scanners (Ji *et al.* (2001)) the best strategy is to ask the patient not to breath during the acquisition. Today, if the patient hold his/her breath and is steady, the only area that may be affected by motion artifact is the area surrounding the heart. Hence, the motion artifacts in the abdominal region appear only in the upper part of the abdomen.

The other main concern with CT images is their contrast. The purpose of these images is to detect anatomical abnormalities. For the liver — its anatomy is described in chapter 2 — it is about localizing the lesions and determine whether they are benign or malignant. Therefore, a high contrast between healthy and tumorous tissue is required. This is achieved by the use of contrast agent injections, which highlight liver lesions. The contrast agent also allows a better visualization of the vascular tree of the

liver, which is important to plan the tumor resection. However, the contrast agent do not reach all the vascular structures at the same time. Actually three phases can be distinguished:

- Arterial phase (about 20 seconds after the injection): the contrast agent is mainly in the liver arteries.
- Early venous phase (after 35 seconds): the contrast agent reaches the parenchyma and the portal vein.
- Late venous phase (after 60 seconds): the hepatic veins are highlighted.

Therefore, three acquisition sequences are needed to obtain all the vascular structures of the liver.

We have seen that resolution as well as the contrast of CT liver images is limited. To obtain the best images the patients should be steady and hold their breath, and a contrast agent injection should be performed to enhance the image contrast. Moreover, three scanner sequences are required to visualize the complete vascular tree of the liver. We will now detail how to process these images to isolate the liver and its internal structures.

1.1.2 Image Segmentation

Images segmentation is the process of selecting structures of interest from the volume image (e.g. the liver, the stomach, etc.). Developing new segmentation methods was beyond the scope of this work, and the purpose of this section is only to explain how the medical image segmentation is performed for the work described here. For a review of segmentation algorithms the interested reader is referred to the review Heimann and Meinzer (2009) which concentrate on methods based on statistical shape model, to the survey Campadelli *et al.* (2009) which details the "state-of-the-art" algorithms for liver segmentation on CT images and proposes a new grey-level based segmentation method, or to Ma *et al.* (2010) which focuses on the application of "state-of-the-art" algorithm for the segmentation of the pelvic cavity.

Despite the important advances in this field over the past ten years, a fully automatic process for the segmentation of the liver and its vessels and tumors is not yet available. Among the different software for quasi-automatic liver segmentation, the solution proposed by MEVIS (Mev) seems to be the more advanced, but still required user interactions and validation. Moreover, this software is not freely available. As a result, an open source software, ITK-Snap Yushkevich *et al.* (2006) has been preferred.

The segmentation method used in this thesis consists of two steps. First, the images are processed to delineate the liver, its vessel tree and its lesions. Then, a post-processing step cleans the segmented map.

Creation of the segmented map

The ITK-Snap semi-automatic segmentation algorithm is based on active contour (Snakes, Kass *et al.* (1988)). First, a pre-processing step defines the Region Of Interest (ROI) and the grey-level range of the structure of interest. Then, a certain number of seeds (bubbles) are placed inside the structure of interest. Theses seeds should be distributed homogeneously within the structure volume. Finally, the iterative algorithm is run until the segmentation result is satisfying. As the voxel size of typical medical images is about $0.7 \times 0.7 \times 0.7$ mm, the segmentation result has an accuracy limited to $\sqrt{0.7^2 + 0.7^2 + 0.7^2} \approx 1$ mm.

Obviously, the quality of this semi-automatic algorithm depends on the contrast of the medical images which is not constant among the different imaging devices and even for different acquisitions set-up of the same device. Thus, a manual validation and correction of the output result is required. This leads to operator-dependent results and difficulties to reproduce exactly the same segmentation from identical input data. Moreover, the manual correction and validation is time consuming. Therefore, the segmentation process should be improved before being used in clinical routine.

Post processing of the segmented map

Occasionally, the segmented map of one organ presents more than one connected components and/or small holes (of size ≤ 7 voxels). These holes are generally due to noise: voxels of intensity significantly greater or lower than the average intensity of the structure of interest are not selected by the Snakes algorithm. The post processing step aims at selecting only the largest connected component and filling the holes inside it. Additionally, this step permits to smooth the segmented map to correct small errors in the segmentation that may lead to the generation of a rough mesh while the liver surface is smooth. Moreover, the convergence properties of mesh generation algorithm are usually ensured for smooth domain. Thus, a smoothed segmented map constitute a better input for the mesh generation algorithm. The impacts of segmented map smoothing are further discussed in section 1.1.4.

We have detailed how to obtain segmented maps of an organ and its

internal structures from volume medical images. We will now see how the segmented maps can be transformed into geometric objects usable by FEM.

1.1.3 Mesh Generation

The mesh generation is an important step for our method. Indeed, as already mentioned in the introduction of this chapter, the registration process (detailed in chapter 4) relies on a biomechanical model to consider the physical properties of the liver. We choose to employ the FEM for its capacity to handle easily complex geometry and the simplicity of this method for combining different types of elements. The point is that FEM is very sensitive to the mesh quality and to the number of elements in the mesh. Indeed, bad mesh quality leads to errors in the FEM solution, and increasing the number of elements increase the computation time required to solve the physical equations and thus the registration problem.

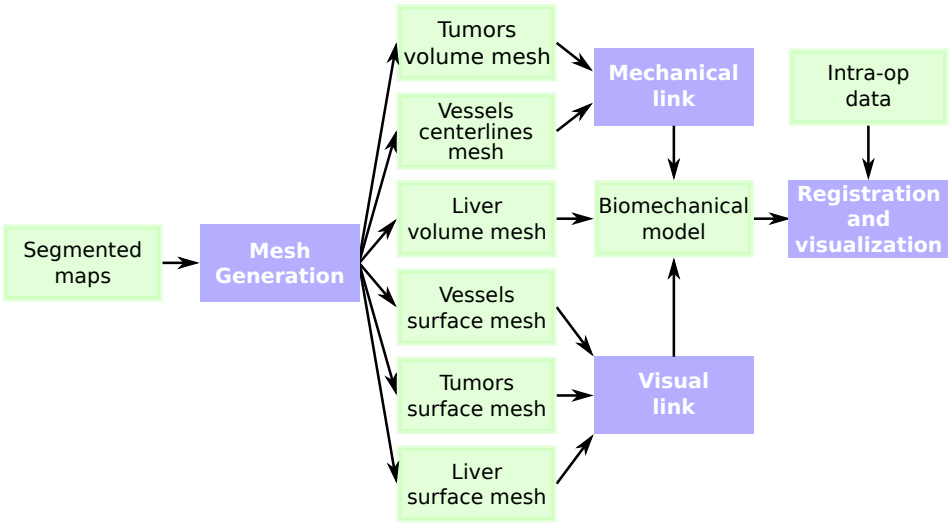

Figure 1.2: Six different meshes are generated from the segmented maps. The physical equation are solved only for the liver volume mesh but the mechanical properties of the tumors and the vessels are taken into account through a mechanical mapping. The visual structures are also mapped to deform with the liver volume.

In this work, three different mesh types are employed, namely one dimensional, two dimensional and three dimensional meshes. Three dimensional meshes are used to represent the liver and tumors volume and two dimensional meshes to render the liver, tumors and vessels surfaces. One dimensional meshes are employed to model the physical behavior of the vessels because a three dimensional mesh which represents faithfully the vessel geometry would contain a very large number of elements and thus increase the computational overhead.

To further reduce the computational time, the physical equations are solved only on the liver volume mesh, the other structures are considered through links (see Fig. 1.2). Two types of link can be distinguished: the visual and the mechanical links. The first type is a unidirectional link: the vertex positions of visual meshes are expressed in term of the vertex coordinates of the liver volume mesh. A change in the vertex position of the liver mesh update the position of the visual meshes. The second type of link is bidirectional: in addition to the update in position, the mechanical properties of the internal structures and the forces exerted on them are transferred to the liver volume mesh. Thus, it is possible to use different representations for the surface and the volume of the modeled objects.

For the purpose of this work, the required characteristics of the desired meshes can be summarized as such:

- The mesh should represent faithfully the shape of modeled structures.
- The quality of the elements should be sufficient to be used with FEM.
- The number of elements of the liver volume meshes should not exceed an order of 10^3.

The development of a mesh generation algorithm is beyond the scope of this thesis, and thus the meshes are generated using already existing mesh generation methods. However, all these methods rely on parameters that have an important influence on the final result. Therefore, the parameters should be tuned to produce meshes with the desired characteristics.

What is a mesh?

A mesh is a discrete representation of a geometric object used in computer software. It is composed of a set of vertices connected by edges. In two dimensions, the vertices and edges are arranged to form faces. In three dimensions, it is possible to define volume elements composed of several — at least four — faces. The FEM requires that only manifold volume meshes are employed. To be manifold, the volume elements of the mesh must define a closed volume without any faces inside: inside the element every edge has to be shared by exactly two faces. Note that it does not mean that in a mesh every edge is shared by exactly two faces as an edge is shared by several volume elements.

The most common kinds of elements used to create meshes are the triangles and quadrangles for two dimensional meshes, and tetrahedra and hexahedra for three dimensional ones. Triangular and tetrahedral meshes are preferred in this work due to the simpler generation of these types of

mesh compared to quadrangular and hexahedral ones. Indeed, very robust automatic algorithms are available to generate good quality tetrahedral meshes. The quality of a mesh depend on the shape of its elements, and FEM requires a good quality mesh to produce accurate results.

The neighborhood relations between the different elements of one mesh (for instance which vertices are connected by an edge, which edges form a face, etc.), is called the mesh topology. In short, with a topology it is possible to access easily the neighboring elements of a vertex, an edge, a face or a volume element. This topology is essential for the applications described in this work as the FEM needs this connectivity information to construct the physical equations of the system.

Volume and surface mesh generation

In this work, volume and surface meshes are generated from segmented maps using the CGAL library (The CGAL Project, 2015). More specifically, the 3D Mesh Generation package (Alliez *et al.*, 2015) is used. This package contains functions to load a segmented map, to convert it into a mesh domain and to generate a mesh composed of triangles or tetrahedra. The mesh generation contains a generation step based on the Delaunay triangulation (Delaunay, 1934) and an optimization step.

The goal of a mesh generation algorithm is to represent the segmented object as faithfully as possible. However, increasing the mesh representation accuracy often requires an higher number of vertices. In addition, the accuracy of the FEM representation is related to the size of the elements: the smaller the element, the smaller the error, but reducing the element size increase the number of element in the mesh. However, increasing the number of elements requires more memory and longer computation time for numerical methods. Therefore a trade-off should be found between the accuracy of the mesh representation and the number of mesh elements.

The next section focus on the parameters of the mesh generation algorithm as they are essential to produce good quality meshes for the FEM. The details of tetrahedral mesh generation using Delaunay refinement algorithms are omitted and the interested reader is referred to Shewchuk (1998) or to Boltcheva *et al.* (2009) for more information on the algorithm.

The final result of the generation step depends on seven parameters: the facet angle α, the facet size s, the facet distance d, the cell radius edge ratio γ, the cell size ζ, the facet topology ξ, and the edge size. However, as the meshes generated in this work are composed of only one material the lest parameter is dropped out and the default value of ξ, which restrict the position of surface vertices, is used. The first three parameters govern

the characteristics of the mesh surface. α gives a lower bound to the angles of a surface triangle. For smooth meshes, the convergence of the meshing algorithm is guaranteed for $\alpha \leq 30°$, but in practice the algorithm usually converge for $\alpha \leq 34°$. s limits the size of the surface triangles and d controls the distance between a facet and the real boundary of the mesh domain. d is the most important parameter to obtain a faithful representation of the object boundary. In practice the size of the surface triangles is limited by d and not by s. Small values of d lead to a better definition of the boundary but increase the number of mesh elements, especially in non smooth area (see Fig. 1.7 and 1.9). The fourth and fifth parameters, γ and ζ, relate to the properties of the volume elements. The parameter γ is related to the shape of the tetrahedra and gives an upper bound to the ratio of the circumscribing sphere radius by the shortest edge. It prevents the generation of wedges, caps, needles, and spindles tetrahedra which have both small and large dihedral angles (see Fig. 1.3). The CGAL developers recommend to use the theoretical bound that guaranty the convergence of the algorithm and to set $\gamma = 2$. The last parameter, ζ, limits the circumradii of the tetrahedra. The optimal value of this parameter depends on the desired result of the mesh generation algorithm. For graded meshes, ζ is usually large compared to s and d, thus the tetrahedra next to the mesh surface are smaller than the tetrahedra which are inside the volume. For homogeneous tetrahedra size in the whole mesh ζ should be set in accordance with s and d. As a good accuracy is needed both at the organ surface and inside the volume, ζ should not be too high, usually we set $\zeta \leq 30$.

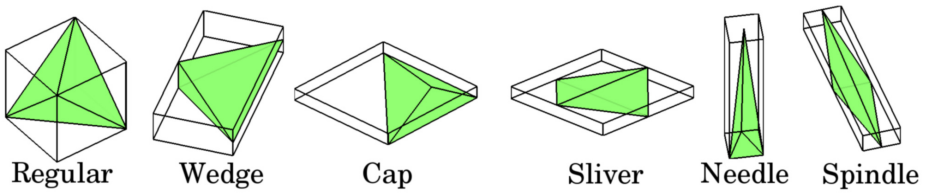

Figure 1.3: Different tetrahedral shapes. To obtain a good quality mesh for FEM, all the tetrahedra that form the mesh should not have too small nor too large dihedral angles.

The optimization process aims at improving the mesh quality. During this phase, bad-shaped tetrahedra are removed. Bad-shaped tetrahedra are tetrahedra whose shapes have both small and large dihedral angles (see Fig. 1.3). These tetrahedra downgrade the mesh quality and may be problematic for numerical methods and particularly for FEM. Indeed, small angles lead to ill-conditioned stiffness matrices (Carey and Oden, 1984), while large dihedral angles cause discretization errors (FEM may not converge to the exact solution when the size of the elements approaches zero (Babuška

and Aziz, 1976)) as well as important errors in interpolated derivatives (Shewchuk, 2002).

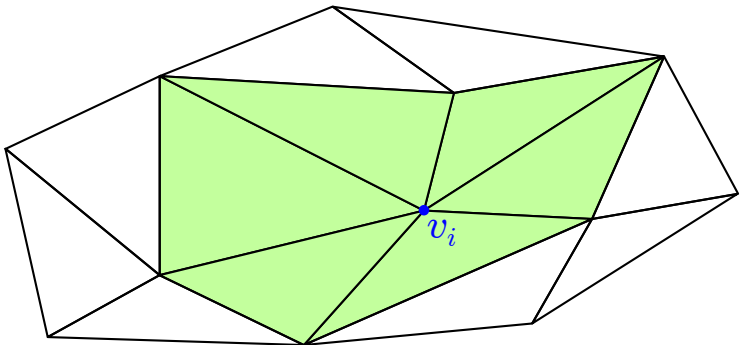

Figure 1.4: The green area is the star of the vertex v_i.

The parameter γ of the generation step helps to avoid bad-shaped tetrahedra with small edge radius ratio, but can not ensure the absence of slivers. Thus, the optimization step aims at identifying and removing slivers. Four optimization algorithms are available in CGAL to improve the mesh quality, two global optimizers, the Lloyd (Du *et al.*, 1999) and the Optimal Delaunay triangulation (ODT) (Chen, 2004) smoothers, and two local optimizers, the perturber and the extruder. The Lloyd optimizer aims at minimizing the functional:

$$\mathcal{F}(\{v_i\}_1^k) = \sum_{i=1}^{k} \int_{V_i} \rho(x)|x - v_i|^2 dx \tag{1.1}$$

where $\{v_i\}_1^k$ are the vertices of the mesh, $\{V_i\}_1^k$ is their corresponding Voronoi tesselation of the mesh domain, ρ is a density function that is set to a constant in our case, and $|.|$ is the euclidean norm. Thus, this optimizer moves the vertices of the mesh in order to make them coincide with the centroids of their corresponding Voronoi tesselation. The ODT smoother works in a similar way, and minimize the functional:

$$\mathcal{G}(\{v_i\}_1^k) = \frac{1}{k+1} \sum_{i=1}^{k} \int_{\Omega_i} \rho(x)|x - v_i|^2 dx \tag{1.2}$$

where Ω_i is the star of the vertex v_i (see Fig. 1.4). However, the ODT smoother implemented in CGAL allows topological modifications in addition to vertex displacement (Alliez *et al.*, 2005). One of these two global optimizer should be used prior to the local optimizers to improve the efficiency of the latter. The perturber algorithm (Tournois *et al.*, 2009) takes advantage of the fact that for a given triangle *abc* the region of location of the vertex *d* which make *abcd* a sliver is small. Therefore, the position of

vertices belonging to a sliver tetrahedron is slightly modified using a computed optimal direction to remove the sliver. The exuder (Cheng *et al.*, 2000) computes the optimal weight of each vertex such as the weighted Delaunay triangulation of these vertices contains no sliver. This algorithm does not move the vertices but removes and creates links between them and thus the topology provided by the generation step is modified. However, as the topology of the mesh boundary is not allowed to change, some slivers may be leftover near the boundary. Both the perturber and exuder algorithms take as parameter the minimum dihedral angle allowed σ_0 for the mesh tetrahedra. In this thesis, we use the ODT smoother in combination with the perturber and the exuder with $\sigma_0 = 15°$ to improve the mesh quality.

The output of the CGAL algorithm is a volume mesh composed of tetrahedra and/or a surface mesh composed of triangles. Both these three dimensional and two dimensional meshes are used in this work as depicted on Fig. 1.2.

Vessels mesh generation

A finite element mesh of the vascular tree consisting of tetrahedra would be composed of a very large number of elements because of the small diameter of the vessels. However, the tubular structure of the vessels can be considered unidimensional. Thus, in order to reduce the number of elements required to describe the liver vascular tree, the vessels are represented by their skeleton. To generate this finite element mesh, the vessel centerlines are first extracted form the segmented map using a slightly modified version of the algorithm presented in Verscheure *et al.* (2013).

The algorithm presented in the paper is as follow: After defining a source node S, it first constructs a Minimum Spanning Tree (MST) from the segmented map of the vascular tree using a modified Dijkstra's algorithm where the weight of a pathlink is not the distance from the source but the inverse of the distance of the pathlink end voxel to the boundary: 1/dfb. However, the distance from the source of each voxel is also stored and used in the next step: the centerline extraction. To extract the centerlines the algorithm starts from the point E which has the largest distance from source S in the MST and then backtracks from E to S following the pathlinks with the minimal distance to the source. Afterward, the algorithm extracts the branches of the first order: it starts from E and follows the centerline, and , for each centerline point C it finds the neighbors which have a pathlink to C and do not lie on the centerline. For each of these neighbors the algorithm finds all the voxels which are pathlinked to it, and set the voxel with the largest distance from the source as the tip of the branch and, if the branch

is long enough, the same backtrack process as the one used for centerline extraction is applied from the tip of the branch to the point C. To extract the branches of higher orders, the same process is repeated on each branch until no branch sufficiently long are found.

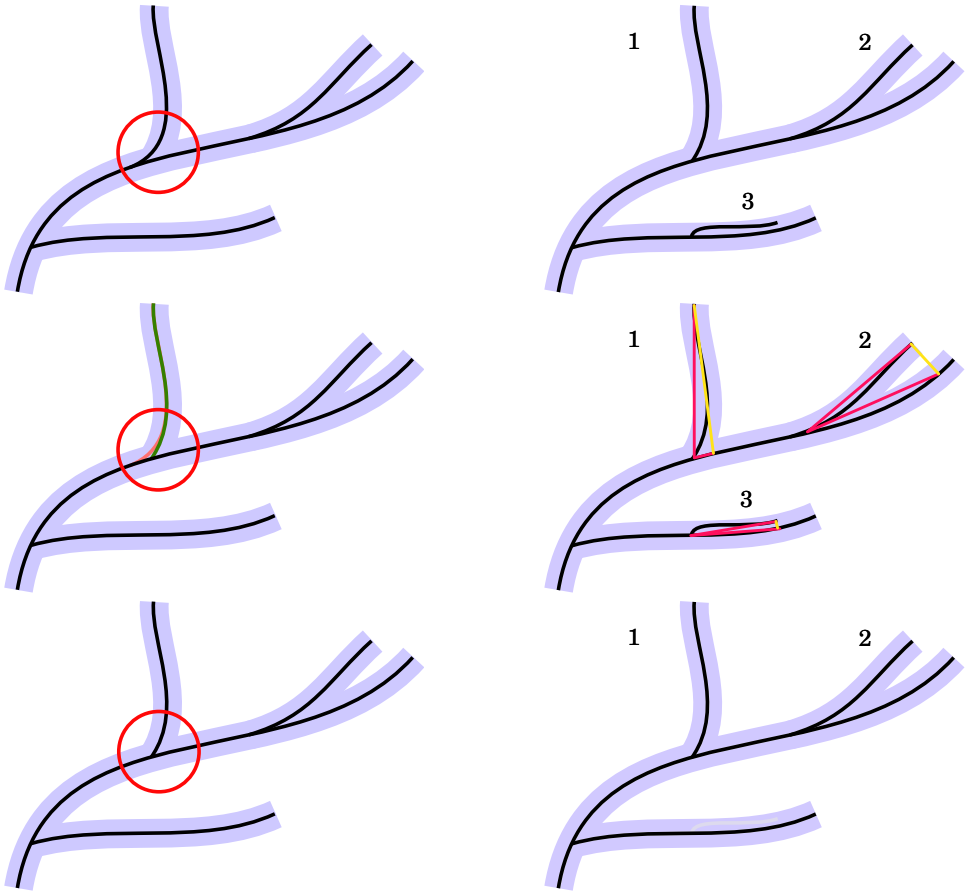

(a) Result of the first heuristic.

(b) Result of the second heuristic.

Figure 1.5: The first heuristic moves the branching point to reduce the length of the branch. The second heuristic does not remove the branch 1 because the angle between the two red lines is in the interval $[\pi - \epsilon; \pi + \epsilon]$. It does not remove the branch 2 because the yellow line does not lie completely inside the segmented volume. However the branch 3 is removed because the angle between the two red lines is not in the interval $[\pi - \epsilon; \pi + \epsilon]$ and the yellow line lies completely in the segmented volume.

Three modifications have been made to this algorithm (Plantefève *et al.*, 2016). First, we evaluated the influence on the centerlines smoothness of different exponents, $e \in \{1, 2, 3, 4, 5, 6\}$, in the definition of the weight of the Dijkstra's algorithm, $1/\text{dfb}^e$. The best results in term of centerline smoothness and continuity were obtained for $e = 4$. Then, we added two heurisctics. The first heuristic reduces the size of branch if possible by

bypassing the pathlink of the MST. For each branch $B(u, v)$ starting at the voxel u on the parent branch and ending at point v, we search for a voxel u' on the parent branch such as the distance form u' to v is less than the distance from u to v and the voxel u' is adjacent to a voxel of the branch $B(u, v)$. If such voxel u' is found we replace the branch $B(u, v)$ by the branch $B(u', v)$ (see Fig. 1.5(a)). The second heuristic detects and removes invalid branch that runs parallel to a previously existing branch inside the same vessel tube. For each branch $B(u, v)$ we find on the parent branch the voxel w with the minimal Euclidean distance from v. Note that this distance is not measured along the path but is just the length of a straight line joining w and v. The branch $B(u, v)$ is removed if the angle between the two straight lines (uv) and (uw) is not in the interval $[\pi - \epsilon; \pi + \epsilon]$ and the line (wv) lies completely inside the segmented volume (see Fig. 1.5(b)). Experimentally, we determined $\epsilon = 0.05$ rad.

However, the skeleton constructed by the graph-based method presented above cannot be used directly as the domain for the finite element method based on the beam formulation, which requires smooth geometrical representation where every node is equipped with both positional and rotational degrees of freedom (DoF). Thus, a Bézier curve is fitted to the centerline tree following the recursive algorithm described in (Schneider, 1990). Finally, the 6 DoF nodes are sampled along the Bézier curves adaptively: the density of sampling increases along the segmented with higher curvature in order to improve the quality of the discretization.

We have seen the main characteristics of a mesh and how it can be generated from a segmented map with the CGAL library. We also detailed some of the parameters that govern the result of the mesh generation process and their importance regarding the quality of the mesh which is essential for the numerical methods which will be detailed in chapter 3. In the next section we give some additional information regarding the generation of a mesh from laparoscopic images.

1.1.4 Discussion

Smoothing the mesh versus smoothing the segmented map

In the section 1.1.2, a post processing step is applied to the segmented map to obtain a better input for the mesh generation step and thus a better mesh. However, one may argue that the mesh can also be smoothed. The differences between both methods are discussed in this section.

The Fig. 1.6 shows the differences between the raw and smoothed segmented maps. The difference between the raw segmented map and the

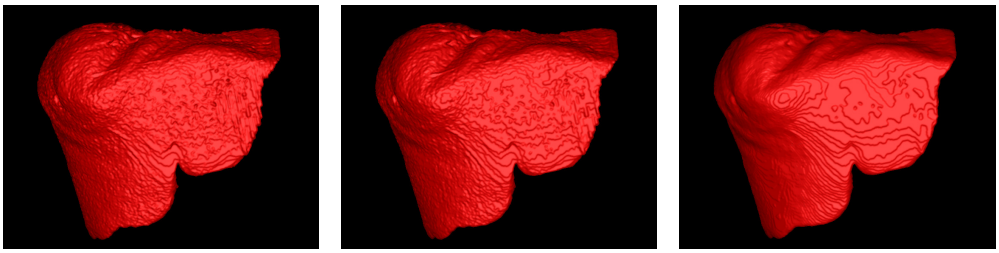

(a) Segmented volume without smoothing (1.363070 dm^3)

(b) Segmented volume after a Gaussian smoothing with σ = 1 voxel (1.363430 dm^3)

(c) Segmented volume after a Gaussian smoothing with σ = 2 voxels (1.361490 dm^3)

Figure 1.6: Segmented maps with and without Gaussian smoothing.

segmented map after a Gaussian smoothing with σ = 1 voxel is not significant. Indeed, this smoothing does not really improve the quality of the segmented map which is still uneven while the liver has a smooth surface. The result after a Gaussian smoothing with σ = 2 voxels has erased the asperity of the raw segmented map, and has changed the volume by less than 1.5 cm^3 indicating a good segmented map quality. However, during the smoothing process, attention should be paid to small segmented regions such as vessels. A too important smoothing may result in the loss of theses small regions. As the gaussian kernel should be a whole number of voxel, a strategy consists of subsampling the segmented image before applying the Gaussian smoothing.

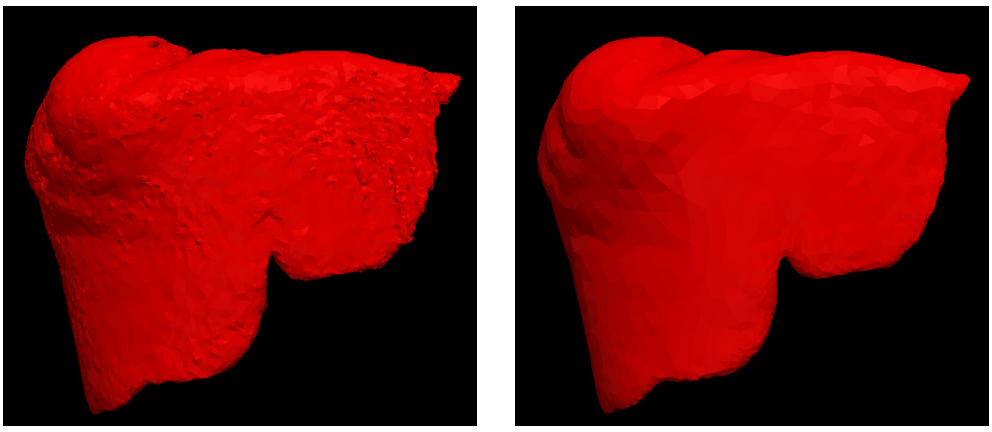

(a) Number of vertices: 18663. Total volume of the mesh: 1.358988 dm^3

(b) Number of vertices: 4899. Total volume of the mesh: 1.354791 dm^3

Figure 1.7: Meshes generated using the raw segmented map (a) or the smoothed segmented map (b) with the following parameters: facet angle=30°, facet size=30, facet distance=0.5, cell radius edge ratio=2, and cell size=20. The mesh (b) is more regular and contains almost 4 times less vertices than the mesh (a).

For the mesh generation the quality of the segmented map is very important. Indeed, as depicted in Fig. 1.7, the result of the mesh generation performed on the raw segmented map is an uneven mesh with 4 times more vertices than the mesh generated using the smoothed segmented map. Thus, the mesh generated from the raw segmented map is less suitable for numerical applications. To be sure that the number of vertices needed to fit the segmented maps depends only on the segmented map, the parameters s and ζ, which influence the size of the mesh element, have been set to 30. In other words, in this example the only parameter that governs the size of the elements and thus the number of vertices is the facet distance, d. The other parameters values are set to $\alpha = 30$, $\gamma = 2$ and $\sigma_0 = 15°$ in order to obtain good quality elements.

However, the mesh generated with the raw segmented map can be smoothed, for instance with a Laplacian smooth, and its number of vertices can be reduced with a decimation method. In term of distance to the smooth segmented map, both methods (mesh generation from the smooth segmented map and mesh generation with the raw segmented map followed by a Laplacian smoothing) lead to similar result with an average distance of about 0.2 mm. Nevertheless, the quality of the meshes are different as depicted on Fig.1.8. Almost all the faces of the mesh generated directly from the smoothed segmented map have a shape close to an equilateral triangle, which is important for numerical methods. This is not the case for the smoothed meshes.

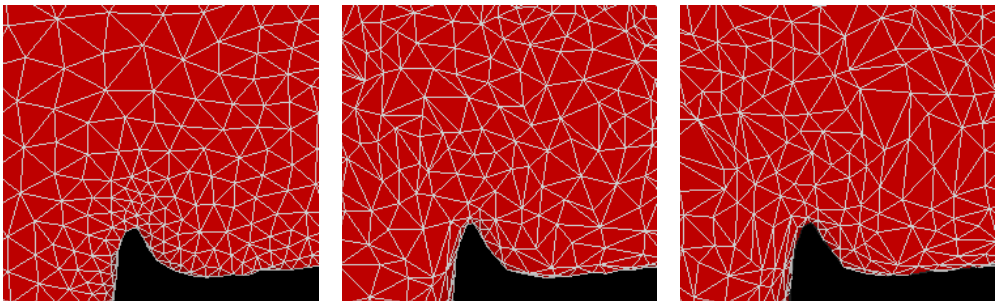

(a) Number of surface vertices: 4899. Total volume of the mesh: 1.354791 dm^3

(b) Number of surface vertices: 4841. Total volume of the mesh: 1.354718 dm^3 (1.355125 dm^3 without decimation)

(c) Number of surface vertices: 4841. Total volume of the mesh: 1.350991 dm^3 (1.351412 dm^3 without decimation)

Figure 1.8: Detailed mesh structures of meshes generated using the smoothed segmented map (a) or the raw segmented map a Laplacian smooth of one iteration (b) or two iterations (c), and a decimation to obtain a similar number of vertices as in (a). The mesh (a) is more regular than the others.

Errors arising from the mesh representation

For the FEM, an ideal mesh should represent faithfully an object while having a reasonable number of elements. Yet, for object with complex geometry like the liver, the use of fewer elements deteriorates the accuracy of the object representation. Therefore a tradeoff should be found between the size of the mesh (in term of element number) and the quality of the object representation.

Fig. 1.9 shows different meshes obtained for d between 0.5 and 5. As in the last paragraph, high values have been used for the other parameters in order to see only the effect of the facet distance. The difference between the meshes (a) and (b) is not significant as both have almost the same distance to the segmented map. However, the mesh (b) should be preferred as it is formed of a fewer number of elements. As for the mesh (c), its distance to the segmented map is too important to be considered as a faithful representation of the liver. In this thesis, depending on the application and on the required accuracy, different meshes of the same object can be employed.

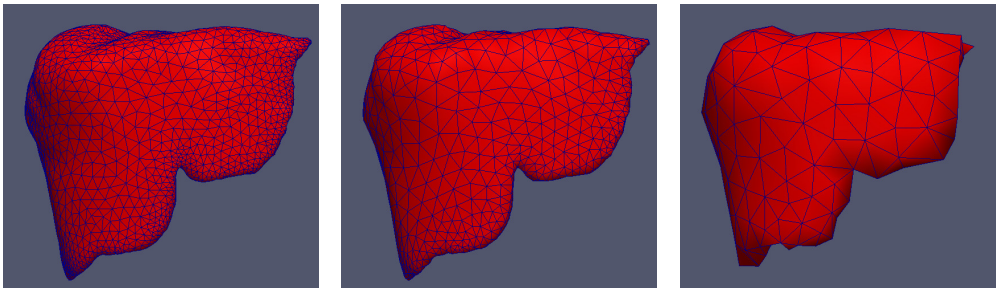

(a) Number of surface vertices: 4899. Maximum/average distance to the segmented map: 4.2 mm/0.2 mm

(b) Number of surface vertices: 1675. Maximum/average distance to the segmented map: 4.7 mm/0.3 mm

(c) Number of surface vertices: 223. Maximum/average distance to the segmented map: 16.4 mm/1.7 mm

Figure 1.9: Errors induced by the mesh representation. The surface meshes where generated from the smoothed segmented map with the following parameters: $\alpha = 30°$, $s = 30$, and $d = 0.5$ (a), $d = 1$ (b), $d = 5$ (c). Increasing the facet distance parameter reduce the number of vertices but increase the distance between the mesh and the segmented map.

In this part we have seen how to obtain a suitable representation of the liver and its internal structures for numerical applications from pre-operative images. The importance of the quality of the segmented map as well as the wise choice of the parameters used for the mesh generation have been highlighted. In the chapter 3 we will see how this geometric representation of the pre-operative shape of the organ will be exploited.

1.2 From intra-operative images to point cloud

This section describes how to reconstruct a partial liver surface from intra-operative images acquired with a laparoscopic camera. First, the principles of surface reconstruction from projective images and the challenges encountered in the reconstruction from laparoscopic images are exposed. Then, an overview of the different steps of the three dimensional reconstruction (feature detection, matching and triangulation) will be presented. This overview will detail the principles of the different algorithms employed in this thesis. Finally, we discuss the use of some alternative methods that allow for the reconstruction of point cloud, representing the visible liver surface, from projective images.

1.2.1 Principles of surface reconstruction from laparoscopic images

Reconstructing a point cloud from an image implies to find the depth of the objects depicted in the image. Laparoscopic images, like all the images acquired with a camera, are projective images. A projective image differ from an orthogonal image: parallel lines in a three dimensional scene are still parallel when transformed into an orthogonal image but this is not true anymore in a projective image. The representation of an object in an orthogonal image has the same size no matter where this object is in the tree dimensional scene. Conversely, in a projective image the size of an object depend on its distance from of the capture tool (Fig. 1.10(a)). The geometric construction of a projective image is depicted on Fig. 1.10(b). Choosing the world reference frame to be the camera coordinate system **c** (the optical center **o** is the origin and the third direction is the direction of the image plane), the point $\mathbf{x} = [X, Y, Z]$ in the three dimensional world is related to the vector **p** which join the optical center **o** and the projection $\mathbf{x}_{proj}$ of **x** in the image plane by:

$$\mathbf{p} = \frac{\mathrm{f}}{Z}\mathbf{x} \tag{1.3}$$

where f is the focal length (i.e. the distance between **o** and the image plane). It is also possible to express the projection of **x** in the image plane in another way. Let $\widetilde{\mathrm{p}} = [x, y, 1]$ where $[x, y]$ is the position of the projection of **x** in the image coordinate system, obtained from the camera coordinate system by removing the third coordinate and choosing the projection of **o** on the image plane to be the origin. We have the following relation:

$$\sigma\widetilde{\mathrm{p}} = \mathbf{P}\mathbf{x} \tag{1.4}$$

where σ is a scale factor and **P** is the projection matrix of the image. Unlike the first relation, this expression is valid for any choice of the world

(a) Two objects of different size may have the same size on a projective image. From Marchant.

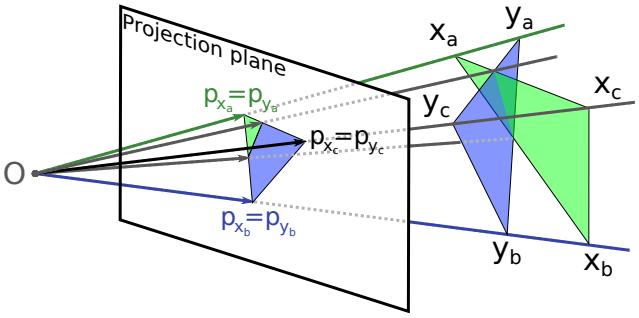

(b) Generation of a projective image. **o** is the position of the camera. The **p** are shown as arrows. This example is a special case: the projection of x_i and y_i for $i \in \{a, b, c\}$ are the same. Adapted from Baecker.

Figure 1.10: Projective geometry

coordinate system, but the form of the matrix **P** depends on this choice.

Theoretically, knowing the real size and the viewing angle of an object as well as its size on one image, it is possible to determine the depth of the object relatively to the camera. However, it could prove cumbersome in practice, especially for laparosocopic images. Indeed, it is almost impossible to know precisely a distance and an orientation on the abdominal organs. For this reason, several images have to be used. Indeed, as two eyes enable you to estimate the depth of an object, two or more camera poses can be used to compute this depth. The only requirement is to know the relative position and orientation of the different viewing angles.

Two methods can be used to obtain different views of a scene: either using a sequence of images acquired with a monoscopic camera or using two cameras at the same time. The first method is known as Structure From Motion (SFM, sometimes also called shape from motion) and has been applied in MIS surgery by Hu *et al.* (2007), while the second implies the use of a stereoscopic device to keep the relative position of the two optics constant. SFM estimates both the relative displacement of the camera from a frame to another and the three dimensional position of the objects in the scene. This method works well for rigid objects and easily detectable features which allow for a good estimation of the camera motion, but is very challenging for laparoscopic images where the tissues are moving due to the patient's breathing and only few easily detectable features are present. Some works using region classification seem promising for the use of SFM in laparoscopic images (Lourenço *et al.*, 2014), and others assume a rigid motion of the camera between two video frames sufficiently close in time to

estimate the global camera motion (Collins *et al.*, 2011), but the reliability of such systems has to be improved. Therefore, the method used in this work rely on the use of a stereoscopic laparoscopic camera, whose optics relative position is determined independently of the laparoscopic images. However, small errors in the determination of the relative position and orientation of the two optics result in important reconstruction errors due to the small baseline (i.e. the distance between the two optics centers) of laparoscopic camera. The process that allows to compute the optics properties and relative position is called the calibration and is detailed in section 1.2.2

Regardless the chosen method, SFM or stereoscopic vision, the reconstruction of a three dimensional position from two images or more follows the same principles. First the images are processed independently to detect salient features. Then, each feature is associated to a vector, the descriptor vector, that describes the feature. This vector is like an identity card for the feature and contain information about the intensity profile in a neighborhood centered at the feature point (see section 1.2.3). Afterward, an algorithm matches salient features corresponding to the same point in the three dimensional space across the images. This algorithm uses the descriptor vectors and eventually some characteristics regarding the relative position of the capture tool for the different images (see section 1.2.4). Finally, the position of paired salient features is exploited to compute the three dimensional position of their corresponding point (see section 1.2.5).

1.2.2 Stereo camera calibration

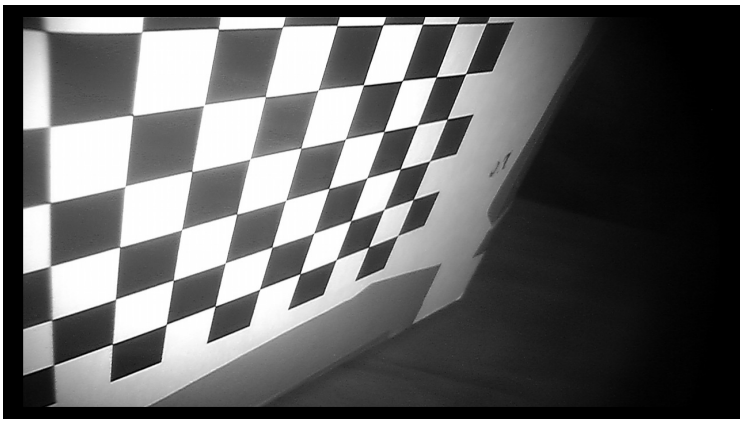

Figure 1.11: Chessboard used for the calibration process viewed by the left camera of the stereoscopic endoscope. The upper left corner of the image is strongly distorted.

To obtain the relative position and characteristics of the two optics, which are essential for the three dimensional point cloud reconstruction, the stereo-

scopic camera has to be calibrated. Given a monocular camera of optical center **o**, the calibration process allows to compute the extrinsic and intrinsic camera parameters. The extrinsic camera parameters links the coordinates of points in the three dimensional word and their coordinates in an ideal camera image plane. Equation 1.4 is the mathematical expression of this relation. The intrinsic camera parameters depend on the hardware set-up of the camera and link the coordinate of the ideal image plane to the coordinates of the image registered by the camera. For a pinhole camera model these parameters are gathered in the following matrix:

$$\mathbf{A} = \begin{bmatrix} k_u & k_u \cot\theta & u_0 \\ 0 & k_v / \sin\theta & v_0 \\ 0 & 0 & 1 \end{bmatrix} \tag{1.5}$$

where k_u (resp. k_v) is the ratio between the unit of the first (resp. second) ideal image axis and the first (resp. second) pixel image axis, θ is the angle between the two pixel image axis, and $[u_0, v_0]$ is the coordinate of the real image center in the ideal image reference frame. Thus the coordinate vector $\widetilde{\mathrm{p}}_{pixel} = [u, v, 1]$ of the point corresponding to $\mathbf{x}$ in the pixel image is given by:

$$\widetilde{\mathrm{p}}_{pixel} = \mathbf{A}\widetilde{\mathrm{p}} = \frac{1}{\sigma}\mathbf{A}\mathbf{P}\mathbf{x} \tag{1.6}$$

where σ is a scale factor, and we note $\mathrm{p} = [u, v]$. The Equation 1.6 holds for each optic of the laparoscopic camera independently (i.e. the intrinsic parameters of two camera optics can be different), thus we have to estimate two matrices $\mathbf{A}_1$ and $\mathbf{A}_2$.

To find the entries of these matrices, an object of known shape and size (usually a chessboard, see Fig.1.11) is captured in different pose by the cameras. The different images are then used to estimate the matrices $\mathbf{A}_1\mathbf{P}_1$ and $\mathbf{A}_2\mathbf{P}_2$ and thus the intrinsic camera parameters. However, for laparoscopic cameras the pinhole model, which suppose that no lens are used to focus the light, is generally not sufficient as a wide angle conversion lens distorts the image. Thus, additional parameters have to be included in the model, but the calibration principle remain the same. Usually, only the first radial distortion parameter is estimated, the other distortion parameters being difficult to compute. Indeed, the images corners, which contain most of the information about the distortion, are difficult to process due to the poor image quality in these area (see Fig.1.11). Details about the methods used to estimate the intrinsic camera parameters are beyond the scope of this thesis, but further information can be found in Tsai (1989), Salvi *et al.* (2002) or in the book Gruen *et al.* (2002).

Once the intrinsic camera parameters are found, the extrinsic camera parameters can be estimated. We choose the first camera coordinate system $\mathbf{c}_1$ to be the world coordinate system and we search the rotation $\mathbf{R}$ and the translation $\mathbf{t}$ such as:

$$\mathbf{c}_2 = \mathbf{R}\mathbf{c}_1 + \mathbf{t}$$

where $\mathbf{c}_2$ is the right camera coordinate system. To find the six parameters of $\mathbf{R}$ and $\mathbf{t}$ we use a set of known corresponding points $\{p_1, p_2\}_i$. To determine the six parameters of the rotation and translation at least seven pairs should be provided. But to limit the impact of localization errors the algorithms which compute the extrinsic parameters employ usually more pairs. Details about epipolar geometry and the calibration of stereoscopic camera can be found in Zhang (2000), or in the books Xu and Zhang (1996) or Hartley and Zisserman (2003).

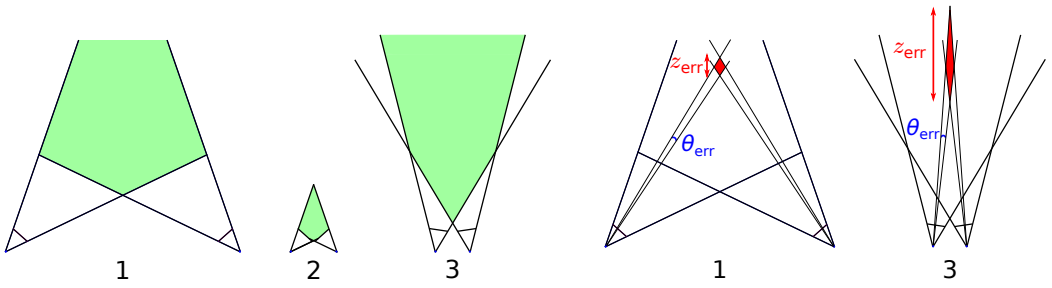

(a) Impact of the baseline length and of the optics relative angle on the three dimensional field of view. The camera 3 is the laparoscopic camera.

(b) The depth error of camera 3, the laparoscopic camera, is more important.

Figure 1.12: Stereoscopic laparoscopic cameras have a high depth error.

One important characteristic of laparoscopic cameras is that the distance between the two optics is small (small baseline). This small baseline is problematic for the stereoscopic vision because a small error in the determination of $\mathbf{R}$ and $\mathbf{t}$ or in the position of a point in the images leads to important errors in the three dimensional point reconstruction. In fact the baseline itself is not problematic, but to obtain a sufficient three dimensional field of view (i.e. the portion of the three dimensional space where the depth of objects can be computed) the angles between the two optics reference frame should be smaller if the baseline is small. On Fig. 1.12(a), the two optics of stereoscopic camera 1 and 2 have the same angle, but the baseline length of the camera 2 is smaller and thus the portion of the three dimensional space which is seen by both optics is smaller. To enlarge the three dimensional field of view, the angle between the optics of camera 3, which correspond to the laparoscopic camera, is reduced (Fig. 1.12(a)). Thus, the depth error z_{err} for the same angle error θ_{err} is more important for camera 3 (Fig. 1.12(b)). To

limit this effect the calibration should be as accurate as possible, but as the calibration is computed with given point correspondences small errors in the position of this points lead to important errors in the calibration result. Therefore, the calibration of a laparoscopic camera is very challenging.

We have seen the main principle of the calibration process for stereoscopic camera and that this process is very challenging for laparoscopic camera due to the relative orientation of its two optics. In the next section we detail how salient features are extracted from theses images, with specific focus on the algorithm employed in this thesis: the SURF algorithm (Bay *et al.*, 2006). The choice of this algorithm is motivated by its robustness to noise and its computational efficiency, and test from Haouchine (2015) showed that SURF perform well on the liver surface, thus making it particularly suited for laparoscopic images.

1.2.3 Feature detection

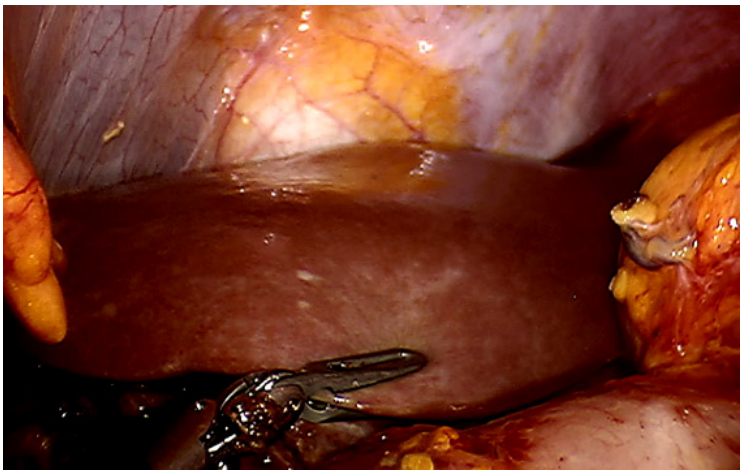

Figure 1.13: The surface of the liver is highly specular and lacks texture.

The feature detection is based on the pixel intensities. Usually, to save computational time, grey level images are used to perform the feature detection: the color images should therefore be converted into grey level images. First, a detection step select salient points, such as corners or T-junctions, on the images. These distinctive points are usually detected with algorithms based on the image derivatives. For SURF the salient point detector rely on an approximation of the hessian matrix (Bay *et al.*, 2006). Given a point p in one image we have:

$$\mathbf{H}_{approx}(\mathrm{p}, \sigma) = \begin{bmatrix} D_{xx_\sigma}(\mathrm{p}) & wD_{xy_\sigma}(\mathrm{p}) \\ wD_{yx_\sigma}(\mathrm{p}) & D_{yy_\sigma}(\mathrm{p}) \end{bmatrix}$$

where $D_{ij_\sigma}(\mathrm{p})$ is the approximation of the Gaussian second order derivative $\frac{\partial}{\partial ij}g(\sigma)$ convolved with the image intensities around point p, and w is a weight that ensure the energy conservation between the Gaussian kernel and its approximation. The point p is considered as a salient point at scale σ if its hessian response, $\det(\mathbf{H}_{approx}(\mathrm{p},\sigma))$ is superior to a threshold τ_d:

$$\det(\mathbf{H}_{approx}(\mathrm{p},\sigma)) > \tau_d \tag{1.7}$$

Then, for each salient point p a descriptor $\mathcal{D}(\mathrm{p})$ is computed using the pixel intensities of the point and its neighbors. The number of neighbors may vary from one descriptor to another, can be a parameter of the descriptor, or may even depend on the result of the detector step and be different for each salient point. In SURF, the neighborhood size depend on the scale σ at which the feature point has been detected.

There exist an important number of descriptors, each of them having their own advantages and drawbacks. (Mikolajczyk and Schmid, 2005). The difficulty is to choose among all the descriptors the most useful to detect reliable features in a laparoscopic image. Several descriptors can be combined into one descriptor vector in order to extract more information for each image pixel. However, as the use of too many descriptors leads to an important increase in computational time, it is wiser to select only the most significant descriptors for a given application. Given two salient points p_1 and p_2 of corresponding three dimensional point $\mathbf{x}_1$ and $\mathbf{x}_2$, a good descriptor should have the following properties:

$$\mathcal{D}(\mathrm{p}_1) \approx \mathcal{D}(\mathrm{p}_2) \qquad \text{, if } \mathbf{x}_1 = \mathbf{x}_2 \tag{1.8}$$

$$\neg(\mathcal{D}(\mathrm{p}_1) \approx \mathcal{D}(\mathrm{p}_2)) \qquad \text{, if } \mathbf{x}_1 \neq \mathbf{x}_2 \tag{1.9}$$

where $\neg$ is the logical NOT. The SURF algorithm use the sum and absolute sum of the Haar wavelet (Haar, 1910) response in the x and y direction in the region around a salient point.

The feature detection is very challenging for laparoscopic images because of the lack of texture, the important specular reflexion and the possible presence of smoke or bleeding (see Fig. 1.13). Due to the lack of texture of the liver surface (Fig. 1.13) the detection of salient points is challenging and the threshold τ_d of equation 1.7 should be small enough to detect a sufficient number of salient points. But small values of τ_d lead to the detection of points p whose descriptors $\mathcal{D}(\mathrm{p})$ are less reliable because the intensities around these points is more homogeneous. Thus, several points $\{\mathrm{p}_1\}_{i=1}^{n}$ across one image may be associated to a very similar descriptor, violating the requirement 1.9:

$$\mathcal{D}(\mathrm{p}_{1_i}) \approx \Delta, \forall i \in \{1,\ldots,n\} \tag{1.10}$$

The presence of specular points $\{p_{spec}\}_i$ is also problematic because they usually have a strong Hessian response $\det(\mathbf{H}_{approx}(p_{spec}, \sigma)) > \tau_d$ but their descriptors may also be similar $\mathcal{D}(p_{spec_i}) \approx \Delta_{spec}\ \forall i$. Moreover, the corresponding position of a specular point on the three dimensional object depend on the position of the capture tool. The point p_{spec_1} in the first image correspond to $\mathbf{x}_{spec_1}$ in the three dimensional world and p_{spec_2} in the second image correspond to $\mathbf{x}_{spec_2} \neq \mathbf{x}_{spec_1}$. For a laparoscopic camera, this means that the two optics see a specular point at different positions on the object: using specular points leads to erroneous three dimensional point position.

The feature detection step leave us with two sets of pairs $\{p_{1_i}, \mathcal{D}(p_{1_i})\}_{i=1}^{n}$ and $\{p_{2_j}, \mathcal{D}(p_{2_j})\}_{j=1}^{m}$ detected on the first and second image respectively. In the next section, we will detail how to match salient points corresponding to the same three dimensional point while taking into account the difficulties expressed in Equation 1.10.

1.2.4 Matching

The hypothesis behind the matching process is that the descriptors corresponding to the same three dimensional point are similar across the stereoscopic images (statement 1.8). Therefore, a distance metric has to be defined to measure the similarity of the descriptor vectors. This distance metric can be for instance the Euclidean distance, the Manhattan distance (L1-distance) or even the Mahalanobis distance (Mahalanobis, 1936) when a confidence measure is available for the descriptors. Once the distance metric is chosen, different strategies can be employed to pair the feature points.

The first strategy consist of selecting for each salient point p_1 in one image the point p_2 with minimum descriptor-based distance measure in the other image:

$$\mathcal{M}(p_1) = \arg\min_{p_2} |\mathcal{D}(p_1) - \mathcal{D}(p_2)| = \arg\min_{p_2} d_{12}$$

where $|.|$ is the chosen distance (the Euclidean distance for instance). But this strategy may match points with very low similarity measure. A solution to this problem is to set a threshold τ_m such that the pair with a similarity measure $\mathcal{S}$ lower than the threshold are discarded:

$$\text{If } \mathcal{S}(\mathcal{D}(p_1), \mathcal{D}(\mathcal{M}(p_1))) < \tau_m, \text{ then } \mathcal{M}(p_1) = \emptyset$$

However, a descriptor vector in one image can be very similar to several descriptor vectors in the other image (Equation 1.10), indicating a lack of discriminating power. It this case, it is better to discard all the points corresponding to these descriptors. A solution is then to compute the

distance ratio between the first and the second closest match. If the distance ratio is close to one, the two first match are very likely to be erroneous and the points are discarded. This matching strategy is called the nearest-neighbor-ratio matching (Lowe, 2004). To further improve the matching quality, theses matching methods can be combined with a double direction search: for each point p_1 the algorithm finds the point p_2 with the smallest distance d_{12} from p_1 and for each point p_2 the point of p'_1 with the smallest distance d_{21} from p_2. The pairs for which the point p_2 elected by p_1 has elected $p'_1 \neq p_1$ are then discarded.

To accelerate the matching step, several algorithm rely on additional information. For instance, to obtain a faster matching, the SURF algorithm takes advantages of the result of the detector phase: it computes the distance only for feature point with the same second derivative sign (computed using the Hessian matrix). But other strategy exist that benefit from knowledge about the relative position of the camera for the different images, such as the use of the fundamental matrix $\mathbf{F}$. This matrix can be estimated during the calibration step from at least seven point correspondences. Given a salient point in one image, $\mathbf{F}$ reduces the search of its corresponding point to a line in the other image. This arises from the fact that a three dimensional point $\mathbf{x}$ and the two camera optics define a plane, and, in the epipolar coordinates system, this plane cuts each image plane along a line. Depending on the position of $\mathbf{x}$ on the plane, its corresponding points on the images, p_1 and p_2, slide along the epipolar lines (see Fig. 1.14). In practice the position of $\mathbf{x}$ is unknown, but the plane equation can be determined from the vector $\mathbf{p}_1$ of one of its corresponding points, p_1. Therefore given the position of the two optics and p_1, the point p_2 is restrained to a line. The fundamental matrix contains the information about the relative position of the two optics $\mathbf{o}_1$ and $\mathbf{o}_2$. For simplicity we assume that the intrinsic camera parameters of the left and right camera are $k_u = k_v = 1$, $\theta = 90°$ and $u_0 = v_0 = 0$, (that is we have two ideal images) and that there is no rotation between the two camera reference frames $\mathbf{c}_1$ and $\mathbf{c}_2$. Thus we have:

$$\mathbf{F}_{spe}\mathbf{p}_1 = (\mathbf{o}_2 - \mathbf{o}_1) \times \mathbf{p}_1 = \mathbf{o}_{12} \times \mathbf{p}_1,$$

$$\text{that is } \mathbf{F}_{spe} = \begin{bmatrix} 0 & -\mathbf{o}_{12_z} & \mathbf{o}_{12_y} \\ \mathbf{o}_{12_z} & 0 & -\mathbf{o}_{12_x} \\ -\mathbf{o}_{12_y} & \mathbf{o}_{12_x} & 0 \end{bmatrix}$$

where $\mathbf{F}_{spe}$ is the special fundamental matrix under the previously given assumption on the stereoscopic camera and $\times$ denotes the cross product of two vectors. The vector $\mathbf{F}_{spe}\mathbf{p}_1$ is therefore a vector normal to the plan defined by $\mathbf{x}$, $\mathbf{o}_1$ and $\mathbf{o}_2$. Hence, p_2 lays in this plane (and thus on the epipolar

line) if and only if $\mathbf{p}_2$ satisfy:

$$\mathbf{p}_2^T \mathbf{F}_{spe} \mathbf{p}_1 = 0.$$

Without any assumption on the intrinsic camera parameters nor on the relative rotation between the two camera reference frame the general form of the fundamental matrix is:

$$\mathbf{F} = \mathbf{A}_1^{-T} \mathbf{F}_{spe} \mathbf{R} \mathbf{A}_2^{-1} = \mathbf{A}_1^{-T} \mathbf{E} \mathbf{A}_2^{-1}$$

where $\mathbf{E}$ is the essential matrix and $\mathbf{p}_2$ satisfy:

$$\mathbf{p}_2^T \mathbf{F}_{spe} \mathbf{p}_1 = 0.$$

However, in practice (and especially for laparoscopic images) this condition should be avoided or replaced by $\mathbf{p}_2^T \mathbf{F} \mathbf{p}_1 \leq \epsilon$, with $\epsilon > 0$ due to possible inaccuracies in the feature position.

Once the matching step is performed the disparity can be computed for each salient point. The disparity is simply the distance in pixel between the position of the salient point on one image and the position of its corresponding salient point on the other image. The disparity value is related to the depth: the closer the object is from the stereo camera the larger is the disparity value of the salient point detected on this object.

Regardless the chosen matching method, the result of this step is a set of paired points $\{\mathrm{p}_1, \mathrm{p}_2\}_i$, each pair corresponding to a three dimensional point $\mathbf{x}_i$. These pairs should now be used in combination with the calibration result to compute the position of each $\mathbf{x}_i$.

1.2.5 Triangulation

The triangulation method discussed here should not be confused with the Delaunay triangulation evoked in section 1.1.3. Here the term triangulation refers to the fact that the three dimensional point $\mathbf{x}$, its corresponding points on the two images p_1 and p_2 and the two optics $\mathbf{o}_1$ and $\mathbf{o}_2$ form a triangle. Theoretically, the parametric lines $\mathbf{o}_1 + t_1\mathbf{p}_1$ and $\mathbf{o}_2 + t_2\mathbf{p}_2$ withe $t_1, t_2 \in \mathbb{R}$, should intersect exactly at $\mathbf{x}$. However, due to errors in the position of p_1 and p_2 the two lines may not be secant (and the vectors $\mathbf{p}_1$ and $\mathbf{p}_2$ may not be on the plane defined by $\mathbf{x}$, $\mathbf{o}_1$ and $\mathbf{o}_2$). Therefore, an optimization algorithm should be employed to estimate the position of x.

This work use the Iterative Linear Least Square Triangulation method (Iterative-LS) presented in Hartley and Zisserman (2003). The idea is to let two points $\widehat{\mathrm{p}}_1$ and $\widehat{\mathrm{p}}_2$ move around the feature point positions p_1 and p_2 until the lines defined by $\mathbf{o}_1 + t_1\widehat{\mathbf{p}}_1$ and $\mathbf{o}_2 + t_2\widehat{\mathbf{p}}_2$ cross (see Fig. 1.14). This is equivalent of requesting that $\widehat{\mathbf{p}}_2^T \mathbf{F} \widehat{\mathbf{p}}_1 = 0$. Thus, the algorithm should

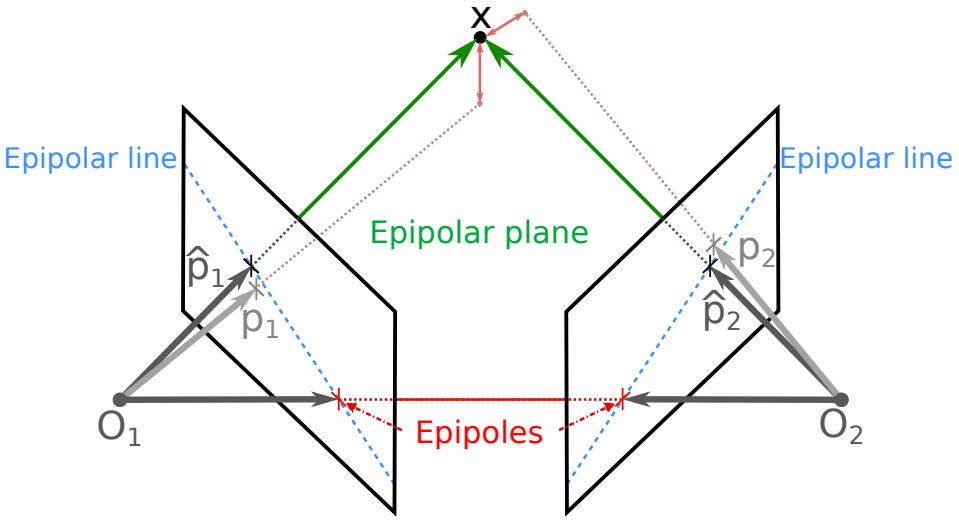

Figure 1.14: Triangulation. The dashed gray lines, in the direction of $\mathbf{p}_1$ and $\mathbf{p}_2$ are not secant. After the optimization algorithm the lines in the direction of $\widehat{\mathbf{p}}_1$ and $\widehat{\mathbf{p}}_2$ intersect at the point $\mathbf{x}$, the reconstructed position of the three dimensional point corresponding to the features p_1 and p_2.

minimize the quantity $\widehat{\mathbf{p}}_2^T \mathbf{F} \widehat{\mathbf{p}}_1$. Obviously, the distance between $\widehat{p}_n$ and p_n for $n \in \{1, 2\}$ should be limited and therefore a penalty term, $\Delta_{12} = d(p_1, \widehat{p}_1)^2 + d(p_2, \widehat{p}_2)^2$ where $d(.,.)$ is the Euclidean distance, is added to the objective function of the minimization algorithm.

The result of the triangulation algorithm is a list of three dimensional coordinate vector $\{\mathbf{x}\}_i$ called a point cloud. To each $\mathbf{x}_i$ can be associated an uncertainty value u_i which is a combination of three error measures. Let $\{p_1^i, p_2^i\}$ be the pair of point whose three dimensional triangulation is $\mathbf{x}_i$. The first error measure is related to the result of the feature detection step: the stronger the response to the detector algorithm the smaller the error measure:

$$\text{err}_D = \alpha_D \frac{1}{\det(\mathbf{H}_{approx}(p_1)) + \det(\mathbf{H}_{approx}(p_2))},$$

where $\alpha_D \in \mathbb{R}^+$. The second confidence measure is the result of the matching algorithm: the larger the distances between the two descriptor vectors the larger the error measure:

$$\text{err}_M = \alpha_M d_{12},$$

where $\alpha_M \in \mathbb{R}^+$. The last error measure is called the re-projection error and is equal to the penalty factor of the minimization algorithm:

$$\text{err}_R = \Delta_{12}.$$

One important point to keep in mind while using tree dimensional surface reconstruction methods, among which is stereoscopic reconstruction,

is that these methods are error-prone. Two types of errors can be distinguished, localization error and matching error. The first kind of error is responsible for the noise in the surface point clouds. Noisy points are close to the real position of the surface that is reconstructed and generally the previously defined errors are good indicators of the noise associated to one point. The second kind of error is more problematic as it produce outliers, that is erroneous points far from the real position of the reconstructed surface. These outliers have an associated error measure which is comparable to the error associated to noisy points and thus cannot be eliminated based on this criteria. In stereoscopic reconstruction, matching strategies using the epipolar lines usually produce points clouds with a small number of outliers. Nonetheless, the presence of these erroneous points should be taken into account in the definition of a efficient and robust registration algorithm involving a reconstructed surface.

We went from laparoscopic images to a list of three dimensional points corresponding to the part of the abdominal organs surface visible through the laparoscopic camera using the SURF detector and a triangulation algorithm. In the next section we will discuss the use of some alternative methods to perform a three dimensional point reconstruction from laparoscopic images.

1.2.6 Discussion

The process described in the previous section is not the only way to reconstruct a surface patch from laparoscopic images. This section present some alternative methods for surface reconstruction from projective images. First, a method that reconstruct a dense point cloud from laparoscopic images is detailed. Then the use of SFM techniques, already evoked in section 1.2.1, for laparoscopic images is discussed. Finally, two methods relying on additional hardware devices are described.

Instead of pre-processing the laparoscopic images to detect salient point whose three dimensional positions are subsequently computed to create a discrete point cloud, a dense surface reconstruction can be obtained. In Röhl *et al.* (2011) the authors compute a corresponding point for each pixel using a recursive algorithm on undistorted and rectified images. Rectified images are used to facilitate the matching step. They are the result of a transformation that project both stereoscopic image into the same image plane making the epipolar lines horizontal. Thus, the search of corresponding points is restricted to horizontal lines. In this application the calibration process is crucial and a probabilistic scheme is employ to generate several possible calibration matrices among which the best candidate is selected. The result

of the matching step is a dense disparity map from which the triangulation is performed.

To avoid the use of stereoscopic endoscope SFM methods have been employed for laparoscopic surface reconstruction. The main challenge with such methods is to estimate the camera motion in an environment where objects are moving an deforming. The movement of a feature may be the result of the camera motion but also of the tissue deformation. This second possibility introduces errors in the motion estimation. The use of relatively static features has already been evoked in section 1.2.1, and methods assuming that the tissues are rigid between two relatively close frames have also been employed (Collins *et al.*, 2011). But, as the main causes of the tissue deformation are the respiration and the heart beating, another possibility is to model this cyclic motion as in Mountney and Yang (2010). In this article the camera motion is estimated using the motion model, the laparoscopic images and a Kalman filter. Another interesting aspect of the work of Mountney *et al.* is the construction of a map that contains the three dimensional position of all features currently visible by the laparoscopic camera together with the position of features that were reconstructed using the previous frames. This allows for the construction of a wider point cloud that contains more information about the intra-operative organ shape.

However, if the constraint to use only medical devices already employed during laparoscopic operation is released, other methods can be considered. This category of method is referred to as active methods in opposite with passive methods which rely solely on already employed devices.

The use of structured light has been first introduced for laparoscopic surgery in Ackerman *et al.* (2002). This technique consist of projecting a known light pattern on the organ surfaces. The resulting pattern is captured by a monocular laparoscopic camera and the distortions provoked by the differences in depth are then analyzed to retrieve the organ shapes. Recently promising devices, the pico lantern (Edgcumbe *et al.*, 2014, 2015) and a endoscope compatible device (Schmalz *et al.*, 2012), have been developed and are very close to be used during a real operation. However, these two technologies still require calibration, and the endoscope three dimensional point cloud reconstruction is limited to small distances around the projector. For the pico lantern two calibration methods are proposed. In the first one the pico lantern projection pattern is captured by a stereoscopic laparoscopic camera which has to be calibrated and thus suffer from the same limitations as our calibration method (section 1.2.2). In the second method the pico lantern is tracked by a monoscopic laparoscopic camera and thus must stay in the camera field of view, which may be problematic during an operation.

Another three dimensional reconstruction method based on additional

hardware setup is called the Time of Flight (ToF). The principle of this technique is to use an intense sinusoidal light signal to illuminate the scene and to measure the time this signal takes to be captured by the camera. This time of flight is propositional to the distance between the camera and the object. To obtain a three dimensional depth map each pixel compute the time of flight independently. A ToF system has been mounted on a standard endoscope in Penne *et al.* (2009), with promising results. Yet, no articles have report the use of such endoscope in *in vivo* studies.

In this first chapter, we explained how to construct a mesh, a geometric representation allowing for the use of mechanical numerical methods such as FEM, from preoperative images. We also highlighted the importance of the mesh quality for the precision and the convergence of FEM. Then we described the method that allows to reconstruct a three dimensional point cloud from a laparoscopic stereoscopic camera. We saw that this process is challenging due to the nature of the images (lack of texture and high specular reflexion) and to the characteristics of the laparoscopic camera (small baseline). Finally we discussed alternative methods that can be use for intra-operative point cloud reconstruction. In the next chapter, we will switch to a medical point of view and describe the liver anatomy, the liver cancer its treatment with a particular focus on laparoscopic tumor resection. This will allow us to enrich our registration problem with anatomical prior knowledge. CT scan are not exactly raw data — and we described the processes that allow to construct a better representation of theses data for numerical applications.

CHAPTER 2

Defining Anatomical Landmarks

Contents

The last chapter left us with a geometric representation of the pre- and intra-operative data. However, a complete model of the liver has been generated from the pre-operative data while only a portion of the liver surface is reconstructed from the intra-operative data. Thus, a natural question arise: to which part of the complete liver surface does the partial intra-operative surface correspond? As the liver surface is smooth, and has deformed between the pre- and intra operative data acquisition, the answer to this question is not trivial: with only geometric knowledge the problem is ill posed, since several areas of the complete surface could correspond to the surface reconstructed from laparoscopic images. Thus, we need additional information to constraint this problem.

In this chapter we see how can be use the knowledge about the liver anatomy to match the part of the liver surface corresponding to the visible intra-operative surface. We first detail the role and the anatomy of the liver, as well as one of its pathology, the liver cancer, and its possible treatments. We then study the execution of a laparoscopic operation for liver cancer

resection with an emphasis on the specific exposition of the liver during this intervention. Afterward, we motivate the use of landmarks for facilitating the correspondence problem described above and list the different methods that can be used to define these landmarks. Finally, we describe the features employed in this work.

2.1 The liver

2.1.1 Function of the liver

The liver is a vital organ endowed with an important regenerative capacity. It is also the largest gland of the human body. A gland is a organ that produce and excrete a substance into or outside of the human body. The main substance produced by the liver is called the bile and plays an important role in digestion. The bile is stored in the gallbladder, also called the biliary vesicle, and released into the duodenum where it participates into the digestion of lipids. However, the role of the liver is not limited to the digestion. This organ plays also a role in the metabolism of carbohydrates, lipids and proteins.

The liver is sensitive to an hormone, the insulin, which is excreted by the pancreas when the blood sugar level is too high. This hormone is a signal for the liver indicating that the sugar present in the blood has to be stored. The liver then transform the glucose present in the blood into glycogen and store it within its cells. Conversely, when the blood sugar lever is too low the pancreas release another hormone, the glucagon, which cause the liver to break down the glycogen molecules and to release the glucose.

The liver can store about 100 g of glycerol. When this limit is reached, the liver start to convert the glucose into lipids, and more specifically into triglyceride, which is the main constituent of the body fat. This process is called the lipogenisis and can be reverted: the liver can convert the triglyceride back to glucose. It is also able to synthesize glucose from glycerol, amino acid or lactate. The liver also synthesize the cholesterol, several proteins, such as albumin, and many lipoproteins.

Additionally, the liver plays an important role in the organism detoxification. Indeed, it is responsible for the breakdown of several toxin, medical drugs and waste products such as ammonia. It also participates in the elimination of byproducts from aged red blood cells destruction. This makes the liver particularly exposed to diseases coming form other part of the human body.

To summarize, the liver is a very important organ with several essential functions. However, the liver is particularly exposed to diseases due to its

detoxification role. To date, a complete liver failure cannot be compensated by drugs or dialysis. The only solution to a complete liver failure is a transplantation, which implies tremendous challenges for finding a compatible donor. Nonetheless, this organ has an important regenerative capacity: it can grow back to its initial state from as few as 20% of its original size. Therefore, in case of hepatic disease, the role of clinicians is to make everything that is possible to preserve sufficient healthy part of the original liver for it to regenerate.

2.1.2 Liver cancer and liver metastasis

As the liver is involved in many metabolic processes, and especially in several detoxification processes, it is prone to numerous diseases. However, this section do not cover all the liver diseases and focus mainly on liver cancer and liver metastasis. Liver cancer should be understood here as primary liver cancer. Indeed, two kind of liver lesions should be distinguished: primary liver cancer and metastasic liver tumors. The first sort of tumors originate in the liver while the second have migrated to the liver from other organs and are sometimes abusively called liver cancer. The main primary liver cancer is the hepatocellular carcinoma (HCC), which affect the hepatocytes. It exist several other primary liver cancer including cancer of the bile duct, and blood vessels tumors. But the majority of liver tumors belong to the second kind of lesion and are called metastases. A study on 96 625 cadaver (Le Treut *et al.*, 2005) reports that among patient with liver tumors (n=8 685), 84% of the tumors are metastases and only 5.4% are primary liver tumor, the remaining 10.6% being benign tumors. Given that the prevalence of primary liver cancer among all cancer in the french population is 2.9% (INC), this means that 48% of cancers affect the liver. The metastases come generally from the colon, the rectum, the pancreas, and the stomach and spread to the liver via the portal vein. The highest prevalence of liver metastasis is observed in colorectal cancer with detected liver metastases in 15% of the patients (Quan *et al.*, 2012).

To cure liver tumors, different strategies may be employed and the choice of a specific treatment depend on the number of tumors, their size, their location and on the existence of other neoplasic cells in other organs. For hepatic metastasis from colorectal cancer the recommendations have evolved towards the use of liver resection as the gold standard due to the high survival rate of patients who underwent this treatment (Wei *et al.*, 2013). Indeed, advances in surgical techniques and technologies, especially in cauterization tools, have made the surgical tumor resection a safe and efficient technique. Today, the main contraindication for surgical resection is

an insufficient remnant of liver volume.

However, laparoscopic surgical interventions, despite their important benefit for patients, are still done in a minority of cases (25% in 2005 for Dagher *et al.* (2007)), even if some center report a percentage of laparoscopic surgery of more than 46% (Vibert *et al.*, 2006). The main reasons for the surgeon's reluctance to perform laparoscopic liver resections are the risk of hemorrhage, which are difficult to control in this kind of intervention, the difficult definition of resection margins and the tumor size and location (Morino *et al.*, 2003; Simillis *et al.*, 2007). In this context, a surgical guidance system could increase the safety and feasibility of laparoscopic liver resection and thus enable more patient to benefit from this kind of intervention.

In patients for which a surgical intervention is not possible, other treatments exist. Apart from surgery, possible treatments of liver tumors include chemotherapy, chemoembolization (the injection of a chemical substance in the tumor to restrict its blood supply), radiotherapy, and thermoablation. This last technique is an interventional radiology technique and consist in the use of heat or cold to kill neoplastic cells. One or more thermoablation probe(s) are inserted in the patient body at the tumor location, covering entirely the tumor area. Thermoablation techniques include radioablation(Shiina *et al.*, 2012), microwave ablation (Groeschl *et al.*, 2014), cryotherapy (Hu, 2014), as well as emerging techniques not yet used on humans such as electroporation (Zhang *et al.*, 2014). For more details about thermoablation procedures the reader is referred to Chu and Dupuy (2014).

2.1.3 Anatomy

The liver measures about 20 cm×15 cm×10 cm and its average weight is approximately 1.4 kilograms. This organ is located in the upper right part of the abdominal cavity and is in direct contact with many other abdominal organs and the diaphragm. Its blood supply is provided by the hepatic artery and the portal vein, while the hepatic veins drain the blood into the vena cava. A thin membrane, known as the Glisson's capsule, constitutes the surface of the liver, while the interior part of this organ is called the parenchyma. The liver is also surrounded by the peritoneum, a serous membrane, except around the gallbladder, the porta hepatis and in a triangular region, called the bare area of the liver, where its surface is in direct contact with the diaphragm (See the nonperitoneal surface on Fig. 2.3).

The liver presents three faces, namely the superior (Fig. 2.1), inferior (Fig. 2.2) and posterior surfaces (Fig. 2.3). The margins delimiting these faces are smooth except the anterior margin, which delineates the inferior

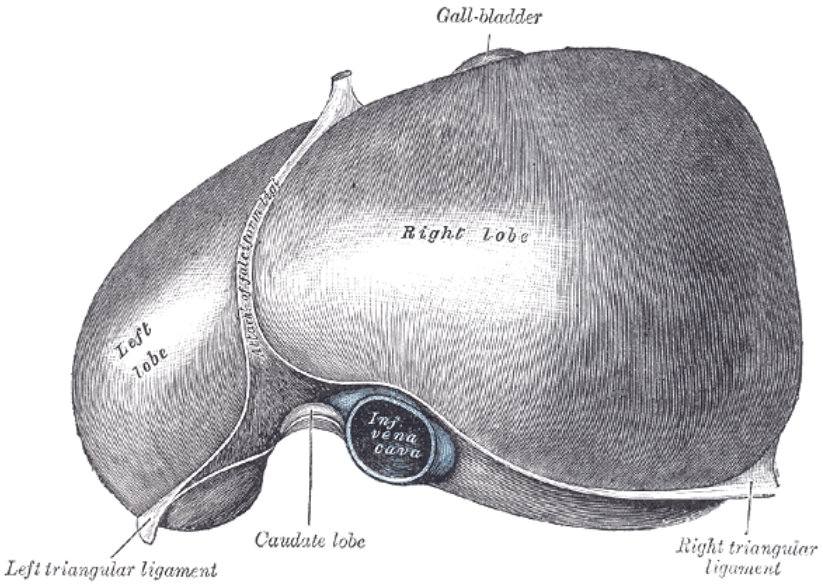

Figure 2.1: Superior liver surface (from Gray (1918))

and the superior faces. This sharp margin is indented in two locations: a deep notch accommodating the round and falciform ligaments, called the umbilical notch, and a shallow notch at the position of the gallbladder.

The superior surface (Fig. 2.1) fits under the vault of the diaphragm and is divided in two parts by the falciform ligament. This ligament goes from the anterior margin to the coronary ligament and attaches the liver to the diaphragm and the anterior abdominal wall. The line of attachment delineates the right and the left lobe of the liver, the first being much larger than the second.

The inferior surface (Fig. 2.2 and 2.3) is in contact with the stomach, the right kidney and its supra-renal gland, the colic and the duodenum. Its shape is uneven and modeled by these organs. Indeed, as the liver takes as much place as possible, the other abdominal organs leave an impression on its surface. At the center of this surface is the hilum where the bile duct, the portal vein and the hepatic artery enter the liver. The gallbladder is located under the right lobe and goes slightly over the anterior margin.

The posterior surface (Fig. 2.3) is mostly behind the right lobe and is in direct contact with the diaphragm for an important part. The inferior vena cava is deeply lodged between the right lobe and the caudate lobe. This face may also present a grove on the left lobe, at the position of the esophagus.

According to Couinaud (Couinaud, 1957), the liver is composed of eight segments, each of them having an independent blood inflow, biliary drainage and lymphatic drainage. This is of interest for surgeons, as to

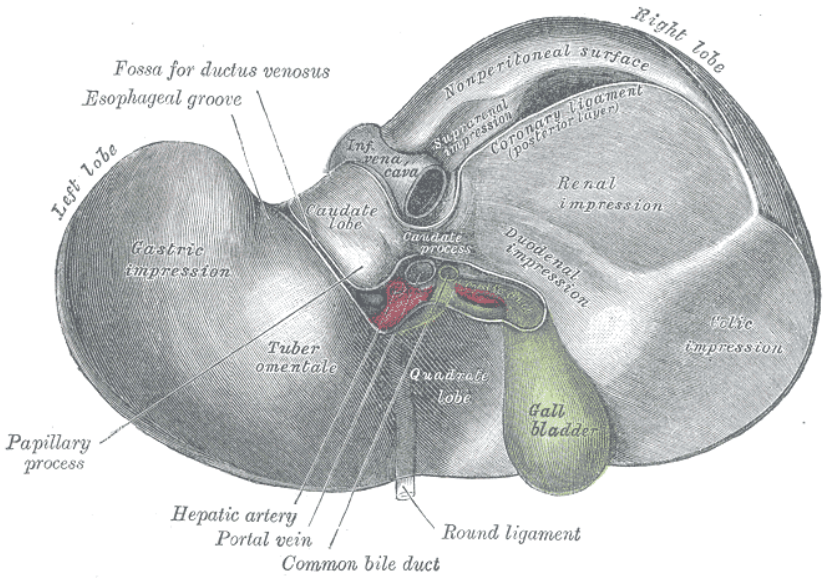

Figure 2.2: Inferior liver surface (from Gray (1918))

prevent post-operative metastases they should resect the tumors together with their lymphatic and blood vessels, while ensuring a sufficient blood supply and drainage of the remaining liver tissue.

2.1.4 Fixation of the liver

Several factors contribute to maintaining the liver in place. The most important fixation of the liver is the vena cava which is closely attached to the liver by connective tissues. Under the liver, the hilum also participates in holding it in place. The liver is also attached to the diaphragm by the coronary and triangular ligaments. The falciform ligament is to loose to support the liver but limits its lateral displacement. Additionally, the other abdominal organs provide some support in standing position, as the liver rest on them. To access the area of the liver where the surgery will take place, surgeons often need to mobilize the organ. However, certain motions are not possible without cutting ligaments.

2.2 Typical laparoscopic surgery

In the last section, we provided some background information about the liver physiology and anatomy. We also detailed one of the main kind of liver pathology, the liver cancer and metastasis, and its possible treatments. We now focus on one type of treatment: the laparoscopic liver resection, detailing the different steps of this type of surgical intervention.

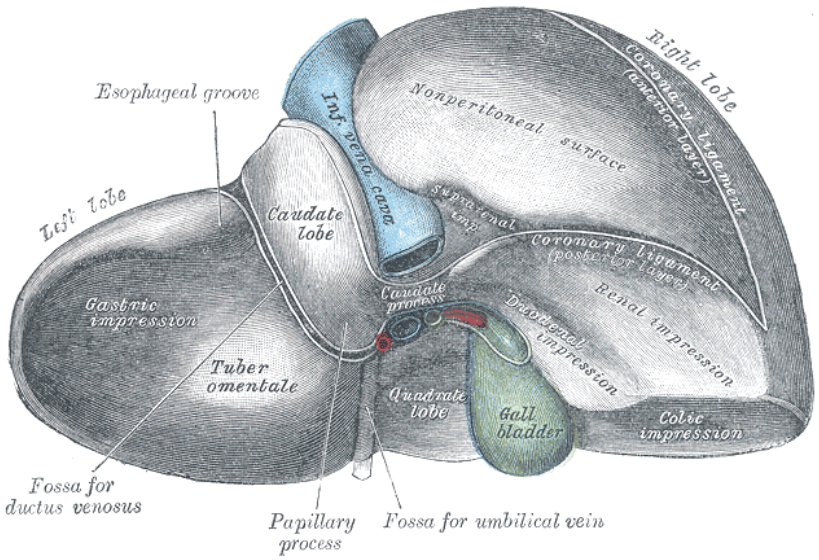

Figure 2.3: Posterior and inferior liver surfaces (from Gray (1918))

2.2.1 Planning

Before any surgical intervention, a surgery planning meeting holds. During this meeting several clinicians discuss the patient's case. They analyze the pre-operative data to be sure that all the tumors which should be resected have been localized. Then, the volume to be resected is estimated. This volume include the surgical safety margin which should be at least of 1 cm around the tumor (Masutani *et al.*, 1994; Shirabe *et al.*, 1997). If the estimated remnant liver volume is insufficient the surgery is canceled. Otherwise, depending on the patient and on the characteristics of the tumors, the clinicians decide to go for laparoscopic or open surgery. Then, the resection plane are defined and the vessels that should be sectioned are identified. For laparoscopy the definition of the surgical path and resection plane should take into account the limited movement of the laparoscopic tools and the cone effect. The cone effect is simply the tendency of surgeons to narrow the size of the resected region as they cut deeper in the tissues during laparoscopic surgery. Additionally, the positioning of the trocars (Fig. 0.1), through which the surgical instrument are inserted, should be defined in accordance with the resection path.

2.2.2 Preparation

After the patient anesthesia, the surgeons set up the pneumoperitoneum. The pneumoperitoneum is the injection of gas inside the peritoneal cavity to provide the surgeon with a sufficient working space inside the patient's

abdomen. A Veress needle is inserted cautiously in the patient's abdomen until the tip of the needle is inside the peritoneal cavity. As the needle is equipped with a pressure sensor, the surgeons can know that their needle is in place by monitoring the pressure (the entrance in the peritoneal cavity is characterized by a pressure drop). Once the needle is in position the abdomen is inflated with carbon dioxide until the pressure reaches the value of 12 mmHg.

Afterward, the trocars are positioned. Trocars are important because they allow easy exchange of laparoscopic tools during the surgery. The first inserted trocar is the camera trocar. For liver surgery, the position and orientation of the camera trocar vary little from one patient to another, and thus the liver is always seen under the same angle (Toni *et al.*, 2015). First, an incision is performed till the facial layer at the position of the umbilicus. Then, the trocar and its obturator are inserted into the incision and pushed into the peritoneal cavity. This step should be performed with care to avoid injuries. Afterward, the obturator is removed and the camera is inserted. The surgeon can now check that no damages have been caused to the abdominal organs and vessels. A part of the superior face of the liver is exposed to the camera. The other trocars are inserted under camera vision.

An alternative method for trocar insertion is the Direct Trocar Insertion (DTI) consisting in the insertion of the first trocar before the pneumoperitoneum is set. In DTI, the patient's skin is grasped to move the abdominal wall away from the abdominal organs during the trocar insertion. More detail about trocars and their positioning can be found in Jafari *et al.* (2015).

2.2.3 Intervention

Once all the laparoscopic tools are inserted in the patient's abdomen, the fat surrounding the liver is moved to better expose the organ. Then, the liver is mobilized to provide an easy access to the tumor site. The first structure to be cut is the falciform ligament, which attaches the liver to the abdominal wall. Then, the pre-operatively defined resection planes are located. Eventually, the liver or other abdominal organs may be retracted to provide a better access to the wound area. The use of an ultrasound probe at this step may help the surgeon to better target the tumor, but is time consuming and therefore only rarely performed. When the resection paths have been defined, some resection lines may be drawn on the liver surface using a cauterization tool to serve as guidelines.

After this preparation phase, the resection begins. Several dissection techniques are available to cut and cauterize liver tissue, the more frequently

used being ultrasonic dissection and electrosurgery. Electrosurgery is the application of high frequency current to burn the tissues. Electrosurgery devices can be monopolar or bipolar. Monopolar devices induce a current between the contact area of the device with the tissue and an electrode located on the patient's skin. Conversely, the bipolar devices induce a current only between its two electrodes. Thus, the action of bipolar devices is more local. The ultrasonic dissector used for liver surgery are low power ultrasonic dissectors. The interest of these devices is their ability to cleave only tissues containing an important quantity of water. Therefore the blood vessels and bile ducts, which contain only a few water, are preserved with ultrasonic dissection. This limits the risk of hemorrhage. However, each time a vessel is encounter, it must be clamped prior to dissection with scissors or electrosurgery devices.

Electrosurgery devices allow to perform the surgery faster. However, to prevent hemorrhage the hepatic artery and the portal vein need to be clamped at the hilum. In this way, small vessels can be cut and then cauterized without blood loss, but larger vessels should be avoided because the cauterization alone is not sufficient to prevent hemorrhage. The clamping should not last more than 30 minutes, and therefore the clamp must be released several times during an operation, checking each time the integrity of large blood vessels.

At the end of the intervention, the resected volume is put inside a plastic bag and removed from the abdomen via the incision performed at the umbilicus, after all laparoscopic tools and trocars have been removed. Finally, the incision wounds are stitched.

2.3 Additional knowledge derived from medical data.

In the previous chapter, medical images were processed to generate a geometric object which does not contain any information about the liver anatomy, except its shape and vascular tree for the mesh of the liver. However, additional anatomical knowledge may greatly help the IGS registration method to find the transformation which best aligns the pre- and intra-operative data. Indeed, some anatomical features can be used as landmarks to guide the registration method. In order to be useful, the landmark positions should be determined in both the pre- and intra-operative images, so that the registration method can use them as anchor points.

To obtain the position of these anatomical landmarks several strategies may be used. In section 2.2.3, the possible use of a laparoscopic ultrasound probe has been evoked. This imaging modality, which allows to see below the organ surface, can be used to locate anatomical landmarks intra-

operatively. One may argue that with such system surgeons would not need an augmented reality system. However, as the probe manipulation is complicated and time consuming, if an augmented reality view can be provided with a quick scan of the liver this augmented view is very likely to have a positive impact. Usually, for the liver, ultrasound data are employed to obtain the position of the vessels branching points. For instance, in Lange *et al.* (2009), the authors use manually segmented vessel bifurcations as anatomical landmarks for an image based registration method to provide the surgeons with an intra-operative guidance system. However, ultrasound data is strongly distorted, making the determination of the exact position of the internal structures difficult. Moreover, as the probe should be pressed against the organs in order to obtain an ultrasound image, the internal organ structures may be deformed.

A second strategy to obtain landmarks for the registration algorithm is the use of markers. This method offers the advantage of being independent of the position of the anatomical structures, as the markers insertion position does not need to correspond to a specific structure. Radiopaque markers such as clips or golden seeds are already used in patients undergoing radiotherapy. Among other markers, radiopaque ink could be used to mark the liver surface. The interest of this solution is twofold. First, the position of the radiopaque features could, as all the other landmarks described before, help find the portion of the pre-operative liver surface which corresponds to the visible intra-operative surface. Second the drawing pattern could help the three dimensional point cloud reconstruction. However, as these markers should be present in both the pre- and intra-operative images, they should be set up before the pre-operative images are taken in order to be visible in the pre-operative data. This means that a first intervention should be performed before the laparoscopic surgery. In addition, a mean to accurately localize these markers intra-operatively should be available. To date, this kind of marker has never been used for minimally invasive surgery guidance.

Finally, a third method to obtain the intra-operative position of anatomical landmarks for laparoscopic IGS is to use images acquired by the endoscope. This modality offers the advantage of being always available during minimally invasive liver surgery, thus, it does not require to change the clinical workflow. The drawback of this method is that only a sub-part of the liver surface can be captured by the laparoscope, limiting the number of anatomical landmarks that could be used. However, the anterior part of the liver offers reliable landmarks.

In our approach, we chose to employ laparoscopic images to define anatomical landmarks for the registration method. Indeed, as we already

employ the laparoscopic images to reconstruct a three dimensional point cloud of the liver surface, the use of the images to define the anatomical landmarks allows to link a reconstructed point with its corresponding anatomical structure straightforwardly.

2.3.1 Selection of the anatomical features

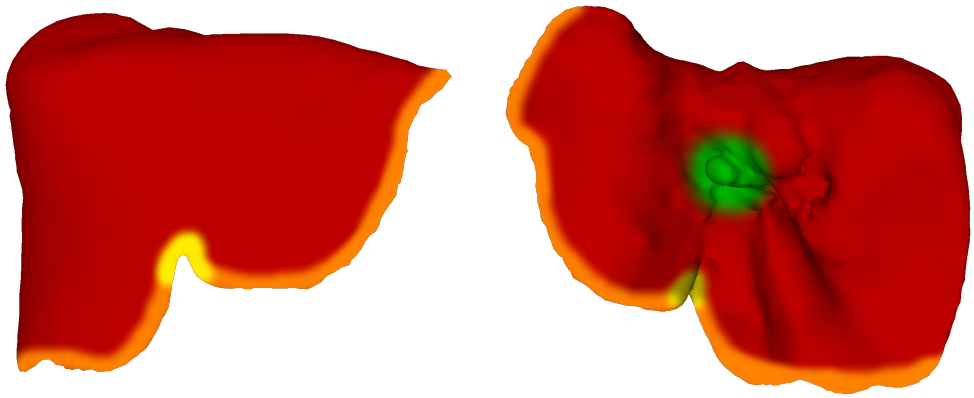

Figure 2.4: The three different anatomical features used in this work: the anterior margin (in orange,) the umbilical notch (in yellow) and the hilum (in green). The left image shows the anterior liver surface, and the right image the posterior and inferior liver surfaces.

During a laparoscopic intervention on the liver, several anatomical landmarks are visible. The exposition of the liver is also similar across patients since the position and orientation of the laparoscopic camera varies little from one patient to another. Therefore a set of anatomical landmarks that are always visible in these laparoscopic images can be defined. However, to be useful, the selected anatomical feature should also be identifiable in the pre-operative data.. Therefore, additional information available only in the laparoscopic images cannot be used.

The first feature used to enrich the intra-operative data is the **anterior margin**. This anatomical landmark is always visible and easily recognizable on the laparoscopic images. As the anterior margin is a sharp transition between the inferior and superior liver surfaces, a curvature analysis can be performed on the mesh to detect this feature. The automatic detection process of the anterior margin on the liver mesh is described in Chapter 5.

The second selected feature is the **umbilical notch**. Its central location on the liver anterior margin makes it visible for resection performed both on the right and on the left part of the liver. As the surgeon cuts the falciform ligament to mobilize the liver at the beginning of the intervention cauterization marks are present around the umbilical notch. These marks facilitate the three dimensional point cloud reconstruction of this region

as they enrich the liver texture (see section 1.2). This feature can be easily defined manually on the three dimensional mesh, but an automatic solution based on the use of a statistical atlas is detailed in Chapter 5.

The last anatomical feature used in this work is the **hilum**. The hilum is not located on the anterior face of the liver, which is visible during the intervention. However, as the surgeon has to clamp the liver artery and the portal vein during the intervention it is possible to see this anatomical structure with the laparoscopic camera. Nonetheless, in order to be useful the position of the different anatomical landmarks should be defined in the same reference frame, and should correspond to the same intra-operative configuration of the liver. Thus, if the camera is moved between the acquisition of the intra-operative images corresponding to the hilum and the acquisition of the images corresponding to the two other anatomical landmarks, the camera motion must be known. As the liver is moved by the surgeon to access the region of the hilum, the liver is not in the same configuration during the acquisition of the hilum and when the umbilical notch and the anterior margin were acquired. To solve this problem we use the fact that the hilum is a strong fixation point of the liver which moves only slightly even when the liver is deformed (see section 2.1.4). Therefore, the position of the hilum can be used with those of the two other anatomical landmarks even if the liver is deformed between the two different acquisition steps.

In this chapter, we detailed the liver function and anatomy as well as one of the diseases that may affect this organ: the presence of neoplastic cells inside the liver. We saw that the origin of these tumors can be a primary liver cancer or metastases from an other cancer. We also described the possible treatments of these tumors with a focus on the laparoscopic liver resection. Based on characteristics of this type of intervention and the review of existing methods for the definition of landmarks during surgical interventions, we selected three anatomical features (the anterior margin, the umbilical notch, and the hilum) to serve as anchor points for the registration method.

CHAPTER 3

BIOMECHANICAL MODEL OF THE LIVER

Contents

From the two previous chapters, we obtained a geometrical representation of the pre- and intra-operative data, which allows us to formulate the registration problem geometrically, and a set of anatomical landmarks. They will be used to find the portion of the pre-operative liver surface corresponding to the intra-operative visible surface. However, only surface information can be extracted from the laparoscopic view. This leads to the following question: how to derive the volume displacement field knowing the surface deformation? Additional knowledge regarding the liver has to be added to answer this question. We proposes to use the liver mechanical behavior to infer the volume deformation from surface data.

Therefore, we need to construct a biomechanical model of the liver. Three components of this model can be distinguished: the model constitutive law, biomechanical parameters and boundary conditions. The constitutive law

and the biomechanical parameters are chosen according to the material properties whereas the boundary conditions depend of the studied mechanical problem.

As we employ a numerical method, the finite element method (FEM), to solve the mechanical equations, new parameters which influence the result of the biomechanical problem and the computational time are introduced: the type of elements (tetrahedra, hexahedra, triangles, beams, etc.), the size and shape of the elements, the shape functions (linear, quadratic, etc.), and, for dynamic formulation of physical problems, the temporal integration scheme (quasi-static, explicit, implicit, etc.).

In this chapter, we first introduce biomechanical models through the physical equations that govern soft tissues motion and we discuss some methods for the determination of the material properties. Then, we present the FEM, the numerical method employed to solve these mechanical equations, and highlight the impact of the chosen numerical organ model on the result. Finally, we detail the automatic construction of a real-time compatible complete biomechanical model of the liver.

3.1 Background on continuum mechanics

A biomechanical model is a mean to represent the physical behavior of a physical object. The prefix "bio" is actually unnecessary but emphasizes the fact that the model corresponds to biological tissues, whose mechanical properties and boundary conditions are difficult to determine compared to engineering mechanical problems where all these parameters are known by design.

The physical modeling of soft (or deformable) objects is studied by a specific branch of physics called continuum mechanics. This sub-part of mechanics makes the assumption that the studied objects cover entirely the space they occupy. Even if fundamentally this assumption is erroneous — matter is composed of atoms which are mostly empty space — it turns to be a sufficiently good approximation for a reliable prediction of the behavior of macroscopic materials given their mechanical properties.

The goal of the continuum mechanics is to predict the behavior of a deformable body from the knowledge of the external forces $\mathbf{f}_{ext}$ applied to the body. From Newton's second law we have:

$$\mathbf{f}_{ext} + \mathbf{f}_{int} = m\mathbf{a}, \tag{3.1}$$

where $\mathbf{f}_{int}$ are the internal forces, m the body mass and $\mathbf{a}$ the acceleration. In the static case we can rewrite this equation as:

$$\mathbf{f}_{ext} = -\mathbf{f}_{int}. \tag{3.2}$$

We want to link the internal forces[1] with the deformation of the deformable body. For this purpose, the effect of the external forces inside the body volume must be known. Applying forces on a deformable body leads to the creation of constraints and deformations inside the body. It is therefore necessary to define these two quantities mathematically.

3.1.1 From forces to the stress tensor

Inside the volume at a point x we define an infinitesimal area dS and a normal $\mathbf{n}$. The stress vector $\mathbf{t_n}$ is the average force per unit area:

$$\mathbf{t_n} = \frac{\mathbf{f}}{dS} \tag{3.3}$$

where $\mathbf{f}$ is the force applied on the infinitesimal surface. The subscript $\mathbf{n}$ emphasizes the fact that the stress vector depends on the direction of the normal (see Fig. 3.1). Therefore, the stress vector is not sufficient to define completely the effect of the force in the volume.

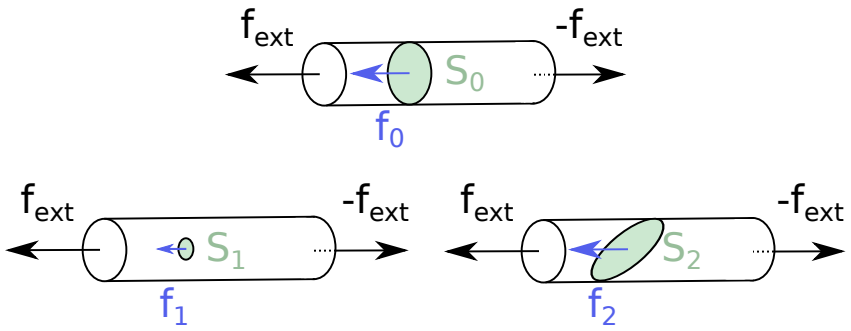

Figure 3.1: Beam subject to uniaxial forces. The tensor vector $\mathbf{t}_0$ is equal to the average force exerted on the surface S_0, thus $\mathbf{t}_0 = \frac{\mathbf{f}_0}{\mathcal{A}(S_0)}$, where $\mathcal{A}(S_0)$ is the area of S_0. Similarly, $\mathbf{t}_1 = \frac{\mathbf{f}_1}{\mathcal{A}(S_1)}$ and $\mathbf{t}_2 = \frac{\mathbf{f}_2}{\mathcal{A}(S_2)}$. We have $\mathbf{t}_0 = \mathbf{t}_1$ because the force and the surface area are proportional. However, $\mathbf{t}_0 \geq \mathbf{t}_2$ as the force exerted on the surface is the same ($\mathbf{f}_0 = \mathbf{f}_2$) but the area of S_2 is larger ($\mathcal{A}(S_2) \geq \mathcal{A}(S_0)$).

Let dV be a infinitesimal tetrahedral volume element with normal surfaces pointing outward as depicted in Fig. 3.2. The force exerted on the larger face of normal $\mathbf{n}$ is:

$$\mathbf{f} = \mathbf{t_n} dS, \tag{3.4}$$

where dS is the area of the surface, while the forces on the three other faces of the tetrahedron are:

$$\mathbf{f}_i = -\mathbf{t}_i dS_i \text{ for } i \in \{1, 2, 3\} \tag{3.5}$$

[1] Internal forces are a reaction against the external forces.

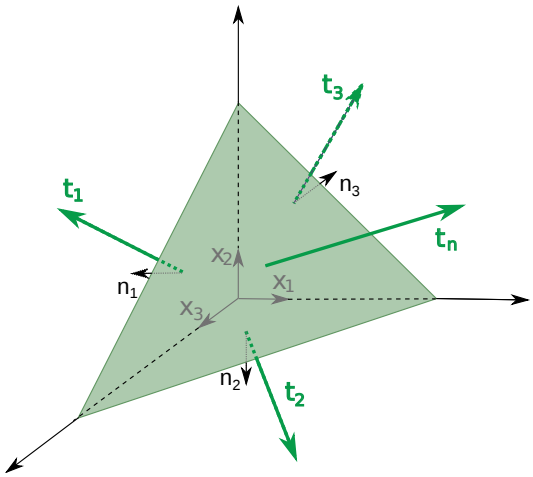

Figure 3.2: Infinitesimal volume element dV. The normal of its faces are $-\mathbf{x}_1$, $-\mathbf{x}_2$, $-\mathbf{x}_3$ and $\mathbf{n}$. The corresponding stress vector are $\mathbf{t}_1$, $\mathbf{t}_2$, $\mathbf{t}_3$ and $\mathbf{t}_\mathbf{n}$.

where $\mathbf{t}_i$ is the stress vector and dS_i is the surface area of the face i. The negative sign comes from the fact that the three faces have normals equal to the coordinate axis multiplied by -1. The volume force inside the tetrahedron is:

$$\mathbf{f}_v dV \tag{3.6}$$

where $\mathbf{f}_v$ has the dimension of force per unit volume. From the conservation of linear momentum we have:

$$\mathbf{f} + \mathbf{f}_1 + \mathbf{f}_2 + \mathbf{f}_3 + \mathbf{f}_v dV = \rho dV \frac{d\mathbf{v}}{dt} \tag{3.7}$$

where ρ is the mass density and $\mathbf{v}$ the velocity of the volume element. Using equations 3.4 — 3.6, this can be rewritten:

$$\mathbf{t}_\mathbf{n} dS - \mathbf{t}_1 n_1 dS - \mathbf{t}_2 n_2 dS - \mathbf{t}_3 n_3 dS + \mathbf{f}_v \frac{h}{3} dS = \rho \frac{h}{3} dS \frac{d\mathbf{v}}{dt} \tag{3.8}$$

where we have expressed the volume of the tetrahedron and all its surfaces in term of the height h of the tetrahedon, the surface dS and the coordinates of the normal $\mathbf{n} = (n_1, n_2, n_3)$. Dividing by dS and letting $h \to 0$ this leads to:

$$\mathbf{t}_\mathbf{n} - \mathbf{t}_1 n_1 - \mathbf{t}_2 n_2 - \mathbf{t}_3 n_3 = 0 \tag{3.9}$$

This means that knowing the stress vectors acting on three faces of normal parallel to the coordinate axes[2] we can compute the stress vector for any

[2] Actually, any three orthonormal vectors would work for the definition of the faces, but the stress vector would be expressed in the coordinate system of these vectors.

normal direction $\mathbf{n}$:

$$\mathbf{t_n} = \begin{pmatrix} \mathbf{t}_1 & \mathbf{t}_2 & \mathbf{t}_3 \end{pmatrix} \begin{pmatrix} n_1 \\ n_2 \\ n_3 \end{pmatrix} = \begin{pmatrix} T_{11} & T_{21} & T_{31} \\ T_{12} & T_{22} & T_{33} \\ T_{13} & T_{23} & T_{33} \end{pmatrix} \begin{pmatrix} n_1 \\ n_2 \\ n_3 \end{pmatrix} = \mathbf{T}^T.\mathbf{n} \tag{3.10}$$

where $\mathbf{T}$ is the Cauchy stress tensor.

We used the conservation of linear momentum to define the stress tensor. From the conservation of the angular momentum[3] we can show that this tensor is symmetric, that is:

$$T_{ij} = T_{ji} \text{ for } i \in \{1, 2, 3\}. \tag{3.11}$$

For more details on the derivation of the stress tensor the reader is referred to the section 2.7.3 of (Slawinski, 2007).

Equipped with the stress tensor we can express the forces exerted on closed surface S as:

$$\mathbf{f} = \oiint_S \mathbf{t_n} dS = \oiint_S \mathbf{T}.\mathbf{n} dS \tag{3.12}$$

And using the divergence theorem we can rewrite:

$$\mathbf{f} = \int_V \nabla.\mathbf{T} dV \tag{3.13}$$

where $\nabla.$ is the divergence operator. Note that $\nabla.\mathbf{T}$ is homogeneous to a force per unit volume and that we omitted the transpose sign because of the tensor symmetry: $\mathbf{T}^T = \mathbf{T}$.

3.1.2 Quantifying the deformation: the strain tensors

In the previous section we have described the relation between the forces exerted on a soft body and their effect in the volume through the stress tensor (equation 3.13). Now we see how to define mathematically the deformation, using a measure of this deformation called the *strain*.

Naively, a first choice can be the displacement $\mathbf{u}$ between the points in the rest configuration $\mathbf{p}$ and the points in the deformed configuration $\widetilde{\mathbf{p}}$. Yet, for a rigid transformation Φ_{rigid}, $\mathbf{u} \neq 0$ even if the object is not deformed. Thus, we need to find a better mathematical definition of the deformation.

Let $\mathbf{p}$ and $\mathbf{p} + \mathbf{dp}$ be two points infinitesimally close in the rest configuration, and $\widetilde{\mathbf{p}}$ and $\widetilde{\mathbf{p}} + \widetilde{\mathbf{dp}}$ be their position after the deformation. We have:

[3] This conservation law leads to the symmetry of the stress tensor in most media. However, if the media has intrinsic angular momentum, like ferromagnetic material or non-Newtonian fluids, the stress tensor is not symmetric.

$$\begin{aligned}\tilde{\mathbf{dp}} - \mathbf{dp} &= \widetilde{\mathbf{p}} + \tilde{\mathbf{dp}} - \widetilde{\mathbf{p}} - (\mathbf{p} + \mathbf{dp} - \mathbf{p}) \\ &= (\widetilde{\mathbf{p}} + \tilde{\mathbf{dp}} - (\mathbf{p} + \mathbf{dp})) - (\widetilde{\mathbf{p}} - \mathbf{p}) \\ &= \mathbf{u}(\mathbf{p} + \mathbf{dp}) - \mathbf{u}(\mathbf{p})\end{aligned} \tag{3.14}$$

We have used here the Lagrangian definition of the displacement, namely the displacement of a point of the soft body that we follow over time. Another definition of the displacement is the Eulerian definition: the displacement is studied at a fixed point of the three dimensional space which may correspond to different points of the soft body over time. However, these two definitions are equivalent for small displacements.

From the expression 3.14 we will try to find a better formulation of the strain. Recall that the Taylor expansion of $\mathbf{u}$ around $\mathbf{p}$ is:

$$\mathbf{u}(\mathbf{p} + \mathbf{dp}) \approx \mathbf{u}(\mathbf{p}) + \nabla\mathbf{u}|_{\mathbf{p}}\mathbf{dp} \tag{3.15}$$

where ∇ is the gradient operator. We can use 3.15 in 3.14:

$$\tilde{\mathbf{dp}} - \mathbf{dp} \approx \nabla\mathbf{u}|_{\mathbf{p}}\mathbf{dp}, \tag{3.16}$$

which can be rewritten as:

$$\begin{aligned}\tilde{\mathbf{dp}} &\approx (\nabla\mathbf{u}|_{\mathbf{p}} + \mathbb{I})\mathbf{dp} \\ \tilde{\mathbf{dp}} &\approx \mathbb{F}|_{\mathbf{p}}\mathbf{dp},\end{aligned} \tag{3.17}$$

where $\mathbb{F} := \nabla\mathbf{u} + \mathbb{I}$ is the gradient of the transformation Φ. $\nabla\mathbf{u}|_{\mathbf{p}}$ links the vectors between two points in the rest and deformed position and $\nabla\mathbf{u}|_{\mathbf{p}} = 0$ if $\tilde{\mathbf{dp}} - \mathbf{dp} = 0$, that is for rigid translations. However, $\nabla\mathbf{u}$ is not null when the soft body undergoes a rotation. Therefore, we need also a measure of the change in angle between two vectors in the rest and deformed configuration. Let $\mathbf{dp}_1$ and $\mathbf{dp}_2$ be two infinitesimal vectors starting at point $\mathbf{p}$, and let $\tilde{\mathbf{dp}}_1$ and $\tilde{\mathbf{dp}}_2$ be their configuration in the deformed state. Their scalar product is:

$$\begin{aligned}\tilde{\mathbf{dp}}_1.\tilde{\mathbf{dp}}_2 &= (\mathbb{F}|_{\mathbf{p}}\mathbf{dp}_1).(\mathbb{F}|_{\mathbf{p}}\mathbf{dp}_2) \\ &= (\mathbb{F}\mathbf{dp}_1)^T(\mathbb{F}\mathbf{dp}_2) \\ &= \mathbf{dp}_1^T\mathbb{F}|_{\mathbf{p}}^T\mathbb{F}|_{\mathbf{p}}\mathbf{dp}_2 \\ &= \mathbf{dp}_1^T\epsilon_c|_{\mathbf{p}}\mathbf{dp}_2\end{aligned} \tag{3.18}$$

where $\epsilon_c = \mathbb{F}^T\mathbb{F}$ is known as the right Cauchy-Green strain tensor. However, this tensor is not null when the difference in angle between the rest and deformed configuration is null. Indeed, if $\tilde{\mathbf{dp}}_1.\tilde{\mathbf{dp}}_2 = \mathbf{dp}_1.\mathbf{dp}_2$, we have $\epsilon_c = \mathbb{I}$. Thus, we take the difference between the two scalar products:

$$\begin{aligned}\tilde{\mathbf{dp}}_1.\tilde{\mathbf{dp}}_2 - \mathbf{dp}_1.\mathbf{dp}_2 &= \mathbf{dp}_1^T\epsilon_c|_{\mathbf{p}}\mathbf{dp}_2 - \mathbf{dp}_1.\mathbf{dp}_2 \\ &= \mathbf{dp}_1^T(\epsilon_c - \mathbb{I})|_{\mathbf{p}}\mathbf{dp}_2 \\ &= 2\mathbf{dp}_1^T\epsilon_g|_{\mathbf{p}}\mathbf{dp}_2\end{aligned} \tag{3.19}$$

where $\epsilon_g = \frac{1}{2}(\epsilon_c - \mathbb{I})$ is the Green Lagrange strain tensor which satisfies $\epsilon_g = 0$ when $\mathbf{dp}_1.\mathbf{dp}_2 = \mathbf{dp}_1.\mathbf{dp}_2$. This tensor can be expressed in terms of $\nabla\mathbf{u}$:

$$\begin{aligned}\epsilon_g &= \frac{1}{2}(\mathbb{F}^T\mathbb{F} - \mathbb{I}) \\ &= \frac{1}{2}((\nabla\mathbf{u} + \mathbb{I})^T(\nabla\mathbf{u} + \mathbb{I}) - \mathbb{I}) \\ &= \frac{1}{2}(\nabla\mathbf{u}^T\nabla\mathbf{u} + \nabla\mathbf{u}^T + \nabla\mathbf{u})\end{aligned} \tag{3.20}$$

From this expression of the Green Lagrange strain tensor, we see that it can be divided into a linear part $\epsilon_{glin} = \frac{1}{2}(\nabla\mathbf{u}^T + \nabla\mathbf{u})$ and a non-linear part $\epsilon_{gnl} = \frac{1}{2}(\nabla\mathbf{u}^T\nabla\mathbf{u})$. For a small displacement gradient ϵ_{gnl} is negligible. Thus the stress tensor can be approximated as:

$$\boldsymbol{\epsilon} := \epsilon_{glin} = \frac{1}{2}(\nabla\mathbf{u}^T + \nabla\mathbf{u}) \tag{3.21}$$

also called the infinitesimal strain tensor. Note that by construction all the strain tensors defined above are symmetric as they are equal to their transpose.

Many other strain tensors can be defined, like the Euler-Almansi strain tensor or the Biot strain tensor, the latter using the polar decomposition of the displacement field (i.e. the separation of the displacement field into a rotational and a symmetric stretch component). Actually, a strain tensor $\widetilde{\epsilon}$ needs only to satisfy the following points (Bažant and Cedolin, 2010).

- $\widetilde{\epsilon}$ vanishes for any rigid-body motion.
- $\widetilde{\epsilon}$ depends on $\nabla\mathbf{u}$ continuously, it is continuously differentiable and monotonic with respect to $\nabla\mathbf{u}$.
- $\widetilde{\epsilon} \to \boldsymbol{\epsilon}$ when $\nabla\mathbf{u} \to 0$

In this section we described a quantitative measure of the deformation known as the strain tensor. The choice of a particular strain tensor should be guided by the type of deformations which are likely to occur in the studied object. For small deformations and small strains the linear tensor is a good choice. Indeed, in this approximation, all strain tensors are equivalent, but it is easier to compute the deformation field (the unknown of the mechanical system) from a linearized strain tensor. For large deformations and small strains, tensors based on the polar decomposition of the displacement field are useful. However, the computation of the displacement field is more complex as it involves the computation of the rotation matrix which is not known *a priori*. In the next section we relate the strain to the force applied on the soft body through the stress tensor.

3.1.3 Linking stress and strain

As we saw in section 3.1.1 the stress is a quantification of the effect of the force inside the body volume. And from section 3.1.2, we have a measure of the deformation. The link between the forces applied on the soft body and the deformation will be set through the relation between the stress and the strain. We have:

External forces $\rightarrow$ Internal forces $\rightarrow$ Stress $\xrightarrow{MP}$ Strain $\rightarrow$ Displacement

$$\mathbf{f}_{ext} \rightarrow \mathbf{f}_{int} \rightarrow \mathbf{T} \xrightarrow{MP} \boldsymbol{\epsilon} \rightarrow \mathbf{u}$$

where MP stand for material properties. Indeed, the relation between the stress and the strain depends on the material properties of the soft body. The function $\Xi(\boldsymbol{\epsilon}, \text{MP})$ linking $\boldsymbol{\epsilon}$ to $\mathbf{T}$ is known as the constitutive law of the material. This function may be very complex, but for linear stress-strain relation and small displacements we can assume its linearity. In this case the constitutive law Ξ is known as Hooke's law.

This linear constitutive law, as it relates two tensor of order 2 each containing 9 elements, can be represented as a four order tensor c_{ijkl} with 81 elements. However, the stress and the strain tensors are symmetric. Therefore, they have only 6 independent elements and the number of elements of c_{ijkl} is reduced to 36. Using the Voigt notation we have:

$$\begin{pmatrix} T_{11} \\ T_{22} \\ T_{33} \\ T_{23} \\ T_{13} \\ T_{12} \end{pmatrix} = \begin{pmatrix} c_{11} & c_{12} & c_{13} & c_{14} & c_{15} & c_{16} \\ c_{21} & c_{22} & c_{23} & c_{24} & c_{25} & c_{26} \\ c_{31} & c_{32} & c_{33} & c_{34} & c_{35} & c_{36} \\ c_{41} & c_{42} & c_{43} & c_{44} & c_{45} & c_{46} \\ c_{51} & c_{52} & c_{53} & c_{54} & c_{55} & c_{56} \\ c_{61} & c_{62} & c_{63} & c_{64} & c_{65} & c_{66} \end{pmatrix} \begin{pmatrix} \boldsymbol{\epsilon}_{11} \\ \boldsymbol{\epsilon}_{22} \\ \boldsymbol{\epsilon}_{33} \\ 2\boldsymbol{\epsilon}_{23} \\ 2\boldsymbol{\epsilon}_{13} \\ 2\boldsymbol{\epsilon}_{12} \end{pmatrix} \tag{3.22}$$

where for the tensor c_{ijkl} we used the transformations $(i, j) \rightarrow m$ and $(k, l) \rightarrow n$ for the indices:

$$\begin{cases} m = i \text{ if } i = j, \\ m = 9 - (i + j) \text{ if } i \neq j \end{cases}, i, j \in \{1, 2, 3\},$$

$$\begin{cases} n = k \text{ if } k = l, \\ n = 9 - (k + l) \text{ if } k \neq l \end{cases}, k, l \in \{1, 2, 3\}.$$

Equation 3.22 can also be written in a more compact way:

$$\begin{aligned} T_n &= \sum_{m=1}^{6} c_{mn} \boldsymbol{\epsilon}_m, \text{ for } n \in \{1, 2, 3, 4, 5, 6\} \\ \mathbf{T} &= \mathbf{C}\boldsymbol{\epsilon} \end{aligned} \tag{3.23}$$

where $\mathbf{C}$ is the matrix form of c_{ijkl}. In this form the tensor c_{mn} is often called the stiffness matrix. Moreover, by analogy with force potential, if we define a scalar strain energy $W(\boldsymbol{\epsilon})$ such that:

$$\frac{\partial W(\boldsymbol{\epsilon})}{\partial \boldsymbol{\epsilon}_{ij}} = T_{ij} \tag{3.24}$$

we can show that $c_{ijkl} = c_{klij}$ (see section 4.2.1 of Slawinski (2007)). Thus, the number of independent elements in the four order tensor is reduced to 21.

$$\begin{pmatrix} T_{11} \\ T_{22} \\ T_{33} \\ T_{23} \\ T_{13} \\ T_{12} \end{pmatrix} = \begin{pmatrix} c_{11} & c_{12} & c_{13} & c_{14} & c_{15} & c_{16} \\ c_{12} & c_{22} & c_{23} & c_{24} & c_{25} & c_{26} \\ c_{13} & c_{23} & c_{33} & c_{34} & c_{35} & c_{36} \\ c_{14} & c_{24} & c_{34} & c_{44} & c_{45} & c_{46} \\ c_{15} & c_{25} & c_{35} & c_{45} & c_{55} & c_{56} \\ c_{16} & c_{26} & c_{36} & c_{46} & c_{56} & c_{66} \end{pmatrix} \begin{pmatrix} \boldsymbol{\epsilon}_{11} \\ \boldsymbol{\epsilon}_{22} \\ \boldsymbol{\epsilon}_{33} \\ 2\boldsymbol{\epsilon}_{23} \\ 2\boldsymbol{\epsilon}_{13} \\ 2\boldsymbol{\epsilon}_{12} \end{pmatrix} \tag{3.25}$$

If, in addition, the material studied is isotropic, the tensor should be invariant by all coordinates transformations. This leads to the equality of certain tensor elements, leaving only two independent elements:

$$\begin{pmatrix} T_{11} \\ T_{22} \\ T_{33} \\ T_{23} \\ T_{13} \\ T_{12} \end{pmatrix} = \begin{pmatrix} c_{11} & c_{11}-2c_{44} & c_{11}-2c_{44} & 0 & 0 & 0 \\ c_{11}-2c_{44} & c_{11} & c_{11}-2c_{44} & 0 & 0 & 0 \\ c_{11}-2c_{44} & c_{11}-2c_{44} & c_{11} & 0 & 0 & 0 \\ 0 & 0 & 0 & c_{44} & 0 & 0 \\ 0 & 0 & 0 & 0 & c_{44} & 0 \\ 0 & 0 & 0 & 0 & 0 & c_{44} \end{pmatrix} \begin{pmatrix} \boldsymbol{\epsilon}_{11} \\ \boldsymbol{\epsilon}_{22} \\ \boldsymbol{\epsilon}_{33} \\ 2\boldsymbol{\epsilon}_{23} \\ 2\boldsymbol{\epsilon}_{13} \\ 2\boldsymbol{\epsilon}_{12} \end{pmatrix} \tag{3.26}$$

These two parameter are often expressed as Lamé's coefficients, which in the present case are related to the material properties of the soft body:

$$\begin{aligned} \lambda &:= c_{11} - 2c_{44} \\ \mu &:= c_{44} \end{aligned} \tag{3.27}$$

We can then write the Hooke's law for isotropic materials 3.26 in a more compact form:

$$T_{ij} = 2\mu\boldsymbol{\epsilon}_{ij} + \delta_{ij}\lambda \sum_{k=1}^{3} \boldsymbol{\epsilon}_{kk} \tag{3.28}$$

Note that Hooke's law is linear in $\boldsymbol{\epsilon}$ but also in $\nabla\mathbf{u}$ because we used a linearized strain tensor. In the general case, when the hypothesis of small displacement and small strain does not hold, the constitutive law is not linear in $\nabla\mathbf{u}$. The material should therefore be modeled using an hyperelastic constitutive law such as the Saint Venant-Kirchhoff, Neo-Hookean or Mooney-Rivlin model. If we rewrite the Equation 3.28 with ϵ_g instead of $\boldsymbol{\epsilon}$, we obtain the Saint Venant-Kirchhoff model where $\mathbf{T}$ is not linear anymore in $\nabla\mathbf{u}$. Moreover, $\Xi(\epsilon)$ may also be non linear in ϵ.

3.1.4 From forces to displacement

We have now all the elements to write down the motion equations. The second law of Newton state that the change in linear momentum is equal to the sum of forces. Given a volume element V of surface S subject to a volume force $\mathbf{g}$ and to external force of stress tensor $\mathbf{T}$ Newton's second law in the Lagrangian formulation is:

$$\frac{d}{dt}\int_V \rho \frac{d\mathbf{u}}{dt} dV = \oint_S \mathbf{t_n} dS + \int_V \mathbf{g} dV \tag{3.29}$$

As this change in momentum can be caused by a change inside the volume or by a flow through the surface, we have:

$$\begin{aligned}\frac{d}{dt}\int_V \rho \frac{d\mathbf{u}}{dt} dV &= \int_V \frac{\partial}{\partial t}\left(\rho \frac{d\mathbf{u}}{dt}\right) dV + \oint_S \rho \frac{d\mathbf{u}}{dt}\mathbf{v}.\mathbf{n} dS \\ &= \int_V \frac{\partial}{\partial t}\left(\rho \frac{d\mathbf{u}}{dt}\right) dV + \int_V \nabla.\left(\rho \frac{d\mathbf{u}}{dt}\mathbf{v}\right) dV \\ &= \int_V \rho\left(\frac{\partial \frac{d\mathbf{u}}{dt}}{\partial t} + \mathbf{v}.\nabla \frac{d\mathbf{u}}{dt}\right) + \frac{d\mathbf{u}}{dt}\left[\frac{\partial \rho}{\partial t} + \nabla.(\rho \mathbf{v})\right] dV\end{aligned} \tag{3.30}$$

where we have used the divergence theorem for the second equality. From the conservation of mass the term in brackets $\left[\frac{\partial \rho}{\partial t} + \nabla.(\rho \mathbf{v})\right]$ is null, and thus:

$$\begin{aligned}\frac{d}{dt}\int_V \rho \frac{d\mathbf{u}}{dt} dV &= \int_V \rho(\frac{\partial \frac{d\mathbf{u}}{dt}}{\partial t} + \mathbf{v}.\nabla \frac{d\mathbf{u}}{dt}) dV \\ &= \int_V \rho(\frac{\partial}{\partial t} + \mathbf{v}.\nabla)\frac{d\mathbf{u}}{dt} dV \\ &= \int_V \rho \frac{d\frac{d\mathbf{u}}{dt}}{dt} dV \\ &= \int_V \rho \frac{d^2\mathbf{u}}{dt^2} dV\end{aligned} \tag{3.31}$$

Using 3.31 and 3.13 we can rewrite the Newton equation 3.29 as:

$$\begin{aligned}\int_V \rho \frac{d^2\mathbf{u}}{dt^2} dV &= \int_V \nabla.\mathbf{T} dV + \int_V \mathbf{g} dV \\ \int_V \left[\rho \frac{d^2\mathbf{u}}{dt^2} - \nabla.\mathbf{T} - \mathbf{g}\right] dV &= 0\end{aligned} \tag{3.32}$$

As this equation holds for any volume V we have obtained the Cauchy equation of motion:

$$\rho \frac{d^2\mathbf{u}}{dt^2} = \nabla.\mathbf{T} + \mathbf{g}. \tag{3.33}$$

This equation is known as the strong form of the Cauchy equation of motion. Assuming linear elastic isotropic materials, we finally link the change in linear momentum with the displacement using Equations 3.28 and 3.21 to obtain the Navier-Cauchy equation:

$$\begin{aligned}\rho \frac{d^2\mathbf{u}}{dt^2}_j &= \sum_{i=1}^{3} \frac{\partial}{\partial x_i}(2\mu\boldsymbol{\epsilon}_{ij} + \delta_{ij}\lambda \sum_{k=1}^{3} \boldsymbol{\epsilon}_{kk}) + \mathbf{g}_j \\ &= \sum_{i=1}^{3} \frac{\partial}{\partial x_i}\left(\mu(\nabla\mathbf{u}^T + \nabla\mathbf{u})_{ij} + \frac{1}{2}\delta_{ij}\lambda \sum_{k=1}^{3}(\nabla\mathbf{u}^T + \nabla\mathbf{u})_{kk}\right) + \mathbf{g}_j\end{aligned} \tag{3.34}$$

3.1.5 Definition of the material properties

For a reliable mechanical modeling of an object, the proper constitutive law should be selected and its parameters should be determined. However, determining these mechanical properties can be very challenging, especially for biological materials. Usually, physicists employ traction experiments to analyze the effect of known forces on an object. Different known forces are applied on a sample of the material and the sample elongation as well as the change in its cross section are quantified. For small strain, the constitutive law can be considered as linear and the Young's modulus E and the Poisson's coefficient ν can be determined from these measurements. The Young's modulus E, which is the linear coefficient between the strain and the stress for small deformations, is computed from the elongation values while the Poisson's coefficient ν, which is related to the compressibility of the material, is estimated from the cross section measurements. These coefficients are related to the Lamé's coefficients:

$$\begin{aligned}\lambda &= \frac{E\nu}{(1+\nu)(1-2\nu)} \\ \mu &= \frac{E}{2(1+\nu)}\end{aligned} \tag{3.35}$$

For biological tissues, the traction experiments are controversial because the biological samples are examined *ex vivo*. Therefore, the mechanical properties obtained may differ from the *in vivo* properties. New methods, such as *in vivo* tissue aspiration (Luboz *et al.*, 2012) or elastography (Gennisson *et al.*, 2013; Doyley and Parker, 2014) attempt to determine these parameters *in vivo*. Elastography is a non invasive technique which allows for the determination of the mechanical properties of biological tissues. Originally developed for diagnosis, as the tissue stiffness is an important indicator of certain disease, this technique has recently reached new application fields with the emergence of patient-specific biomechanical models

(Vappou, 2012). The idea behind elastography is the following: if the deformation of soft tissues can be predicted from their mechanical properties it should be possible to determine these properties from soft tissue deformations. Thus, the principle of elastography is to apply a force on the tissues and to image the resulting deformation and movements to deduce the material properties. Elastography measurements are performed with an ultrasound transducer or using MRI (in this case it is referred to as Magnetic Resonance Elastography, MRE). An actuator, provoking a static, harmonic or transient deformation is coupled to the imaging system.

Techniques using static and dynamic deformation can be distinguished. In the first case, the patient organs are imaged only twice: once when no forces are applied and once while a force is applied on the patient's skin. The relative stiffness of the organs can be determined by comparing the two images. However, a quantitative value of the Young's modulus E cannot be obtained with this experiment as the stress is not known. In the second case, a transient or harmonic mechanical perturbation is applied on the tissues while a detector register the induced tissue reaction. Usually, the actuator generates shear waves which provoke soft tissue deformation and their speed, related to the tissue mechanical properties, is monitored. For instance, in Hookean elastic incompressible materials, the square of the shear wave velocity is proportional to the material Young's modulus E. The proportionality coefficient is 3ρ where ρ is the material density (taken to be the density of water ($1000\,\mathrm{kg.\,m^{-3}}$) for the soft tissues of the human body) allowing for a quantitative estimation of the Young's modulus: $E \approx 3\rho v_s^2$, where v_s is the shear wave velocity.

First limited to the rheological characterization of homogeneous Hookean elastic tissues, elastography is now able to provide quantitative measures of the mechanical properties in a large variety of media. The only remaining issue with elastography techniques is their limited imaging depth, which is of about 5 cm to 6 cm maximum. Thus, large organs like the liver cannot be entirely imaged yet. Nonetheless, elastography methods are advancing fast and biomechanically based methods will surely benefit from patient-specific rheological measurement. Indeed, if a patient-specific map of the liver mechanical properties was available, our patient specific liver model would be physically exact in addition to being geometrically accurate. Meanwhile, the mechanical parameters are chosen in accordance with mean literature values Umale *et al.* (2011). The impact of this choice will be discussed in Chapter 4.

3.1.6 The boundary conditions

We have derived the differential equation which governs the mechanical behavior of a deformable object. The exact form of this equation depends on the constitutive law chosen for the deformable object and its mechanical parameters. However, this equation alone is not sufficient to find the displacement field $\mathbf{u}$. Indeed, Equation 3.33 is a general equation and does not define a specific problem, thus it does not have a unique solution. To obtain a unique solution, boundary condition should be imposed on the function $\mathbf{u}$. Boundary conditions determine the effect of the exterior environment on the studied object, and two types of boundary conditions can be distinguished: the Dirichelet and the Neumann boundary conditions. Let $\delta\Omega$ be the domain boundary. The Dirichelet conditions, which apply on $\Gamma_D \in \delta\Omega$, specify the value of physical quantities, for instance $\mathbf{u}$, on the domain boundary, while the Neumann conditions, $\Gamma_N \in \delta\Omega$, impose a traction at the boundary.

The boundary conditions are actually more important than the mechanical properties of the studied body. They are so important that with the same constitutive law and mechanical parameters, but different boundary conditions, the resulting deformation of a soft body is completely different. These conditions should be specified properly, because an over-specification of the boundary condition lead to an inconsistent problem. We must have $\Gamma_D \cap \Gamma_N = \emptyset$. That is, at each point on the boundary either the value of $\mathbf{u}$ or the value of its derivative should be specified, not both. For further information on this subject, the interested reader can found a nice explanation stating the importance of boundary conditions in fluid mechanics in Moretti (1968).

Nevertheless, we have to moderate, bearing in mind that the correct definition of the mechanical properties is also important. Indeed, with appropriate boundary condition the deformation of an hyperelastic material cannot be captured by a linear elastic law. Thus, both the boundary conditions and the mechanical properties should be correctly determined. However, if many papers address the determination of the material properties through rheological experiments, very few actually determine the exact boundary condition of their system.

In this section, we derived the Cauchy equation of motion that holds in a deformable solid from the second equation of Newton. This partial differential equation links the external forces applied on the soft body with its internal displacements through the constitutive law of the object. We also highlighted the important impact of the boundary conditions on the equation solution. However, the equations of motion need to be solved

for all the points inside the object. As the object is continuous this is not possible except if an analytical solution exists, which is the case only for very simple problems. The next section describes a numerical method, the Finite Element Method (FEM), which allows to solve this equation on a discrete representation of the soft body.

3.2 Numerical solution for the equation of motion

We seek the spatial distribution of the displacement field inside the soft body. Mathematically, this field problem is described by the Cauchy equation of motion, which is difficult to solve. Indeed, the differential equation 3.34 is impossible to solve analytically for the general case, as the geometry of the domain where the equation holds may be very complex. A solution to this difficulty is to approximate the solution using numerical methods.

Numerical methods discretize the problem and construct a linear system of physical equations. The physical problem can then be solved by taking advantages of the properties of linear systems, whose resolution has been extensively studied by mathematicians and engineers. The FEM is one of these approximation methods that find the solution of physical equations inside a closed domain. The FEM presents several advantages, for instance it can be applied to any field problem, it needs no restriction regarding the geometry of the application domain, and different types of elements can be used together in the same problem.

However, the necessity to generate a mesh to construct the system of equation constitute an important limitation of this method. Indeed, as already evoked in section 1.1.3 the generation of a suitable mesh for FEM may be difficult. Thus, meshless methods have also been investigated for biomechanical simulations (see for instance Horton *et al.* (2007)).

This section proposes an overview of the FEM.

3.2.1 Domain discretization

The first step of the FEM is to discretize the application domain into elements. Inside each element the complex physical field (the displacement field in the present case) is approximated with simple functions (usually at most quadratic functions). The elements are composed of nodes and are assembled to cover the entire domain. For our application tetrahedral mesh elements are used. Indeed, even if attention must be paid to the quality of the tetrahedral elements with regards to the FEM, automatic optimization algorithms exist (see section 1.1.3). Conversely, the generation of hexahedral

meshes which fulfill the quality requirement of the FEM is very challenging and cannot be entirely automatized. The nodes are the degree of freedom of the domain, i.e. the points where the physical equations are solved. The value of the field inside the element is determined by the simple functions, usually polynomials, chosen to approximate the field and the value of the field computed at the nodes: the shape functions.

Obviously, the size of the elements influence the quality of the approximation. We have seen in section 1.1.4 that a fine mesh represent more faithfully the geometry and therefore leads to a better approximation of the solution. Nonetheless, the size of the elements is also related to the approximation accuracy of the physical field, which is represented inside the element as a simple function. Indeed, the order of convergence of the FEM is $O(h^{p+1})$ where h is the characteristic size of an element and p is the polynomial degree of the shape function (Liu and Quek, 2013). Therefore, for linear elements the convergence is quadratic, which means that if the size of the elements is divided by a factor 2 the error is divided by 4. However, as the number of element increase so does the number of nodes, which is equal to the number of physical equations to solve, and thus the computation time increase. The complexity is in $O(N^2)$ for three dimensional problems where N is the number of nodes, but this exact arithmetic cost can be reduced (Zhou and Jiao, 2013).

3.2.2 Weak form of Cauchy's equation of motion

In order to apply the FEM to the physical problem described in section 3.1.4 the strong form of the Cauchy equation of motion 3.33 cannot be used. Indeed, this equation requires that the displacement field be twice differentiable inside the domain and differentiable at the boundary. However, some displacement fields which are physically acceptable do not belong to this category. Moreover, imposing the continuity of the derivatives between the elements is more difficult than simply ensuring the continuity of the displacement field. Thus, the strong form has to be modified to allow the displacement field to be only differentiable in the elements and C^0 at the boundary of the elements. This variational formulation is known as the weak form. Instead of looking at the effect of the equation at a point of the domain V, the equation is studied through its effect on a test function f, an infinitely differentiable function with compact support, over the domain V.

The weak form of the Cauchy's equation of motion is expressed as follows:

$$\begin{aligned}\int_V \rho \frac{d^2\mathbf{u}}{dt^2} f dV &= \int_V \nabla.\mathbf{T} f dV + \int_V f\mathbf{g} dV \\ \int_V \rho \frac{d^2\mathbf{u}}{dt^2} f dV &= \int_V \mathbf{T}\nabla f dV + \oint_S f\mathbf{T}.\mathbf{n} dS + \int_V f\mathbf{g} dV\end{aligned} \tag{3.36}$$

where S is the boundary of the domain V. On the second line we have used integration by parts and the fact that f is infinitely differentiable with compact support on the domain V and a corollary of the divergence theorem to transfer the differential operator to the function f. The weak form is equivalent to the strong form for function twice differentiable inside the domain and differentiable at the boundary. Physically, using the weak form, the equation of motion is satisfied over a domain in an integral sense rather than at every point.

3.2.3 Equation inside an element

Now that we have a better form for the Cauchy equation of motion we can choose the form of the functions N_m that approximate the displacement field inside each element. These functions are called basis functions or shape functions, and should have the following properties:

- One basis function has to be defined for each node of the element and have a local support.
- The basis functions are piecewise continuous.
- The basis functions are equal to one at their corresponding node and zero at all the other nodes of the element.
- At each point inside the element the sum of the basis functions must be equal to one.
- The basis functions of one element are linearly independent.

In the scope of this work, these functions are taken to be piecewise linear. As each node k is shared between several elements, a shape function associated to the node can also be defined:

$$\eta_k = \sum_{\mathcal{E}} \sum_m N_m \delta_{\mathsf{c}(m)k}, \tag{3.37}$$

where $\mathcal{E}$ is the set of all mesh elements and $\mathsf{c}(m)$ is the function which associates the index m of the node inside an element with its global index in the mesh.

We then use the Galerkin method, which means that the shape functions are used to define the test function f in equation 3.36:

$$f = \sum_m f_m N_m \tag{3.38}$$

where f_m are the value of f at the node m, index of the node inside the element. Using this test function inside an element e we have:

$$\begin{aligned}\int_{V_e} \rho \frac{d^2\mathbf{u}}{dt^2} \left(\sum_m f_m N_m \right) dV = & \int_{V_e} \mathbf{T}\nabla \left(\sum_m f_m N_m \right) dV \\ & + \oint_{S_e} \left(\sum_m f_m N_m \right) \mathbf{T}\mathbf{n} dS \\ & + \int_{V_e} \left(\sum_m f_m N_m \right) \mathbf{g} dV\end{aligned} \tag{3.39}$$

As the f_m are constant, we can rewrite:

$$\begin{aligned}\sum_m f_m \left(\int_{V_e} \rho \frac{d^2\mathbf{u}}{dt^2} N_m dV \right) = & \sum_m f_m \left(\int_{V_e} \mathbf{T}\nabla N_m dV \right) \\ & + \sum_m f_m \left(\oint_{S_e} N_m \mathbf{T}\mathbf{n} dS \right) \\ & + \sum_m f_m \left(\int_{V_e} N_m \mathbf{g} dV \right)\end{aligned} \tag{3.40}$$

where the first term of the right hand side is the stiffness matrix of the element:

$$\mathbf{K}^e = \int_{V_e} \mathbf{T}\nabla N_m dV \tag{3.41}$$

In the hypothesis of small deformations and linear elastic constitutive law, this term depends linearly on the displacement $\mathbf{u}$. Using the discretized form of the displacement field:

$$\mathbf{u} = \sum_m U_m N_m, \tag{3.42}$$

where U_m is the displacement of node m, and using Equations 3.21 and 3.28 we can rewrite the stress tensor as:

$$T_{ij} = 2\mu \left(\sum_m U_{mi} \frac{\partial N_m}{\partial x_j} + \sum_m U_{mj} \frac{\partial N_m}{\partial x_i} \right) + \delta_{ij} \lambda \sum_k \left(\sum_m U_{mk} \frac{\partial N_m}{\partial x_k} \right) \tag{3.43}$$

where $U_m i$ is the displacement of node m in the direction i. For tetrahedral elements and linear shape functions $N_m = a_{m0} + a_{m1}x_1 + a_{m2}x_2 + a_{m3}x_3$ we have $\frac{\partial N_m}{\partial x_j} = a_{mj}$. Thus we have:

$$T_{ij} = 2\mu\left(\sum_m U_{mi}a_{mj} + \sum_m U_{mj}a_{mi}\right) + \delta_{ij}\lambda\sum_k\left(\sum_m U_{mk}a_{mk}\right) \tag{3.44}$$

Using the Voigt notation we can rewrite the stiffness matrix of the element as:

$$\mathbf{K}_e = \int_{V_e} \mathbf{B}^T\mathbf{C}\mathbf{B}dV \tag{3.45}$$

where $\mathbf{C}$ is the stress-strain matrix defined in Equation 3.23 and $\mathbf{B}$ is the strain-displacement matrix computed from the shape functions as:

$$\begin{pmatrix} a_{11} & 0 & 0 & a_{21} & 0 & 0 & a_{31} & 0 & 0 & a_{41} & 0 & 0 \\ 0 & a_{12} & 0 & 0 & a_{22} & 0 & 0 & a_{32} & 0 & 0 & a_{42} & 0 \\ 0 & 0 & a_{13} & 0 & 0 & a_{23} & 0 & 0 & a_{33} & 0 & 0 & a_{43} \\ a_{12} & a_{11} & 0 & a_{22} & a_{21} & 0 & a_{32} & a_{31} & 0 & a_{42} & a_{41} & 0 \\ a_{13} & 0 & a_{11} & a_{23} & 0 & a_{21} & a_{33} & 0 & a_{31} & a_{43} & 0 & a_{41} \\ 0 & a_{13} & a_{12} & 0 & a_{23} & a_{22} & 0 & a_{33} & a_{32} & 0 & a_{43} & a_{32} \end{pmatrix}$$

Note that, as expected, the stiffness matrix $\mathbf{K}^e$ is 12×12. To derive this stiffness matrix we made the assumption that both the strain and the displacement are small. However, it is possible to release the small displacement constraint and to obtain a stiffness matrix for large displacement and small strain. To obtain this result we use the co-rotational formulation (Müller and Gross, 2004). Another solution would have been to use an hyper-elastic material law, but the co-rotational model is more robust and computationally efficient. The co-rotational formulation allows to extend the hypothesis of small displacement by splitting, inside each element, node displacements into a rotational and a translational part. The co-rotational stiffness matrix of an element e is computed from the matrix $\mathbf{K}^e$ defined in equation 3.41 as follows:

$$\begin{aligned} \mathbf{K}^e_{rot} &= \mathbf{R}_e\mathbf{K}^e\mathbf{R}_e^T \\ \mathbf{K}^e_{rot} &= \mathbf{R}_e\left(\int_{V_e}\mathbf{B}^T\mathbf{C}\mathbf{B}dV\right)\mathbf{R}_e^T \end{aligned} \tag{3.46}$$

where $\mathbf{R}_e$ is the rotation matrix associated to the element e. In the rotated frame associated to the element e, the displacement of the nodes are smaller and thus the small strain approximation can still be used (see Fig. 3.3). However, as the rotation $\mathbf{R}_e$ depend on the nodes displacement ($\mathbf{R}_e = \mathbf{R}_e(\mathbf{u})$) the co-rotational formulation introduce non-linearity in the system.

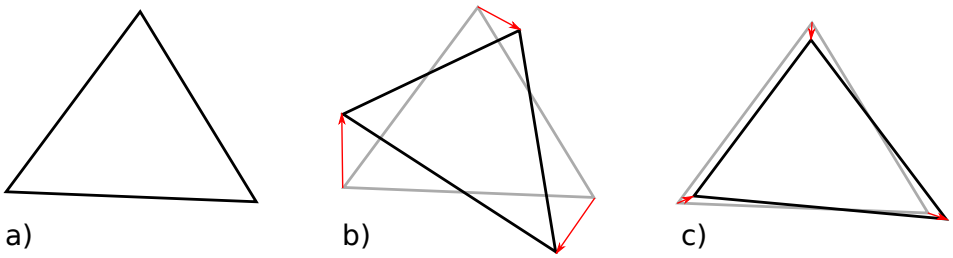

Figure 3.3: The co-rotational formulation allows to extend the validity of Hooke's law to large displacement if the strain is small. a) Initial shape of an element. b) The shape of the element after deformation. The initial shape is displayed in grey and the node displacement as red arrows. c) Deformed shape without the rotational component of the displacement.

In the same way we defined $\mathbf{K}^e$ we can define the vectors $\mathbf{b}^e$ of the volume forces and $\mathbf{s}^e$ of the surface forces that apply on the element e:

$$\begin{aligned} \mathbf{b}^e_{3(m-1)+j} &= \int_{V_e} N_m g_j dV \\ \mathbf{s}^e_{3(m-1)+j} &= \oint_{S_e} N_m t_j dS \end{aligned} \quad , m \in \{1, 2, \ldots, n_N\},\ j \in \{1, 2, 3\} \tag{3.47}$$

where n_N is the number of nodes in the element e. To compute the term on the left hand side of Equation 3.40, we define the mass matrix as:

$$\mathbf{M}^e = \int_{V_e} \rho dV \tag{3.48}$$

or as:

$$\mathbf{M}^e = \frac{m^e}{n_N} \mathbb{I}_{3n_N} \tag{3.49}$$

where m^e the mass of the element e. This second mass matrix, used in this work, is called the lumped mass matrix. Finally, given that the f_m are arbitrary and letting

$$\mathfrak{u}^e = (u_{1,1}, u_{1,2}, \ldots, u_{n_N,3})^T$$

$$\frac{d^2\mathfrak{u}^e}{dt^2} = (\frac{d^2\mathbf{u}}{dt^2}_{1,1}, \frac{d^2\mathbf{u}}{dt^2}_{1,2}, \ldots, \frac{d^2\mathbf{u}}{dt^2}_{n_N,3})^T$$

we can rewrite equation 3.40 inside an element e as:

$$\mathbf{M}^e \frac{d^2\mathfrak{u}^e}{dt^2} = \mathbf{K}^e \mathfrak{u}^e + \mathbf{b}^e + \mathbf{s}^e \tag{3.50}$$

3.2.4 Assembly of the system matrices and numerical resolution

Once we have the matrices for all the elements we can assemble the system. We have:

$$\mathbf{K}_{3(m_1-1)+n_1,3(m_2-1)+n_2} = \sum_{e\in\mathcal{E}}\sum_{i=1}^{n_{N_e}} \mathbf{K}^e_{3(i_1-1)+n_1,3(i_2-1)+n_2}\delta_{\mathsf{c}(i_1)m_1}\delta_{\mathsf{c}(i_2)m_2} \tag{3.51}$$

with $n_1, n_2 \in \{1,2,3\}$, n_{N_e} the number of node in the element e and

$$n_1, n_2 \in \{1, \ldots, n_{N_{tot}}\}$$

with N_{tot} being the total number of nodes representing the object. We also compute the complete force vectors using equation 3.37:

$$\begin{aligned} \mathbf{b}_{3(i-1)+j} &= \int_V \eta_i g_j dV \\ \mathbf{s}_{3(i-1)+j} &= \int_S \eta_i t_j dS \end{aligned} \quad , i \in \{1, \ldots, n_{N_{tot}}\},\ j \in \{1,2,3\} \tag{3.52}$$

And the complete lumped mass matrix is defined as:

$$\mathbf{M} = \frac{m_{tot}}{n_{N_{tot}}}\mathbb{I}_{n_{N_{tot}}} \tag{3.53}$$

where m_{tot} is the total mass of the modeled object. Finally, letting

$$\mathfrak{u} = (u_{1,1}, u_{1,2}, \ldots, u_{n_{N_{tot}},3})^T$$

$$\frac{d^2\mathfrak{u}}{dt^2} = (\frac{d^2\mathbf{u}}{dt^2}_{1,1}, \frac{d^2\mathbf{u}}{dt^2}_{1,2}, \ldots, \frac{d^2\mathbf{u}}{dt^2}_{n_{N_{tot}},3})^T$$

we have the equation for the complete system:

$$\mathbf{M}\frac{d^2\mathfrak{u}}{dt^2} = \mathbf{K}\mathfrak{u} + \mathbf{b} + \mathbf{s} \tag{3.54}$$

This equation is a spatially linearized numerical approximation of the equation 3.33 for the complete object. To provide a source of energy dissipation a damping matrix $\mathbf{D}$ is generally added to Equation 3.54:

$$\mathbf{M}\frac{d^2\mathfrak{u}}{dt^2} = \mathbf{K}\mathfrak{u} + \mathbf{D}\frac{d\mathfrak{u}}{dt} + \mathbf{b} + \mathbf{s} \tag{3.55}$$

the damping matrix is obtained by an approximation:

$$\mathbf{D} = r_M\mathbf{M} + r_K\mathbf{K} \tag{3.56}$$

where r_M and r_K are Rayleigh mass and damping, respectively.

If the left term is null — static case : the system is at equilibrium — any linear system solver can be employed to solve the equation. In this case, the solution is the value of the displacement for which the internal forces, the forces trying to return the object in its rest position, are equal to the external forces exerted on the object. However, while solving a static system, the boundary conditions have to be carefully defined. Without a proper definition of the boundary conditions, the stiffness matrix of the system defined in 3.54 is singular, and thus any attempt to solve the system fails or gives only one of the possible solution. For instance, imagine a soft ball subject to gravity. If the ground is not defined as a boundary condition the ball will never deform: the ball undergo a rigid body motion without introducing elastic forces. Thus the internal forces are always null and will never compensate the gravity. This system has no static solution.

Conversely, if the left term of 3.54 is not null, a temporal integration scheme has to be used prior the linear system solver. This involves the definition of a time step Δt whose value impact the accuracy and the computational cost of the numerical problem solution. A small Δt increases the accuracy, but to simulate 1 second, $1/\Delta t$ integration steps are required, thus the computational time increases. Two strategies can be employed to perform the temporal integration, the explicit temporal integration or the implicit temporal integration. While the explicit method uses the values of velocity, acceleration and forces computed at time $t - \Delta t$ to solve the system at time t, the implicit method approximates the values of these quantities at time t before solving the linear system for $\mathbf{u}$. The main difference between these two techniques is that the first one is only conditionally stable, whereas the second is unconditionally stable. The stability of the explicit method depend on the value of Δt. The explicit integration scheme is stable only if (Gosz, 2005):

$$\Delta t < \frac{h}{\sqrt{E/\rho}},$$

where h is characteristic size of the smallest mesh element, E is the Young's modulus, and ρ is the material density. Thus, for a finite element mesh with a characteristic size $h = 10^{-2}$m, a Young's modulus of $E = 9.10^3$Pa and a density $\rho = 1.10^3$kg.m^{-3}, we must choose $\Delta t \leq 10^{-3}$s. This means that to simulate 1 second, 10^3 simulation steps are required. However, implicit time integration allows to set $\Delta t = 10^{-1}$s, while ensuring the system stability. In the dynamic problem formulation, the specification of the boundary conditions that should be applied on the system is less restrictive. Indeed, for the problem of the ball described in the previous paragraph, a dynamic formulation would lead to an acceptable solution: the ball fall with a constant acceleration.

3.3 Real-time compatible biomechanical model of the liver

We have now all the elements to construct a biomechanical liver model which takes into account its different constituents: the parenchyma, the tumors, the Glisson's capsule and the vascular tree. As a patient specific biomechanical model construction is required for our surgical guidance system, this process should be as automatic as possible in order to be easily integrated in the clinical workflow. However, the automatic generation of tetrahedral meshes whose qualities are sufficient to be used in the finite element formulation of the physical problem is very challenging. The two more challenging structures are the Glisson's capsule and the vascular tree. The Glisson's capsule, which is a thin layer (of thickness <20μm) that surround the parenchyma, cannot be efficiently modeled with tetrahedra. Indeed, obtaining well shaped tetrahedra that can be employed in the FE formulation (i.e. tetrahedra with dihedral angles between 15 and 160) with automatic mesh generator may fail or require an important amount of time.The same problem also applies to the vascular structures which are very small and whose segmented map is often irregular due to the voxel size of the pre-operative images. Moreover, even if the mesh generation succeed, the number of nodes of the resulting meshes would be extremely large and thus would have an important computational cost.

To alleviate this difficulty, the mesh generated from the vascular tree segmented map is not a tetrahedral mesh. Instead, this mesh is composed of Bézier edges, taking advantage of the fact that the FEM allows for the simultaneous use of different elements type (see section 1.1.3). Following this idea, the surface mesh generated for the visualization can be used as the FE mesh of the capsule (see Fig. 3.4). Thus, three different kind of elements are employed to construct the biomechanical model of the liver: tetrahedral element for the liver parenchyma and the tumors, triangular elements for the capsule, and Bézier elements for the vascular tree.

To each mesh should now be associated a biomechanical model that represents faithfully the mechanical behavior of their biological counterpart. The choice of the constitutive laws employed for the different models has been guided by two observations:

- To be employed for surgical guidance the complete biomechanical model should be real-time compatible.

- The boundary conditions play a more important role than the mechanical properties of soft tissues (constitutive law + mechanical parameters).

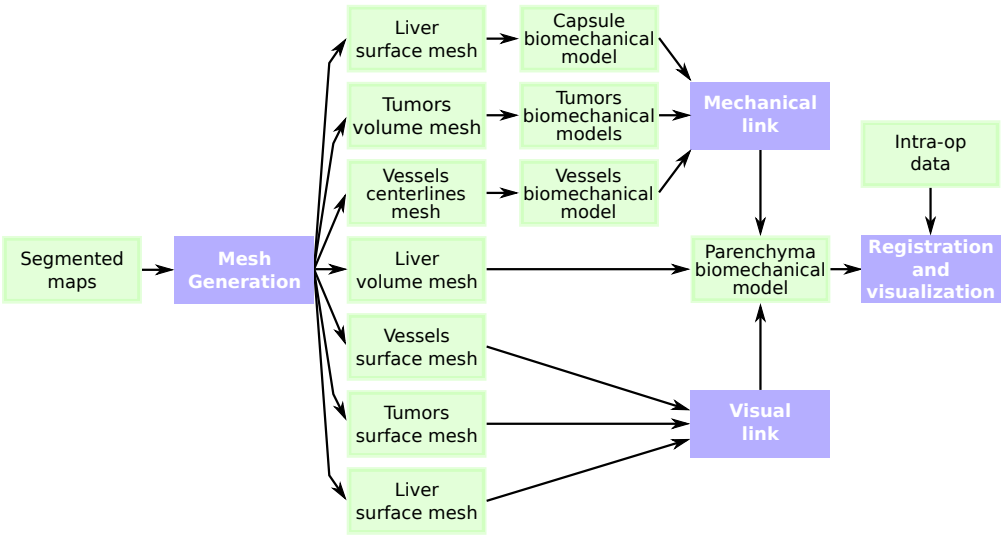

Figure 3.4: The liver surface is represented by two meshes: one for the visualization of the organ and the other for the mechanical model of the Glisson capsule. These two meshes can be the same or the visual mesh can be finer than the mechanical one.

The definition of an hyper-elastic model for the volume element of the liver biomedical model do not present any significant challenge. However, even if hyper-elastic models are known to offer a better accuracy for important displacement, they also increase the computational time. Moreover, in some biomedical application cases, the constitutive law of soft tissues does not influence the simulation result (Wittek *et al.*, 2009). As in our case the boundary conditions definition influences more the results than the mechanical properties of the tissues, we employ a linear elastic model for the volume elements and the co-rotational formulation.

The stiffness matrix of a tetrahedral element e of the liver parenchyma and the tumor is expressed as:

$$\begin{aligned} \mathbf{K}^e_{rot} &= \mathbf{R}_e \mathbf{K}^e \mathbf{R}_e^T \\ \mathbf{K}^e_{rot} &= \mathbf{R}_e \left(\int_{V_e} \mathbf{B}^T \mathbf{C} \mathbf{B} dV \right) \mathbf{R}_e^T \end{aligned} \tag{3.57}$$

The thickness of the Glisson's capsule is taken into account with the use of membrane elements. To maintain simplicity of the composite model we choose constant strain triangular (CST) elements based on co-rotational

formulation. For each CST element c, the 9×9 stiffness matrix $\mathbf{K}^c$ is given as

$$\mathbf{K}^c = \mathbf{R}_c \left(\int_V \mathbf{B}_c^T \mathbf{C}_c \mathbf{B}_c dV \right) \mathbf{R}_c^T \tag{3.58}$$

$$= h\mathbf{R}_c \left(\int_A \mathbf{B}_c^T \mathbf{C}_c \mathbf{B}_c dA \right) \mathbf{R}_c^T \tag{3.59}$$

$$= hA\mathbf{R}_c \mathbf{B}_c^T \mathbf{C}_c \mathbf{B}_c \mathbf{R}_c^T \tag{3.60}$$

where $\mathbf{B}_c$ is the strain-displacement matrix, $\mathbf{C}_c$ the material matrix, h is the thickness, and A the area of the element. The thickness is assumed constant which allow to go from 3.58 to 3.59, and the passage from 3.59 to 3.60 holds because $\mathbf{B}_c$ is constant in our case. More details on the derivation of this stiffness matrix can be found in Felippa (2003).

Finally, the vessels are modeled as Tymoshenko beam elements. Their hollow structure is taken into account via the proper definition of their moments of inertia. As the beam formulation considers both positional and rotational degrees of freedom (allowing for modeling the twists and torques), each beam element is modeled with a 12×12 elements stiffness matrix $\mathbf{K}^v$ which is defined in Duriez *et al.* (2006).

As already mentioned in chapter 1 section 1.1.3, the mechanical equations of motion are only solved for the biomechanical model of the parenchyma to reduce the computational time and the other structures are taken into account through links. The visual links relate the vertex positions of visual meshes to the vertex positions of the reference mesh (the parenchymal mesh) as follow:

- For each point of a visual mesh, the tetrahedron of the reference mesh which contains the point is found.
- Then, the barycentric coordinates of the point in the tetrahedron are used as the new coordinate system of the point.

This computation has to be done only once, unless the mesh undergo topological changes. A modification in the position of the reference mesh vertices is thus instantly reflected in the position of the coupled mesh vertices.

The mechanical links works also with the barycentric coordinates. However, in addition to the update in position, the mechanical links should take into account the forces which apply on the other structures as well as the specific biomechanical behavior of these structures. First, the forces on each vertex are computed as if the physical system would be solved in the classical way, that is for all the points of all the mechanical meshes. Then, each force that should be applied on a point which does not belong to the reference mesh is distributed to the vertices of the reference mesh tetrahedron

containing the point using the barycentric coordinates as weight. In this way, all the mechanical structures are taken into account with no additional cost for the system resolution.

The coupling between the vessel elements (beams) and parenchyma elements (tetrahedra) is described in detail in Peterlík *et al.* (2012). Briefly, each vessel node (having 6 degrees of freedom to account for torques in vessels) is coupled with a tetrahedra in which it is located via barycentric coordinates. This coupling remains constant during the simulation and can be described via matrix $\mathbf{J}_{v\to p}$ which is the Jacobian matrix of the coupling. The coupling between the parenchyma and capsule is straightforward, since the triangles used as the domain for the CST formulations are the surface faces of the volume mesh. Therefore, for a given triangle with vertices v_1, v_2 and v_3, the corresponding tetrahedron (sharing the same three vertices) is found and a 9×12 permutation matrix $\mathbf{P}_{c\to p}$ mapping the triangle vertices to tetrahedra vertices is computed.

Without loss of generality, let us suppose a tetrahedral element e which receives a mechanical contribution from both the capsule and vessels. The composite element stiffness matrix $\mathbf{K}_e$ is then computed as

$$\mathbf{K}_e = \mathbf{K}_p + \mathbf{J}_{v\to p}^{\top}\mathbf{K}_v\mathbf{J}_{v\to p} + \mathbf{P}_{c\to p}^{\top}\mathbf{K}_c\mathbf{P}_{c\to p}. \tag{3.61}$$

The beam and triangular elements together with the areas of the parenchyma having different Young's modulus introduce heterogeneity and anisotropy into the simulation of the organ. Therefore, either direct solver or preconditioners must be used to solve the system in each step of the simulation.

In this chapter we exposed the main principles of continuum mechanics and one of the numerical method which allow to solve complex mechanical equations: the finite element method (FEM). Using this framework we defined a complete biomechanical model of the liver taking into account its three mechanical component: the paranchyma, the vascular tree, and the Glisson's capsule. This biomechanical model is automatically generated from the meshes of the different structures generated in Chapter 1. Moreover, the use of the mechanical links, or coupling, allows to limit the number of physical equations and thus allow this model to be real-time compatible. Additionally, we described the importance of the boundaries conditions in mechanical problems. In the next part of this manuscript, we will see that the point cloud, described in chapter 1 section 1.2, can be viewed as a boundary condition for our pre-operative biomechanical model and the actual boundary condition of the liver will be determined.

Part II

Registration of Pre- and Intra-Operative Data

Introduction

The first part of this manuscript was dedicated to the different processing steps of the pre- and intra-operative data. This second part contains the main contributions of this work and explains how the processed data are employed to register the pre-operative shape of the liver onto its intra-operative configuration.

However, even with all the information extracted from the medical data, the registration problem is still ill-posed. Firstly, as the reconstructed point cloud is subject to noise and outliers, the visible surface position is not entirely accurate. Secondly, the precise definition of the anatomical landmarks position in both the pre- and intra operative data is challenging. Thirdly, the boundary conditions of the liver in the part that is not visible by the laparoscopic camera, corresponding to its inferior and posterior surface, are not known. These boundary conditions are required by the temporal registration methods based on optical tracking. Thus the initial registration should provide both the intra-operative shape of the liver and the position of its boundary conditions.

In this part we propose a method for the alignment of pre-operative data into an intra-operative laparoscopic view that is able to handle the previously mentioned issues. We first introduce an automatic and robust physically-based registration method that uses the reconstructed point cloud as boundary conditions for the biomechanical liver model. Then, we present a method to estimate the real boundary conditions of the liver from a patient data set using a statistical atlas. This atlas, associated with the registration method, allows to obtain the position of the liver boundary conditions at the end of the registration. In addition, the atlas can be used to automatically transfer the position of the anatomical landmarks to the biomechanical liver model used for the registration.

CHAPTER 4

RIGID TO NON RIGID PHYSICALLY BASED REGISTRATION

Contents

The work presented in this Chapter is partially based on the articles Plantefève *et al.* (2014a) and Plantefève *et al.* (2016).

4.1 State of the art

The specificity of medical data registration is that it is a multidisciplinary problem at the interface between computer vision, image processing, biomechanics and robotics. Therefore, numerous approaches, using the research background of each community, have been proposed. The purpose of this state of the art is not to cover entirely the related field but rather to give an overview of the methods proposed to solve the two main challenges faced by registration methods for IGS: the important of deformation of organs between the pre- and intra-operative state and the limited amount of intra-operative data. The solutions that have been proposed in the literature can be classified with respect to two criteria: the type of deformation they can handle and the available intra-operative modalities (see Table 4.1).

Intra-operative modality \ Deformation	Rigid	Small deformation	Large deformation
CT or MRI	*	*	* *
Fluoroscopy	*	* *	* * *
Ultrasound	*	* *	* * *
Surface digitizer or Laparoscope	* *	* * *	* * *

Table 4.1: The difficulty of the registration of pre-operative data onto the intra-operative data increases from the upper left corner — rigid transformation with three dimensional intra-operative images — to the lower right corner — large deformation with only surface information. The number of stars represents the level of difficulty.

4.1.1 IGS systems using only intra-operative data

The classification of the registration difficulty shown in Table 4.1 takes into account only IGS systems which rely on pre-operative data to provide additional information to the surgeon. However, some guidance systems rely only on intra-operative data. For instance, in Fleute and Lavallée (1998), the author rely on intra-operative manual surface digitization[1] to register a statistical shape model of the femur while Zheng *et al.* (Zheng *et al.*, 2002)

[1]The principle of surface digitization is to employ a tracked instrument that is swept along the bone surface to generate a point cloud which represents the surface.

combine fluoroscopy with surface digitization to obtain the intra-operative pose of the patient's femur for guidance in total hip arthroplasty. More recently, methods relying only on intra-operative fluoroscopy and statistical shape model have been developed for orthopedic surgery (Zheng *et al.*, 2007). Purely intra-operative methods have also been proposed for the brain: in Gronningsaeter *et al.* (2000) the authors have developed a neuronavigation system based on an improved optically tracked ultrasound device, SonoWand, to obtain a three dimensional intra-operative image of the wound area. Motion tracking for radiotherapy or focused ultrasound tumor ablation relying only on four dimensional intra-operative ultrasound has also been proposed by Vijayan *et al.* (Vijayan *et al.*, 2013). Even for laparoscopic liver surgery, navigation systems based only on intra operative data have been proposed. For instance, in Cheung *et al.* (2010) the authors have developed an image guidance system which fuses the images obtained by a laparoscopic ultrasound probe with the laparoscopic view. However, the size of the region imaged by the laparoscopic ultrasound is very limited and thus the localization of the vascular structures and tumors is still challenging for surgeons. In Tsutsumi *et al.* (2013) the authors have performed laparoscpic cholecystectomy and laparoscopic ventral hernia repair inside an open MRI operating theater, while in Feuerstein *et al.* (2007) the authors register a tracked C-arm and a tracked and calibrated laparoscope in a common reference frame, thus, the laparoscopic view of the liver is automatically aligned with the intra-operative CT images. Nonetheless, the image quality of intra-operative CT and MR imaging is lower than their pre-operative counterparts as the radiation dose is reduced for intra-operative CT and the strength of intra-operative MRI is limited. To overcome these problems, Shekhar *et al.* (Shekhar *et al.*, 2010) register a high resolution CT image acquired at the beginning of the intervention onto low dose CT images during the intervention. However, this method requires the use of a pre-operative CT scan during the intervention as well as a quasi-continuous low dose CT acquisition which is problematic for the patient and the surgical team. Moreover, for hepatic surgery, the interest of surgeons is to locate the resection planes that have been defined pre-operatively. In this case, methods based only on intra-operative data are of limited interest.

4.1.2 IGS systems relying on volume intra-operative imaging

Among the different intra-operative images modality, two dimensional (2D) fluoroscopy was first used for surgical guidance in orthopedic surgery. Indeed, as fluoroscopy was already used in most orthopedic interventions, some teams concentrated on a mean to register the two dimensional fluoro-

scopic images with CT pre-operative images (Lemieux *et al.*, 1994; Lavallée and Szeliski, 1995). Nonetheless, fluoroscopy has also been used in guidance systems for heart surgery: Turgeon *et al.* proposed to rely on intra-operative angiograms to register four dimensional pre-operative images (Turgeon *et al.*, 2005) Moreover Hipwell *et al.* have developed a guidance system for vascular intervention based on intra-operative digital subtraction angiography (Hipwell *et al.*, 2002). However, 2D fluoroscopy does not provide enough intra-operative data on the liver deformation because the three dimensional information is projected in one plane and the image signal is dominated by rigid structures such as bones. Intra-operative CT or MRI image-based registration methods for IGS have been extensively studied (see Sotiras *et al.* (2013) for a complete survey). Intra-operative CT and MRI are often used for neurosurgical guidance, but, as their quality is lower than their pre-operative counterparts, some teams have proposed to register pre- and intra-operative images. Clatz *et al.* employ an iconic registration method for MR images coupled with a finite element model of the brain to compensate for the brain shift (Clatz *et al.*, 2005). The use of intra-operative MRI has also been reported for robotic assisted prostate biopsy (DiMaio *et al.*, 2007). However, this modality require the use of MRI compatible surgical tools which do not exist for laparoscopic surgery. Thus, all the instrument should be removed before each image acquisition, which could prove cumbersome in practice. In Baumhauer *et al.* (2008) the authors have employed an intra-operative CT scanner to image the abdomen under pneumoperitoneum. These images are segmented and used to register the pre-operative kidney surface, then the registration result is aligned onto a laparoscopic view of the kidney using fiducials visible both in the laparoscopic and intra-operative CT images. Similar approaches have also been developed for the liver, but to place the marker another intervention is required prior to the surgery, which increases the patient's stay in hospital as well as the intervention cost. In Bano *et al.* (2013) the authors register pre-operative and intra-operative CT images in two steps: first, the images are rigidly registered using the spine, then, the inta-operative anterior surface of the liver is segmented and used to register a finite element model of the liver. Oktay *et al.* employ another method and simulate the effect of the pneumoperitoneum on the liver using a biomechanical model to initialise a diffeomorphic registration scheme based on image intensities (Oktay *et al.*, 2013). This work has been extended in Mountney *et al.* (2014) to detect automatically the laparoscope and register the intra-operative CT images on the laparoscopic view while taking into account respiratory motion. However, CT or MRI intra-operative imaging only provide a static view of the organs, while on the other hand the organs are deformed during surgery. Moreover,

the radiation dose required to obtain the intra-operative images limits the number of images that can be acquired and may hinder the acceptance of such systems. Due to these issues, these intra-operative modalities are not used in the present work.

4.1.3 IGS systems based on rigid registration

Rigid registration of pre-operative data using intra-operative ultrasound images or surface reconstruction have been first developed for orthopedic surgery. In Amiot *et al.* (1995) the authors employs a tracked stylus to digitize the intra-operative surface and register the pre-operative bones model using the reconstructed surface, while other teams use an ultrasound probe as digitizer to avoid the exposition of the bone surface (Maurer Jr *et al.*, 1999). However, rigid registration methods have also been proposed for guidance system for soft tissues interventions. Pioneers in augmented reality IGS for the brain have proposed a system for an operating microscope which register rigidly the patient's brain using tracked fiducials (Edwards *et al.*, 1995, 2000). In urology, even if the kidneys move significantly due to the respiratory motion, (Leroy *et al.*, 2006; Brandner *et al.*, 2006), their deformation remains limited (Schneider *et al.*, 2013), even during laparoscopic surgery (see Fig. 4.1: the pneumoperitoneum does not change much the shape of the left kidney (in green)). Thus, almost all the proposed guidance system for urology rely only on rigid registration. For percutaneous procedures, some authors have employed ultrasound to register pre-operative data to avoid the use of intra-operative CT, the classical modality used to guide needle insertion. In Leroy *et al.* (2007), for instance, the authors have used a correlation ratio and the Powell-Brent's non-derivative minimization scheme to rigidly register the pre-operative CT images and intra-operative ultrasound images acquired with a tracked probe. For laparoscopic urologic surgery, intra-operative surface data has also been used, as in Altamar *et al.* (2011) where the authors employ a tracked stylus to reconstruct the intra operative kidney surface and register pre-operative CT data using an iterative closest point algorithm. Registration methods relying on stereoscopic laparoscope have also been proposed. For instance, Su *et al.* combine manual registration with optical tracking to keep the pre-operative kidney model aligned with the laparoscopic view (Su *et al.*, 2009) while Pratt *et al.* propose a semi-automatic registration using the three dimensional reconstruction of a point on the kidney surface and an intuitive user interface (Pratt *et al.*, 2012). Nicolau *et al.* rely on skin markers, an external stereoscopic visualization system and a respiratory gating technique to guide thermal ablation (Nicolau *et al.*, 2009). In Mårvik *et al.* (2004) the authors employ a similar

technique for laparoscopic surgery. The markers are registered before the pneumoperitoneum, thus, the internal structures that deforms little under pneumoperitoneum, like the kidney and the aorta, are still well registered during the laparoscopic procedure. However, rigid registration has also been applied to situation where the organs are known to deform significantly. In liver surgery for instance, rigid registration methods for guidance systems have been proposed. In Marescaux *et al.* (2004) a manual rigid registration of a three dimensional model on a laparoscopic view is performed to provide the tumor and vessels location to the surgeon, while in Ellsmere *et al.* (2003) a tracked ultrasound probe is registered to the pre-operative three dimensional model of the patient to help surgeons locate the image plane. The use of a laparoscopic laser range scanner has also been proposed by Rauth *et al.* who have used this technology to register a segmented pre-operative liver model (Rauth *et al.*, 2007). For open surgery, in Clements *et al.* (2006), the authors use a laser range scanner to acquire the intra-operative liver surface during open surgery and employ anatomical landmarks and a weighted iterative closest point (ICP) scheme to register the pre-operative images. Even commercial systems which rely on rigid registration have been proposed for open (Kingham *et al.*, 2012; Peterhans *et al.*, 2011; Banz *et al.*, 2014) and laparoscopic (Kingham *et al.*, 2013) liver surgery. Despite their limited accuracy due to the rigid registration, these methods already provide valuable information to the surgeons. Nevertheless, to improve the registration accuracy, non rigid methods have to be investigated as suggested by Miga *et al.* (Miga *et al.*, 2003).

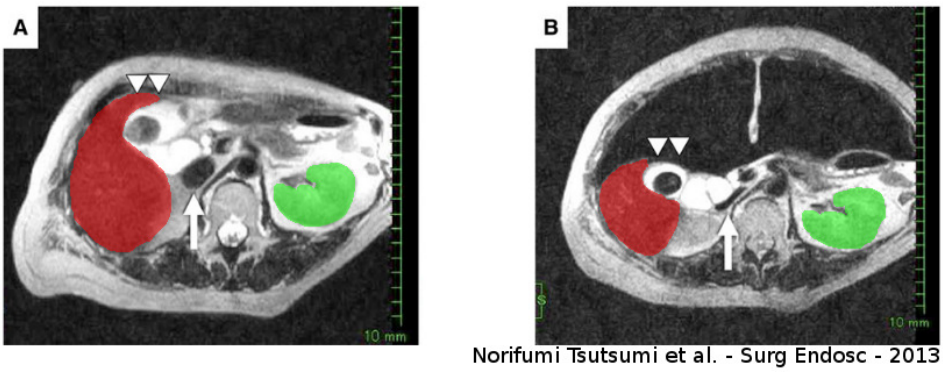

Figure 4.1: Deformation induced by the pneumoperitoneum. The liver (in red) is strongly deformed while the shape of the left kidney (in green) is almost the same in both images. MRI images from Tsutsumi *et al.* (2013)

4.1.4 IGS systems for weakly deformable organs

Registration algorithms using the same intra-operative imaging modality as above (ultrasound or surface reconstruction), but able to handle small deformation have been developed for per-cutaneous procedures, prostate biopsy and brain shift. For instance, in Maier-Hein *et al.* (2008) the authors employ tracked needle markers to follow the liver movement during per-cutaneous procedures. In this article, a pre-operative image of the liver with the markers is registered on the intra-operative configuration using spline interpolation. For prostate biopsy, the main intra-operative imaging technique employed is transrectal ultrasound (TRUS) in which the probe push on the organ in order to get images, causing small changes in the organ shape (Deurloo *et al.*, 2005). To register automatically intra-operative TRUS onto pre-operative MR images, Hu *et al.* (Hu *et al.*, 2012) employ a statistical shape model of deformation trained with biomechanical simulations, while in Sun *et al.* (2013) the authors use a coarse to fine registration scheme based on an image feature descriptor (Heinrich *et al.*, 2012). Neurosurgical guidance systems relying on non-rigid registration methods have also been proposed, even if the deformations are small Letteboer *et al.* (2005) because the accuracy of the IGS system is critical in this kind of surgery. Several methods employ intra-operative ultrasound, as in Bucki *et al.* (2012) where the authors rely on tracked Doppler ultrasound data to register pre-operative MRI angiograms onto the intra-operative reference frame using an elastic registration method based on the vascular tree, while Rivaz *et al.* (Rivaz *et al.*, 2015) use a image correlation method and free-form cubic B-splines to register pre-operative MR images onto intra-operative ultrasound images. However, some groups have investigated the use of the cortical surface alone, usually acquired by a laser range scanner, to register pre-operative images. For instance, to estimate the brain shift, Audette *et al.* use the cortical surface to constrain a biomechanical finite element model of the brain (Audette *et al.*, 2003). This approach has also been used more recently by Wittek *et al.* (Wittek *et al.*, 2009). The use of a stereoscopic camera has also been investigated in Škrinjar *et al.* (2002) where the reconstructed cortical surface is used as a boundary condition for a biomechanical model. Despite the limited amount of intra-operative data, these biomechanical-based registration method are accurate, highlighting the interest of biophysical modeling for this type of problems. The registration methods presented above perform well, but the deformations of the tissues of interest are small. Thus, a rigid registration is always a good initialization for these registration techniques. This assumption is unfortunately not valid for liver surgery where the organ may undergo important deformation.

4.1.5 Ultrasound IGS for highly deformable organs

To handle large organ deformation the use of intra-operative ultrasound probe has been extensively studied. Indeed this imaging modality is safe, inexpensive and provide in-depth information of the organ structures. For instance, in cardiac interventions, Huang *et al.* employ an ECG gating technique and mutual information image based registration to register pre-operative three dimensional CT onto the dynamic ultrasound images (Huang *et al.*, 2009). In Zhang *et al.* (2011), the authors employ cross correlation ratio on the cardiovascular magnetic resonance imaging and three dimensional ultrasound image sequences to detect the end-systolic and end-diastolic volume frames which they use to register temporally both signals. Then a poly-affine registration using mutual information is employed to align spatially all pairs of images. In open liver surgery, several teams have investigated the use of ultrasound, which is a common and low cost imaging modality. Nevertheless, a conventional ultrasound image gives only in-depth information on a slice of the imaged volume. Thus, methods to increase the amount of intra-operative data provided by this imaging modality have been developed. In Lange *et al.* (2003) the authors use an optically tracked 3D Doppler ultrasound probe to register pre- and intra-operative images using vessel centerlines and a two-step registration scheme: first, a rigid iterative closest point is performed, then B-splines are employed to account for the deformation. However, Doppler ultrasound suffers from low acquisition rates and artifacts which can disrupt the centerlines extraction algorithm. Nam *et al.* present an automatic feature-based affine registration procedure of 3D B-mode intra-operative ultrasound images and pre-operative CT images (Nam *et al.*, 2011) using automatically segmented vascular structures and liver surface, but the processing time (40 seconds) which is far from real-time. Moreover, 3D ultrasound probes are not widespread in the operating rooms. In Peterhans *et al.* (2009) the authors register a biophysical model containing the position of the tumors and vessels and tracked instruments onto a common intra-operative reference frame using 2D ultrasound images obtained with an optically tracked probe. Ultrasound probes have also been used to register pre-operative images during laparoscopic procedure, but optical tracking techniques cannot be used for laparoscopic ultrasound probe. In Song *et al.* (2015) the authors employ an electromagnetically tracked probe and a locally rigid registration scheme using the vessels centerlines to register the imaged plane onto a pre-operative model of the organ obtain from CT images. However, due to the interferences of the other surgical devices the electromagnetic tracking is error prone. Moreover, in order to obtain a clear ultrasound image the

probe should be pressed against the organs, and thus induces a deformation of the imaged region. Therefore, the imaged structures position are distorted. Despite these drawbacks, ultrasound based methods are very interesting as they are inexpensive and provide in-depth information of the organ structure. Nonetheless, solving the challenges of ultrasound based IGS is beyond our area of expertise.

4.1.6 IGS based on surface reconstruction for highly deformable organs

Methods based on surface reconstruction have also been proposed as intra-operative data for registration of large deformation. In cardiac surgery techniques relying on laparoscopic images instead of ultrasound images have been developed. In Pratt *et al.* (2010) the authors register four dimensional pre-operative CT images onto a stereoscopic laparoscopic view by solving an inverse mechanical problem where the displacement are prescribed by a reconstructed three dimensional point cloud of the heart surface. A motion model is generated from the images and the initial phase of the cardiac motion is obtained through a least square minimization of fiducial distance over several beating cycles. However, this technique is applicable only for cyclic motion, but during liver surgery, the liver is mobilized by surgeons to access tumors area, and thus important and unpredictable deformations may occur. In Cash *et al.* (2005) the authors register an undeformed phantom onto a point cloud obtained with a laser range scanner in a deformed configuration using a FEM model and three different type of boundary conditions (fixed, stress free, and prescribed by the point cloud). In Cash *et al.* (2007) the same team have applied their methods on clinical data with a registration error of 2 to 6 mm on the visible surface. In Miga *et al.* (2011) the authors compare three different ways to infer the deformation in the non visible part of the liver: an altlas of deformation; a method based on the Laplacian; and a radial filter method. All three methods lead to similar results. However, the results are obtained on a liver phantom that is only slightly deformed. Rucker *et al.* have proposed to estimate the boundary condition on an invisible surface given the deformation on the visible part for open liver surgery guidance (Rucker *et al.*, 2013). In this article the non-visible surface deformation is modeled as a two dimensional polynomial function and the deformation modes are optimized to match the deformation on the visible part. However, their results are obtained on phantom data for which the experimental set up matches the methods hypothesis (the deformation of the phantom is only due to a deformation of the lower phantom surface). While a laser range scanner allows for a very good surface reconstruction with low noise level, such scanners exist only as prototypes

for laparoscopic interventions (Rauth *et al.*, 2007; Fusaglia *et al.*, 2015). Thus, alternative techniques for laparoscopic procedure have been investigated. Unlike in open surgery, the portion of the liver which is visible during the operation is small, thus surface reconstruction techniques only provide little information on the intra-operative organ shape. In (Wu *et al.*, 2014) the authors have extended the work of (Rucker *et al.*, 2013) to the laparoscopic case using a tracked conoscope, which rely on interference measurements of a laser beam reflected on the organ surface to determine the depth, and mock-ultrasound images generated from CT data. Nevertheless, a laparoscopic conoscope does not yet exist, using mock ultrasound simplify the problem of probe tracking and the deformation proposed in the set up is small. Another approach to this registration problem has been proposed in Suwelack *et al.* (2014). The authors employ a electrostatic potential field generated by the intra-operative surface, which can be reconstructed from stereoscopic images (Röhl *et al.*, 2011), to register a biomechanical model of the liver, and show good registration result when using 50% of te entire liver surface. Nonetheless, the portion of surface obtained from stereoscopic reconstruction never attain 50% of the entire surface in real laparoscopic scenario. Moreover, a portion of the biomechanical model has to be fixed by Dirichelet boundary condition before the registration. Thus, a good initial alignment is required. A pose-independent matching of intra-operative data acquired by a camera was proposed by the same team in Dos Santos *et al.* (2014). The method is automatic and takes into account data noise and tissue deformations. However, the approach requires to have access to an advanced camera hardware providing depth information, which facilitates the reconstruction of the surface, but is not usable in clinical (minimally invasive) conditions.

4.1.7 An IGS system for laparoscopic surgery compatible with the clinical workflow

The proposed method relies on standard available clinical data, thus intra-operative information is provided only by the stereoscopic camera. As biomechanical organ modeling has proven to be useful for large deformation as well as limited amount of intra-operative data, we choose to use a physically-based registration method. This method should be robust to noise, outliers and to limited amount of intra-operative data. Additionally, it should be robust to poor initial alignment in order to be used without any pre-registration method. Moreover, the registration method should be fast enough to be used during a surgical intervention (registration time below 2 minutes). Finally, the method is designed to be able to integrate easily

additional data source, such as a laparoscopic ultrasound probe, into the registration problem.

4.2 Method

4.2.1 Algorithm overview

As already explained in the general introduction of this thesis, registration problems are usually cast as constrained minimization problems which can be decomposed in three parts. First, a distance measure, $\mathcal{E}$, or a similarity measure, $\mathcal{S}$, between the input data is chosen, then, constraints are applied to the problem, and finally, an optimization method maximizes the similarity measure given the constraint set to find the transformation, $\mathcal{T}$, that best aligns the input data. Commonly, the input data that is transformed is referred to as the source, $\mathbb{S}$, while the other is called the target, $\mathbb{T}$.

With these notation the registration problem can be written as one of the following optimization problems over $\mathcal{T}$:

$$\arg\min_{\mathcal{T}} \left[\mathcal{E}(\mathbb{T}, \mathcal{T}(\mathbb{S})) + \mathcal{R}_1\right]$$

or

$$\arg\max_{\mathcal{T}} \left[\mathcal{S}(\mathbb{T}, \mathcal{T}(\mathbb{S})) + \mathcal{R}_2\right]$$

where $\mathcal{R}_1$ and $\mathcal{R}_2$ are regularization terms which contain non-parametric constraints on the transformation $\mathcal{T}$.

The proposed methods takes as input a three dimensional point cloud reconstructed from a stereoscopic camera view of the organ surface and the biomechanical model described in section 3.3. Both data sets are labeled with the three landmarks corresponding to the umbilical notch (UN) the anterior margin (AM) and the hilum (defined in section 2.3). The registration method, like the methods proposed in Besl and McKay (1992) or in Chui and Rangarajan (2003), is an iterative and alternating method which recompute the correspondences at each step. However, unlike these two algorithms, it recast the registration problem as a system of biomechanical equations. At the beginning of the registration process, the biomechanical model (source) is in its pre-operative configuration and needs to be deformed to match the intra-operative point cloud (target). This match is only partial since the target represents only 30% to 40% of the total surface of the liver in the best cases. The biomechanical model is used to simulate the behavior of the tissue while the registration constraints imposed to the deformable object are modeled with penalty forces f_{ext} computed from the set of correspondences. During the registration process, theses penalty forces are increased progressively in an annealing scheme each time the registration process reaches an

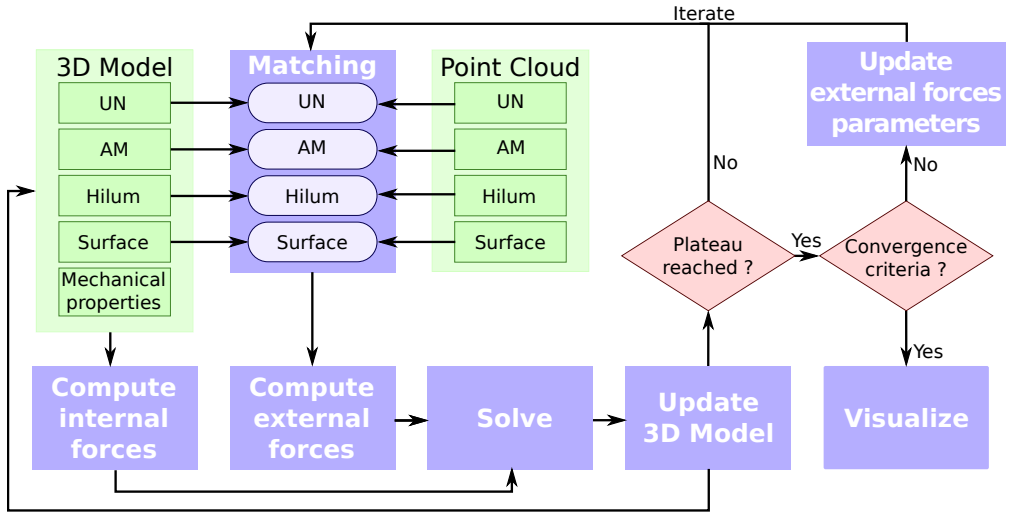

Figure 4.2: Main steps of the registration method. First, a matching is performed between the selected anatomical features (the umbilical notch (UN) the anterior margin (AM) and the hilum) as well as for the whole surface. This matching is used to compute penalty forces which will deform the biomechanical model of the liver. Then, the matching is recomputed and new forces are applied on the model. The penalty forces are increased each time the registration has reached an equilibrium. This process is iterated until the convergence criterion is met.

equilibrium until the convergence criterion is met. Fig. 4.2 summarizes the pipeline.

4.2.2 Similarity Measure and Matching

The similarity measure quantifies the degree of alignment between the source and the target. This measure may be global (e.g. the dice measure) for rigid, affine or projective registration, but as soon as deformations are allowed, global distance measures are generally not sufficient and local distances have to be employed. However, the computation of these similarity measures implies the definition of matching features in the source and target data. Several strategies for defining these correspondences can be adopted, depending on the input data. The matching itself requires the definition of a distance between the source and the target, which may be different from the distance used for the similarity measure. This matching can be computed only once, as in rigid registration marker-based methods (Edwards *et al.*, 2000; Zheng *et al.*, 2002), or can be recomputed during the registration process, using the current estimation of the transformation $\mathcal{T}$.

For geometric objects, correspondences may be defined using several distance measures. For instance, the Euclidean distance on $\mathbb{R}^n$. When a point location covariance measure on either the source or target data

position is available, the Mahalanobis distance can be used instead of the classical Euclidean distance (Pennec *et al.*, 1998, 2005; Feldmar *et al.*, 1995). Geodesic distances have also been employed, as in Bano *et al.* (2013) where the authors define several landmarks on both the source and target surfaces to compute geodesic distance to landmarks on the meshes and match points with the same geodesic distances. In Davatzikos (1997) the authors use distances on geometric descriptors spaces to define correspondences on the cortical surface.

The geodesic distance and distance based on geometric descriptors require the definition of surface topology. However, the surface generation process take time and would slow down the registration. On the other hand, the choice of the Mahalanobis distance to define the correspondences may lead to unwanted corresponding pairs. Indeed, a point with a high covariance matrix may be matched with a point which is actually far from its real position. In addition, this distance is designed to works with point sets, thus the generalization of this distance to point to surface registration is not straightforward.

Thus, in this work we have selected the euclidean distance to define the correspondences.

Once the distance is selected, a wide variety of algorithm for correspondences determination can be used. They can be classified according to three criteria: whether the algorithm is deterministic or probabilistic, whether it is binary or fuzzy and and whether it is one-to-one or many-to-many in nature. Binary algorithms consider that all corresponding pairs have the same weight in the computation of the similarity measure, while fuzzy algorithms allow to associate different weight to different pairs, usually based on the distance used to define the correspondences.

In Chui and Rangarajan (2003) the authors view the matching problem as a probabilistic problem and propose a fuzzy one-to-one matching algorithm for point sets. However, the definition of fuzzy correspondences between a point cloud and a surface is not straightforward, and may be problematic in our case. Indeed, fuzzy correspondences matches one target point with several source points (because our matching need to cope with partial target data the matching is only performed from the target points to the source surface). If the point cloud density is too low, several source points will be attached only to one target point. Thus, all the source points attached to the same target point will be attracted only to this point, causing the biomechanical model to shrink in this area as the correspondences are used to define the forces which apply on the surface.

One of the most well known deterministic binary algorithm is the matching algorithm of the iterative closest point method (ICP, Besl and McKay

(1992)) which pairs each point of the source (or of the target) with its closest neighbor on the target (or on the source) according to the chosen distance. However, this simple approach has important drawbacks, it does not handle properly outliers or points which are only in the source or the target data and does not guarantee one to one correspondences. Therefore, many improvements of ICP matching algorithm have been proposed. For instance in Masuda and Yokoya (1995) the authors match only a random subset of the points and estimate the quality of the matching with the rest of the points. However, this method is not efficient for non-rigid registration purpose. Another approach is the one of Penney *et al.* where the position of the point are perturbed by a random Gaussian noise before computing the closest points (Penney *et al.*, 2001). However, despite their efficiency, such methods are time consuming. In Clements *et al.* (2006), the authors define feature region on both the source and the target and employ a weighted ICP scheme which biases the distance between the points by lowering the distance between points belonging to the same region.

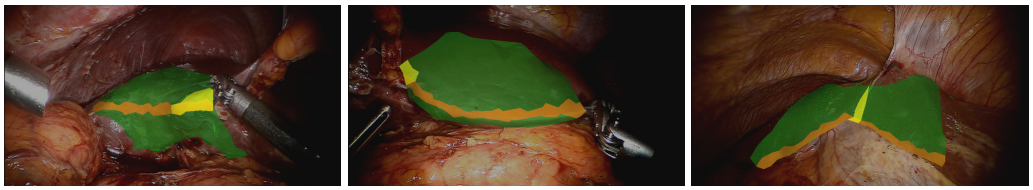

(a) (b) (c)

Figure 4.3: Detection of anatomical landmarks on laparoscopic images: The liver surface (in green), the anterior margin (in orange) and the umbilical notch (in yellow) are extracted from the laproscopic images using a stereoscopic matching method to obtain a 3D labeled point cloud. The hilum is not visible because is is located under the liver, but the surgeon can visualize it by moving the liver lobes.

Our method adopts a similar principle, and uses the anatomical features defined in Chapter 2, but does not allow for inter-region correspondences. This presents the advantage of reducing the computational cost. The matching algorithm has a complexity of $O(\mathbf{nt})$ where $\mathbf{n}$ is the number of points on the point cloud and $\mathbf{t}$ the number of triangles of the mesh surface. Several matchings are achieved simultaneously: one for each labeled area (UN,AM, and hilum, see Fig. 4.3) and one for the rest of the liver surface. For each area the points of the target model are projected onto their corresponding area on the source model surface as shown in Fig. 4.2. We do not project the source model points on the target since the target only corresponds to a part of the source model, thus an important number of matches would be inaccurate. Each target point is projected onto all the triangles of the source model surface with the same label. To decrease the computational

time, the surface mesh used for the determination of correspondences may be coarser that the surface mesh of the Glisson's capsule. A matching pair $\{p_t, p_s\}$ consisting of the target point and its closest projection is then defined. The outliers are pruned with a relative distance threshold and optionally, if the point cloud is smooth enough to accurately compute the normal at each point, a relative normal threshold. The relative distance threshold keeps the pairs of points for which:

$$|\mathbf{p}_{ts}| < d_t \max(\{|\mathbf{p}_{ts}|\}_{\text{all pairs}}), \text{ with } d_t \in [0;1]$$

where $\mathbf{p}_{ts}$ is the vector which goes from p_t to p_s and $|\cdot|$ is the Euclidean distance. The normal threshold prunes the pairs whose normal dot product is smaller than a threshold:

$$\mathbf{n}_{p_t} \cdot \mathbf{n}_{p_s} < n_t, \text{ with } n_t \in [0;1].$$

These thresholds must be set according to the deformation characteristics and they should be smaller for larger deformations. On average $d_t = 0.9$ and $n_t = 0.7$.

To speed up the registration process an heuristic can be introduced in the early phase of the registration: each point on the point cloud has a certain probability to be discarded. If a point p_t is associated with an uncertainty u_t on its position, this uncertainty is used to compute the probability of the point to be discarded:

$$P(p_t \text{ is discarded}) = \frac{u_t}{\sum_{t'} u_{t'}}.$$

In practice, a percentage α of points which have to be discarded is given and the process discards randomly αn points.

4.2.3 Constrains on the model

Prior knowledge on the transformations which are valid to register the data is introduced in the registration problem thought parametric or non parametric constraints. Parametric constraints explicitly restrain the set of allowed transformations to a subset of parametric transformations such as rigid (Lemieux *et al.* (1994)), projective (Feldmar *et al.*, 1995), or affine. In this case, the solution of the registration problem is the set of parameters which gives the best similarity measure. However, biologic tissues deformation can not be easily model by parametric transformations. Thus, non-parametric transformations with a high number of degrees of freedom have been introduced in medical data registration, but, to limit the dimensionality of the solution space, constraints must be imposed to these transformations.

One solution to reduce the degrees of freedom of the transformation is to define a set of control points and to use their displacement interpolate or approximate the deformation in the whole domain. Examples of these methods include the thin plate spline, introduced in medical imaging by Bookstein (Bookstein, 1991), or free-form deformations coupled with B-splines (Bardinet *et al.*, 1996; Rueckert *et al.*, 1999). Another solution is to embed the source data into a physical model — this is usually done for image registration — like elastic body models (Broit, 1981; Davis *et al.*, 1997) or viscous fluids models (Christensen *et al.*, 1996). These methods set the regularization term, $\mathcal{R}$, as the energy of the physical deformation. However, neither geometrical methods nor the previously cited physical methods take into account the real mechanical properties of the registered structures. Moreover, even if the choice of these deformation models already limit the degree of freedom of the transformations, the dimensionality of the registration problem remains very large. This results in an important computational cost and may lead to erroneous solutions due to the presence of local minima, especially when the amount of intra-operative information is limited.

Therefore, additional knowledge is required to decrease the dimensionality of the solution space. This can be done by adding constraints on the transformation, such as a volume preserving constraint (Dauguet *et al.*, 2009) or requiring the transformation to be a diffeomorphism (Vercauteren *et al.*, 2007), but another point of view may be adopted and instead of focusing on the regularization of the transformation, the prior knowledge may be directly associated with the registered data. In this case, tree approaches can be distinguished: organ motion modeling, statistical shape modeling and biomechanical modeling (Hawkes *et al.*, 2005). For cyclic motion, it is possible to use a four dimensional (4D) pre-operative image of the organs to construct a motion model and to reduce the search for the transformation to a one dimensional space as in Pratt *et al.* (2010). Statistical shape modeling can be used when the deformation are predictable and when a training data set is available. This method has been used for instance in Hu *et al.* for prostate deformation with a training data-set obtained by biomechanical simulation. However, the motion of the liver due to the pneumoperitoneum is not cyclic and neither intra-operative images of human patient under pneumoperitoneum nor simulations of the organ motion are accurate enough to be used as training sets (Oktay *et al.*, 2013). Biomechanical modeling methods, on the other hand, have proven to accurately extrapolate the intra-operative shape of organs, even when a very limited amount of intra-operative data is available (Wittek *et al.*, 2007).

Thus, in this work, we selected the biomechanical modeling approach

to restrict the degrees of freedom of the registration problem. The difference between biomechanical modeling and the physical registration methods presented above is that the first take into account the real mechanical properties of the registered object. The idea behind the use of a biomechanical model is that if the rest shape and the mechanical properties of an object are known, any registration problem would be easily solved if the boundary conditions of this specific problem are known. Two biomechanical models are used for the registration method described in this section, the first one being the complete heterogeneous liver model described in section 3.3 and the other one being an homogeneous model composed only of the liver parenchyma. The corotational formulation has been preferred over the hyperelastic one due to its lowest computational cost and its highest stability. In this work we impose the deformation of the biomechanical model through penalty forces. Theses penalty forces can be seen as a mean of imposing a displacement with a tolerance — which is important because the intra-operative data are subject to noise and outliers. Therefore, the result of the registration does not depend on the absolute values of the stress parameters but rather on their relative ratio, as already shown in Wittek *et al.* (2009), and on the relative intensity of external forces versus internal forces.

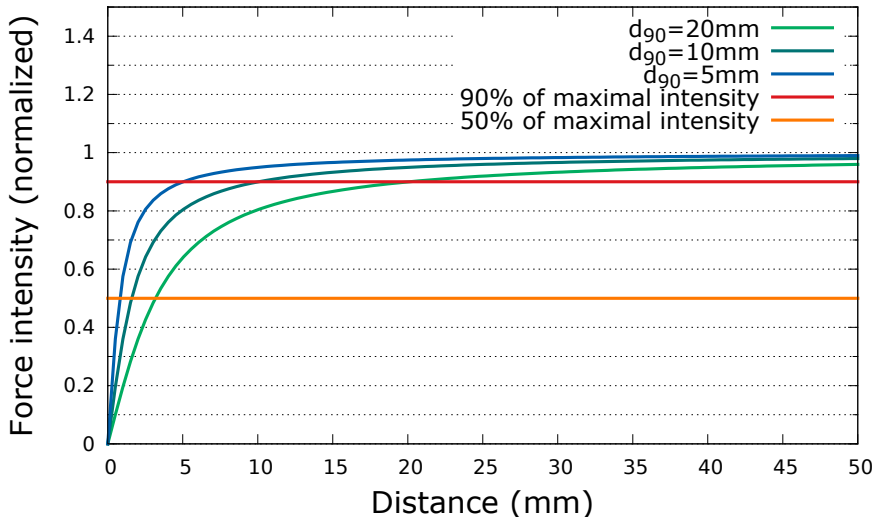

Figure 4.4: Force profile as a function of the distance $|\mathbf{p}_{st_i}|$ for different values of d_{90}.

For each pair $\{p_{t_i}, p_{s_i}\}$ we define an external force:

$$\mathbf{f}_{ext_i} = k(1 - \frac{2}{\pi}\arctan(\sigma|\mathbf{p}_{st_i}|))\frac{\mathbf{p}_{st_i}}{|\mathbf{p}_{st_i}|} \tag{4.1}$$

where k is a scalar **stiffness coefficient** (in [N/m]) and the term $(1 -$

$\frac{2}{\pi}\arctan(\sigma|\mathbf{p}_{st_i}|)$ is an asymptotic penalty function of the distance (in [m]) which includes also the scale factor σ. The distance $|.|$ is the Euclidean distance or the Mahalanobis distance when an uncertainty measure is associated to the position of each point of the point cloud. This scale factor is used to avoid over-fitting when the pre-operative model is registered to a noisy point cloud: a lower value of σ decrease the force intensity for small distances. In practice, we set:

$$\sigma = \tan\left(0.9\frac{\pi}{2}\right)\frac{1}{d_{90}}$$

where d_{90} is the distance for which the force intensity is equal to 90% of the maximal force intensity (see Fig. 4.4). The stiffness coefficient k is defined in three different ways depending on the type of the corresponding feature: thus, k is one of k_{UN}, k_{AM}, k_{hilum} and k_{surf} where the identifiers stand for the umbilical notch, the anterior margin, the hilum and the surface, respectively. When registering non-rigidly the complete surface model w.r.t. the reconstructed part, the process may suffer from inaccuracy due to the limited knowledge of correspondence between the two. Therefore, the labeled areas are penalized differently to use the anatomical landmarks as anchor points for the registration. At the beginning of the registration, the reliability of matching associated to each type of feature is reflected in the corresponding values of the stiffness coefficients: $k_{UN} \geq k_{hilum} \geq k_{AM} \geq k_{surf}$. Moreover, the registration evolves from a quasi-rigid (i.e. the applied forces are too small to produce a significant deformation) to a non-rigid state. k_{AM} and k_{surf} are equal to zero at the beginning of the registration, whereas both k_{UN} and k_{hilum} are not null. As the registration proceeds, all stiffness coefficient are increased. This makes the objective function more convex in the early stage of registration, which prevents the energy minimization process from falling into a local minimum, and the minimum become more precise over time.

To update the values of k_j for $j \in \{UN, hilum, AM, surf\}$, during the registration an algorithm is detected when the mechanical system has reached a plateau. At each registration step s the position of the degree of freedom of the biomechanical model are compared to their position at $s-1$ and an average displacement Δ is computed. If Δ remains below a certain threshold ϵ for more than l steps, then the algorithm consider that the registration process has reach is optimum for the actual k_j for $j \in \{UN, hilum, AM, surf\}$ and update the values of the stiffness coefficients:

$$k_{j_{\min}} + \frac{n^e}{r_j^e}(k_{j_{\max}} - k_{j_{\min}}) \text{ for } n < r_j \quad \text{and} \quad k_{j_{\max}} \text{ for } n \geq r_j \tag{4.2}$$

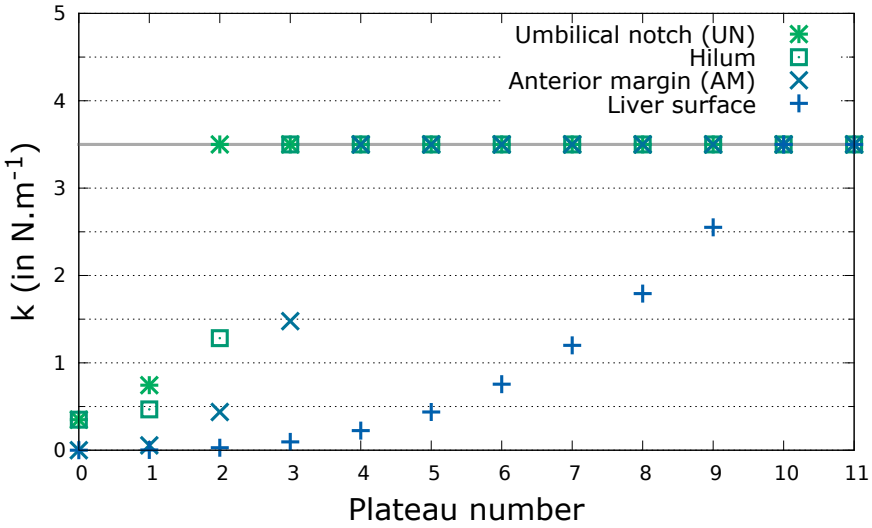

Figure 4.5: Example of the time evolution of the stiffness coefficient during the registration. Here $k_{\mathrm{UN}_{\min}} = k_{\mathrm{hilum}_{\min}} = 0.35\,\mathrm{N.m^{-1}}$, $k_{\mathrm{AM}_{\min}} = k_{\mathrm{surf}_{\min}} = 0\,\mathrm{N.m^{-1}}$, $k_{\mathrm{UN}_{\max}} = k_{\mathrm{hilum}_{\max}} = k_{\mathrm{AM}_{\max}} = k_{\mathrm{surf}_{\max}} = 3.50\,\mathrm{N.m^{-1}}$, $r_{\mathrm{UN}} = 2$, $r_{\mathrm{hilum}} = 3$, $r_{\mathrm{AM}} = 4$, $r_{\mathrm{surf}} = 10$.

where $n \geq 0$ is the plateau index (which is incremented each time a new plateau is detected) $r_j > 0$ an integer which controls the increase rate of k_j and e an exponent which control the shape of the force intensity evolution (see Fig. 4.5). Experimentally, we found that setting $e = 3$ leads to a better robustness of the algorithm. Moreover, we tested several values of l and found that $l = 20$ is sufficient for a reliable plateau detection. The convergence criterion of this registration process is not defined by a threshold on the residual error. Indeed, this error can only be computed on the visible surface and depends highly on the data noise. Thus, the registration is stopped when the maximal stiffness is reached for all features, that is as soon as $n = \max(r_j) + 1$.

4.2.4 Registration methods

As our registration problem has been recast into a biomechanical problem we solve it using the solvers developed for this type of system. Similarly as in Suwelack *et al.* (2014), we consider the registration as a dynamic process. This avoids having to set Dirichlet boundary conditions such that the stiffness matrix is invertible. Such boundary conditions would not make sense as the initial position of the biomechanical model may be far from the target point cloud at the beginning of the registration. The dynamic system of equations is given by:

$$\mathbf{M}\ddot{\mathbf{u}} = \mathbf{K}\mathbf{u} + \mathbf{D}\dot{\mathbf{u}} + \mathbf{f}_{ext} \tag{4.3}$$

where **M** is the mass matrix, **D** is the damping matrix, **K** is the stiffness matrix, and u is the vector of nodal displacements.

At each step of the registration process this dynamic system is integrated using implicit backward Euler scheme presented in Baraff and Witkin (1998). This requires to solve the linear system at each time step. Since the system matrix consists of the contributions from the vessels and capsule which introduce heterogeneity and anisotropy, the convergence of iterative solvers such as the conjugate gradient (CG) is jeopardized Shewchuk (1994). In our case, due to the heterogeneity and anisotropy introduced by the vessels, the CG requires an important number of iteration or might even not converge. Therefore, either direct solver or preconditioners must be used to solve the system in each step of the simulation. In order to reduce the computational time, we choose to use the LDL decomposition that factors the system matrix $\mathbf{A}$ — $\mathbf{A} = \mathbf{L}\mathbf{D}\mathbf{L}^T$ where **D** is a diagonal matrix and **L** a lower triangular matrix — instead of performing the classical Gauss elimination.

After each resolution of the system, the pairing is recomputed, generating a new force. Thus, the system do not reach its equilibrium position for a certain matching before it is updated. This helps the matching to converge toward its optimum in case of large initial misalignment. Finally, during the simulation the anatomical landmarks provide a coarse registration that improves the robustness of the matching algorithm, whereas the biomechanical model plays a role of regularization and allows for an accurate solution of local deformations.

4.3 Evaluation of the registration method

The aim of the method is to estimate the location of internal structures of the organ which undergoes important intra-operative deformations when compared to its initial pre-operative configuration. Validating the registration in this context is very challenging, since the optimal ground truth would be a 3D reconstruction of the organ at the intra-operative stage, which requires the intra-operative CT or MR scan of the patient, and a mean to track the position of the laparoscope relatively to the patient anatomy. To the best of our knowledge such data does not exist. Indeed, access to these techniques is very limited and almost impossible to use on human subjects. On the other hand, using swines to validate the registration method would be an issue since the geometry and the surrounding environment of a swine liver differ significantly from a human liver and thus the deformation induced by the pneumoperitoneum is very different in the two cases. We believe that results of a registration method on swines would not predict what this method can achieve in humans. Therefore, we used both phantom data

and synthetic data to validate quantitatively our registration method, the later offering the advantage to control all the parameters, thus allowing for a better characterization of the method.

4.3.1 Generation of synthetic data

In order to obtain the ground truth for the registration we have deformed the biomechanical models using a physical simulation of a pneumoperoitoneum. As we control the mechanical properties of the biomechanical model used for the simulation we can measure the influence of the biomechanical model used for the registration. Two sets of parameters were used; one representing a healthy liver (parameter values are set as reported in Umale *et al.* (2011)):

$$E_{parenchyma} = 3.5\,\text{kPa}, \qquad \nu_{parenchyma} = 0.45,$$
$$E_{vessels} = 620\,\text{kPa}, \qquad \nu_{vessels} = 0.4,$$
$$E_{capsule} = 8000\,\text{kPa}, \qquad \nu_{capsule} = 0.45,$$

and the other a cirrhotic liver with $E_{parenchyma}$=30 kPa, all the other parameters are identical to the one of the normal liver.

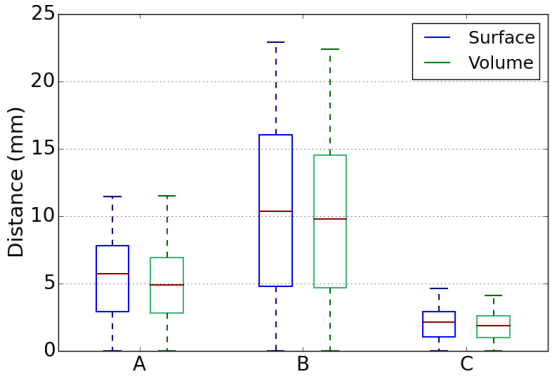

Figure 4.6: Distances in the surface and volume mesh nodes position between the different deformed configurations. A) heterogeneous liver model: cirrhotic (deformation #3) vs. healthy (deformation #4) , B) healthy liver: homogeneous vs. heterogeneous model, C) cirrhotic liver: homogeneous vs. heterogeneous model.

In total, we use six deformations generated using different liver models. Deformation #1 and #2 were obtained using an homogeneous liver model, while deformation #3, #4, #5, and #6 were generated using an heterogeneous model of the liver. For deformation #3 and #4, we evaluated the influence of the mechanical liver properties and of the use of an heterogeneous liver model on the deformation. Results, presented in Fig. 4.6, show that the

vessels and the capsule influence the deformation, particularly in the case of the healthy liver where the distances between the degrees of freedom of the final configuration of the heterogeneous and homogeneous model is 10.1 mm. This error represents 43% of the homogeneous healthy liver deformation. The same analysis performed for the cirrhotic liver quantifies the influence of the vessels being 18% w. r. t. the entire deformation.

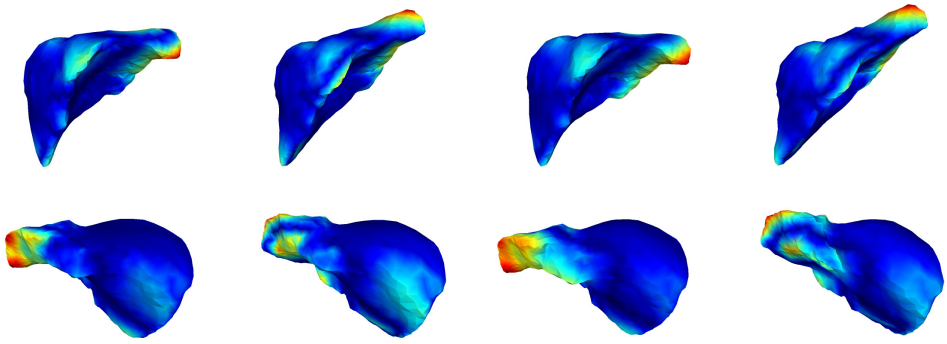

Figure 4.7: Non deformed and deformed configurations of deformation #5 and #6. The first and third columns show the non-deformed configuration, the second column the deformed configuration obtained using the cirrhotic mechanical parameters and the fourth column the deformed configuration obtained using the healthy mechanical parameters. The colors correspond to a relative Hausdorff distance between the deformed and the non-deformed configurations for the cirrhotic and healthy liver.

In real situations only partial surface information is acquired by the laparoscopic camera. Thus, to evaluate the amount of information needed to achieve an accurate registration faces of the deformed model are deleted to keep only a portion of its surface from 50% to 10%. In order to mimic the real intra-operative conditions, we added a zero-mean Gaussian noise; the standard deviation of the noise were 2.5 mm and 5 mm in the direction of the virtual camera view and 0.5 mm in the orthogonal directions. We performed experiments on all data with and without added noise.

4.3.2 Error measure

To measure the accuracy of the registration, several error measures are used. For synthetic data three quantitative error measures are employed: the Hausdorff distance, the target registration error (TRE), and the feature registration error (FRE). Mathematically, the Hausdorff distance H_D is a measure which quantifies the distance between two surfaces S_1 and S_2, and is defined as follows:

$$H_D = \max(\max(\min_{s_1 \in S_1} d(s_1, S_2)), \max(\min_{s_2 \in S_2} d(s_2, S_1)))$$

Figure 4.8: Partial surface generated from deformation #5. The first column correspond to 50% of the entire surface, the second to 40%, the third to 30%, the fourth to 20% and the fifth to 10%. The data are represented as surfaces but the algorithm ignore the topology and the normals of these surfaces.

where $d(s_i, S_j)$ is the Euclidean distance between the point s_i and the surface S_j. However, in practice, the algorithm which calculates the Hausdorff distance samples a certain number of points on one surface, computes their distances to the other surface and gives statistics on the measured distances. Thus, in the following we use the mean and the maximum Hausdorff distances, which are respectively the mean and the maximum of the sampled distances. The TRE is the distance between two points which correspond to the same position on the source and on the target and that have not been used in the registration algorithm. The FRE is similar to the TRE, but for points which have been used for the registration.

Additionally a global estimation of the distance between the target and registered data may be used: the dice measure. This measure compute the degree of overlapping between the rasterized images of the source and the target. We only use this measure with real data, that is when no ground truth is available.

4.3.3 Results

To evaluate the registration method, the undeformed healthy and cirrhotic biomechanical models were registered onto the partial surfaces generated in Section 4.3.1. Then, the shapes of the models after registration were compared with the deformed configurations of the whole meshes used for the generation of partial surfaces. For all registrations we adjusted the stiffness parameters k_j for $j \in \{UN, hilum, AM, surf\}$ according to the Young's modulus value. In this manner, we ensured that the ratio between the external and the internal forces remains the same independently of the actual value of the Young's modulus. Unless stated differently, we always use a conversion factor 10^{-3} m for $k_{UN_{\max}}$, $k_{AM_{\max}}$, and $k_{surf_{\max}}$, a factor 10^{-4} m

Deformation / DoF distance in mm	#3	#4	#5	#6
minimum	0.2	0.5	0.3	1.4
Q1	1.2	2.3	5.7	9.2
mean	1.7	3.0	8.3	13.4
Q3	2.5	4.6	11.5	19.3
maximum	6.2	10.3	25.5	40.6
average	1.9	3.6	9.2	15.2

Table 4.2: Statistics on the deformations obtain with heterogeneous models. Deformation #3 and #4 are small compared to deformations #5 and #6.

for $k_{UN_{\min}}$ and we set $k_{surf_{\min}} = 0\,\mathrm{N.m^{-1}}$, $r_{UN} = 2$, $r_{AM} = 4$, and $r_{surf} = 10$. For the implicit Euler integration scheme the Rayleigh mass and the Rayleigh damping coefficients were set to 0.1. In order to insure the success of the method, the anatomical features must be at least partially visible.

Influence of the amount of visible surface

As a first step, the impact of the amount of visible surface on the registration results. The different synthetic intra-operative data representing 50% to 10% of the liver surface were used as target for the registration method.

In a first version of the method, an homogeneous liver model of the parenchyma was used as the source biomechanical model for the registration. This biomechanical model was composed of 1278 nodes and 5466 tetrahedra. Two deformations — deformation #1 and #2 — mimicking the pneumoperitoneum were tested for this model. The evaluation of the registration method was performed using the Hausdorff distance because the mesh used to generate the surface patches was not the same as the one used for the registration. The Young's modulus used for the deformed data generation and the registration task was the same. The results, presented in Fig. 4.9, show that even with only 10% of visible surface our method is able to perform the registration with a mean Hausdorff distance lower than 4 mm. Compared to deformation 2, the deformation #1 was more important on the liver face opposed to the camera view. This fact could explain the lower quality of the results obtained for this deformation. We also note that the registration result obtained for deformation #2 with 10% of surface is better that the one obtained for 20% of visible surface. This can be explained as the surface representing only 10% of the liver surface was not included in the one representing 20% of the surface (see Fig. 4.18). More interestingly,

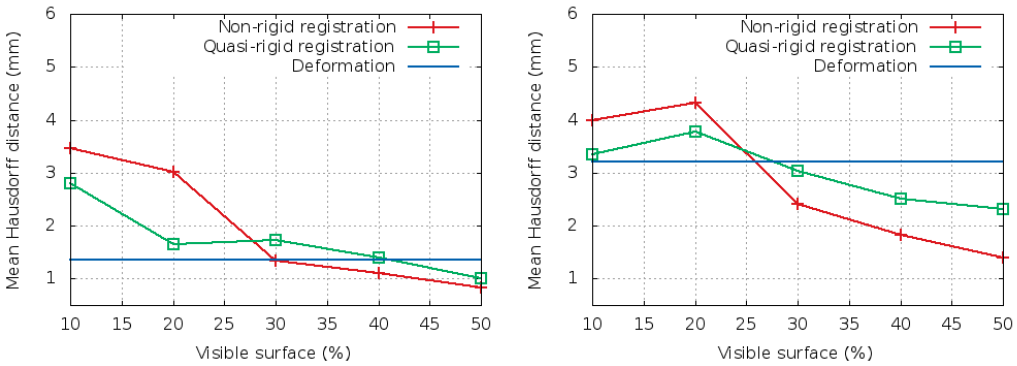

(a) Deformation 1 (b) Deformation 2

Figure 4.9: Registration results on synthetic data showing the error w.r.t. the variation in visible surface area for deformation 1 and 2. Liver Young modulus: $E = 50kPa$. The conversion factors for the stiffness coefficient were 10^{-4} m for $k_{un_{min}}$ and $k_{un_{max}}$, 3.10^{-4} m for $k_{am_{max}}$, 2.10^{-3} m for $k_{surf_{max}}$, $r_{am} = 5$, $r_{surf} = 25$ and $d_{90} = 10$mm. The blue line is the mean Hausdorff distance between the non-deformed and the deformed configuration after a rigid registration using **100% of the deformed surface**.

the plots suggests that the non-rigid part of the method does not introduce any improvement when compared to the quasi-rigid part as soon as 20% or less of the surface is visible. In this case the information on the deformation is too small to improve the registration result with the non-rigid part of the algorithm. These results are interesting but needed to be confirmed on more data sets and with a more precise evaluation of the registration accuracy.

Therefore, in a second version of the method, two complete biomechanical liver models were used to generate four deformed configurations, two with the parameters of an healthy liver, and two with the parameters of a cirrhotic liver. The statistics on the deformations are given in Table 4.2 and in Fig. 4.18. The first finite element model, used to generate the deformation #3 with cirrhotic mechanical parameters and the deformation #4 with healthy mechanical parameters, was composed of 547 nodes and 2193 tetrahedra and the second, employed to generate the deformation #5 with cirrhotic mechanical parameters and the deformation #6 with healthy mechanical parameters, of 1292 nodes and 3846 tetrahedra (see Table 4.2 and Fig. 4.7). Moreover, the meshes used to generate the deformed surface patches were the same as the meshes used for the registration, allowing the use of TRE on the degrees of freedom as error measure. The mechanical parameters, Young's modulus an Poisson's ratio, of the liver biomechanical model used for the registration were the same as those used to generate the deformations. However, we evaluated the impact of the choice of these

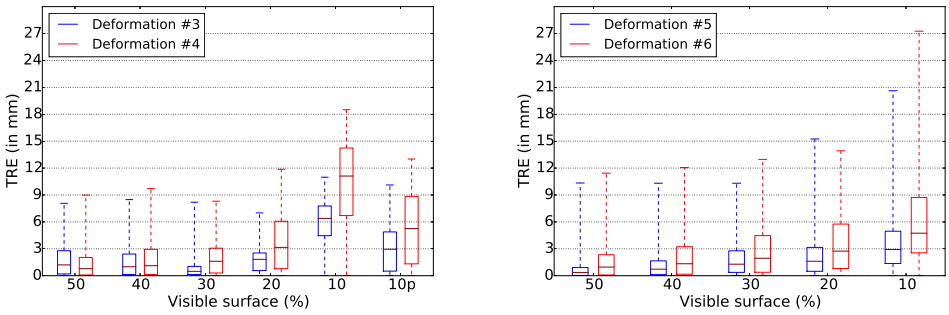

(a) Cirrhotic liver (deformation #3) and healthy liver (deformation #4)

(b) Cirrhotic liver (deformation #5) and healthy liver (deformation #6)

Figure 4.10: TRE of the volume degrees of freedom after registration (the bar-and-whisker graph shows the mean, upper and lower quartiles, and the maximal and minimal error). For the deformation #3 and #4 we also measured the errors on a sub-part corresponding only to the volume under the visible surface from the camera viewpoint for the partial surface representing 10% of the liver surface (10p).

parameters in the next paragraph (4.3.3). The results obtained for these new deformations are presented in Fig. 4.10.

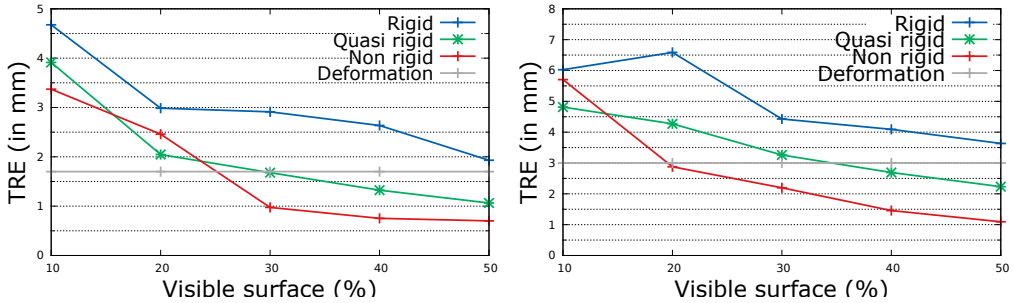

(a) Cirrhotic liver. Deformation #3

(b) Healthy Liver. Deformation #4

Figure 4.11: Comparison of the mean TRE obtained for a rigid registration, a quasi-rigid registration — the result of the proposed algorithm after the second plateau detection — and the proposed non rigid registration using deformation #3 and #4.

For the first model and deformations #3 and #4, we obtained a mean error below 3 mm in all cases except when the visible surface represented less than 20% of the liver surface for deformation #4 and less that 10% for deformation #3, which would correspond to a very limited surface reconstruction. However, as the deformation of the model was small, these results do not guaranty that the method would perform well for important deformation. Thus, we repeated the experiments with a more significant deformation. The results obtained were similar to the ones obtained for

the smaller deformation, with a mean error below 3 mm when the visible surface represent more than 10% of the entire surface for the deformation #5 and #6 (see Fig. 4.10).

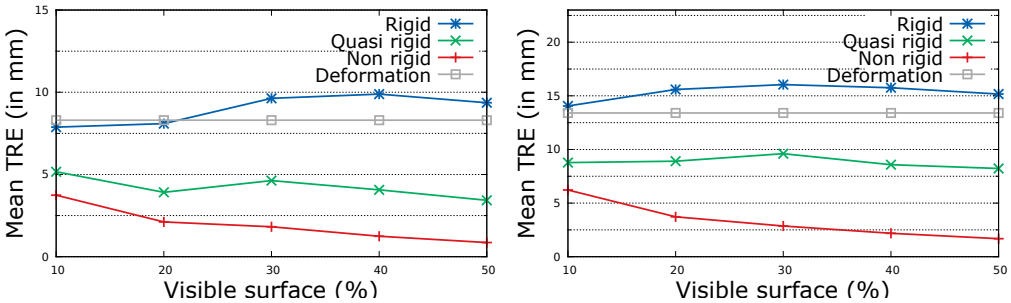

(a) Cirrhotic liver. Deformation #5 (b) Healthy liver. Deformation #6

Figure 4.12: Comparison of the mean TRE obtained for a rigid registration, a quasi-rigid registration — the result of the proposed algorithm after the second plateau detection — and the proposed non rigid registration using deformation #5 and #6.

Nonetheless, the result obtained for the homogeneous biomechanical liver model were not confirmed even if the same tendency is obtained for the cirrhotic deformation of the first heterogeneous model (see Fig. 4.11 and 4.12). If the visible surface represents less than 20% of the entire surface the quasi-rigid part of the registration method improves the registration accuracy for the three of the four additionally tested scenario. This result is not related to the use of an heterogeneous model. A registration of an homogeneous model on the deformed point clouds led to similar results. It is rather the nature of the deformation which plays an important role. Indeed, the first deformations obtained with the homogeneous liver model were localized on the right lobe of the liver, while we imposed a more global deformation on the two heterogeneous liver models. However, as the cirrhotic liver deforms less, the deformation of the cirrhotic model of the first heterogeneous liver (deformation 3) was also relatively localized.

Influence of the mechanical properties

Additionally, we studied the impact of the mechanical properties on the registration results. We compared the registration accuracy obtained for the complete heterogeneous liver model composed of the Glisson's capsule, the vascular three and the parenchyma with the results obtained using a simplified model composed only of the liver parenchyma. The results are presented in Fig. 4.13.

The results show that using a complete liver model does not significantly improve the registration accuracy. Indeed, the registration accuracy

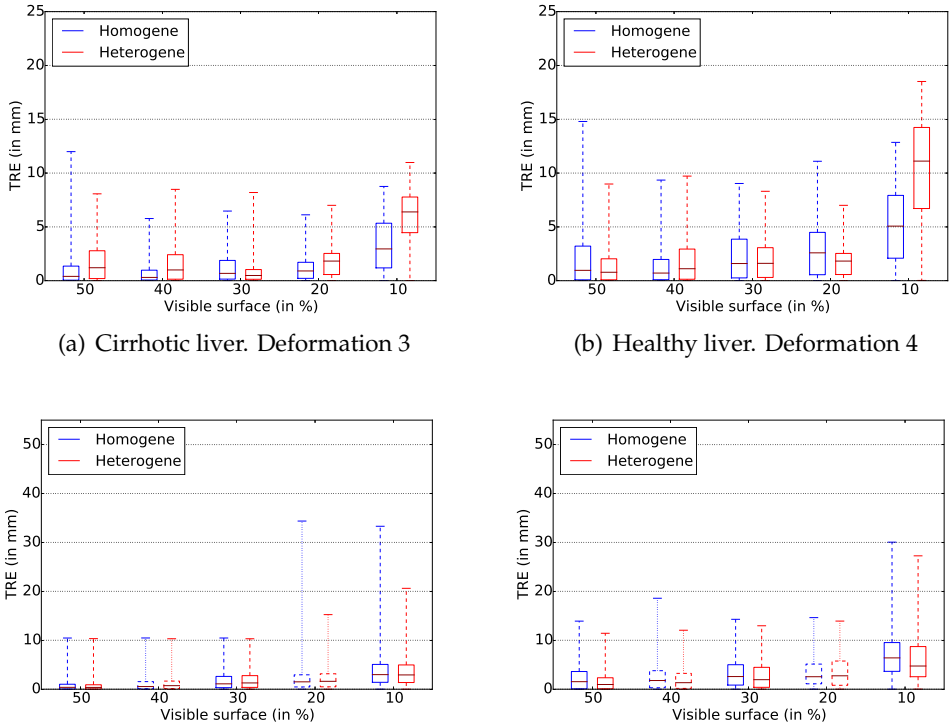

(a) Cirrhotic liver. Deformation 3

(b) Healthy liver. Deformation 4

(c) Cirrhotic liver. Deformation 5

(d) Healthy liver. Deformation 6

Figure 4.13: Comparison of the TRE obtained after registration with the homogeneous and heterogeneous liver model using deformation 3, 4, 5 and 6.

is sometimes better with the homogeneous model and sometimes with the heterogeneous model. It indicates that the exact modeling of the liver might not be necessary for this specific application. This can be due to the particularities of the deformations applied to the liver ("pneumoperitoneum mimiking" deformations). Moreover, as the use of an heterogeneous model increases the computation time (by a factor 2), the homogeneous liver model should be preferred.

We also varied the Young's moduli of the different models for the same registration task and measured its influence on the results. The Young's moduli of all the component of the heterogeneous model were multiplied by the same factor ranging from 10^{-1} to 10^{2} (see Fig. 4.14).

The registration accuracies are similar for all tested scenario, indicating that the absolute value of the Young's moduli of the liver parenchyma, vessels and capsule does not influence the registration results. We also tested whether or not the relative stiffness of these three components of the liver have an impact on the registration accuracy. The results are presented in Fig. 4.15. The maximum TRE obtained by the registration of the healthy liver

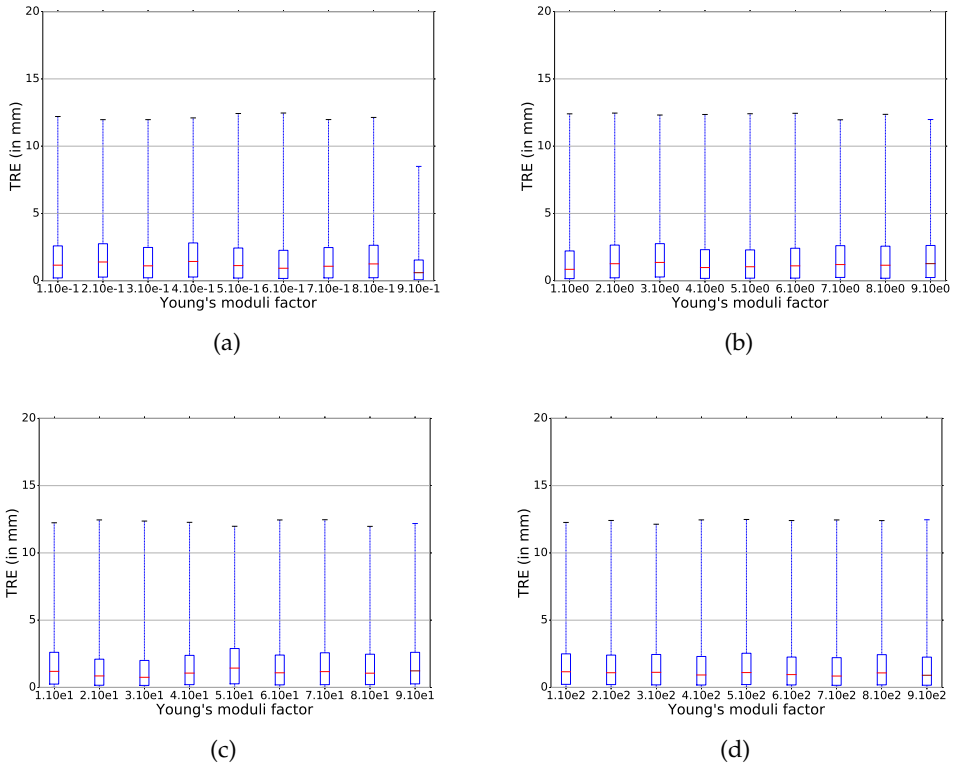

Figure 4.14: Comparison of the TRE obtained for different values of the multiplicative factor used to modified the Young's moduli of all the component of the heterogeneous model. The simulation were performed using deformation 3.

on the cirrhotic deformation (deformation #6) are slightly better than the maximum TRE obtained by the cirrhotic liver. Nonetheless, if we compare the mean TRE and the values of the first and third quartile, the results do not show a statistically significant difference between the use of an healthy or a cirrhotic liver to perform the registration, indicating that the exact value of the parenchyma Young's modulus is not necessary to obtain accurate results.

Robustness to noise

Point clouds reconstructed from real stereoscopic images are subject to noise. Thus, we tested the impact of noisy point cloud on the registration algorithm. We compared the registration accuracy of the method on point cloud without added noise, and with Gaussian Noise of standard deviation of $\sigma = 2.5\,\text{mm}$ and $\sigma = 5.0\,\text{mm}$ in the direction of the camera of $0.5\,\text{mm}$ in the orthogonal plane. Usually, the noise present in the reconstructed point cloud correspond to a Gaussian Noise of standard deviation of $\sigma = 2.5\,\text{mm}$.

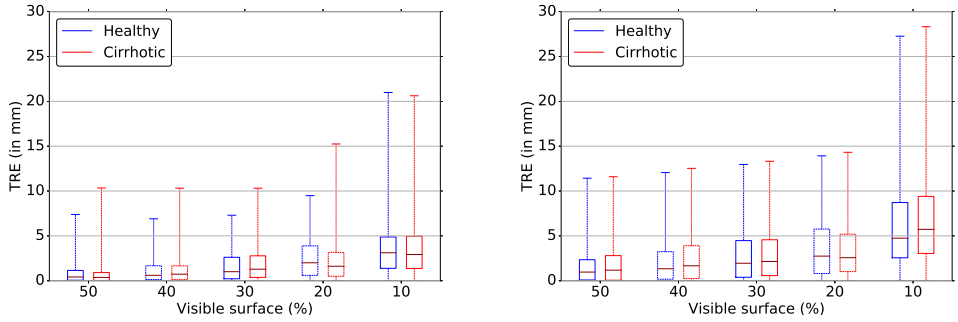

(a) (b)

Figure 4.15: Comparison of the TRE obtained using the cirrhotic or healthy liver for the registration task on deformation #5 (a) and using the cirrhotic or healthy liver for the registration task on deformation #6 (b).

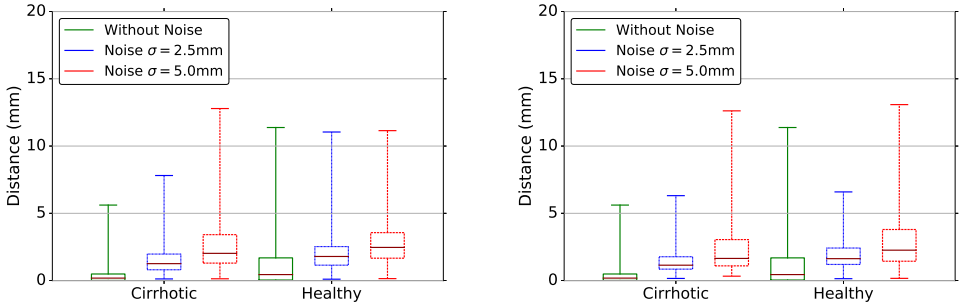

(a) d_{90} identical for all samples (b) d_{90} depends on the noise level

Figure 4.16: Comparison of the TRE obtained after registration with non-noisy and noisy data of standard deviation $\sigma = 2.5\,\text{mm}$ and $\sigma = 5.0\,\text{mm}$ for the deformation 5 and 6. For (a) $d_{90} = 10\,\text{mm}$, for (b) $d_{90} = 10\,\text{mm}$, $d_{90} = 25\,\text{mm}$ and $d_{90} = 50\,\text{mm}$ for non noisy data, noisy data with $\sigma = 2.5\,\text{mm}$ and $\sigma = 5.0\,\text{mm}$ respectively.

The results are presented in Fig. 4.16.

Unsurprisingly, the graphs show that the presence of noise reduces the quality of the registration. Indeed the minimal, first quartile, mean, and third quartile of the TRE increase with the noise level in all cases. However, form the graph plots, increasing d_{90} does not seems to improve the registration result except for maximum TRE of deformation 6 (healthy liver) with a noise of standard deviation $\sigma = 2.5\,\text{mm}$, indicating that the noise has perturbed the global position of the mesh which thus better align it with the deformed reference mesh.

Nonetheless, visually the improvement obtained by using higher values for d_{90} in the presence of noise is obvious (see Fig. 4.17). Indeed, the

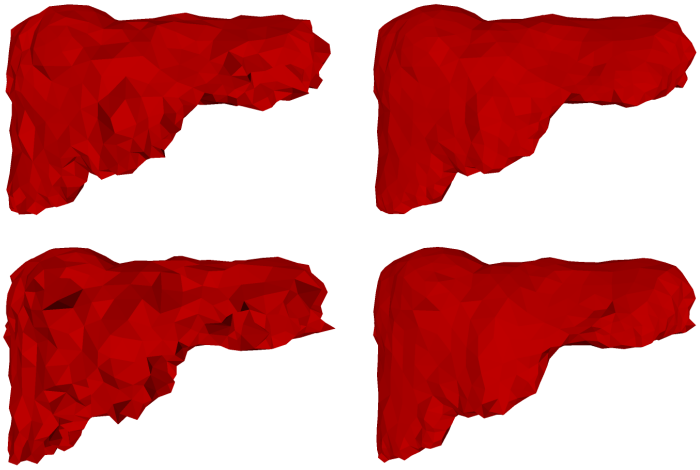

Figure 4.17: Comparison of the registered surfaces in the presence of noise. The top row shows results for $\sigma = 2.5$ and the bottom row for $\sigma = 5.0$. The first column shows results for $d_{90} = 10\,\text{mm}$, and the second for $d_{90} = 10\sigma\,\text{mm}$.

registered meshes are more smooth when d_{90} is increased.

Robustness to poor initial alignment

We also tested the robustness of the method to poor initial alignment by applying different rigid transformations to the source model before the registration. Fig. 4.18 shows the result for a 90 degree rotation around the y axis.

These results were obtained using only two anatomical landmarks, the umbilical notch and the anterior margin. The registration accuracy, measured using the mean Hausdorff distance, of the experiments presented in Fig. 4.18 are reported in Fig. 4.9 and show that the registration method is robust to rotation around an axis which is almost perpendicular to the liver surface. However, if the initial pose of the source mesh is above the surface, the posterior face of the source mesh may be matched with the point cloud — which represent anterior face of the liver — and the registration could fail. To alleviate this issues an additional landmark, the hilum, may be used (see paragraph 4.3.3)

When a good initial alignment is available, the parameter set described at the beginning of the section perform well. However, if the initial position of the source mesh is misaligned with the target point cloud is important the stability of the system may be compromised. In this case the initial forces imposed on the biomechanical model of the liver should be reduced. Thus the multiplicative factor of the ligament stiffness should be reduced.

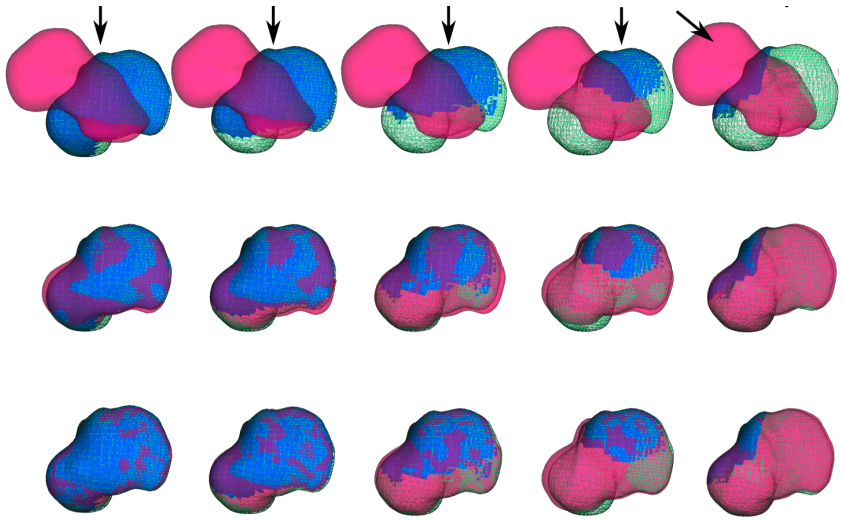

Figure 4.18: Registration results on synthetic data. The source model is in transparent red, the target surface used for the registration is in blue and the whole target surface in green wireframe. The first row shows the initial pose, the second row the result after the quasi-rigid registration and the last row the final result. Each column shows the results for different target surface areas. The target surface of the columns from left to right correspond to 50%, 40%, 30%, 20% and 10% of the whole surface. The black arrows indicate the virtual camera angle.

Fig. 4.19 show the comparison of the final registration result using the parameter set previously described or another parameter set: a factor of 2.10^{-5} for $k_{UN_{\min}}$, a factor of 2.10^{-4} for $k_{AM_{\max}}$ and we kept all the other parameters unchanged.

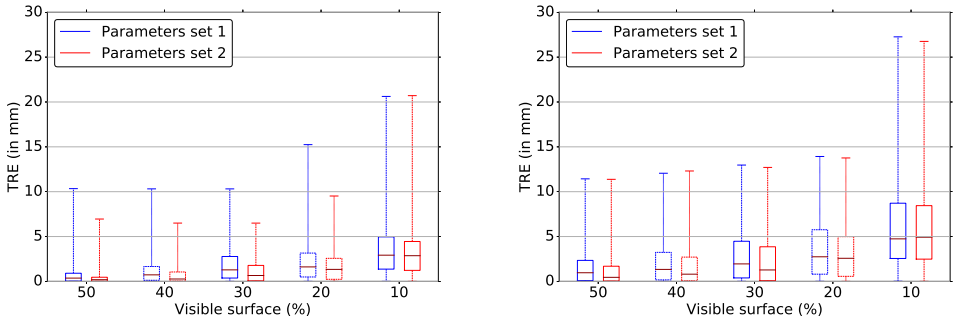

(a) Deformation #5 (b) Deformation #6

Figure 4.19: Comparison of the result obtained for two different parameter sets for a non ideal initial alignment.

The results show a significant improvement of the value of the third quartile and the mean of the TRE for the deformation #5 and #6, ranging from

49% to 10% for the deformation #5 and from 27% to 13% for deformation #6 except for 10% of visible surface. This reveals that lower forces allows the matching to change more during the firsts plateau of the registration process and thus to reach a better initial alignment.

Impact of the point cloud density

In addition, we studied the influence of the point cloud density on the registration results. We decimated the point cloud used to register the three dimensional model and kept from 100% to 10% of the points, which correspond to 1.6 points per square centimeters to 0.16 points per square centimeters respectively. Provided that the density of points remains above 0.5 points per square centimeter (30% of the maximal density), the difference in the mean TRE between the registration result using the complete point cloud and the down sampled ones does not exceed 1 mm. Fig. 4.20 show the evolution of the mean and maximal TRE with respect to the point cloud density.

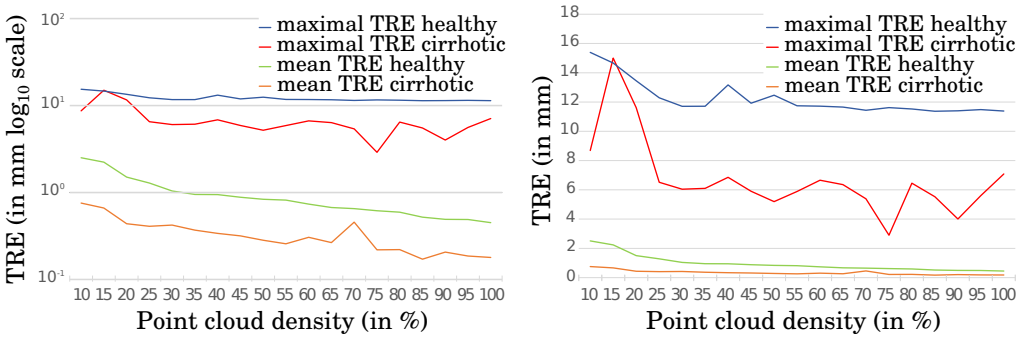

Figure 4.20: Impact of the point cloud density on the registration accuracy using deformation 5 (cirrhotic) and 6 (healthy) presented in Log_{10} scale (a) and in standard scale(b).

The density of a point cloud reconstructed from laparoscopic data is very dependent of the texture of the patient liver. For cirrhotic patient the liver texture is usually better for the point cloud reconstruction than the one of non-cirrhotic liver, but exceptions exist. Therefore, it is difficult to estimate the mean density of an intra-operative point cloud, and to predict the density that will be obtained for a particular patient.

However, the reconstructed point cloud density is known at the beginning of the registration method. Thus, an indication of the final accuracy of the registration can be given to the medical team before the registration process.

Influence of the Hilum

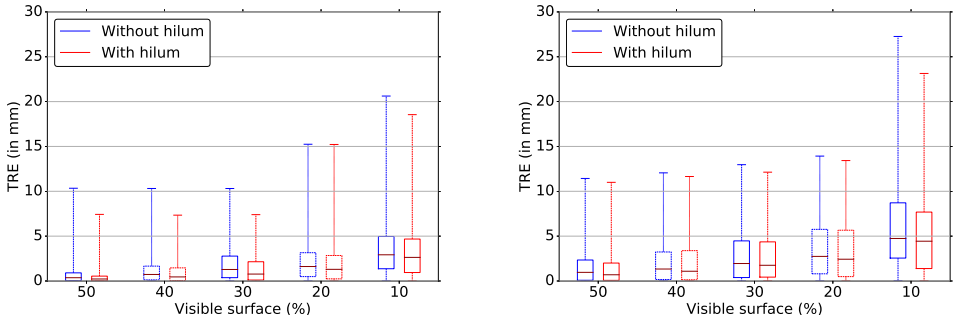

(a) Cirrhotic liver. Deformation #5 (b) Healthy liver. Deformation #6

Figure 4.21: Influence of the hilum on the registration accuracy for deformation #5 and #6.

All the preceding results were performed using only two anatomical features: the umbilical notch and the anterior margin. This is due to the fact that the method first used only these two anatomical landmarks, the hilum was included after the feasibility to obtain a point cloud of this landmark was ensured. We set a conversion factor of 10^{-4} m for $k_{hilum_{min}}$ and of 10^{-3} m for $k_{hilum_{max}}$ and we set $r_{hilum} = 3$.

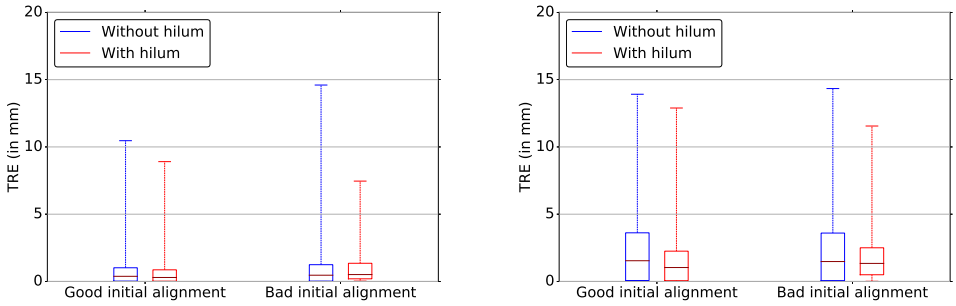

(a) Cirrhotic liver. Deformation #5 (b) Healthy liver. Deformation #6

Figure 4.22: Influence of the hilum on the registration accuracy for deformation #5 and #6 using 50% of the liver surface and poor initial alignment. We used a multiplicative factor of $10^{-}6$ m for k_{hilum} and $10^{-}5$ m for k_{UN} for the simulation performed with poor initial alignment in order to have low registration forces at the beginning of the registration.

The results, obtained with a dense and non noisy point cloud and under good initial alignment, show that the hilum improves the registration accuracy only slightly, especially for the deformation #6 (see Fig. 4.21). For the cirrhotic liver, the presence of the additional landmark improve surprisingly much the registration accuracy when a large amount of surface is

visible. This indicates that for the deformation #5 the additional registration forces applied in this region help to deform the model toward its accurate configuration. Thus, the presence of this additional landmark, even if it improves the registration results, is not crucial for the studied deformations when the input point cloud is optimal. However, in real situations, with very sparse intra-operative data, the presence of an additional landmark may be useful.

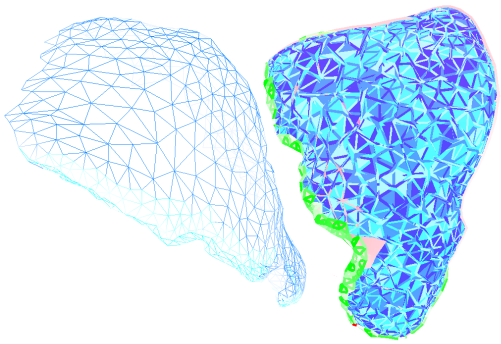

Figure 4.23: Poor initial alignment used for the results of Fig. 4.22.

In particular, if a good initial alignment cannot be obtained, the presence of this additional landmark improves the robustness of the registration and decrease the computation time (for poor initial alignment the first plateau is reached twice faster in when for deformation #6), but does not necessarily improve the registration accuracy. Indeed the maximum TRE is reduced, but the other statistical values of the TRE are comparable for the cirrhotic case (see Fig. 4.22).

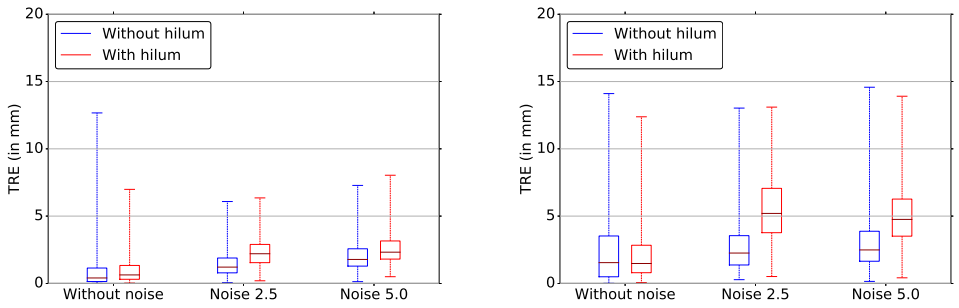

(a) Cirrhotic liver. Deformation #5

(b) Healthy liver. Deformation #6

Figure 4.24: Influence of the hilum on the registration accuracy for noisy data using deformation #5 and #6.

In the presence of noise, result obtained using this additional landmark

are usually worse (see Fig. 4.24). The noise present on the hilum surface, instead of compensating for the noise present on the surface, perturb the global position of the mesh. This could be explained by the fact that the principal direction of the noise is almost parallel to the hilum surface, while it is mainly perpendicular to the visible surface, the anterior margin and the umbilical notch. Thus, the global position of the hilum may be displaced relatively to the mesh surface which is not the case for the other features. This situation is not a side effect of the synthetic data generation but reflects a real problem that may happen on real data. Therefore, if the previous hypothesis is confirmed by further investigations, the best strategy would be to use the hilum at the beginning of the registration process and to progressively decrease its influence to zero.

Computation time

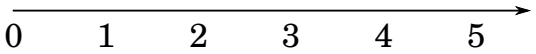

Figure 4.25: Total time of the registration pipeline (in minutes). In green: the time required for the surgeon to position the camera (maximum 30 seconds). In blue: time required for the point cloud generation and the landmarks labeling. In grey: the registration process itself.

All experiment were conducted on a CPU Intel Core i7 975 and it takes between two and three minutes to the algorithm to reach the convergence criterion for input point clouds similar to real laparoscopic data. However, the code is not completely optimized, thus, the performances of the registration algorithm can be greatly improved. The computational time required for the complete pipeline is depicted in Fig. 4.25. This time is the time required for the initialization of the registration. Subsequent registration are much faster (Haouchine *et al.*, 2013).

Experiments with *in vivo* data

To assess our approach in a real surgical environment (specular lights, instrument occlusions, etc.) and to evaluate the ability of our non-rigid registration to estimate the initial pose, we tested our method on *in vivo* laparoscopic images of a human liver. Results illustrated in Fig. 6.12 report a visually correct initial non-rigid registration of the liver model on the laparoscopic image with only a partial and noisy three-dimensional surface

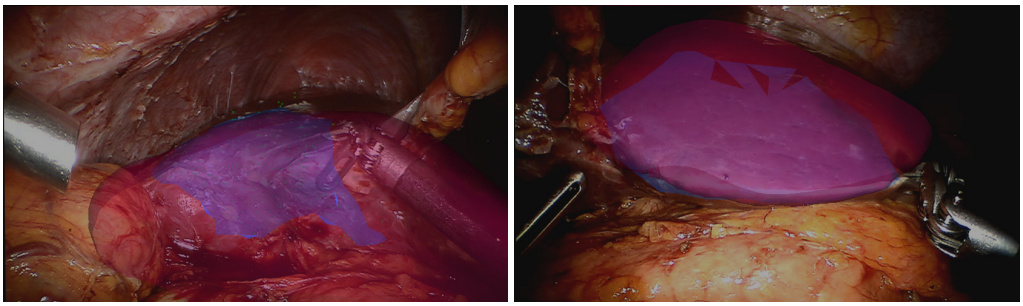

(a) (b)

Figure 4.26: Registration results on *in vivo* data on two different views of a human liver. The registered mesh is shown in red while the partial reconstructed patch is depicted in blue.

reconstruction. For this simulation we used the same parameter values as for the *in silico* data (see the caption of Fig. 4.9) except for $d_{90} = 20\,\text{mm}$ (90% of the force intensity at $10^{-1}\,\text{mm}$). The mean Hausdorff distance between the point clouds and the three-dimensional model is 0.5 mm and 0.6 mm for the cases (a) and (b) of Fig. 6.12 respectively.

4.4 Discussion

Throughout the various stages of the pipeline, different sources of errors may degrade the quality of the final result, and the value and impact of these errors are difficult to evaluate. First, the segmentation of the liver and its vascular network is operator-dependent and sensitive to the quality of the medical images. The error arising from the segmentation is not easy to evaluate but a lower bound is given by the voxel size which in our case is 0.7 mm x 0.7 mm x 0.7 mm (see Section 1.1.2). Second, the quality of the three-dimensional mesh generated from the segmented maps depends notably on the number of its vertices. We generated a high-quality mesh and computed the Hausdorff distance between this mesh and the mesh that we use for computation. We found a mean Hausdorff distance of 0.3 mm and a maximal error of 4.7 mm (see Fig. 1.9). Third, the point cloud quality is subject to errors arising from the calibration of the camera, the image quality (sharpness, texture, etc.) and from the triangulation method (features detection, matching, etc.). As we do not have any ground truth for the laparoscopic data, it is difficult to estimate the error in millimeters between the point cloud and the actual position of the organ.

The result section has shown that the proposed method is able to perform well even with noisy and partial surface information, and that it is robust to

poor initial alignment and sparse point cloud. Additionally, with only two of the three anatomical landmarks defined in the Chapter 2, the registration accuracy of the method is already very good. Moreover, the computational time of the method is under 2 minutes for all tested scenario, which is acceptable for an application in the OR. Besides, the code works on CPU only and a GPU optimization would certainly reduces the computational time. Thus, this method is well suited for the alignment of pre- and intra-operative data for laparoscopic liver surgery.

The results also suggest that the heterogeneous liver model does not improve significantly the registration result. Indeed, excluding the results obtained for 10% of visible surface, the difference in accuracy for the two models for is on average of 0.29 mm, which represent a relative error of 2.5% with respect to the deformations, and the homogeneous model performs sometimes better. Moreover, the results shows that the knowledge of the patient's liver actual Young's modulus is not necessary for the initial registration. However, this result does not mean that this information is not important for the next step of the IGS registration. Indeed, the temporal registration employ an optical tracking method which limits the number of point that can be reconstructed and thus the amount of intra-operative data. In this context, an accurate value of the liver Young's modulus may lead to better results.

The non-rigid part of the registration method has demonstrated an improvement in the registration result only when the area of the intra-operative reconstructed surface correspond to at least 30% of the entire liver surface. Moreover, the amount of visible surface significantly influence the registration quality. Thus, methods which increase the amount of intra-operative surface that can be reconstructed should be explored. Some researches on this subject have already been conducted and different methods have been proposed. For instance, the SLAM algorithm (Mountney and Yang, 2010), by which the camera motion is estimated from optical tracking information combined with a Kalman filter, or the approach presented in Reichard *et al.* (2015), which relies on the stitching of several three dimensional surface reconstructions obtained from different viewpoint, have been proposed and should be used in combination with the proposed registration algorithm.

Another improvement to this registration method would be the use of laparoscopic ultrasound data to increase the amount of intra-operative information (Langø *et al.*, 2012). Ultrasound imaging is an inexpensive intra-operative modality which provides in-depth information on the organ structures. With this kind of data, information concerning the position of the vessels could be used to better register the volume of the liver. Currently, the use of laparoscopic ultrasound probes is not widespread. Indeed, as they

have a very limited field of view, it takes time to image a sufficiently large area around the structures of interest and it may be difficult for surgeons to have an accurate mental image of the structure positions. Moreover, laparoscopic ultrasound is not easy to manipulate because of the limited motion of the laparoscopic tools. However, if a quick sweeping of a small part of the liver improves the positioning of the pre-operative liver model, this technique could be widely adopted by surgeons. Thus, even if some challenges remain (see section 4.1.5), the combination of ultrasound and laparoscopic images to register a pre-operative model of the liver would be an interesting improvement.

Additionally, an improvement that should be explored in the future is the reduction of the number of parameters used in this algorithm. Indeed, even if the method is not too sensitive to the different parameters, deeper investigations should be conducted to better characterize their impact on the registration results in relation with the input data characteristics. More specifically, a quantitative link should be sought between the input data characteristics and the parameters of the registration method. This would allow to automatically set the parameter values from an analysis of the input data.

One of the main difficulties encountered when developing a registration method for laparoscopic IGS is the validation of the algorithm on real patient data. Indeed, obtaining a gold standard for the registration would require having the intra-operative shape of the patient organs and the position of the laparoscopic camera relative to the patient reference frame. This could be obtained by intra-operative volume imaging techniques, but it would require a specially equipped operating room as well as the consents of the patient and that the medical team agrees to change its workflow. The data set which is closer to the requirements is the one obtained by Tsutsumi *et al.* in an open MRI theater (Tsutsumi *et al.*, 2013). However, as no MRI compatible endoscope exists, the endoscope has to be removed before imaging the abdominal cavity and changes in the pneumoperitoneum pressure may change the shape of the organs shape between the image acquisition and the capture of the laparoscopic images. The use of pigs to validate registration method for IGS is widespread but, as already stated in this chapter, even if the properties of a pig liver are close to the properties of a human liver, the organ geometry and environment differ significantly from those of a human. This could lead to the development of methods which are "pig specific". Therefore, the results obtained on pigs cannot ensure that the method will shows similar results in humans and efforts should be made to obtain gold standard data in humans.

CHAPTER 5

TAKING INTO ACCOUNT THE ENVIRONMENT

Contents

The work presented in this chapter is partially based on the article Plantefève *et al.* (2014b).

5.1 Problem statement

In the last chapter we described and evaluated a registration method based on biomechanical modeling in order to align pre- and intra-operative data. No real boundary conditions were used for this initial registration algorithm. The position of the anatomical structures surrounding the liver is not known at the beginning of the registration, they cannot be used for the registration method. However, for temporal registration using tracking methods (Haouchine *et al.*, 2013; Mountney *et al.*, 2010) a good initial alignment as well as good boundary conditions need to be provided. Indeed, contrary to the initial registration method, the temporal registration has to be performed in real time, and needs to reconstruct points from features

that have a robust descriptor. In practice the feature descriptors should be invariant under rotations, translations, illumination changes and affine deformations. This guarantees that the feature point will be easily identifiable in the different video frames, but that less points can be reconstructed from the laparoscopic images, thus providing less intra-operative information. This lack of information should be compensated by the knowledge of the boundary conditions. Therefore, at the end of the initial registration accurate boundary conditions should be provided.

The boundary conditions of the liver, already described in Chapter 2, can be divided in two categories: the unilateral and the bilateral boundary conditions (see Fig. 5.2). The unilateral boundary conditions result from the contract with the surrounding anatomical structures, while bilateral constraints correspond to the ligaments and vessels. Unfortunately, defining such boundary conditions for a patient takes time. Also, the ligaments present in the abdominal cavity are not even visible on classical pre-operative MR or CT images (see Fig. 5.1). Thus, a mean to obtain these boundary conditions automatically is essential.

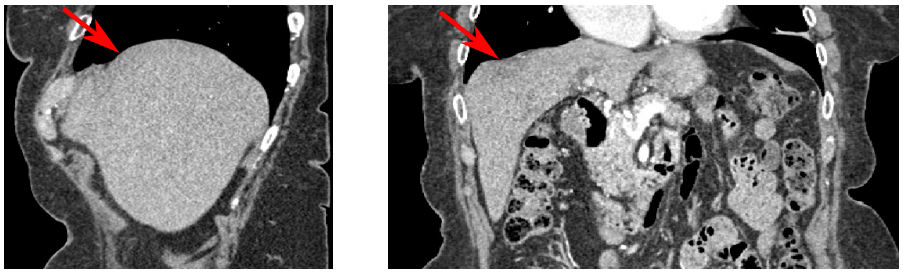

Figure 5.1: CT images of a patient abdomen. The red arrows indicate the position of the falciform ligament which is not visible in the images.

5.2 State of the art

The identification of boundary conditions has been studied in the field of structural analysis and computer-aided design. For example, in Ahmadian *et al.* (2001) boundary conditions are identified using a boundary stiffness matrix which is obtained as a solution of characteristic equations formulated for different modes of the object. It is assumed that the object follows a linear elastic law and that the boundary conditions also behave linearly. In Ahmadian and Zamani (2009), the non-linear effects are also taken into account in a method based on non-linear normal modes; the method is validated using a simple beam. In Suzuki *et al.* (2006), accurate determination of boundary conditions including non-linear effects as friction and

slip is presented for a two-dimensional circular plate. While these methods achieve an accurate identification of boundary conditions, they are limited to scenarios where the objects have simple and well-defined boundaries and where the required experiments can be performed. Unfortunately, the anatomical structures considered in medical simulations have complex boundaries which are subject to different types of interactions (bilateral and unilateral constraints with and without friction) and the experiments described in the articles cannot be applied to these structures. In Peterlik *et al.* (2014) the authors used a biomechanical simulation and two CT images of a swine acquired in supine and flank positions, to estimate the location and stiffness of the boundary conditions. However, the boundary conditions that can be estimated are limited to those responsible for the deformation between the two configurations and as two image acquisitions are needed this requires to change the clinical workflow. The work closest to our objective is described in Hu *et al.* (2012) in the context of a multi-modality registration method for image-guided prostate interventions. In this work, a finite-element patient-specific model is built using preoperative MR data and a set of deformations corresponding to different boundary conditions, and randomly sampled material properties are computed and evaluated statistically using a principal component analysis. Nonetheless, the boundary conditions described here result from the interaction of a TRUS probe with the patient's prostate, but this method is not aimed at determining the boundary conditions imposed on the prostate by its surrounding anatomical structures.

In the area of medical image registration, it is relatively common to use an atlas to register information that is not available in the target image. This is the case for instance in brain imaging, where an histological atlas containing detailed anatomical information is mapped onto an MRI of the patient to help targeting small structures during neurosurgery planning Bardinet *et al.* (2009). The idea presented here is to use a similar approach to first build an atlas of liver models including the regions where the ligaments are located, and then register the atlas onto the patient's liver to transfer the boundary conditions. In this process, the atlas creation is an important step, as well as the quality of the registration method. The most common type of atlas consists in a mean shape (or image) generated from a database of several shapes (or images). The creation of the atlas involves the segmentation of anatomical structures in each image of the database followed by the registration of each image into a common reference frame. Variations of this process include multiple images of the same patient using different imaging techniques or parameters, or the use of a single image in the database, obtained from a high-resolution imaging process. Statistical atlases rely

on a similar idea, but take into account inter-subject anatomical variations. The shape correlations between different anatomical structures are usually described using a conditional Gaussian model Wang *et al.* (2012). A two-step registration process is then required to estimate the probability of having a certain anatomical information in the low resolution or low contrast target image.

The registration process can take many forms, either in the image space or using reconstructed geometrical models. In the following, we essentially focus on registration methods applied between surface representations but involving a physics-based approach to estimate a volumetric displacement field. For instance, in Ferrant *et al.* (2001) a registration of intra-operative MR brain images is proposed where the model is based on linear elasticity and a finite element method. The method is driven by active surface matching which deforms the brain boundary in one scan towards the boundary in the following scan. A multi-organ deformable image registration based on a biomechanical model is presented in Brock *et al.* (2005). The model driven by surface deformation and displacements of landmarks is used to analyze and predict the motion of abdominal organs during respiration.

In this chapter, we propose a combination of a statistical atlas and a physics-based registration method to estimate the patient specific boundary conditions of the liver. This method is also used to obtain automatically the location of the anatomical structures which are required for the registration method described in Chapter 4.

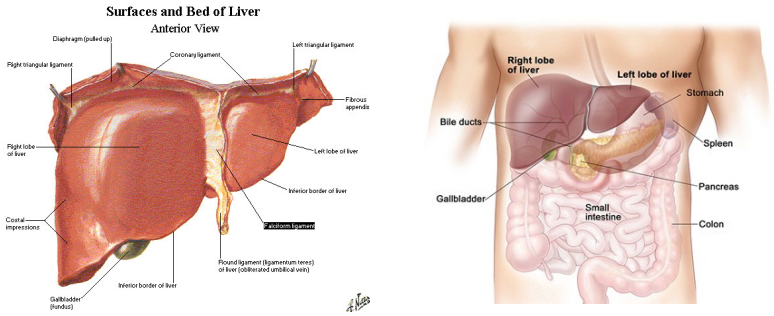

(a) Liver anatomy (b) Liver in the abdomen

Figure 5.2: The liver is a good example of an organ with a mechanical behavior highly influenced by its environment, mainly by bilateral constraints (ligaments and vessels) and unilateral constraints (contacts with the surrounding anatomical structures).

5.3 Methods

The main idea of our method is to create a statistical atlas of the boundary conditions and the anatomical structures of interest. Both the boundary conditions locations and their mean elastic properties found in the literature Umale *et al.* (2011) are stored in the atlas. In the reminder of this work we consider the ligaments, arteries and veins that "connect" the liver to the surrounding anatomy as the boundary conditions (see Fig 5.2). As we want to obtain statistical results on the atlas and use this atlas to transfer the boundary conditions on a biomechanical model we chose to construct a geometric atlas.

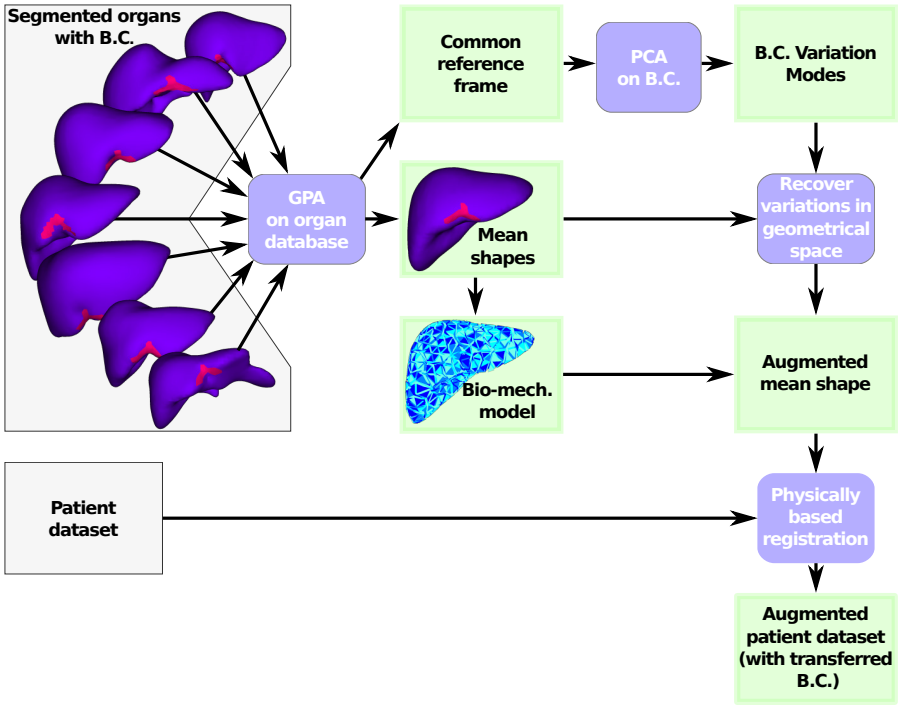

Figure 5.3: Main steps of the atlas creation process and its application to the transfer of boundary conditions.First all the shape are align in a common reference frame by a GPA. This allows for the mean shape computation. Then a PCA is conducted on the aligned shapes to obtain the variation modes and the variation in the features position. Finally, the mean shape is augmented with this information and a biomechanical model to be registered on a patient's liver.

The creation process for the statistical atlas is partially based on the work of Wang *et al.* Wang *et al.* (2012). It assumes that we have three-dimensional surface models of the different structures of interest (in our case the organ and the regions where the boundary conditions are located). These models are obtained from the segmentation of medical images by an expert. Then, a

number of points is sampled onto the surface of each mesh. The same number of points and numbering is used for each point cloud. From this set of points, a GPA is performed to determine a set of similarity transformations $SIM_i(.)$ that aligns best all models of the database into a common reference frame. This transformation is specific for each model i, where S_i is the space of the segmented model and C is the common reference frame. Then, a principal component analysis (PCA) is performed on each structure of interest (organ and boundary conditions) to compute the principal modes of deformation across the database. We keep only the most significant modes, i.e. the modes responsible for more than 90% of the deformations. Assuming the Gaussian distribution of the modes, we can determine the mean and standard deviation associated to each structure. The same is done for the elastic modulus of each boundary condition. Finally, a physically-based registration method is used to register the statistical atlas on the patient specific liver. The technique is summarized in Fig. 5.3.

5.3.1 Atlas Construction

Segmentation of the boundary conditions

For each liver used to create the atlas the segmentation and the boundary conditions labeling require anatomical expertise and can take several hours. A set of pre-operative medical images of the organ of interest is segmented manually by an expert to obtain segmented maps of the organ and anatomical landmarks. From each segmented map a surface mesh is generated using the method described in section 1.1.3. The anatomical landmarks are then delineated on each surface mesh manually using the segmented images and a three dimensional cursor that links the images to a three dimensional model of the liver. Thus, we obtain one surface mesh — which is a sub-mesh of the liver surface — for each anatomical feature.

Obtaining the same numbering

The key to the GPA method is to have the same numbering in all liver shapes, that is, the points corresponding to the same anatomical region should be labeled with the same number in all liver shape. In order to obtain the same numbering for every liver, we register one liver shape, the source liver, onto the others, using a slightly modified version of the registration algorithm presented in Chapter 4. First, we use only one anatomical landmark, the anterior margin (AM) because it is the only one that can be easily automatically identified. Then, as the registrations are performed inter-patient and not intra-patient, the source liver should be able to undergo plastic defor-

mations and its volume should be modified in order to correspond to each target liver volume.

Automatic detection of the anterior margin: The anterior margin is an anatomical structure that is defined as a sharp transition between the inferior and anterior faces of the liver and is located on the segment 6, 5, 4b and 3 of the liver surface. Crossing the entire length of the liver, it gives a robust landmark for the registration method. This landmark can be easily identified in most human liver segmentation. The automatic detection of the anterior margin on the 3D model of the liver is performed as follows. First all the edges $\{e\}$ separating two triangles with sufficiently different face normals are selected as seeds:

$$E_{seeds} = \{e \mid \mathbf{n}_{t_{1_e}} \times \mathbf{n}_{t_{2_e}} > \tau_1\}$$

where $\mathbf{n}_{t_{1_e}}$ and $\mathbf{n}_{t_{2_e}}$ are the normals of the two triangles adjacent to the edge e and $\times$ is the cross product. Then, the anterior margin is extended from the seed edges. All the edges $\{e\}$ adjacent to a seed edge are processed. They are selected as edges of the anterior margin if:

- Their direction $\mathbf{e}_e$ is close enough to the direction of their parent edge $\mathbf{e}_{e_p}$:

  $$\mathbf{e}_e.\mathbf{e}_{e_p} > \tau_2,$$

  where . is the dot product.

- The normals of their adjacent triangles are sufficiently different:

  $$\mathbf{n}_{t_{1_e}} \times \mathbf{n}_{t_{2_e}} > \tau_3 \qquad \text{with } \tau_3 < \tau_1.$$

If no extension is found for a certain seed, the seed is removed. Iteratively the anterior margin is reconstructed. The values of the thresholds are defined according to statistics on the mesh: τ_1 and τ_3 are set as the 98th percentile and the 9th decile respectively of the cross product of the normals of adjacent triangles, and τ_2 is set as the median of the adjacent edges cross product. Finally, all the triangles adjacent to an edge of the anterior margin are defined as a triangle of the anterior margin.

One heuristic is additionally applied to the anterior margin detection, since the zone of the hilum may presents an uneven surface and thus unwanted seed edges could be detected in this region. The hilum is close to the center of gravity G of the mesh. Thus, we remove all the seed edges which are inside a sphere centered at G and of diameter equal to 45% of the distance between G and the point of the mesh with the maximal distance to G.

Volume adjustment and plastic deformation: In order to facilitate the inter-subject registration the size of the object was modified by the following factor:

$$\frac{\sqrt[3]{V_t}}{\sqrt[3]{V_s}},$$

where V_s is the volume of the source liver and V_t is the volume of the target liver. Moreover, in order to allow for plastic deformation, instead of increasing the force intensities at each plateau the liver rest shape is updated with its current configuration.

Obtaining a common reference frame and the mean shape

Once we have obtained the same numbering for all liver shapes, the GPA can be performed. This algorithm aligns all the point clouds in a common reference frame and allows for the computation of the mean shape. The GPA determines for each point cloud the similarity transformation $\mathbf{SIM}_i$ providing an optimal alignment of all the models in the database:

$$\mathbf{SIM}_i : \mathcal{S}_i \rightarrow C \qquad \mathbf{SIM}_i = s_i \mathbf{R}_i \mathbf{T}_i \tag{5.1}$$

$$\mathbf{P}_i \mapsto \mathbf{P}'_i \tag{5.2}$$

where $\mathcal{S}_i$ is the space of the i-th segmented model, C the space of the aligned models, $\mathbf{P}_i$ the initial point cloud, $\mathbf{P}'_i$ the aligned point cloud, $\mathbf{T}_i$ the translation matrix which aligns the center of mass of the ith point cloud and the origin, $\mathbf{R}_i$ a rotation, and s_i a scale factor. Both $\mathbf{R}_i$ and s_i are computed iteratively using the matrix $\mathbf{P}_i\bar{\mathbf{P}}^\top$, where $\bar{\mathbf{P}}$ is the mean shape recomputed at each iteration. We have:

$$\mathrm{SVD}(\mathbf{P}_i\bar{\mathbf{P}}^\top) = \mathbf{U}_i\Sigma_i\mathbf{V}_i^\top \tag{5.3}$$

$$\mathbf{R}_i = \mathbf{U}_i\mathbf{V}_i^\top \tag{5.4}$$

$$s_i = \sqrt{\frac{\mathrm{tr}(\mathbf{P}_i\bar{\mathbf{P}}^\top)}{n\|\mathbf{P}_i\|_F\|\bar{\mathbf{P}}^\top\|_F}} \tag{5.5}$$

where SVD(.) denotes the singular value decomposition, tr(.) the trace of a matrix, and $\|.\|_F$ the Frobenius norm of a matrix.

Statistical analysis

Then, the PCA is performed on each structure of interest to compute the principal modes of shape variation across the database.

Given a certain number of samples and a certain number of characteristics know for each sample, the PCA computes the linear combination of the

different characteristics which best explain the variance present across the samples. In our case, the samples are the point numbered on the meshes, and their characteristics are their three dimensional positions in each of the atlas mesh. These information are gathered in a martix $\mathbf{P}$ of size $3n \times m$ where n is the number of sampled points on the mesh and m is the number of meshes in the atlas.

First, the covariance matrix $\mathbf{C}$ of the data set matrix is computed:

$$\mathbf{C} = \mathbf{P}^T\mathbf{P}.$$

Then, a eigenvalue decomposition is performed on the correlation matrix:

$$\mathbf{C} = \mathbf{U}\mathbf{D}\mathbf{U}^T$$

where $\mathbf{U}$ is the matrix of eigenvectors, and $\mathbf{D}$ is a diagonal matrix containing the eigenvalues. The eigenvectors corresponding to the higher eigenvalues are the principal modes of the the atlas. We keep only the k most significant modes, i. e. the modes responsible for more than 90% of the shape variations. Assuming the Gaussian distribution of the modes, we can determine the standard deviation associated with the position of each anatomical structure present in the atlas from the mode vector corresponding to the different features of all the livers of the atlas.

5.3.2 Atlas to patient registration

The aim of this step is to find the boundary conditions of a patient-specific organ model, and to automatically locate the anatomical landmarks used in the registration method described in the Chapter 4. The patient's anatomy augmented by the atlas includes a typical stiffness and mean position associated to each boundary condition, and the variance around this mean. Having a 3D model obtained from pre-operative data and the atlas described above, the aim is to compute an elastic transformation which maximizes the shape similarity between the atlas model and the patient specific model. The procedure is done as follows: the three-dimensional mean shape organ model, containing the information about the boundary conditions location, is registered to the patient's data. The registration method is the same as the one used for the atlas construction and is described in the previous section. The standard deviation associated with each boundary condition in the atlas is also transferred to the patient's data. However, while the position variability in the atlas is a three-dimensional distribution, it must be projected onto the surface of the patient's liver mesh (by definition, boundary conditions are only applied to the boundaries). Additionally, the elastic modulus of each boundary condition, available in the atlas, is also associated to this geometrical description.

5.4 Results

5.4.1 Atlas Construction

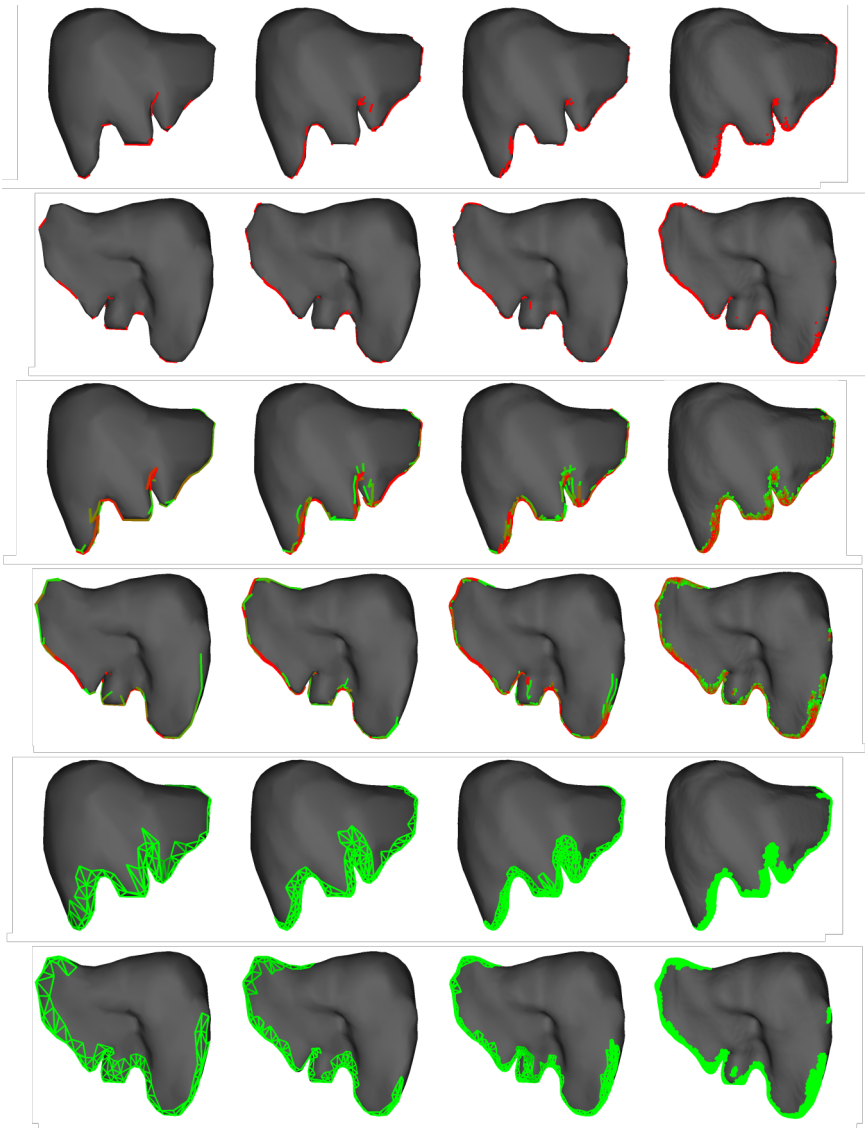

Figure 5.4: Comparison of the results of the anterior margin detection algorithm for different mesh resolution. The columns show, from left to right, the result for meshes composed of 533 vertices and 1602 faces, 1065 vertices and 2126 faces, 2128 vertices and 4252 faces, and 35770 vertices and 71536 faces. The first two rows show the detected seed edges, the third and fourth rows show all the detected edges (the red ones being the seed edges and the green ones the last added edges), and the last two rows show the triangles of of the anterior margin.

The atlas was created using ten liver models, presented on Fig. 5.5, and

their respective anatomical features obtained from segmented abdominal CT scans. To ensure the quality of the atlas, we evaluated the standard deviation of the umbilical notch and vena cava positions over the samples; we obtained σ_{UN} =11.12 mm and σ_{VC} =16.56 mm respectively. The average variability represents less than 9.7% of the size of the organ showing a strong consistency among the feature positions.

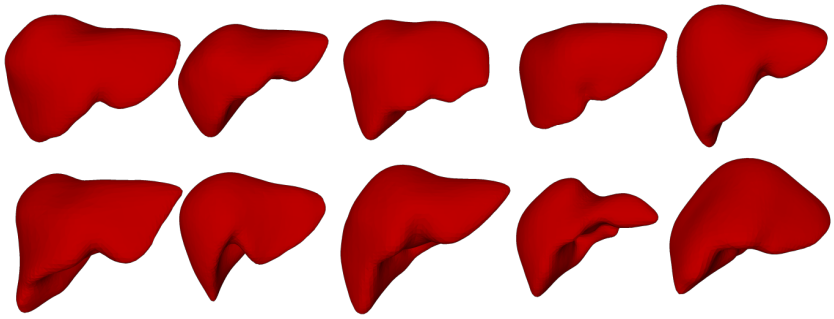

Figure 5.5: The ten livers used to construct the atlas

First, we studied the robustness of the anterior margin detection algorithm. A very fine mesh has been decimated using the quadratic edge collapse decimation algorithm of Meshlab several times and the algorithm has been applied on each generated mesh. The results, presented in Fig. 5.4, show that the anterior margin detection is robust to the mesh finesse. The anterior margin is very similar for the coarsest and the finest mesh, the latter having only two wrong seed edges detected on the inferior surface of the liver.

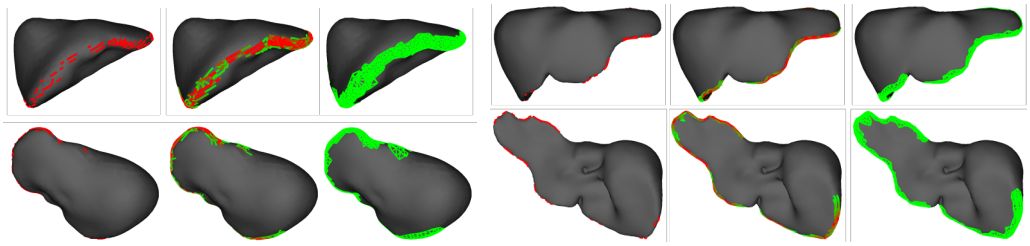

Figure 5.6: Results of the anterior margin detection on a smooth mesh (a) and an uneven mesh (b)

Additional results showing the detected anterior margin on two other livers are given in Fig. 5.6. The anterior margin is successfully detected both on smooth and uneven meshes (Fig. 5.6 (a)). For long and slim livers, such as the one of Fig. 5.6 (b), the heuristic employed to avoid edge detection

in the hilum region may suppress a part of the anterior margin around the umbilical notch. This is not an issue for the registration as long as these livers are not used as source meshes.

The mean Hausdorff distance between the source and the target liver for the registration performed to obtain the same numbering is 0.4 mm.

Fig. 5.7 presents the livers shapes of the atlas before and after the GPA, and Fig. 5.8 the mean shape of the atlas.

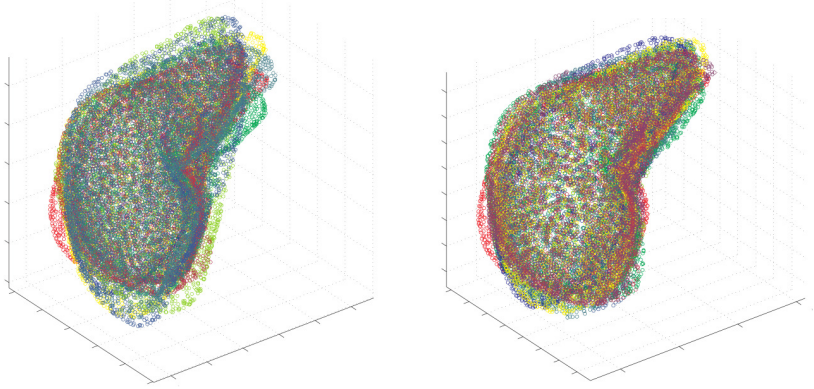

(a) (b)

Figure 5.7: Liver shapes before (a) and after (b) GPA

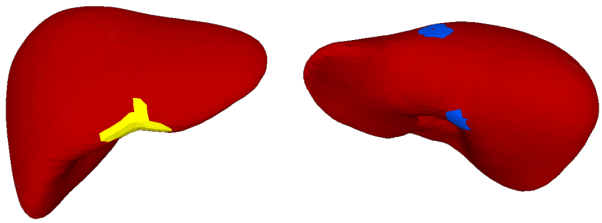

Figure 5.8: Mean shape of the liver, the umbilical notch (in yellow) and the entry and exit points of the *vena cava* (in blue) after GPA

5.4.2 Transfer of Boundary Condition

In this section we assess the quality of the boundary conditions transfer and its influence on the biomechanical model behavior. We registered the atlas onto several livers: ten from the atlas following the left-one-out principle

and two livers not included in the atlas (sample #11 and #12). The registration errors for all livers are presented in Fig. 5.9 and Fig. 5.10 shows the result for the sample #5.

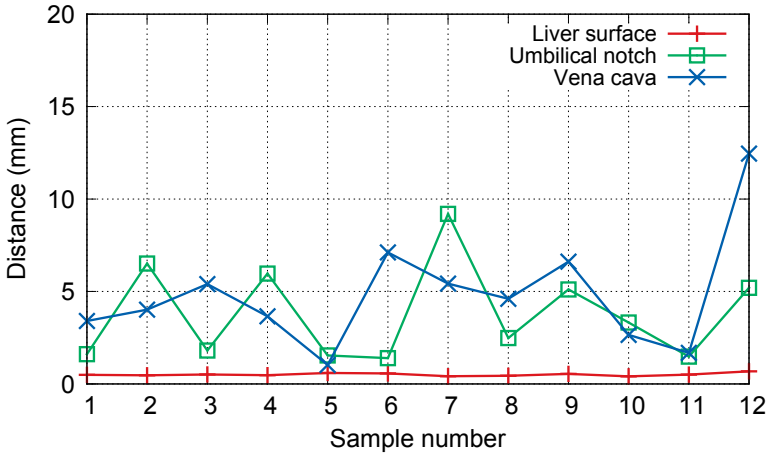

Figure 5.9: Mean Hausdorff distances between the segmented liver surface and the registered mean shape (in red) between the manually segmented umbilical notch and the umbilical notch transferred from the atlas (in green) and between the manually segmented vena cava and the vena cava transferred from the atlas (in blue).

The results show that the surface registration is very accurate and all the boundary conditions locations errors are under 10 mm except for sample #12, indicating that the biological variability of this sample is not well represented in the atlas. We also note that in all cases the error obtained on the boundary conditions location is less than the atlas variance.

5.4.3 Influence of Boundary Conditions on biomechanical simulation

To evaluate the influence of errors in boundary conditions locations on biomechanical simulations, we altered the position of the boundary conditions. We used only the boundary conditions present in the atlas to conduct the experiments. We used a liver segmented in the supine position to set up a simulation where gravity is re-oriented in order to simulate a deformation of the organ in the flank position (see Fig. 5.12 (a)). Then, we compared the final shape of the liver simulated with altered boundary conditions to the final shape of the reference liver. Fig. 5.12 (b) shows the result for one liver using the manually segmented boundary conditions versus the boundary conditions obtained with the atlas. We also conducted a sensitivity study. The simulation was performed using several altered boundary condition positions, and we measured for each of them the distance of the final deformed mesh with the mesh deformed using the reference bound-

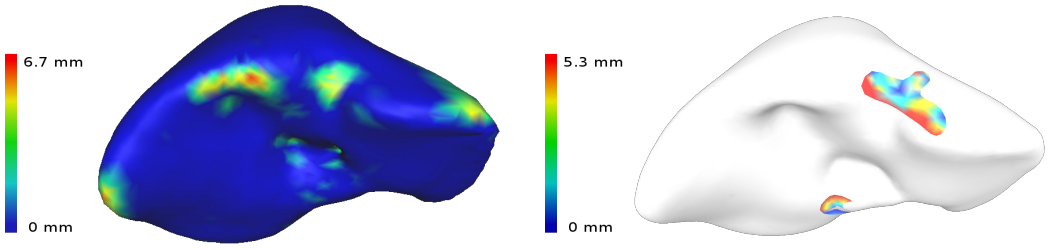

(a) (b)

Figure 5.10: (a) Error in registration of the atlas to the patient-specific data. The mean Hausdorff distance after registration is 0.5 mm. (b) Error between estimated boundary conditions and ground truth obtained by manual segmentation. The umbilical notch and the vein features are recovered with a mean Hausdorff error of 4.2 mm.

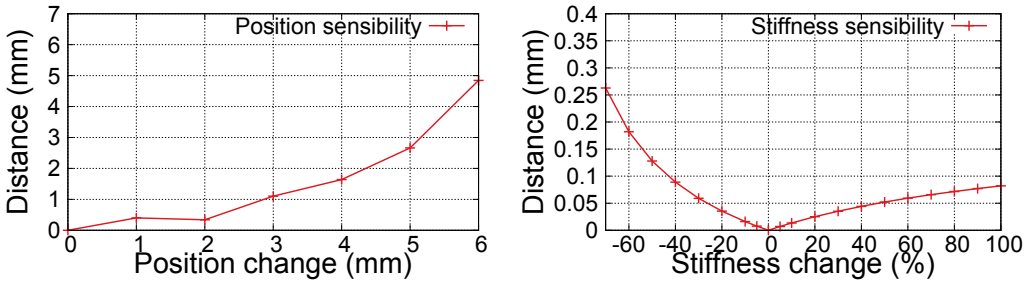

(a) (b)

Figure 5.11: Sensitivity study. Mean Hausdorff distance between the final configurations of a reference model and a biomechanical model with altered boundary conditions position (a) and stiffness (b).

ary conditions. The results are presented in Fig. 5.11(a). They show that small displacement (below 3 mm) leads to an error below 1 mm, however, the relation between the displacement and the error seems to be quadratic, but, a deeper analysis is needed to confirm this trend. The same kind of experiments was conducted to evaluate the influence of errors in the boundary conditions stiffness, the results are shown in Fig. 5.11(b). The values of the reference stiffness were set according to the ligament and *vena cava* Young's moduli found in the literature Umale *et al.* (2011) (20 MPa for both) and their geometry. The results show that the influence of the stiffness is very small when compared to the influence of the location of the boundary conditions. This can be justified since the ratio between the liver internal forces and the external forces imposed by the boundary conditions is very low. Therefore using twice or half the reference stiffness does not change

this ratio significantly.

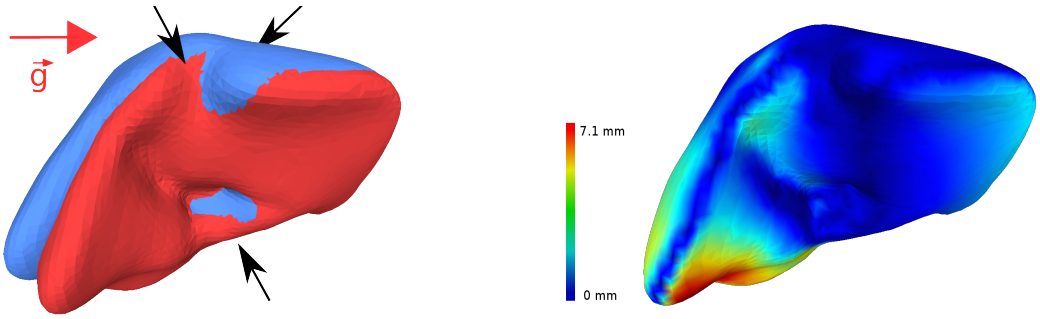

(a) (b)

Figure 5.12: Simulation of flank to supine deformation of the liver: (a) shows the displacement between flank and supine position. The black arrows indicate the position of boundary conditions and the red arrow represents gravity; (b) Hausdorff error with boundary conditions constructed using the atlas.

In both cases, a very good match between the resulting shapes is obtained after the equilibrium is achieved as shown in Fig. 5.12: the comparison gives the mean error of 1.6 mm and a maximum error of 7.1 mm.

5.4.4 Atlas influence on registration

As the umbilical notch position is transferred to the patient liver via an atlas, we conducted a preliminary study to evaluate the influence of its position on the registration results. We moved the umbilical notch around its real position on the liver mesh surface and did not take into account the variance of the atlas — only the mean position of the ligament was used. In this way we force bad correspondences in the matching step. The TRE between the registered source mesh using the reference umbilical notch position versus the altered position highly depends on the displacement direction. The errors are more important when the umbilical notch is displaced along the anterior margin towards the right lobe. In this case, the mean TRE is increased by 3.5 mm for a position shift of 17.5 mm (mean Hausdorff distance of 4.8 mm). However, for all tested scenarios, the TRE remains below 2 mm as long as the displacement of the ligament does not exceed 10 mm (mean Hausdorff distance of 1.0 mm). Nevertheless, additional experiments would be necessary to conduct a proper analysis of the impact of position error of the umbilical notch on the registration result.

5.5 Discussion

Taking into account the environment of the abdominal organs for physical simulation and registration is very challenging. In this chapter we have constructed an atlas of the liver boundary conditions which achieve a feature localization error below the atlas variance, indicating an excellent prediction capability of the locations of boundary conditions. The stiffness of the boundary conditions, being several order of magnitude bigger than the liver stiffness, does not influence significantly the result of physical simulations. On the other hand, the location of the boundary conditions has a strong impact on the simulation result. The precise location of the boundary conditions is more important than the value of their stiffness to simulate the behavior of the liver. However, not all the liver boundary conditions are taken into account in this statistical atlas. The unilateral boundary conditions, which result from contacts with the surrounding environment, and the coronary and triangular ligaments are not included in the atlas. These boundary conditions should be added in future work in order to obtain a complete description of the liver environment which could be used for simulation or registration purposes.

As the statistical atlas is also employed to automatically define the positions of the anatomical landmarks used by the registration method, its impact on the registration accuracy has been evaluated. The detection of the anterior margin is very robust. Thus, the position of this anatomical structure is always accurate and does not influence negatively the registration results — all the results presented in Chapter 4 were obtained using the automatic anterior margin detection algorithm. Nonetheless, the registration algorithm is sensitive to the position of the umbilical notch and improvements should be made to reduce the position error. Additionally, the impact of the boundary conditions positions on temporal registration should be investigated.

The current numbering method may introduce a bias in the atlas. Indeed, one of the livers is registered onto all other livers using a physically-based registration method, and the final position of its surface degrees of freedom are used as the numbering of the other livers. Different strategies may be employed to improve this shortcoming. For instance, an iterative atlas construction may be used: after the first generation of the mean shape, this shape could be used to define a new numbering of each liver in the atlas and a new GPA could be performed until the difference between the mean shapes of two consecutive iteration is small enough. Another strategy is to register all livers on all livers and to use the mean position of each numbered point projected on the livers surface to perform the GPA.

The power of the statistical atlas developed in this work is limited because of the reduced number of subjects present in the atlas. With a few number of subjects, it is difficult to fit a statistical law on the data set and the errors associated with the statistical values computed from the atlas are important. For instance, conditional statistical models, which would allow to have the mean position and the variance of the boundary conditions as a function of the mode vector of the liver shape, cannot be employed since the error associated to the conditional mode vectors would be bigger than their variance. Therefore, the number of subjects included in the atlas should be increased significantly in future work. However, obtaining the data needed for the atlas is difficult, and the segmentations are time consuming.

The present atlas was constructed from CT images, but can be enriched with MRI data or even cadaver data. As the ligaments are not visible in CT images, their position can only be determined approximately by anatomical experts. MRI devices could allow to visualize the ligaments, but new MRI impulsion sequences have to be developed since the sequences used for ligaments joining bones are not efficient for the ligaments of the liver. In addition, the power of the MRI scanner should be at least 3 Tesla in order to have a sufficiently small slice thickness to precisely locate the structures of interest. Such imaging devices are not standard in many hospitals. Therefore, the use of cadaver would be an appealing alternative. After a dissection, the attach points of the different ligament could be marked with a radiopaque ink and a high resolution CT scanner would allow for an easy segmentation of the liver shape and anatomical landmarks.

An alternative to the use of a statistical atlas would be to define the boundary conditions with elastography measurements. Currently, elastography methods may have difficulties to determine the material properties because the exact boundary conditions — position and stiffness — of the images region are not known. However, qualitative elastography measurement could be used to determine the location of certain boundary conditions.

The boundary conditions which have been described in this chapter are defined with respect to the liver surface. However, the positions of some boundary conditions are not fixed, but are subject to cyclic motion. This is for instance the case of the coronary ligament, which attaches the liver to the diaphragm. Therefore, the motion of these boundary conditions should be modeled in order to have an accurate placement of the liver boundary conditions at each instant.

Part III

Experimental Deployment in the OR

CHAPTER 6

EXPERIMENTS IN THE OPERATING ROOM WITH THE SOFA-OR FRAMEWORK

Contents

In this chapter, we detail the deployment of the registration method developed in this thesis in the operating room. A complete pipeline has been developed for laparoscopic hepatic surgery guidance. This pipeline comprises an acquisition system of OR streams, a processing system which generates the input data of the registration algorithm from the raw medical data, the registration algorithm itself, and a visualization engine. First, the characteristics of the OR environment and of the medical devices that we used during this work are detailed. Then, both the hardware and software architecture of the designed pipeline are detailed, highlighting the challenges that needed to be overcome to obtain the input data of the registration algorithm. Afterward, new visualization techniques that allow

for an intuitive augmented view are presented. Finally, some results of the pipeline on both phantom and real data are presented.

6.1 The operating room

Bringing numerical simulations in the operating room is challenging for several reasons. Firstly, the OR environment is cluttered with many medical devices, cables, monitors, making it difficult to find a place to set up hardware equipment. Secondly, the sterility constraint limits the possible interaction with the surgical devices. Thirdly, most sources of data provided by the various medical apparatuses are designed to be displayed to the clinical team, not to be processed by third party software.

6.1.1 The environment

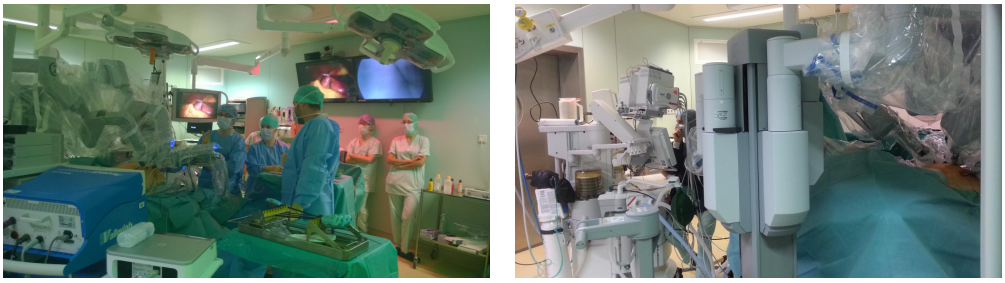

Figure 6.1: The operating room.

The standard operating room size is $35\,m^2$. This may seem big, but the number of medical devices and other furniture is important (see Fig. 6.1). The organization of the various medical apparatuses in the OR is difficult since most of them should be close to the operating table because of the cables and tubes that are connected to the patient or to the surgical instruments. Sterile areas should also be preserved around the patient and the surgical instrument tables. Thus, very little space is left for additional hardware, and the physical connection to the medical devices should not interfere with the operation.

In this work we capture the images of the stereoscopic camera of the *da Vinci®* robot. This surgical device is composed of three distinct parts: the robot itself, the vision cart, and the surgeon console (see Fig. 6.2). Very often, two consoles are connected to the same robot to allow surgeons to collaborate on challenging tasks. These apparatuses add to the standard medical devices present in an OR, and thus reduce even further the available space.

Figure 6.2: The *da Vinci*® robot. On the left is the surgeon console, in the center the vision cart, and on the left the robot itself.

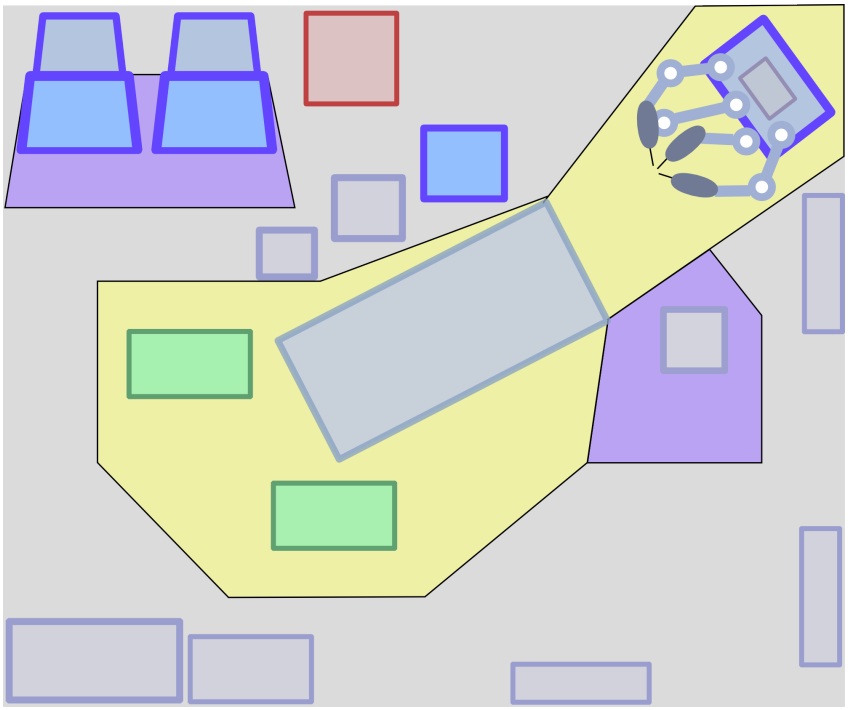

Figure 6.3: Scheme of an operating room viewed from above.

Fig. 6.3 shows a sketch of the OR organization. The yellow areas are the main working space of the medical team which have to be sterile. The blue areas are the others working spaces, which are not sterile. The green rectangles are the instrument tables. The three parts of the *da Vinci*® robot are in vivid blue. Our experimental setup has to be connected to the vision cart (vivid blue square). In order to disturb the medical team as little as possible, we are restrained to the red area depicted in Fig. 6.3. For the moment, our registration algorithm relies only on the laparoscopic images

for the intra-operative data. Thus, we have to connect our setup only to the *da Vinci®* vision cart. However, if US data is used in addition to the laparoscopic view, the setup has to be connected to both the ultrasound device and the vision cart, which may be very complex.

6.1.2 Data streams in the operating room

The data streams that we need for our pipeline are generally already used by the medical team. This means that we should provide a loopback so that the data can still be used for their original purpose. In addition, the format of the output stream of the *da Vinci®* is not directly usable for our purposes. Thus, a conversion of the data stream has to be performed in the pipeline.

The left and right streams of the laparoscopic camera do not need to be synchronized for live processing, as they have the same frame rate. However, to be able to use the acquired data after the operation, the data should be registered and synchronized during the replay. As we register the two streams in two different files, the synchronization during the replay is not guaranteed. Thus, the data should be timestamped before being saved (Belhaoua *et al.*, 2016).

6.2 Experimental setup

6.2.1 Hardware setup

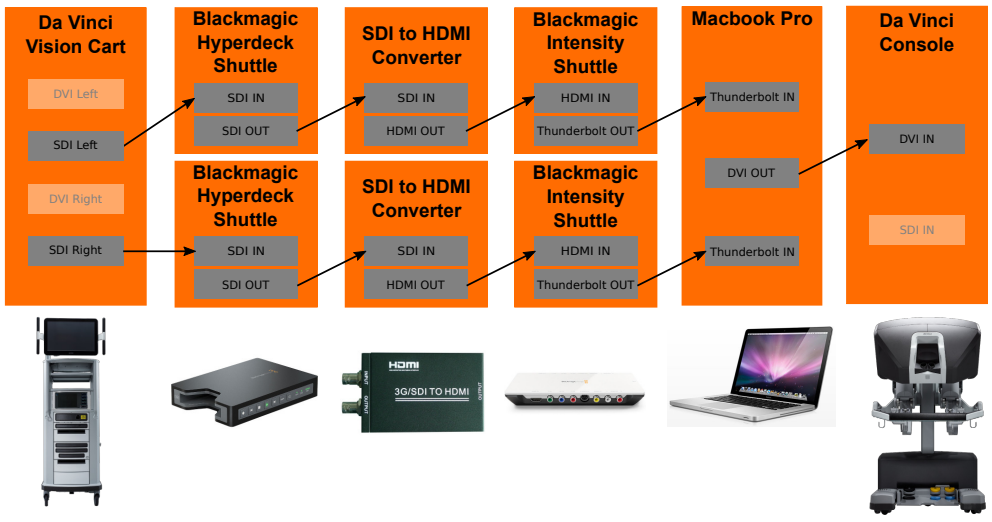

Figure 6.4: Hardware setup for per-operative liver registration.

We present in this section the hardware setup. An overview of this is presented in Fig.6.4. Our approach relies on the extraction of 3D points

from stereoscopic frames, and therefore, a calibrated stereoscopic camera is required. We chose to interface our framework with the *da Vinci*® surgical robot, but a stereoscopic camera from Storz™ like the Tipcam1® could be used instead of the *da Vinci*® endoscope. In order to retrieve the video streams from the *da Vinci*® video cart, we need two video editing cards (Blackmagic™ Intensity shuttle). A Macbook™ Pro is used to connect the video editing cards in order to benefit from the thunderbolt ports. For research and post-operation processing purposes, we also need two video recorders to retrieve the raw video streams from the operation (Blackmagic™ Hyperdeck shuttle). These recorders allow for the data loopback. This very compact setup allows us to go in the operating room.

6.2.2 The software

The software implementation is divided into three distinct processes: the AcquisitOR, the ProcessOR, and the SimulatOR (see Fig.6.5). This architecture allows for the distribution of the workload on different machines without suffering from high latency as long as it runs on a local area network or a wireless ad hod network. The AcquisitOR retrieves data from specialized hardware devices, the ProcessOR processes this data for further usage in the registration method, and the SimulatOR runs the registration algorithm according to the patient-specific data retrieved and processed in the previous steps.

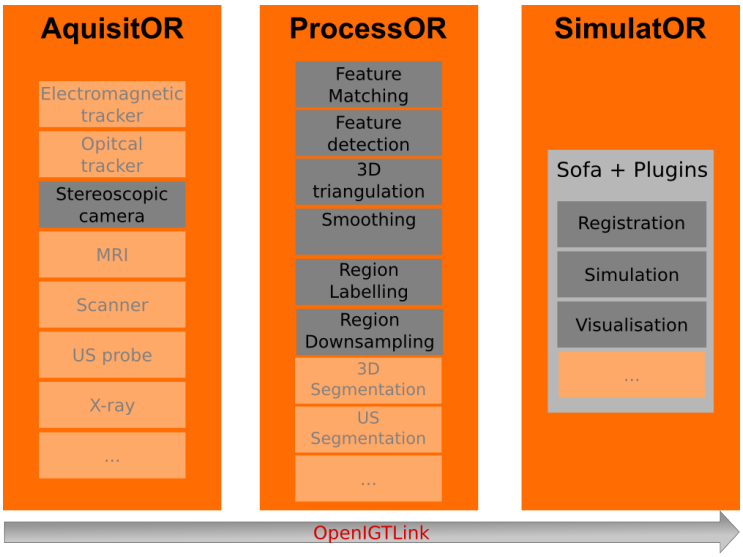

Figure 6.5: Our framework architecture.

AquisitOR

The video streams fetched from the stereoscopic endoscope are the input of our augmented reality pipeline. To retrieve these streams from the *da Vinci®* endoscope, the left and right video output from the *da Vinci®* are connected to two video editing cards (Blackmagic™ intensity). These video editing cards have no driver implementation in Plus Toolkit. Therefore, it was relevant to implement our own device acquisition server that would retrieve the video streams from the video editing card and convert its raw data into regular RGB frames. In order to connect the video editing card to AcquisitOR, the Blackmagic™ driver is implemented as a separate library, loaded at runtime according to the arguments passed on the command line.

ProcessOR

In the case of liver registration, our ProcessOR needs to generate a point cloud from the acquired stereoscopic frames. Extracting a good point cloud from endoscopic frames is a complicated matter, as image processing relies on the quality of the frames acquired, the quality of the environment inside the abdominal cavity (lighting, smoke, frame blurriness, lens cleanliness, etc.), and the quality of the liver texture which can be very different from a patient to another (see Fig. 6.6). If the texture is too smooth, the extraction will perform badly. Thus, we need to apply several filters (feature detection and matching, triangulation, epipolar constraint, downsampling, etc.), each of them requiring manual tuning. In addition, the anatomical landmarks should be labeled in the intra-operative image before the point cloud reconstruction.

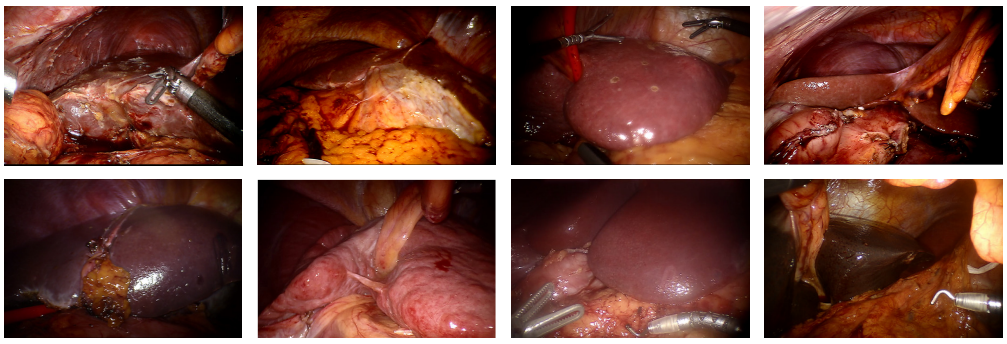

Figure 6.6: The textures of the patient's liver are very different. The top left liver has an irregular texture which allows for a robust feature point extraction and 3D point cloud reconstruction, while feature point extraction is extremely challenging with the texture of the third liver in the bottom row.

Thus, an intuitive graphical user interface has been designed. The filters

parameters are set to default values that work well in most cases, but each of them can be changed manually in case of a poor point extraction. The selection of the different labeled regions is performed manually by clicking in the image to define polygonal areas (see Fig. 4.3). This process takes only a few seconds. Once the labeled regions are selected, we build for each of them a 3D point cloud using the method described in Chapter 1 section 1.2. These labeled point clouds are then sent to SimulatOR, through OpenIGTLink.

SimulatOR

The simulator is the part of the pipeline that performs the registration of pre-operative data onto the intra-operative view. The implementation of the algorithm, described in Chapter 4, has been performed using the SOFA framework. The result of the SilulatOR is then sent to one of the OR monitor, or to the *da Vinci*® console.

6.2.3 Protocol for the surgeon

The modification of the surgical procedure is light. When the surgeon asks for an augmented view of the liver, he should ensure that the camera is cleaned, that the focus is correct and that the view of the liver is wide and clear. Then, the camera should not be moved until the end of the registration procedure.

If the hilum is employed, the surgeon has to lift the left lobe of the liver in order to expose the hilum a few seconds to reconstruct the point cloud of this region. The liver is then put back in its original position, and the point cloud reconstruction of the other labeled regions begins. Then, the surgeon, or one of its assistant, draws the polygonal regions using the graphical interface.

The complete process (from the positioning of the camera to the display of the registration result) takes approximately 5 min for the initial registration. Subsequent registration are much much faster.

6.3 Visualization for augmented reality

All the described pipeline is useless if the surgeons do not understand the AR view, that is the only output of the algorithm for them. The challenge is to help the clinicians to estimate the position of the internal structures without hiding important information present in the endoscopic view of the operative field.

6.3.1 Rasterization on the laparoscopic view

3D rendering on a computer works as follows: since the final visualization is a 2D image, the rendering part of a computer program takes as an input a 3D mesh and project it onto a plane, creating a flat image that can be displayed on the computer screen. The projection is performed using the virtual camera intrinsic parameters and this process is called rasterization. The virtual camera can then be rotated around the visualized object, zoomed in or out to obtain different view points of the object. In this way, it is easy to mentally reconstruct a 3D image of the object.

To display an overlay of the liver internal structures onto the laparoscopic view, the intrinsic parameters of the real laparoscopic camera must be used to render the liver virtual model. However, the laparoscopic camera provides a close-up view of the organ and only very little rotations can be performed around the organ due to the fulcrum effect. This makes difficult the estimation of the internal structures positions. Therefore, the augmented reality view must compensate for this lack of depth information.

As the liver is opaque, displaying its internal structures on the intraoperative view leads to the erroneous perception that the internal structures are outside of the liver. This impression is counter intuitive and perturbs the comprehension of the image. Thus, transparency effects should be used in order to create a more intuitive augmented view of the liver.

6.3.2 Giving a sense of depth

Transparency

The first method that has been explored to compensate for the shortcoming described above is the use of contour rendering and alpha blending. The alpha value corresponds to the degree of opacity of a color. This value ranges from 0 (completely transparent) to 1 (completely opaque).

The organ surface is rendered using a contour rendering technique. To each vertex v_i of the mesh surface is associated an alpha value according to the direction of its normal $\mathbf{n}_i$ relative to $\mathbf{d}_c$, the direction of the camera:

$$\alpha_{surf_i} = \max(1 - k.\text{abs}(\mathbf{n}_i.\mathbf{d}_c), 0),$$

$\mathbf{n}_i$ and $\mathbf{d}_c$ being normalized vectors, k a scalar factor controlling the contour thickness and abs(.) the absolute value. Thus, only the vertices with normals perpendicular to the camera are completely opaque.

The internal structures are displayed using alpha blending. A ray is cast from the camera position to each vertex of each internal structure. The intersections of this ray with the surface mesh are used to compute the alpha value of the vertex. If the position of the internal structure vertex is behind

all the intersection points of the ray with the surface mesh, the alpha value of the vertex is set to zero. If the vertex v_i has both intersecting points in the direction of the camera $\mathbf{p}_{\text{front}}$ and in the opposite direction $\mathbf{p}_{\text{back}}$, its alpha value is set to:

$$\alpha_{int_i} = \max\left(1 - \frac{|v_i - \mathbf{p}_{\text{front}}|}{d_{\max}}, 0\right),$$

where $d_{\max}$ sets the depth at which the internal structures are completely transparent. Finally, if the vertex is before the intersecting point, its alpha value is set to 1.

Adding a projection plane

The second method that we have tested was inspired by the work of Lawonn *et al.* (2015). This method was designed to display the vascular tree of a liver alone on a clean background. The principle is to define a plane below the mesh of the vascular tree and to project the mesh onto the plane. Then, lines are drawn between some vertices of the vessel mesh and their projection on the plane.

We improved this visualization technique in order to display the liver internal structures on the laparoscopic view. In particular, the plane position has to be set on a part of the laparoscopic view such that it would not hide the operative field. Thus, we defined a parameter to place the plane above, below, on the left or on the right of the image. We also used the contour rendering described in the previous method to display the liver surface, since its position is important to assess the quality of the registration. The vessels are displayed using either the contour rendering or the alpha blending algorithm.

Wave propagation

The last technique that has been investigated is the a dynamic visualization method. As an accurate mental representation of a three dimensional object is easier to obtain from several images than from only one image, a dynamic visualization method has been developed. Two planes, perpendicular to the camera direction $\mathbf{d}_c$ and distant from h mm, are displaced from the camera position to the point of the surface mesh that has the highest distance to the camera. Three different colors are used to display the mesh points: one for the point before the planes, one for the points between the planes and one for the points behind the planes. This technique is perhaps not completely intuitive, but surgeons are used to work with medical images, which are slices of the organ, and this visualization method relies on the same principle.

For both this technique and the previous one, the liver surface is rendered using contour rendering, and the vascular tree using either contour rendering or alpha blending. The projection plane may also be added to the visualization, but this often overloads the AR image.

6.4 Results

6.4.1 Visualization methods

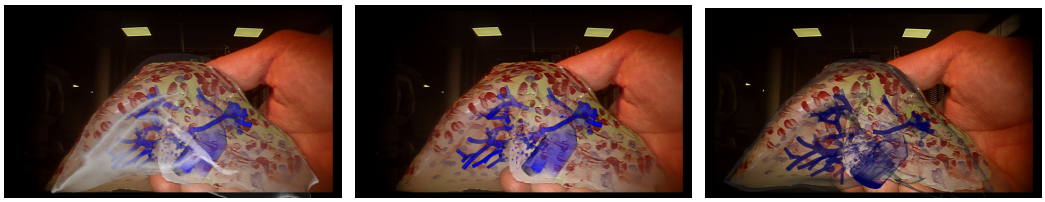

Figure 6.7: Visualization results on a liver phantom. From left to right: alpha blending rendering of the vessels and contour rendering of the surface, alpha blending rendering of the vessels only, contour rendering and alpha blending of the vessels and contour rendering of the surface.

This section provide the results of the different visualization algorithms tested in this work, except the wave propagation, which is given as a supplementary material. Fig. 6.7 gives the results of three different visualization techniques on a silicon liver phantom. Fig. 6.8 shows the results of the same visualization technique on an *ex vivo* kidney, and Fig. 6.9 on an patient's liver.

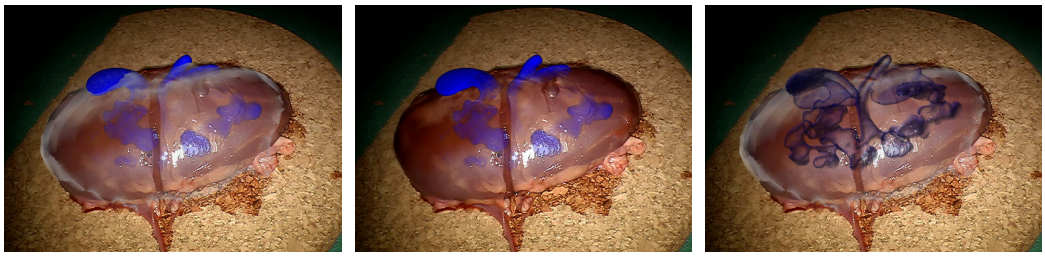

Figure 6.8: Visualization results on an *ex vivo* kidney. From left to right: alpha blending rendering of the vessels and contour rendering of the surface, alpha blending rendering of the vessels only, contour rendering of the vessels and the surface.

The last two examples were not registered using the pipeline. The kidney was seen only with a monocular camera, thus a three dimensional point cloud reconstruction was not possible. For the liver mesh, despite the apparent texture of the liver, the feature detection algorithm performs poorly

and does not extract enough points for the deformation part of the algorithm to be useful. Thus, only a rigid transformation has been performed, explaining the visual misalignment.

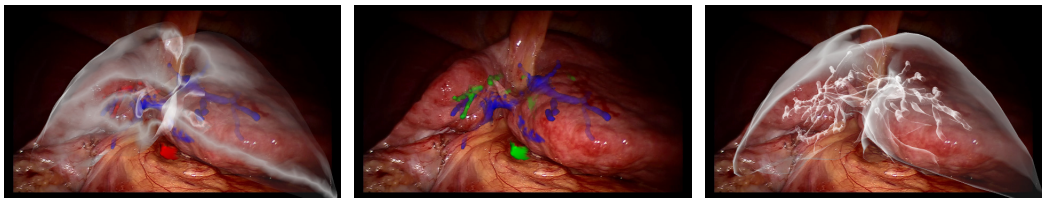

Figure 6.9: Visualization results on a patient's liver. From left to right: alpha blending rendering of the vessels and contour rendering of the surface, alpha blending rendering of the vessels only, contour rendering of the vessels and the surface.

Fig. 6.10 shows the result for the plane projection. This visualization needs to be improved. The dense wireframe meshes projected on the plane are not very informative. Maybe it could be better to project only the vessels centerlines.

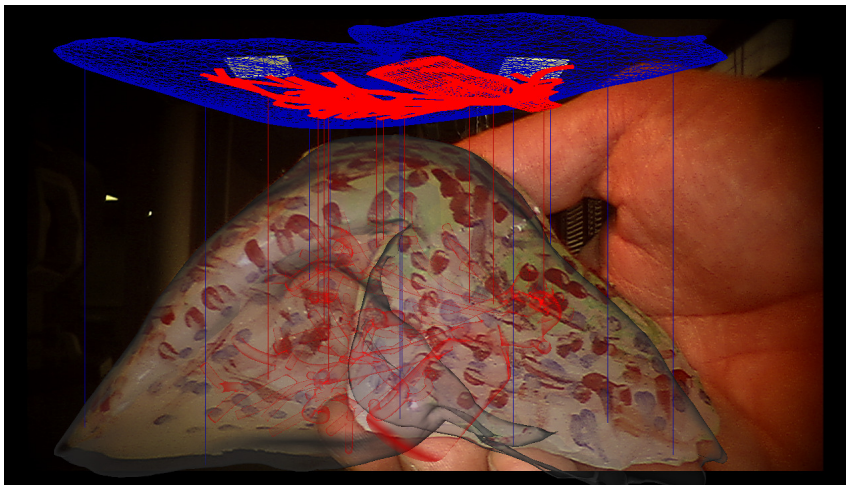

Figure 6.10: Result of the plane projection on the liver phantom.

6.4.2 Complete pipeline

The pipeline described in this section allows us to display an augmented reality view of the liver in an OR during a laparoscopic intervention without changing significantly the clinical workflow.

Fig. 6.11 shows screenshots of the ProcessOR. The green dots represent the position of the detected feature points.

The whole pipeline has be tested on human patients data registered during laparoscopic hepatectomies. As *in-vivo* a direct quantitative evaluation

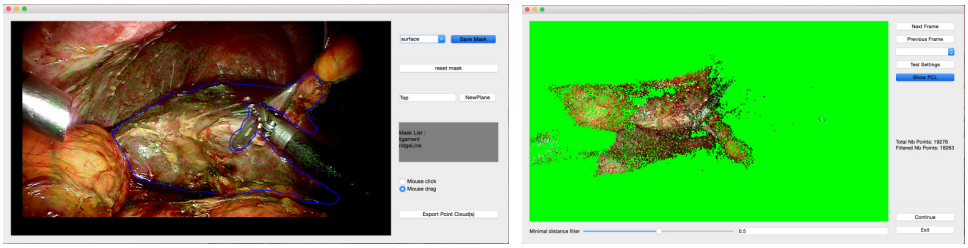

Figure 6.11: ProcessOR manual mask edition window and overview of the 3D point cloud

is not possible, we perform only a visual qualitative assessment presented in Fig. 6.12. The point cloud was accurately matched to its corresponding part onto the three-dimensional mesh and the mean Hausdorff distance between the surface mesh and the point cloud was below 1.1 mm. However, the visualization techniques were not yet included in the pipeline and thus the images are difficult to understand.

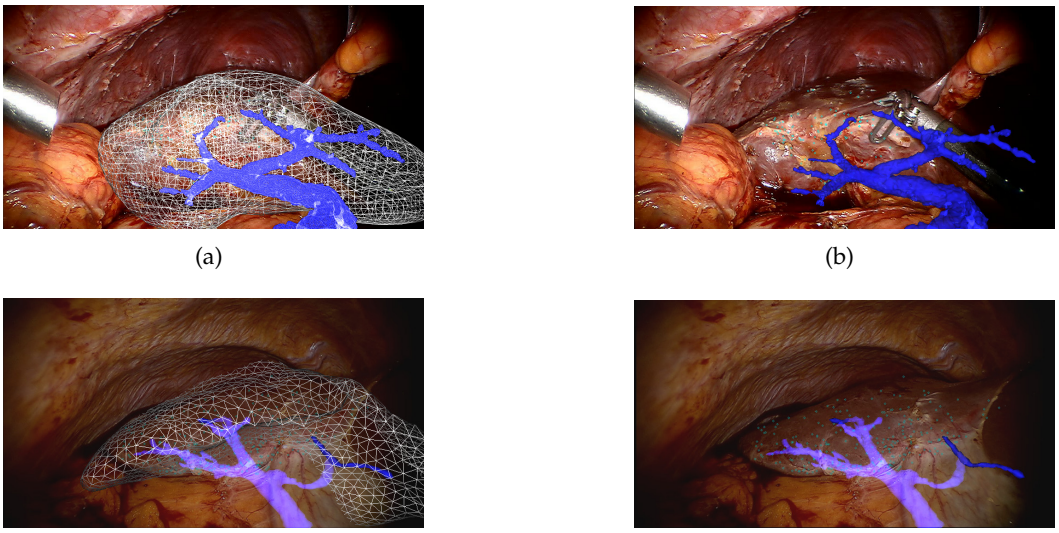

(a) (b)

(c) (d)

Figure 6.12: Non-rigid registration between intra-operative and pre-operative data using *in-vivo* human data. The overlay of the liver surface and the vascular network permits to guide surgeon during the operation.

6.5 Discussion

In this chapter we presented a complete pipeline for augmented reality guidance during laparoscopic surgery. This pipeline is compatible with the operating room environment thanks to its compactness and the limited

interaction required from the medical team and with the medical devices. The overall time needed to obtain an augmented view of the liver is below 5 minutes, and the subsequent registrations are much faster. This is far less than the time required for three-dimensional intra-operative imaging techniques, and thus reasonable of an intra-operative use.

The validation on real data is difficult due to the lack of ground truth data. The only measure that can be used is the dice measure, but since the liver may be partially hided by other abdominal organs, the dice values are not very informative.

The quality of the reconstructed point cloud is very important for the registration result. This quality depends on several factors such as the liver texture or the cleanliness of the camera lens but also on the calibration matrix. Only an accurate calibration matrix allows for a correct depth estimation of the feature points. However, obtaining an accurate calibration matrix for a laparoscopic camera is non-trivial, and the matrix may change from on operation to another due to the sterilization process. Therefore, additional work is required to ensure the accuracy of a calibration matrix before an operation and to determine whether or not the camera intrinsic parameters are stable over time.

Conclusion

In this work, we have developed an automatic method to align pre-operative data of the liver onto a laparoscopic view while introducing very little changes in the clinical routine. Only the laparoscopic view and the pre-operative medical images are required as input data. From segmented pre-operative images, a biomechanical model of the patient's liver is automatically generated, and a three dimensional point cloud is reconstructed automatically from the stereoscopic laparoscopic view. This information is the input of a robust registration method based on the biomechanical model and anatomical landmarks to reduce the set of acceptable transformations. The anatomical landmarks are defined automatically via a statistical atlas on the pre-operative mesh and segmented manually using an intuitive interface in the intra-operative images. The tests performed show that the method reaches a clinically acceptable accuracy (mean TRE below 3.5 mm in all tested scenarios where at least 30% of the liver surface is visible), and is robust to noise and poor initial alignment. In addition, the computational time of the complete intra-operative pipeline (<5 min), which includes the laparoscopic images segmentation, the point cloud reconstruction and the registration, is compatible with the deployment of the method in the operating room. Once the initialization is performed subsequent registrations are faster thanks to the knowledge of boundary conditions transferred to the patient specific model from the statistical atlas.

The current method remains however sensitive to the amount of visible surface and the quality of its reconstruction. Obtaining a sufficiently dense and smooth reconstructed surface, which corresponds to more than 30% of the whole liver surface is challenging. Thus, methods which improve the accuracy of the point cloud reconstruction as well as the amount of surface which is reconstructed should be investigated. To improve the quality of the reconstruction, the triangulation method could be combined with other reconstruction algorithms such as shape from shading or structured light methods. On the other hand, shape from motion techniques can be used to increase the amount of surface reconstructed from the laparoscopic view. Monocular structure from motion methods perform poorly on laparoscopic data, but the use of a stereoscopic endoscope offers the possibility to employ stitching methods to obtain a broader surface reconstruction from several

reconstructed point clouds.

Ultimately, the goal of the IGS system presented in this work is to provide the location of the internal structures of the liver. Therefore, the accuracy of the registration inside the liver volume is crucial. From surface information only, the task is very challenging, and even if the registration method proposed in this work reaches a reasonable accuracy, in-depth information could improve the localization of internal structures. Laparoscopic ultrasound probe, being an inexpensive and safe imaging modality, could be used to obtain in-depth information to enrich the intra-operative input of the registration method. In particular, as the liver is a highly vascularized organ, the ultrasound probe can be used to localize vessels bifurcations providing additional landmarks for the registration method. To do so, the position in the laparoscopic camera reference frame of the anatomical structures present in the ultrasound images should be known. This requires both the calibration of the ultrasound probe and a mean to obtain the probe position relatively to the laparoscope, which are two challenging problems.

The statistical atlas proposed for the automatic identification of the liver boundary conditions in a patient specific mesh is not entirely mature. It does not contain all the liver boundary conditions due to the limitation of the imaging modality used to generate the atlas data set. In addition, as the number of present subjects in the atlas is limited, advanced statistical tools cannot be employed. New protocols or other imaging modalities could be used to enrich the atlas, but alternatives approaches can be employed to identify the boundary conditions on a patient specific liver. Data assimilation and elastography seems to be the most promising methods that could allow a fast patient specific determination of the boundary conditions. In the proposed method, the knowledge of the liver boundary condition allows for an easier and faster registration of pre-operative data on the intra-operative view once an accurate initialization is known. However, the estimated location of the boundary conditions could be combined with data assimilation techniques and the registration method presented in this work to obtain the intra-operative shape of the liver.

One of the main limitations to the development of new registration methods for IGS systems is the difficulty to have ground truth data sets to validate and improve the registration algorithms. This is especially true

for laparoscopic guidance systems as intra-operative imaging devices are rarely available during the interventions and that realistic phantoms which can mimic pneumoperitoneum deformation do not exist. Synthetic data are an interesting alternative, but cannot account fully for the real environment complexity. Therefore, the development of new phantoms and the sharing of data sets should be addressed in the future.

Throughout this thesis, we tried to answer a challenging problem for which accuracy and robustness are key requirements. To further improve these two aspects, additional intra-operative information could certainly prove helpful. The different methods we have proposed can be applied in other contexts, and in particular to problems with less constraints on the input data. As a consequence, we believe that a next step is the extension of our approach to benefit from hybrids operating rooms equipped with intra-operative imaging devices such as magnetic resonance imaging of computer tomography scanners. Such operating rooms have seen an important development over the past five years. If this trend continues, our method could be coupled with three-dimensional intra-operative imaging to attain a higher accuracy and improved robustness, but with the ability to function also in less exclusive environments.

List of publications

Journal papers

- [Plantefève *et al.* (2016)] R. Plantefève, I. Peterlik, N. Haouchine and S. Cotin. **Patient-Specific Biomechanical Modeling for Guidance During Minimally-Invasive Hepatic Surgery**. Annals of biomedical engineering, vol. 44, no. 1, pages 139–153, 2016

Conference papers

- [Plantefève *et al.* (2014b)] R. Plantefève, I. Peterlik, H. Courtecuisse, R. Trivisonne, J.-P. Radoux and S. Cotin. **Atlas-based transfer of boundary conditions for biomechanical simulation**. In **Medical Image Computing and Computer-Assisted Intervention–MICCAI 2014**, pages 33–40, Springer, 2014b

- [Plantefève *et al.* (2014a)] R. Plantefève, N. Haouchine, J.-P. Radoux and S. Cotin. **Automatic Alignment of pre and intraoperative Data using Anatomical Landmarks for Augmented Laparoscopic Liver Surgery**. In **Biomedical Simulation**, pages 58–66, Springer, 2014a

- [Marques *et al.* (2015a)] B. Marques, N. Haouchine, R. Plantefève and S. Cotin. **Improving depth perception during surgical augmented reality**. In **ACM SIGGRAPH 2015 Posters**, page 24, ACM, 2015a

- [Marques *et al.* (2015b)] B. Marques, R. Plantefève, F. Roy, N. Haouchine, E. Jeanvoine, I. Peterlik and S. Cotin. **Framework for Augmented Reality in Minimally Invasive Laparoscopic Surgery**. In **Proceedings of iOR15: 1st International Workshop on Intelligent Operating Rooms, 17th International Conference on E-health Networking, Application Services (IEEE Healthcom 2015)**, Boston, 2015b

Other

- [Al-Sarray *et al.* (2013)] B. Al-Sarray, B. Bogosel, E. Dalissier, J.-M. Etancelin, J.-K. Günther and R. Plantefève. **Représentation des fonctions de réponse radiométrique**. Semaine d'Etude Mathématiques et Entreprises, vol. 6, 2013 (in french)

Bibliography

[Mev] **MEVIS**. http://www.mevis.de/, accessed: 2016-01-20.

[NHC] **Nouvel Hôpital Civil. 1, place de l'hôpital, 67091 Strasbourg, FRANCE**.

[WHO] **World Health Organization**. http://www.who.int, accessed: 2015-12-06.

[Ackerman *et al.*, 2002] J. D. Ackerman, K. Keller and H. Fuchs. **Surface reconstruction of abdominal organs using laparoscopic structured light for augmented reality**. In **Electronic Imaging 2002**, pages 39–46, International Society for Optics and Photonics, 2002.

[Ahmadian and Zamani, 2009] H. Ahmadian and A. Zamani. **Identification of nonlinear boundary effects using nonlinear normal modes**. Mech. Systems and Signal Proc., vol. 23, no. 6, pages 2008–2018, 2009, ISSN 0888-3270.

[Ahmadian *et al.*, 2001] H. Ahmadian, J. Mottershead and M. Friswell. **Boundary condition identification by solving characteristic equations**. J. of Sound and Vibration, vol. 247, no. 5, pages 755–763, 2001, ISSN 0022-460X.

[Al-Sarray *et al.*, 2013] B. Al-Sarray, B. Bogosel, E. Dalissier, J.-M. Etancelin, J.-K. Günther and R. Plantefève. **Représentation des fonctions de réponse radiométrique**. Semaine d'Etude Mathématiques et Entreprises, vol. 6, 2013.

[Alliez *et al.*, 2005] P. Alliez, D. Cohen-Steiner, M. Yvinec and M. Desbrun. **Variational tetrahedral meshing**. ACM Transactions on Graphics (TOG), vol. 24, no. 3, pages 617–625, 2005.

[Alliez *et al.*, 2015] P. Alliez, C. Jamin, L. Rineau, S. Tayeb, J. Tournois and M. Yvinec. **3D Mesh Generation**. In **CGAL User and Reference Manual**, CGAL Editorial Board, 4.7 ed., 2015.

[Altamar *et al.*, 2011] H. O. Altamar, R. E. Ong, C. L. Glisson, D. P. Viprakasit, M. I. Miga, S. D. Herrell and R. L. Galloway. **Kidney deformation and intraprocedural registration: a study of elements of image-guided kidney surgery**. Journal of Endourology, vol. 25, no. 3, pages 511–517, 2011.

[Amiot *et al.*, 1995] L.-P. Amiot, H. Labelle, J. A. DeGuise, M. Sati, C.-H. Rivard *et al.*. **Computer-Assisted Pedicle Screw Fixation-A Feasibility Study.** Spine, vol. 20, no. 10, pages 1208–1212, 1995.

[Audette *et al.*, 2003] M. A. Audette, K. Siddiqi, F. P. Ferrie and T. M. Peters. **An integrated range-sensing, segmentation and registration framework for the characterization of intra-surgical brain deformations in image-guided surgery**. Computer Vision and Image Understanding, vol. 89, no. 2, pages 226–251, 2003.

[Babuška and Aziz, 1976] I. Babuška and A. K. Aziz. **On the angle condition in the finite element method**. SIAM Journal on Numerical Analysis, vol. 13, no. 2, pages 214–226, 1976.

[Baecker] J. Baecker. **Projection on an image plane**. https://commons.wikimedia.org/wiki/File:Zentralprojektion.jpg, accessed: 2015-12-31.

[Bano *et al.*, 2013] J. Bano, S. A. Nicolau, A. Hostettler, C. Doignon, J. Marescaux and L. Soler. **Registration of preoperative liver model for laparoscopic surgery from intraoperative 3d acquisition**. In **Augmented Reality Environments for Medical Imaging and Computer-Assisted Interventions**, pages 201–210, Springer, 2013.

[Banz *et al.*, 2014] V. M. Banz, M. Baechtold, S. Weber, M. Peterhans, D. Inderbitzin and D. Candinas. **Computer planned, image-guided combined resection and ablation for bilobar colorectal liver metastases**. World journal of gastroenterology: WJG, vol. 20, no. 40, page 14,992, 2014.

[Baraff and Witkin, 1998] D. Baraff and A. Witkin. **Large Steps in Cloth Simulation**. In **Proceedings of the 25th Annual Conference on Computer Graphics and Interactive Techniques**, SIGGRAPH '98, pages 43–54, ACM, New York, NY, USA, 1998, ISBN 0-89791-999-8.

[Bardinet *et al.*, 1996] E. Bardinet, L. D. Cohen and N. Ayache. **Tracking and motion analysis of the left ventricle with deformable superquadrics**. Medical image analysis, vol. 1, no. 2, pages 129–149, 1996.

[Bardinet *et al.*, 2009] E. Bardinet, M. Bhattacharjee, D. Dormont, B. Pidoux, G. Malandain, M. Schupbach, N. Ayache, P. Cornu, Y. Agid and J. Yelnik. **A three-dimensional histological atlas of the human basal ganglia. Atlas deformation strategy and evaluation in deep brain stimulation for Parkinson disease**. J. of Neurosurgery, vol. 110, no. 2, 2009.

[Baumhauer *et al.*, 2008] M. Baumhauer, T. Simpfendörfer, B. P. Müller-Stich, D. Teber, C. N. Gutt, J. Rassweiler, H.-P. Meinzer and I. Wolf. **Soft tissue navigation for laparoscopic partial nephrectomy**. International Journal of Computer Assisted Radiology and Surgery, vol. 3, no. 3-4, pages 307–314, 2008.

[Bay *et al.*, 2006] H. Bay, T. Tuytelaars and L. Van Gool. **Surf: Speeded up robust features**. In **Computer vision–ECCV 2006**, pages 404–417, Springer, 2006.

[Bažant and Cedolin, 2010] Z. P. Bažant and L. Cedolin. **Stability of structures: elastic, inelastic, fracture and damage theories**. World Scientific, 2010.

[Belhaoua *et al.*, 2016] A. Belhaoua, J. Moreau, A. Krebs, J. Waechter, J.-P. Radoux and J. Marescaux. **Multiple video sequences synchronization during minimally invasive surgery**. pages 97,861S–97,861S–9, 2016.

[Besl and McKay, 1992] P. J. Besl and N. D. McKay. **Method for registration of 3-D shapes**. In **Robotics-DL tentative**, pages 586–606, International Society for Optics and Photonics, 1992.

[Boltcheva *et al.*, 2009] D. Boltcheva, M. Yvinec and J.-D. Boissonnat. **Mesh generation from 3d multi-material images**. In **Medical Image Computing and Computer-Assisted Intervention–MICCAI 2009**, pages 283–290, Springer, 2009.

[Bookstein, 1991] F. L. Bookstein. **Thin-plate splines and the atlas problem for biomedical images**. In **Information Processing in Medical Imaging**, pages 326–342, Springer, 1991.

[Brandner *et al.*, 2006] E. D. Brandner, A. Wu, H. Chen, D. Heron, S. Kalnicki, K. Komanduri, K. Gerszten, S. Burton, I. Ahmed and Z. Shou. **Abdominal organ motion measured using 4D CT**. International Journal of Radiation Oncology* Biology* Physics, vol. 65, no. 2, pages 554–560, 2006.

[Brock *et al.*, 2005] K. Brock, M. Sharpe, L. Dawson, S. Kim and D. Jaffray. **Accuracy of finite element model-based multi-organ deformable image registration**. Med Physics, vol. 32, no. 6, 2005, ISSN 00942405.

[Broit, 1981] C. Broit. **Optimal registration of deformed images**. Ph.D. thesis, University of Pennsylvania, 1981.

[Bucki *et al.*, 2012] M. Bucki, O. Palombi, M. Bailet and Y. Payan. **Doppler ultrasound driven biomechanical model of the brain for intraoperative brain-shift compensation: a proof of concept in clinical conditions**. In **Soft tissue biomechanical modeling for computer assisted surgery**, pages 135–165, Springer, 2012.

[Campadelli *et al.*, 2009] P. Campadelli, E. Casiraghi and A. Esposito. **Liver segmentation from computed tomography scans: A survey and a new algorithm**. Artificial Intelligence in Medicine, vol. 45, no. 2, pages 185–196, 2009.

[Carey and Oden, 1984] G. F. Carey and J. T. Oden. **Finite elements. 3. Computational aspects**. Prentice-Hall, 1984.

[Cash *et al.*, 2005] D. M. Cash, M. I. Miga, T. K. Sinha, R. L. Galloway and W. C. Chapman. **Compensating for intraoperative soft-tissue deformations using incomplete surface data and finite elements**. Medical Imaging, IEEE Transactions on, vol. 24, no. 11, pages 1479–1491, 2005.

[Cash *et al.*, 2007] D. M. Cash, M. I. Miga, S. C. Glasgow, B. M. Dawant, L. W. Clements, Z. Cao, R. L. Galloway and W. C. Chapman. **Concepts and preliminary data toward the realization of image-guided liver surgery**. Journal of Gastrointestinal Surgery, vol. 11, no. 7, pages 844–859, 2007.

[Chen, 2004] L. Chen. **Mesh smoothing schemes based on optimal Delaunay triangulations**. Proceedings of 13th International Meshing Roundtable, pages 109–120, 2004.

[Cheng *et al.*, 2000] S.-W. Cheng, T. K. Dey, H. Edelsbrunner, M. A. Facello and S.-H. Teng. **Silver exudation**. Journal of the ACM (JACM), vol. 47, no. 5, pages 883–904, 2000.

[Cheung *et al.*, 2010] C. L. Cheung, C. Wedlake, J. Moore, S. E. Pautler and T. M. Peters. **Fused video and ultrasound images for minimally invasive partial nephrectomy: a phantom study**. In **Medical Image Computing and Computer-Assisted Intervention–MICCAI 2010**, pages 408–415, Springer, 2010.

[Christensen *et al.*, 1996] G. E. Christensen, R. D. Rabbitt and M. I. Miller. **Deformable templates using large deformation kinematics**. Image Processing, IEEE Transactions on, vol. 5, no. 10, pages 1435–1447, 1996.

[Chu and Dupuy, 2014] K. F. Chu and D. E. Dupuy. **Thermal ablation of tumours: biological mechanisms and advances in therapy**. Nature Reviews Cancer, vol. 14, no. 3, pages 199–208, 2014.

[Chui and Rangarajan, 2003] H. Chui and A. Rangarajan. **A new point matching algorithm for non-rigid registration**. Computer Vision and Image Understanding, vol. 89, no. 2, pages 114–141, 2003.

[Clatz *et al.*, 2005] O. Clatz, H. Delingette, I.-F. Talos, A. J. Golby, R. Kikinis, F. A. Jolesz, N. Ayache and S. K. Warfield. **Robust nonrigid registration to capture brain shift from intraoperative MRI**. Medical Imaging, IEEE Transactions on, vol. 24, no. 11, pages 1417–1427, 2005.

[Clements *et al.*, 2006] L. W. Clements, D. M. Cash, W. C. Chapman, R. L. Galloway Jr and M. I. Miga. **Robust surface registration using salient anatomical features in image-guided liver surgery**. In **Medical Imaging**, pages 61,410E–61,410E, International Society for Optics and Photonics, 2006.

[Collins *et al.*, 2011] T. Collins, B. Compte and A. Bartoli. **Deformable shape-from-motion in laparoscopy using a rigid sliding window**. In **Medical Image Understanding and Analysis Conference**, 2011.

[Couinaud, 1957] C. Couinaud. **Le foie: études anatomiques et chirurgicales**. Masson & Cie, 1957.

[Dagher *et al.*, 2007] I. Dagher, J. Proske, A. Carloni, H. Richa, H. Tranchart and D. Franco. **Laparoscopic liver resection: results for 70 patients**. Surgical endoscopy, vol. 21, no. 4, pages 619–624, 2007.

[Dauguet *et al.*, 2009] J. Dauguet, A.-S. Hérard, J. O. Declerck and T. Delzescaux. **Locally constrained cubic b-spline deformations to control volume variations**. In **Biomedical Imaging: From Nano to Macro, 2009. ISBI'09. IEEE International Symposium on**, pages 983–986, IEEE, 2009.

[Davatzikos, 1997] C. Davatzikos. **Spatial transformation and registration of brain images using elastically deformable models**. Computer Vision and Image Understanding, vol. 66, no. 2, pages 207–222, 1997.

[Davis *et al.*, 1997] M. H. Davis, A. Khotanzad, D. P. Flamig and S. E. Harms. **A physics-based coordinate transformation for 3-D image matching**. Medical Imaging, IEEE Transactions on, vol. 16, no. 3, pages 317–328, 1997.

[Delaunay, 1934] B. Delaunay. **Sur la sphere vide**. Izv. Akad. Nauk SSSR, Otdelenie Matematicheskii i Estestvennyka Nauk, vol. 7, no. 793-800, pages 1–2, 1934.

[Deurloo *et al.*, 2005] K. E. Deurloo, R. J. Steenbakkers, L. J. Zijp, J. A. de Bois, P. J. Nowak, C. R. Rasch and M. van Herk. **Quantification of shape variation of prostate and seminal vesicles during external beam radiotherapy**. International Journal of Radiation Oncology* Biology* Physics, vol. 61, no. 1, pages 228–238, 2005.

[DiMaio *et al.*, 2007] S. DiMaio, S. Pieper, K. Chinzei, N. Hata, S. Haker, D. Kacher, G. Fichtinger, C. Tempany and R. Kikinis. **Robot-assisted needle placement in open MRI: system architecture, integration and validation**. Computer Aided Surgery, vol. 12, no. 1, pages 15–24, 2007.

[Dos Santos *et al.*, 2014] T. R. Dos Santos, A. Seitel, T. Kilgus, S. Suwelack, A.-L. Wekerle, H. Kenngott, S. Speidel, H.-P. Schlemmer, H.-P. Meinzer, T. Heimann *et al.*. **Pose-independent surface matching for intra-operative soft-tissue marker-less registration**. Medical image analysis, vol. 18, no. 7, pages 1101–1114, 2014.

[Doyley and Parker, 2014] M. M. Doyley and K. J. Parker. **Elastography: general principles and clinical applications**. Ultrasound clinics, vol. 9, no. 1, pages 1–11, 2014.

[Du *et al.*, 1999] Q. Du, V. Faber and M. Gunzburger. **Centroidal Voronoi tessellations: applications and algorithms**. SIAM review, vol. 41, no. 4, pages 637–676, 1999.

[Duriez *et al.*, 2006] C. Duriez, S. Cotin, J. Lenoir and P. Neumann. **New approaches to catheter navigation for interventional radiology simulation**. Computer Aided Surgery, vol. 11, no. 6, pages 300–308, 2006.

[EASL] EASL. **European Association for the Study of the Liver**. `http://www.easl.eu`, accessed: 2015-12-06.

[Edgcumbe *et al.*, 2014] P. Edgcumbe, P. Pratt, G.-Z. Yang, C. Nguan and R. Rohling. **Pico lantern: A pick-up projector for augmented reality in laparoscopic surgery**. In **Medical Image Computing and Computer-Assisted Intervention–MICCAI 2014**, pages 432–439, Springer, 2014.

[Edgcumbe *et al.*, 2015] P. Edgcumbe, P. Pratt, G.-Z. Yang, C. Nguan and R. Rohling. **Pico Lantern: Surface Reconstruction and Augmented Reality in Laparoscopic Surgery Using a Pick-Up Laser Projector**. Medical Image Analysis, 2015.

[Edwards *et al.*, 1995] P. Edwards, D. Hawkes, D. Hill, D. Jewell, R. Spink, A. Strong and M. Gleeson. **Augmentation of reality using an operating microscope for otolaryngology and neurosurgical guidance**. Computer Assisted Surgery (formerly Journal of image guided surgery), vol. 1, no. 3, pages 172–178, 1995.

[Edwards *et al.*, 2000] P. J. Edwards, A. P. King, C. R. Maurer Jr, D. A. De Cunha, D. J. Hawkes, D. L. Hill, R. P. Gaston, M. R. Fenlon, A. Jusczyzck, A. J. Strong *et al.*. **Design and evaluation of a system for microscope-assisted guided interventions (MAGI)**. Medical Imaging, IEEE Transactions on, vol. 19, no. 11, pages 1082–1093, 2000.

[Ellsmere *et al.*, 2003] J. Ellsmere, J. Stoll, D. Rattner, D. Brooks, R. Kane, W. Wells, R. Kikinis and K. Vosburgh. **A navigation system for augmenting laparoscopic ultrasound**. In **Medical Image Computing and Computer-Assisted Intervention-MICCAI 2003**, pages 184–191, Springer, 2003.

[Feldmar *et al.*, 1995] J. Feldmar, N. Ayache and F. Betting. **3D-2D projective registration of free-form curves and surfaces**. In **Computer Vision, 1995. Proceedings., Fifth International Conference on**, pages 549–556, IEEE, 1995.

[Felippa, 2003] C. A. Felippa. **A study of optimal membrane triangles with drilling freedoms**. Computer Methods in Applied Mechanics and Engineering, vol. 192, no. 16, pages 2125–2168, 2003.

[Ferrant *et al.*, 2001] M. Ferrant, A. Nabavi, B. Macq, F. a. Jolesz, R. Kikinis and S. K. Warfield. **Registration of 3-D intraoperative MR images of the brain using a finite-element biomechanical model**. IEEE Trans. on Medical Imaging, vol. 20, no. 12, pages 1384–1397, 2001, ISSN 0278-0062.

[Feuerstein *et al.*, 2007] M. Feuerstein, T. Mussack, S. M. Heining and N. Navab. **Registration-free laparoscope augmentation for intra-operative liver resection planning**. In **Proceedings of SPIE**, pages 650,915–650,915, 2007.

[Fleute and Lavallée, 1998] M. Fleute and S. Lavallée. **Building a complete surface model from sparse data using statistical shape models: Application to computer assisted knee surgery**. In **Medical Image Computing and Computer-Assisted Interventation—MICCAI'98**, pages 879–887, Springer, 1998.

[Fusaglia *et al.*, 2015] M. Fusaglia, H. Hess, M. Schwalbe, M. Peterhans, P. Tinguely, S. Weber and H. Lu. **A clinically applicable laser-based image-guided system for laparoscopic liver procedures**. International journal of computer assisted radiology and surgery, pages 1–15, 2015.

[Gagner *et al.*, 2004] M. Gagner, T. Rogula and D. Selzer. **Laparoscopic liver resection: benefits and controversies**. Surgical Clinics of North America, vol. 84, no. 2, pages 451–462, 2004.

[Gennisson *et al.*, 2013] J.-L. Gennisson, T. Deffieux, M. Fink and M. Tanter. **Ultrasound elastography: principles and techniques**. Diagnostic and interventional imaging, vol. 94, no. 5, pages 487–495, 2013.

[Gosz, 2005] M. R. Gosz. **Finite element method: Applications in solids, structures, and heat transfer**. CRC Press, 2005.

[Gray, 1918] H. Gray. **Anatomy of the human body**. Lea & Febiger, 1918.

[Groeschl *et al.*, 2014] R. T. Groeschl, C. H. Pilgrim, E. M. Hanna, K. A. Simo, R. Z. Swan, D. Sindram, J. B. Martinie, D. A. Iannitti, M. Bloomston, C. Schmidt *et al.*. **Microwave ablation for hepatic malignancies: a multiinstitutional analysis**. Annals of surgery, vol. 259, no. 6, pages 1195–1200, 2014.

[Gronningsaeter *et al.*, 2000] A. Gronningsaeter, A. Kleven, S. Ommedal, T. E. Aarseth, T. Lie, F. Lindseth, T. Langø and G. Unsgård. **SonoWand, an ultrasound-based neuronavigation system**. Neurosurgery, vol. 47, no. 6, pages 1373–1380, 2000.

[Gruen *et al.*, 2002] A. Gruen *et al.*. **Calibration and orientation of cameras in computer vision**, vol. 13. IOP Publishing, 2002.

[Haar, 1910] A. Haar. **Zur Theorie der orthogonalen Funktionensysteme**. Mathematische Annalen, vol. 69, no. 3, pages 331–371, 1910, ISSN 0025-5831.

[Haouchine, 2015] N. Haouchine. **Image-guided Simulation for Augmented Reality during Hepatic Surgery**. Ph.D. thesis, Université de Lille1, 2015.

[Haouchine *et al.*, 2013] N. Haouchine, J. Dequidt, I. Peterlik, E. Kerrien, M.-O. Berger and S. Cotin. **Image-guided simulation of heterogeneous tissue deformation for augmented reality during hepatic surgery**. In **Mixed and Augmented Reality (ISMAR), 2013 IEEE International Symposium on**, pages 199–208, IEEE, 2013.

[Hartley and Zisserman, 2003] R. Hartley and A. Zisserman. **Multiple view geometry in computer vision**. Cambridge university press, 2003.

[Hawkes *et al.*, 2005] D. J. Hawkes, D. Barratt, J. M. Blackall, C. Chan, P. J. Edwards, K. Rhode, G. P. Penney, J. McClelland and D. L. Hill. **Tissue deformation and shape models in image-guided interventions: a discussion paper**. Medical Image Analysis, vol. 9, no. 2, pages 163–175, 2005.

[Heimann and Meinzer, 2009] T. Heimann and H.-P. Meinzer. **Statistical shape models for 3D medical image segmentation: a review**. Medical image analysis, vol. 13, no. 4, pages 543–563, 2009.

[Heinrich *et al.*, 2012] M. P. Heinrich, M. Jenkinson, M. Bhushan, T. Matin, F. V. Gleeson, M. Brady and J. A. Schnabel. **MIND: Modality independent neighbourhood descriptor for multi-modal deformable registration**. Medical Image Analysis, vol. 16, no. 7, pages 1423–1435, 2012.

[Hipwell *et al.*, 2002] J. H. Hipwell, G. P. Penney, T. C. Cox, J. V. Byrne and D. J. Hawkes. **2D-3D intensity based registration of DSA and MRA-a comparison of similarity measures**. In **Medical Image Computing and Computer-Assisted Intervention—MICCAI 2002**, pages 501–508, Springer, 2002.

[Horton *et al.*, 2007] A. Horton, A. Wittek and K. Miller. **Subject-specific biomechanical simulation of brain indentation using a meshless method**. In **Medical Image Computing and Computer-Assisted Intervention–MICCAI 2007**, pages 541–548, Springer, 2007.

[Hsieh, 2009] J. Hsieh. **Computed tomography: principles, design, artifacts, and recent advances**. SPIE Bellingham, WA, 2009.

[Hu, 2014] K.-Q. Hu. **Advances in clinical application of cryoablation therapy for hepatocellular carcinoma and metastatic liver tumor**. Journal of clinical gastroenterology, vol. 48, no. 10, pages 830–836, 2014.

[Hu *et al.*, 2007] M. Hu, G. Penney, P. Edwards, M. Figl and D. J. Hawkes. **3D reconstruction of internal organ surfaces for minimal invasive surgery**. In **Medical Image Computing and Computer-Assisted Intervention–MICCAI 2007**, pages 68–77, Springer, 2007.

[Hu *et al.*, 2012] Y. Hu, H. U. Ahmed, Z. Taylor, C. Allen, M. Emberton, D. Hawkes and D. Barratt. **MR to ultrasound registration for image-guided prostate interventions**. Medical image analysis, vol. 16, no. 3, pages 687–703, 2012.

[Huang *et al.*, 2009] X. Huang, J. Moore, G. Guiraudon, D. L. Jones, D. Bainbridge, J. Ren and T. M. Peters. **Dynamic 2D ultrasound and 3D CT image registration of the beating heart**. Medical Imaging, IEEE Transactions on, vol. 28, no. 8, pages 1179–1189, 2009.

[INC] INC. **Incidence et mortalité estimées des cancers en France métropolitaine en 2012**. `http://lesdonnees.e-cancer.fr`, accessed: 2016-01-04.

[Jafari *et al.*, 2015] M. D. Jafari, M. J. Stamos and S. Mills. **Patient Positioning, Instrumentation, and Trocar Placement**. In **Minimally Invasive Approaches to Colon and Rectal Disease**, pages 15–24, Springer, 2015.

[Ji *et al.*, 2001] H. Ji, J. D. McTavish, K. J. Mortele, W. Wiesner and P. R. Ros. **Hepatic Imaging with Multidetector CT 1**. Radiographics, vol. 21, no. suppl_1, pages S71–S80, 2001.

[Kalender, 2006] W. A. Kalender. **X-ray computed tomography**. Physics in medicine and biology, vol. 51, no. 13, page R29, 2006.

[Kass *et al.*, 1988] M. Kass, A. Witkin and D. Terzopoulos. **Snakes: Active contour models**. International journal of computer vision, vol. 1, no. 4, pages 321–331, 1988.

[Kingham *et al.*, 2012] T. P. Kingham, M. A. Scherer, B. W. Neese, L. W. Clements, J. D. Stefansic and W. R. Jarnagin. **Image-guided liver surgery: intraoperative projection of computed tomography images utilizing tracked ultrasound**. HPB, vol. 14, no. 9, pages 594–603, 2012.

[Kingham *et al.*, 2013] T. P. Kingham, S. Jayaraman, L. W. Clements, M. A. Scherer, J. D. Stefansic and W. R. Jarnagin. **Evolution of image-guided liver surgery: transition from open to laparoscopic procedures**. Journal of Gastrointestinal Surgery, vol. 17, no. 7, pages 1274–1282, 2013.

[Landreau *et al.*, 2015] P. Landreau, A. Drouillard, G. Launoy, P. Ortega-Deballon, V. Jooste, C. Lepage, J. Faivre, O. Facy and A.-M. Bouvier. **Incidence and survival in late liver metastases of colorectal cancer**. Journal of gastroenterology and hepatology, vol. 30, no. 1, pages 82–85, 2015.

[Lange *et al.*, 2003] T. Lange, S. Eulenstein, M. Hünerbein and P.-M. Schlag. **Vessel-based non-rigid registration of MR/CT and 3D ultrasound for navigation in liver surgery**. Computer Aided Surgery, vol. 8, no. 5, pages 228–240, 2003.

[Lange *et al.*, 2009] T. Lange, N. Papenberg, S. Heldmann, J. Modersitzki, B. Fischer, H. Lamecker and P. M. Schlag. **3D ultrasound-CT registration of the liver using combined landmark-intensity information**. International journal of computer assisted radiology and surgery, vol. 4, no. 1, pages 79–88, 2009.

[Langø *et al.*, 2012] T. Langø, S. Vijayan, A. Rethy, C. Våpenstad, O. V. Solberg, R. Mårvik, G. Johnsen and T. N. Hernes. **Navigated laparoscopic ultrasound in abdominal soft tissue surgery: technological overview and perspectives**. International journal of computer assisted radiology and surgery, vol. 7, no. 4, pages 585–599, 2012.

[Lavallée and Szeliski, 1995] S. Lavallée and R. Szeliski. **Recovering the position and orientation of free-form objects from image contours using 3D distance maps**. Pattern Analysis and Machine Intelligence, IEEE Transactions on, vol. 17, no. 4, pages 378–390, 1995.

[Lawonn *et al.*, 2015] K. Lawonn, M. Luz, B. Preim and C. Hansen. **Illustrative Visualization of Vascular Models for Static 2D Representations**. In **Medical Image Computing and Computer-Assisted Intervention–MICCAI 2015**, pages 399–406, Springer, 2015.

[Le Treut *et al.*, 2005] Y. P. Le Treut, J. Hardwigsen and S. Garcia. **Tumeurs du foie, primitives et secondaires**. 2005.

[Lemieux *et al.*, 1994] L. Lemieux, R. Jagoe, D. Fish, N. Kitchen and D. Thomas. **A patient-to-computed-tomography image registration method based on digitally reconstructed radiographs**. Medical physics, vol. 21, no. 11, pages 1749–1760, 1994.

[Leroy *et al.*, 2006] A. Leroy, P. Mozer, P. Conort, E. Chartier-Kastler, F. Richard, Y. Payan and J. Troccaz. **3D evaluation of kidney movement during respiration using 2.5 D ultrasound**. In **Engineering and Urology Society–Annual Meeting**, 2006.

[Leroy *et al.*, 2007] A. Leroy, P. Mozer, Y. Payan and J. Troccaz. **Intensity-based registration of freehand 3D ultrasound and CT-scan images of the kidney**. International journal of computer assisted radiology and surgery, vol. 2, no. 1, pages 31–41, 2007.

[Letteboer *et al.*, 2005] M. M. Letteboer, P. W. Willems, M. A. Viergever and W. J. Niessen. **Brain shift estimation in image-guided neurosurgery using 3-D ultrasound**. Biomedical Engineering, IEEE Transactions on, vol. 52, no. 2, pages 268–276, 2005.

[Liu and Quek, 2013] G.-R. Liu and S. S. Quek. **The finite element method: a practical course**. Butterworth-Heinemann, 2013.

[Lourenço *et al.*, 2014] M. Lourenço, D. Stoyanov and J. P. Barreto. **Visual odometry in stereo endoscopy by using PEARL to handle partial scene deformation**. In **Augmented Environments for Computer-Assisted Interventions**, pages 33–40, Springer, 2014.

[Lowe, 2004] D. G. Lowe. **Distinctive image features from scale-invariant keypoints**. International journal of computer vision, vol. 60, no. 2, pages 91–110, 2004.

[Luboz *et al.*, 2012] V. Luboz, E. Promayon, G. Chagnon, T. Alonso, D. Favier, C. Barthod and Y. Payan. **Validation of a Light Aspiration device for in vivo Soft TIssue Characterization (LASTIC)**. In **Soft Tissue Biomechanical Modeling for Computer Assisted Surgery**, pages 243–256, Springer, 2012.

[Ma *et al.*, 2010] Z. Ma, J. M. R. Tavares, R. N. Jorge and T. Mascarenhas. **A review of algorithms for medical image segmentation and their applications to the female pelvic cavity**. Computer Methods in Biomechanics and Biomedical Engineering, vol. 13, no. 2, pages 235–246, 2010.

[Mahalanobis, 1936] P. C. Mahalanobis. **On the generalized distance in statistics**. Proceedings of the National Institute of Sciences (Calcutta), vol. 2, pages 49–55, 1936.

[Maier-Hein *et al.*, 2008] L. Maier-Hein, S. A. Müller, F. Pianka, S. Wörz, B. P. Müller-Stich, A. Seitel, K. Rohr, H.-P. Meinzer, B. M. Schmied and I. Wolf. **Respiratory motion compensation for CT-guided interventions in the liver**. Computer Aided Surgery, vol. 13, no. 3, pages 125–138, 2008.

[Marchant] J. Marchant. **Playing with perspectives**. https://www.flickr.com/photos/tigerzeye/169345435/, accessed: 2015-12-31.

[Marescaux *et al.*, 2004] J. Marescaux, F. Rubino, M. Arenas, D. Mutter and L. Soler. **Augmented-reality–assisted laparoscopic adrenalectomy**. Jama, vol. 292, no. 18, pages 2211–2215, 2004.

[Marques *et al.*, 2015a] B. Marques, N. Haouchine, R. Plantefève and S. Cotin. **Improving depth perception during surgical augmented reality**. In **ACM SIGGRAPH 2015 Posters**, page 24, ACM, 2015a.

[Marques *et al.*, 2015b] B. Marques, R. Plantefève, F. Roy, N. Haouchine, E. Jeanvoine, I. Peterlik and S. Cotin. **Framework for Augmented Reality in Minimally Invasive Laparoscopic Surgery**. In **Proceedings of iOR15: 1st International Workshop on Intelligent Operating Rooms, 17th International Conference on E-health Networking, Application Services (IEEE Healthcom 2015)**, Boston, 2015b.

[Mårvik *et al.*, 2004] R. Mårvik, T. Langø, G. A. Tangen, J. O. Andersen, J. H. Kaspersen, B. Ystgaard, E. Sjølie, R. Fougner, H. E. Fjøsne and T. A. Nagelhus Hernes. **Laparoscopic navigation pointer for three-dimensional image–guided surgery**. Surgical Endoscopy And Other Interventional Techniques, vol. 18, no. 8, pages 1242–1248, 2004, ISSN 1432-2218.

[Masuda and Yokoya, 1995] T. Masuda and N. Yokoya. **A robust method for registration and segmentation of multiple range images**. Computer Vision and Image Understanding, vol. 61, no. 3, pages 295–307, 1995.

[Masutani *et al.*, 1994] S. Masutani, Y. Sasaki, S. Imaoka, S. Iwamoto, I. Ohashi, M. Kameyama, T. Kabuto, O. Ishikawa, H. Furukawa, H. Koyama *et al.*. **The prognostic significance of surgical margin in liver resection of patients with hepatocellular carcinoma**. Archives of Surgery, vol. 129, no. 10, pages 1025–1030, 1994.

[Maurer Jr *et al.*, 1999] C. R. Maurer Jr, R. P. Gaston, D. L. Hill, M. J. Gleeson, M. G. Taylor, M. R. Fenlon, P. J. Edwards and D. J. Hawkes. **AcouStick:**

a tracked A-mode ultrasonography system for registration in image-guided surgery. In **Medical Image Computing and Computer-Assisted Intervention–MICCAI'99**, pages 953–962, Springer, 1999.

[Miga *et al.*, 2003] M. I. Miga, D. M. Cash, Z. Cao, R. L. Galloway Jr, B. M. Dawant and W. C. Chapman. **Intraoperative registration of the liver for image-guided surgery using laser range scanning and deformable models**. In **Medical Imaging 2003**, pages 350–359, International Society for Optics and Photonics, 2003.

[Miga *et al.*, 2011] M. I. Miga, P. Dumpuri, A. L. Simpson, J. A. Weis and W. R. Jarnagin. **The sparse data extrapolation problem: strategies for soft-tissue correction for image-guided liver surgery**. In **SPIE Medical Imaging**, pages 79,640C–79,640C, International Society for Optics and Photonics, 2011.

[Mikolajczyk and Schmid, 2005] K. Mikolajczyk and C. Schmid. **A performance evaluation of local descriptors**. Pattern Analysis and Machine Intelligence, IEEE Transactions on, vol. 27, no. 10, pages 1615–1630, 2005.

[Moretti, 1968] G. Moretti. **The importance of boundary conditions in the numerical treatment of hyperbolic equations**. Tech. rep., DTIC Document, 1968.

[Morino *et al.*, 2003] M. Morino, I. Morra, E. Rosso, C. Miglietta and C. Garrone. **Laparoscopic vs open hepatic resection: a comparative study**. Surgical Endoscopy and Other Interventional Techniques, vol. 17, no. 12, pages 1914–1918, 2003.

[Mountney and Yang, 2010] P. Mountney and G.-Z. Yang. **Motion compensated SLAM for image guided surgery**. In **Medical Image Computing and Computer-Assisted Intervention–MICCAI 2010**, pages 496–504, Springer, 2010.

[Mountney *et al.*, 2010] P. Mountney, D. Stoyanov and G.-Z. Yang. **Three-dimensional tissue deformation recovery and tracking**. Signal Processing Magazine, IEEE, vol. 27, no. 4, pages 14–24, 2010.

[Mountney *et al.*, 2014] P. Mountney, J. Fallert, S. Nicolau, L. Soler and P. W. Mewes. **An augmented reality framework for soft tissue surgery**. In **Medical Image Computing and Computer-Assisted Intervention–MICCAI 2014**, pages 423–431, Springer, 2014.

[Müller and Gross, 2004] M. Müller and M. Gross. **Interactive virtual materials**. In **Proceedings of Graphics Interface 2004**, pages 239–246, Canadian Human-Computer Communications Society, 2004.

[Nam *et al.*, 2011] W. H. Nam, D.-G. Kang, D. Lee, J. Y. Lee and J. B. Ra. **Automatic registration between 3D intra-operative ultrasound and pre-operative CT images of the liver based on robust edge matching**. Physics in medicine and biology, vol. 57, no. 1, page 69, 2011.

[Nicolau *et al.*, 2009] S. Nicolau, X. Pennec, L. Soler, X. Buy, A. Gangi, N. Ayache and J. Marescaux. **An augmented reality system for liver thermal ablation: design and evaluation on clinical cases**. Medical Image Analysis, vol. 13, no. 3, pages 494–506, 2009.

[Oktay *et al.*, 2013] O. Oktay, L. Zhang, T. Mansi, P. Mountney, P. Mewes, S. Nicolau, L. Soler and C. Chefd'hotel. **Biomechanically driven registration of pre-to intra-operative 3d images for laparoscopic surgery**. In **Medical Image Computing and Computer-Assisted Intervention–MICCAI 2013**, pages 1–9, Springer, 2013.

[Penne *et al.*, 2009] J. Penne, K. Höller, M. Stürmer, T. Schrauder, A. Schneider, R. Engelbrecht, H. Feußner, B. Schmauss and J. Hornegger. **Time-of-flight 3-D endoscopy**. In **Medical Image Computing and Computer-Assisted Intervention–MICCAI 2009**, pages 467–474, Springer, 2009.

[Pennec *et al.*, 1998] X. Pennec, C. R. Guttmann and J.-P. Thirion. **Feature-based registration of medical images: Estimation and validation of the pose accuracy**. In **Medical Image Computing and Computer-Assisted Interventation—MICCAI'98**, pages 1107–1114, Springer, 1998.

[Pennec *et al.*, 2005] X. Pennec, R. Stefanescu, V. Arsigny, P. Fillard and N. Ayache. **Riemannian elasticity: A statistical regularization framework for non-linear registration**. In **Medical Image Computing and Computer-Assisted Intervention–MICCAI 2005**, pages 943–950, Springer, 2005.

[Penney *et al.*, 2001] G. P. Penney, P. J. Edwards, A. P. King, J. M. Blackall, P. G. Batchelor and D. J. Hawkes. **A stochastic iterative closest point algorithm (stochastICP)**. In **Medical Image Computing and Computer-Assisted Intervention–MICCAI 2001**, pages 762–769, Springer, 2001.

[Peterhans *et al.*, 2009] M. Peterhans, B. Dagon, L.-P. Nolte, C. Baur, A. Vom Berg, D. Interbitzin and S. Weber. **Soft tissue navigation: Transferring pre-operative planning data into the operation room**. In **European Congress of Radiology**, no. LSRO-CONF-2009-008, 2009.

[Peterhans *et al.*, 2011] M. Peterhans, A. vom Berg, B. Dagon, D. Inderbitzin, C. Baur, D. Candinas and S. Weber. **A navigation system for open liver**

surgery: design, workflow and first clinical applications. The International Journal of Medical Robotics and Computer Assisted Surgery, vol. 7, no. 1, pages 7–16, 2011.

[Peterlík *et al.*, 2012] I. Peterlík, C. Duriez and S. Cotin. **Modeling and real-time simulation of a vascularized liver tissue**. In **Medical Image Computing and Computer-Assisted Intervention–MICCAI 2012**, pages 50–57, Springer, 2012.

[Peterlik *et al.*, 2014] I. Peterlik, H. Courtecuisse, C. Duriez and S. Cotin. **Model-based identification of anatomical boundary conditions in living tissues**. In **Information Processing in Computer-Assisted Interventions**, pages 196–205, Springer, 2014.

[Plantefève *et al.*, 2014a] R. Plantefève, N. Haouchine, J.-P. Radoux and S. Cotin. **Automatic Alignment of pre and intraoperative Data using Anatomical Landmarks for Augmented Laparoscopic Liver Surgery**. In **Biomedical Simulation**, pages 58–66, Springer, 2014a.

[Plantefève *et al.*, 2014b] R. Plantefève, I. Peterlik, H. Courtecuisse, R. Trivisonne, J.-P. Radoux and S. Cotin. **Atlas-based transfer of boundary conditions for biomechanical simulation**. In **Medical Image Computing and Computer-Assisted Intervention–MICCAI 2014**, pages 33–40, Springer, 2014b.

[Plantefève *et al.*, 2016] R. Plantefève, I. Peterlik, N. Haouchine and S. Cotin. **Patient-Specific Biomechanical Modeling for Guidance During Minimally-Invasive Hepatic Surgery**. Annals of biomedical engineering, vol. 44, no. 1, pages 139–153, 2016.

[Pratt *et al.*, 2010] P. Pratt, D. Stoyanov, M. Visentini-Scarzanella and G.-Z. Yang. **Dynamic guidance for robotic surgery using image-constrained biomechanical models**. In **Medical Image Computing and Computer-Assisted Intervention–MICCAI 2010**, pages 77–85, Springer, 2010.

[Pratt *et al.*, 2012] P. Pratt, E. Mayer, J. Vale, D. Cohen, E. Edwards, A. Darzi and G.-Z. Yang. **An effective visualisation and registration system for image-guided robotic partial nephrectomy**. Journal of Robotic Surgery, vol. 6, no. 1, pages 23–31, 2012.

[Quan *et al.*, 2012] D. Quan, S. Gallinger, C. Nhan, R. A. Auer, J. J. Biagi, G. G. Fletcher, C. H. Law, C.-A. E. Moulton, L. Ruo, A. C. Wei *et al.*. **The role of liver resection for colorectal cancer metastases in an era of multimodality treatment: a systematic review**. Surgery, vol. 151, no. 6, pages 860–870, 2012.

[Rauth *et al.*, 2007] T. P. Rauth, P. Q. Bao, R. L. Galloway, J. Bieszczad, E. M. Friets, D. A. Knaus, D. B. Kynor and A. J. Herline. **Laparoscopic surface scanning and subsurface targeting: implications for image-guided laparoscopic liver surgery**. Surgery, vol. 142, no. 2, pages 207–214, 2007.

[Reichard *et al.*, 2015] D. Reichard, S. Bodenstedt, S. Suwelack, B. Mayer, A. Preukschas, M. Wagner, H. Kenngott, B. Müller-Stich, R. Dillmann and S. Speidel. **Intraoperative on-the-fly organ-mosaicking for laparoscopic surgery**. Journal of Medical Imaging, vol. 2, no. 4, pages 045,001–045,001, 2015.

[Rethy *et al.*, 2013] A. Rethy, T. Langø and R. Mårvik. **Laparoscopic ultrasound for hepatocellular carcinoma and colorectal liver metastasis: an overview**. Surgical Laparoscopy Endoscopy & Percutaneous Techniques, vol. 23, no. 2, pages 135–144, 2013.

[Rivaz *et al.*, 2015] H. Rivaz, S. J.-S. Chen and D. L. Collins. **Automatic deformable MR-ultrasound registration for image-guided neurosurgery**. Medical Imaging, IEEE Transactions on, vol. 34, no. 2, pages 366–380, 2015.

[Röhl *et al.*, 2011] S. Röhl, S. Bodenstedt, S. Suwelack, H. Kenngott, B. Mueller-Stich, R. Dillmann and S. Speidel. **Real-time surface reconstruction from stereo endoscopic images for intraoperative registration**. In **SPIE Medical Imaging**, pages 796,414–796,414, International Society for Optics and Photonics, 2011.

[Rucker *et al.*, 2013] D. C. Rucker, Y. Wu, J. E. Ondrake, T. S. Pheiffer, A. L. Simpson and M. I. Miga. **Nonrigid liver registration for image-guided surgery using partial surface data: A novel iterative approach**. In **SPIE Medical Imaging**, pages 86,710B–86,710B, International Society for Optics and Photonics, 2013.

[Rueckert *et al.*, 1999] D. Rueckert, L. I. Sonoda, C. Hayes, D. L. Hill, M. O. Leach and D. J. Hawkes. **Nonrigid registration using free-form deformations: application to breast MR images**. Medical Imaging, IEEE Transactions on, vol. 18, no. 8, pages 712–721, 1999.

[Salvi *et al.*, 2002] J. Salvi, X. Armangué and J. Batlle. **A comparative review of camera calibrating methods with accuracy evaluation**. Pattern recognition, vol. 35, no. 7, pages 1617–1635, 2002.

[Schmalz *et al.*, 2012] C. Schmalz, F. Forster, A. Schick and E. Angelopoulou. **An endoscopic 3D scanner based on structured light**. Medical image analysis, vol. 16, no. 5, pages 1063–1072, 2012.

[Schneider *et al.*, 2013] C. Schneider, C. Nguan, M. Longpre, R. Rohling and S. Salcudean. **Motion of the kidney between preoperative and intraoperative positioning**. Biomedical Engineering, IEEE Transactions on, vol. 60, no. 6, pages 1619–1627, 2013.

[Schneider, 1990] P. J. Schneider. **An algorithm for automatically fitting digitized curves**. In **Graphics gems**, pages 612–626, Academic Press Professional, Inc., 1990.

[Shekhar *et al.*, 2010] R. Shekhar, O. Dandekar, V. Bhat, M. Philip, P. Lei, C. Godinez, E. Sutton, I. George, S. Kavic, R. Mezrich *et al.*. **Live augmented reality: a new visualization method for laparoscopic surgery using continuous volumetric computed tomography**. Surgical endoscopy, vol. 24, no. 8, pages 1976–1985, 2010.

[Shewchuk, 2002] J. Shewchuk. **What is a good linear finite element? interpolation, conditioning, anisotropy, and quality measures (preprint)**. University of California at Berkeley, vol. 73, 2002.

[Shewchuk, 1994] J. R. Shewchuk. **An introduction to the conjugate gradient method without the agonizing pain**. Tech. rep., 1994.

[Shewchuk, 1998] J. R. Shewchuk. **Tetrahedral mesh generation by Delaunay refinement**. In **Proceedings of the fourteenth annual symposium on Computational geometry**, pages 86–95, ACM, 1998.

[Shiina *et al.*, 2012] S. Shiina, R. Tateishi, T. Arano, K. Uchino, K. Enooku, H. Nakagawa, Y. Asaoka, T. Sato, R. Masuzaki, Y. Kondo *et al.*. **Radiofrequency ablation for hepatocellular carcinoma: 10-year outcome and prognostic factors**. The American journal of gastroenterology, vol. 107, no. 4, pages 569–577, 2012.

[Shirabe *et al.*, 1997] K. Shirabe, K. Takenaka, T. Gion, Y. Fujiwara, M. Shimada, K. Yanaga, T. Maeda, K. Kajiyama and K. Sugimachi. **Analysis of prognostic risk factors in hepatic resection for metastatic colorectal carcinoma with special reference to the surgical margin**. British journal of surgery, vol. 84, no. 8, pages 1077–1080, 1997.

[Simillis *et al.*, 2007] C. Simillis, V. A. Constantinides, P. P. Tekkis, A. Darzi, R. Lovegrove, L. Jiao and A. Antoniou. **Laparoscopic versus open hepatic resections for benign and malignant neoplasms — a meta-analysis**. Surgery, vol. 141, no. 2, pages 203–211, 2007.

[Škrinjar *et al.*, 2002] O. Škrinjar, A. Nabavi and J. Duncan. **Model-driven brain shift compensation**. Medical image analysis, vol. 6, no. 4, pages 361–373, 2002.

[Slawinski, 2007] M. Slawinski. **Waves and rays in elastic media**. San Francisco, California: Creative Commons, pages 118–119, 2007.

[Song *et al.*, 2015] Y. Song, J. Totz, S. Thompson, S. Johnsen, D. Barratt, C. Schneider, K. Gurusamy, B. Davidson, S. Ourselin, D. Hawkes *et al.*. **Locally rigid, vessel-based registration for laparoscopic liver surgery**. International journal of computer assisted radiology and surgery, vol. 10, no. 12, pages 1951–1961, 2015.

[Sotiras *et al.*, 2013] A. Sotiras, C. Davatzikos and N. Paragios. **Deformable medical image registration: A survey**. Medical Imaging, IEEE Transactions on, vol. 32, no. 7, pages 1153–1190, 2013.

[Su *et al.*, 2009] L.-M. Su, B. P. Vagvolgyi, R. Agarwal, C. E. Reiley, R. H. Taylor and G. D. Hager. **Augmented reality during robot-assisted laparoscopic partial nephrectomy: toward real-time 3D-CT to stereoscopic video registration**. Urology, vol. 73, no. 4, pages 896–900, 2009.

[Sun *et al.*, 2013] Y. Sun, J. Yuan, M. Rajchl, W. Qiu, C. Romagnoli and A. Fenster. **Efficient convex optimization approach to 3D non-rigid MR-TRUS registration**. In **Medical Image Computing and Computer-Assisted Intervention–MICCAI 2013**, pages 195–202, Springer, 2013.

[Suwelack *et al.*, 2014] S. Suwelack, S. Röhl, S. Bodenstedt, D. Reichard, R. Dillmann, T. dos Santos, L. Maier-Hein, M. Wagner, J. Wünscher, H. Kenngott *et al.*. **Physics-based shape matching for intraoperative image guidance**. Medical physics, vol. 41, no. 11, page 111,901, 2014.

[Suzuki *et al.*, 2006] A. Suzuki, K. Kamiya and K. Yasuda. **Identification technique for nonlinear boundary conditions of a circular plate**. J. of Sound and Vibration, vol. 289, no. 1–2, 2006, ISSN 0022-460X.

[The CGAL Project, 2015] The CGAL Project. **CGAL User and Reference Manual**. CGAL Editorial Board, 4.7 ed., 2015.

[Toni *et al.*, 2015] Y. Toni, A. Belhaoua and J.-P. Radoux. **Real-Time Surgical Tools Tracking based on Markerbased Approach**. In **International Workshop on Learning Semantics for Multimedia Big Data, ACPR**, Springer, 2015.

[Torzilli *et al.*, 2013] G. Torzilli, J. Belghiti, N. Kokudo, T. Takayama, L. Capussotti, G. Nuzzo, J.-N. Vauthey, M. A. Choti, E. De Santibanes, M. Donadon *et al.*. **A snapshot of the effective indications and results of surgery for hepatocellular carcinoma in tertiary referral centers: is it adherent to the EASL/AASLD recommendations?: an observational study of the**

HCC East-West study group. Annals of surgery, vol. 257, no. 5, pages 929–937, 2013.

[Tournois *et al.*, 2009] J. Tournois, R. Srinivasan and P. Alliez. **Perturbing slivers in 3D Delaunay meshes**. In **Proceedings of the 18th international meshing roundtable**, pages 157–173, Springer, 2009.

[Tsai, 1989] R. Tsai. **Synopsis of recent progress on camera calibration for 3D machine vision**. MIT Press, 1989.

[Tsutsumi *et al.*, 2013] N. Tsutsumi, M. Tomikawa, M. Uemura, T. Akahoshi, Y. Nagao, K. Konishi, S. Ieiri, J. Hong, Y. Maehara and M. Hashizume. **Image-guided laparoscopic surgery in an open MRI operating theater**. Surgical endoscopy, vol. 27, no. 6, pages 2178–2184, 2013.

[Turgeon *et al.*, 2005] G.-A. Turgeon, G. Lehmann, G. Guiraudon, M. Drangova, D. Holdsworth and T. Peters. **2D-3D registration of coronary angiograms for cardiac procedure planning and guidance**. Medical physics, vol. 32, no. 12, pages 3737–3749, 2005.

[Umale *et al.*, 2011] S. Umale, S. Chatelin, N. Bourdet, C. Deck, M. Diana, P. Dhumane, L. Soler, J. Marescaux and R. Willinger. **Experimental in vitro mechanical characterization of porcine Glisson's capsule and hepatic veins**. Journal of biomechanics, vol. 44, no. 9, pages 1678–1683, 2011.

[Vappou, 2012] J. Vappou. **Magnetic Resonance- and Ultrasound Imaging-Based Elasticity Imaging Methods: A Review**. Critical Reviews™ in Biomedical Engineering, vol. 40, no. 2, 2012.

[Vercauteren *et al.*, 2007] T. Vercauteren, X. Pennec, A. Perchant and N. Ayache. **Non-parametric diffeomorphic image registration with the demons algorithm**. Medical Image Computing and Computer-Assisted Intervention–MICCAI 2007, pages 319–326, 2007.

[Verscheure *et al.*, 2013] L. Verscheure, L. Peyrodie, A.-S. Dewalle, N. Reyns, N. Betrouni, S. Mordon and M. Vermandel. **Three-dimensional skeletonization and symbolic description in vascular imaging: preliminary results**. International journal of computer assisted radiology and surgery, vol. 8, no. 2, pages 233–246, 2013.

[Vibert *et al.*, 2006] E. Vibert, T. Perniceni, H. Levard, C. Denet, N. Shahri and B. Gayet. **Laparoscopic liver resection**. British Journal of Surgery, vol. 93, no. 1, pages 67–72, 2006.

[Vigano *et al.*, 2009] L. Vigano, C. Tayar, A. Laurent and D. Cherqui. **Laparoscopic liver resection: a systematic review**. Journal of hepato-biliary-pancreatic surgery, vol. 16, no. 4, pages 410–421, 2009.

[Vijayan *et al.*, 2013] S. Vijayan, S. Klein, E. F. Hofstad, F. Lindseth, B. Ystgaard and T. Lango. **Validation of a non-rigid registration method for motion compensation in 4D ultrasound of the liver**. In **Biomedical Imaging (ISBI), 2013 IEEE 10th International Symposium on**, pages 792–795, IEEE, 2013.

[Wang *et al.*, 2012] H. Wang, D. B. Stout and A. Chatziioannou. **Estimation of Mouse Organ Locations Through Registration of a Statistical Mouse Atlas With Micro-CT Images.** IEEE Trans. Med. Imaging, vol. 31, no. 1, pages 88–102, 2012.

[Wei *et al.*, 2013] A. C. Wei, L. Sandhu, K. S. Devitt, A. R. Gagliardi, E. D. Kennedy, D. R. Urbach, S. Gallinger and N. N. Baxter. **Practice patterns for the management of hepatic metastases from colorectal cancer: a mixed methods analysis**. Annals of surgical oncology, vol. 20, no. 5, pages 1567–1574, 2013.

[Wittek *et al.*, 2007] A. Wittek, K. Miller, R. Kikinis and S. K. Warfield. **Patient-specific model of brain deformation: Application to medical image registration**. Journal of biomechanics, vol. 40, no. 4, pages 919–929, 2007.

[Wittek *et al.*, 2009] A. Wittek, T. Hawkins and K. Miller. **On the unimportance of constitutive models in computing brain deformation for image-guided surgery**. Biomechanics and modeling in mechanobiology, vol. 8, no. 1, pages 77–84, 2009.

[Wu *et al.*, 2014] Y. Wu, D. C. Rucker, R. H. Conley, T. S. Pheiffer, A. L. Simpson, S. K. Geevarghese and M. I. Miga. **Registration of liver images to minimally invasive intraoperative surface and subsurface data**. In **SPIE Medical Imaging**, pages 90,360V–90,360V, International Society for Optics and Photonics, 2014.

[Xu and Zhang, 1996] G. Xu and Z. Zhang. **Epipolar geometry in stereo, motion and object recognition: a unified approach**, vol. 6. Springer Science & Business Media, 1996.

[Yushkevich *et al.*, 2006] P. A. Yushkevich, J. Piven, H. Cody Hazlett, R. Gimpel Smith, S. Ho, J. C. Gee and G. Gerig. **User-Guided 3D Active Contour Segmentation of Anatomical Structures: Significantly Improved Efficiency and Reliability**. Neuroimage, vol. 31, no. 3, pages 1116–1128, 2006.

[Zhang *et al.*, 2011] W. Zhang, J. M. Brady, H. Becher and J. A. Noble. **Spatio-temporal (2D+ T) non-rigid registration of real-time 3D echocardiography and cardiovascular MR image sequences**. Physics in medicine and biology, vol. 56, no. 5, page 1341, 2011.

[Zhang *et al.*, 2014] Y. Zhang, S. B. White, J. R. Nicolai, Z. Zhang, D. L. West, D.-h. Kim, A. L. Goodwin, F. H. Miller, R. A. Omary and A. C. Larson. **Multimodality imaging to assess immediate response to irreversible electroporation in a rat liver tumor model**. Radiology, vol. 271, no. 3, pages 721–729, 2014.

[Zhang, 2000] Z. Zhang. **A flexible new technique for camera calibration**. Pattern Analysis and Machine Intelligence, IEEE Transactions on, vol. 22, no. 11, pages 1330–1334, 2000.

[Zheng *et al.*, 2002] G. Zheng, A. Marx, U. Langlotz, K.-H. Widmer, M. Buttaro and L.-P. Nolte. **A hybrid CT-free navigation system for total hip arthroplasty**. Computer Aided Surgery, vol. 7, no. 3, pages 129–145, 2002.

[Zheng *et al.*, 2007] G. Zheng, X. Dong and M. A. G. Ballester. **Unsupervised reconstruction of a patient-specific surface model of a proximal femur from calibrated fluoroscopic images**. In **Medical Image Computing and Computer-Assisted Intervention–MICCAI 2007**, pages 834–841, Springer, 2007.

[Zhou and Jiao, 2013] B. Zhou and D. Jiao. **A linear complexity direct finite element solver for large-scale 3-D electromagnetic analysis**. In **Antennas and Propagation Society International Symposium (APSURSI), 2013 IEEE**, pages 1684–1685, IEEE, 2013.